



TECHNISCHE  
UNIVERSITÄT  
WIEN

Dissertation

# **Vibrational Circular Dichroism in the liquid phase – Opportunities through mid-IR lasers**

A thesis submitted for the degree of  
Doctor of Technical Sciences (Dr. techn.)

at

Technische Universität Wien

Faculty of Technical Chemistry

Institute of Chemical Technologies and Analytics

under supervision of

Univ. Prof. Dr. Bernhard Lendl

&

Dr. Georg Ramer

defended by

**Daniel-Ralph Hermann, MSc**

Mat. Nr. 51818034

Vienna, July 2024



*“No one can pass through life, any more than he can pass through a bit of country, without leaving tracks behind, and those tracks may often be helpful to those coming after him in finding their way.”*  
- Robert Baden-Powell



## Abstract

Chirality refers to the inability of a compound to be superimposed on its mirror structure. This characteristic is prevalent in the biochemical world, occurring both in small molecules as well as in the large structures of enzymes and receptors. Due to this broad occurrence of chirality, a closer understanding of the specific chirality of a given analyte is essential in fields such as pharmaceutical production or catalysis.

One of the most versatile chiral analytical methods is vibrational circular dichroism (VCD), which relies on the difference in absorbance for left and right-handed circular polarized light. Due to its operation in the infrared spectral region, it is broadly applicable for the study of organic and inorganic molecules. However, VCD is also characterized by its low signal intensity, commonly in the order of  $10^{-5}$  less compared to its absorbance counterpart. As a result, typical measurements using state of the art Fourier-transform infrared (FT-IR) spectrometers require several hours of averaging to achieve satisfactory signal to noise ratios (SNR), limiting its applicability to carefully controlled end of the line experiments instead of possible monitoring applications.

In this thesis a quantum cascade laser (QCL) based VCD system was constructed as a possible way to counteract the challenges of VCD measurements. QCLs constitute high power, tunable lasers in the mid-infrared region. Their inherently polarized emission lends itself well to VCD applications. The constructed system was based on a balanced detection scheme, which compensates for the intensity noise introduced by the light source. In this way it was possible to report for the first time the outperformance of FT-IR-VCD in terms of SNR and acquisition time. It was possible to record low noise VCD spectra at measurement times of a few minutes. Indeed, this enabled monitoring of chiral changes at a time resolution below 3 minutes for small molecules in organic solvents. Dedicated chemometrics were explored to further advance the instrument design as sensor application.

QCL-VCD was further employed to explore secondary structure evaluation of proteins in solution. For this, the system was optimized by tailoring the emission spectrum in order to compensate for the strong absorbance of  $\text{H}_2\text{O}$ . Therefore a longer pathlength ( $26\text{ }\mu\text{m}$  vs  $8\text{ }\mu\text{m}$ ) could be used and concentrations down to  $10\text{ mg/mL}$  were accessible. Following this, even lower concentrated solutions were investigated by switching from  $\text{H}_2\text{O}$  to  $\text{D}_2\text{O}$  and increase the pathlength to  $204\text{ }\mu\text{m}$ . With the constructed QCL-VCD system it was possible to measure low concentrations of proteins in  $\text{D}_2\text{O}$  down to  $2\text{ mg/mL}$  over the amide I and amide II spectral range at 1 h measurement time. Since most of the structural information is contained in the amide I band, the laser could be set to only cover this area. This enabled secondary structure evaluations at a measurement time of 5 minutes. This is a significant improvement compared to the FT-IR measurement time for the equivalent noise which was 40 min. This proved both the versatility of QCL-VCD and also the potential applications it enables, ranging from sensor design to protein structure evaluation at a dynamic level.

**Keywords:** Mid-infrared spectroscopy | Vibrational circular dichroism | Quantum cascade lasers | Chiral monitoring | Liquid-phase analytics | Protein analytics

## Kurzfassung

Unter Chiralität versteht man die Unfähigkeit einer Verbindung, sich mit ihrem Spiegelbild zu überlagern. Diese Eigenschaft ist in der biochemischen Welt weit verbreitet, sie kommt sowohl in kleinen Molekülen als auch in den großen Strukturen von Enzymen und Rezeptoren vor. Aufgrund dieses breiten Vorkommens von Chiralität ist ein genaueres Verständnis der spezifischen Chiralität eines bestimmten Analyten in Bereichen wie der pharmazeutischen Produktion oder der Katalyse von entscheidender Bedeutung.

Eine der vielseitigsten chiralen Analysemethoden ist Vibrationszirkulardichroismus (VCD), der auf dem Unterschied in der Absorption für links- und rechtsdrehend zirkular polarisiertes Licht beruht. Da die Technik im infraroten Spektralbereich arbeitet, ist sie für die Untersuchung organischer und anorganischer Moleküle vielseitig einsetzbar. VCD zeichnet sich jedoch auch durch eine geringe Signalintensität aus, die üblicherweise in der Größenordnung von  $10^{-5}$  weniger im Vergleich zu seinem Gegenstück in der Absorption liegt. Daher erfordern typische Messungen mit Stand der Technik Fourier-transform infrared (FT-IR) Instrumenten Mittelungen über mehrere Stunden, um zufriedenstellende Signal-Rausch-Verhältnisse (SNR) zu erzielen, was ihre Anwendbarkeit auf sorgfältig kontrollierte End-of-the-Line-Experimente anstelle möglicher Monitoring-Anwendungen einschränkt.

In dieser Arbeit wurde ein auf einem Quantenkaskadenlaser (QCL) basierendes VCD-System konstruiert, um die Herausforderungen von VCD-Messungen auszugleichen. QCLs sind leistungsstarke, durchstimmbare Laser im Infrarotbereich. Ihre inhärent polarisierte Emission eignet sich gut für VCD-Anwendungen. Das konstruierte System basierte auf einem „Balanced detection“ Schema, dass das durch die Lichtquelle verursachte Intensitätsrauschen kompensiert. Auf diese Weise war es erstmals möglich, eine bessere Leistung als Fourier-Transform-Infrarot (FT-IR) VCD in Bezug auf SNR und Aufnahmezeit zu melden. Es konnten rauscharme VCD-Spektren bei Messzeiten von wenigen Minuten aufgenommen werden. Dies ermöglichte tatsächlich die Überwachung chiraler Veränderungen mit einer Zeitauflösung von weniger als 3 Minuten für kleine Moleküle in organischen Lösungsmitteln. Dezidierte Chemometrie wurde untersucht, um das Instrumentendesign als Sensoranwendung weiter voranzutreiben.

QCL-VCD wurde außerdem eingesetzt, um die Sekundärstrukturanalyse von Proteinen in Lösungen zu untersuchen. Dafür wurde das System optimiert indem das Emissionsspektrum angepasst hat um die starke Absorption von  $\text{H}_2\text{O}$  zu kompensieren. Daher konnte eine längere Schichtdicke ( $26\text{ }\mu\text{m}$  gegenüber  $8\text{ }\mu\text{m}$ ) verwendet werden und Konzentrationen bis hinunter zu  $10\text{ mg/mL}$  waren messbar. Anschließend wurden noch niedriger konzentrierte Lösungen untersucht, indem von  $\text{H}_2\text{O}$  auf  $\text{D}_2\text{O}$  umgestellt hat und die Schichtdicke auf  $204\text{ }\mu\text{m}$  erhöht wurde. Mit dem konstruierten QCL-VCD-System war es möglich, niedrige Proteinkonzentrationen in  $\text{D}_2\text{O}$  bis hinunter zu  $2\text{ mg/mL}$  über den Amid-I- und Amid-II-Spektralbereich bei einer Messzeit von 1 Stunde zu messen. Da die meisten Strukturinformationen im Amid-I-Band enthalten sind, konnte der Laser so eingestellt werden, dass er nur diesen Bereich abdeckte. Dies ermöglichte Sekundärstrukturanalysen bei einer Messzeit von 5 Minuten. Dies ist eine erhebliche Verbesserung im Vergleich zur FT-IR-Messzeit für das äquivalente Rauschen, die 40 Minuten betrug. Dies bewies sowohl die Vielseitigkeit von QCL-VCD als auch die damit verbundenen potenziellen Anwendungsmöglichkeiten, die vom Sensordesign bis zur Bewertung der Proteinstruktur auf dynamischer Ebene reichen.

**Schlagworte:** Mid-infrarot Spektroskopie | Vibrationszirkulardichroismus | Quantenkaskadenlaser | Chirales Monitoring | Flüssigphasen Analytik | Proteinanalytik

## Acknowledgements

On a research project of 4+ years there are numerous challenges that can and will occur. Luckily for me, there were even more people to provide advice and support, and who in turn deserve my thanks.

Firstly, I would like to thank my supervisors Bernhard Lendl and Georg Ramer. Bernhard, thank you for the opportunity to join your research group and also for your input on the broader context of the research as well as on the planning of further research. The research of our group as well as the group itself is proof of your ability in regards to science, funding acquisition and also on a personal level. And I will try to refrain from using “quite” during presentations from now on.

Georg thank you for all the help and support and for welcoming me to the world of lasers (and python). Without your understanding of all things laser (and more or less everything else), implementing VCD would have been impossible and I would have probably quit somewhere around EOM iteration 5. Thank you for your advice, time and all the memes.

I would also like to thank Markus for all the help on understanding polarization phenomena and on the work you spent on the EOM setup.

I would also like to thank all the current and former members of the CAVS research group: Stephan, Bettina, Karim, Catarina, Dominik, Felix, Stefan, Elisabeth, Harald, Karin, Paul, Nikolaus, Pily, Markus, Daniela, Shilpa, Leo, Margaux, Giovanna, Davide, Alicja, Alina, Andreas, Giulia, Iskander, Jesus, Miranda, Savda, Sebastian, Yide, Elizandra, Gustavo, Adea, Alex, Lena, Lisa, Verena and Ufuk. Even when everything in the lab goes wrong, it is only  $\sim 1/e^2$  as bad as it could be when you have colleagues and friends like you all.

Stephan, your introduction to the day to day work in the lab as well as to 3d design and printing has helped me numerous times during the last years and made my life so much easier.

Pily, without you the group would probably have collapsed at some point. Thank you for all the work you do to keep the finances and bureaucracy at bay. Also thank you for being supportive and welcoming to all new members of the group.

Special thanks to all the people in the liquid lab, for providing an awesome working environment and all the joint troubleshooting actions. Alicja, it was a pleasure to share an optical table and the best (non-) scientific discussions with you. Neighbors are always an important thing to consider, both in real estate and in the lab. Fortunately, I had the best lab neighbor in Giovanna, thank you for our motivational talks when things were not working at they should (dry air, leaking cells,...). Jesus, thank you for being probably the friendliest person I know, and another good lab neighbor, even though private space was something neither of us had in the lab. Shilpa, thank you for being a constant companion in the lab, in the boulder hall, for a quick coffe and at concerts. And please do not kill me with the “Strafschnaps”. Catarina thank you for being just a good person overall (if the coffee machine is correctly used) and a perfect travel companion, across multiple continents. Andreas, thank you for all the support and advice you had for me and everyone else that asked. Elisabeth, with the amount of time you spent at the Hyperion I would count you as non-newtonian fluid group member. Thank you for always being up for a motivational talk.

Of course people deserving of special thanks do not only work in the liquid lab. Davide, thanks for

your humor, good nature and your willingness to always have more coffee. The coffee list is no fun without competition. Ufuk, thank you for always being up for a good talk and coffee, and all the work with the coffee machine, and sorry about the shoulder. And also, just thank you, because that is the law.

Besides the friends I found at TU, I would also like to thank all my friends from Upper and Lower Austria.

For the former, I would like to thank all the Schwochswoaba for being always motivated for everything, for helping when possible and for sticking with me since basically forever.

For the latter, I would like to thank all Marumerizers, both for keeping me sane enough during my previous studies, and for being just good friends and people overall. And sorry Sandra, by now you are long enough in Lower Austria that you can't complain about being counted as such.

I would also like to thank my family for always supporting me and trusting my decisions. I could not have done anything I have achieved without your love and support.

Finally, I would like to thank my girlfriend Conny, for always being understanding even though I rarely stopped talking about work long. You always know how to keep me from spiraling and supported me through all ups and downs. Without you I am pretty sure I would have not made it that far. You helped me immensely by just being you, and that all without trying to wrap me in bubble wrap.

## Table of Content

Abstract.....	v
Kurzfassung.....	vi
Acknowledgements.....	vii
Table of Content.....	ix
Abbreviations.....	x
Symbols.....	xi
<b>1. Introduction .....</b>	<b>1</b>
1.1 <i>Motivation and scope of the work</i> .....	1
1.2 <i>Chirality in the chemical world</i> .....	1
1.2.1     Definitions and impact of chirality .....	2
1.2.2     Chiral analytics.....	3
<b>2. Vibrational circular dichroism.....</b>	<b>6</b>
2.1 <i>Fundamentals of spectroscopy</i> .....	7
2.2 <i>Vibrational transitions</i> .....	10
2.2.1     Harmonic vs. anharmonic oscillator .....	10
2.2.2     IR absorption processes.....	13
2.2.3     Coupled oscillators .....	14
2.2.4     Oscillators in optical active molecules.....	16
2.3 <i>Instrumentation for vibrational circular dichroism</i> .....	19
2.4 <i>Mid-IR laser technology</i> .....	25
<b>3. Laser based Vibrational Circular Dichroism .....</b>	<b>30</b>
3.1 <i>Synergies between quantum cascade lasers and vibrational circular dichroism</i> .....	31
3.2 <i>Laser based vibrational circular dichroism</i> .....	32
3.2.1     Challenges of laser based vibrational circular dichroism .....	32
3.2.2     Balanced detection for laser spectroscopy .....	35
3.2.3     Development of low noise laser based vibrational circular dichroism.....	36
3.2.4     Steps towards chiral monitoring.....	39
3.2.5     Proteins – Chirality in macromolecules studied by QCL-VCD .....	45
3.3 <i>Further opportunities for QCL-VCD technology</i> .....	56
3.3.1     High frequency polarization modulation.....	56
<b>4. Conclusions and outlook .....</b>	<b>60</b>
<b>Bibliography .....</b>	<b>62</b>
<b>Appendix .....</b>	<b>73</b>
Appendix A: <i>Published scientific papers</i> .....	73
Appendix B: <i>Curriculum Vitae</i> .....	101

## Abbreviations

1,1'-bi-2-naphthol	BINOL
Antireflective	AR
Atomic force microscope	AFM
Beam splitter	BS
Bovine serum albumin	BSA
Capillary electrophoresis	CE
Chemical Analysis and Vibrational Spectroscopy	CAVS
Common mode rejection ratio	CMRR
Continuous wave	CW
Critical process parameter	CPP
Critical quality attributes	CQA
degree of freedom	DOF
Difference-frequency generation	DFG
Distributed feedback lasers	DFB
Electronic circular dichroism	ECD
Electro-optical modulator	EOM
Enantiomeric excess	EE
European Medicines Agency	EMA
External cavity	EC
External cavity quantum cascade laser	EC-QCL
Fabry-Pérot	FP
Far-infrared	FIR
Federal drug administration	FDA
Fourier-transform Infrared	FT-IR
Infrared	IR
International Union of Pure and Applied Chemistry	IUPAC
Inter-subband	ISB
Latent variables	LV
Least absolute shrinkage and selection operator	Lasso
Limit of detection	LOD
Mercury-cadmium-telluride	MCT
Mid-infrared	mid-IR
Near-infrared	NIR
Nuclear resonance spectroscopy	NMR
Optical parametric oscillator	OPO
Optical rotation	OR
Partial least squares regression	PLSR
Photoelastic modulator	PEM
Process analytical technology	PAT
Quantum cascade laser	QCL
Raman optical activity	ROA
Root mean square	RMS
Root mean square error of cross validation	RMSECV
Root mean square error of prediction	RMSEP
Signal-noise ratio	SNR
Transistor-transistor logic	TTL
Ultraviolet-visible	UV-vis
Vibrational circular dichroism	VCD

## Symbols

Absorbance	$A$
Amplitude of electric field in direction x	$E_x$
Amplitude of electric field in direction y	$E_y$
Angle of incidence	$\theta_i$
Angular frequency	$\omega$
Atomic charge	$e_i$
Concentration	$c$
Difference in molar concentration	$diffM$
Dipole moment	$\mu$
Electronic transition dipole moment	$\vec{\mu}_T$
Enantiomeric Excess	$EE$
Finesse	$F$
Free spectral range	$\Delta\omega_r$
Frequency	$\nu$
Intensity of IR single channel spectrum	$I_{DC}$
Intensity of the chiral intensity	$I_{AC}$
Magnetic dipole transition moment	$m_T$
Optical path difference	$\delta$
Pathlength	$d$
PEM phase shift	$\alpha_M^0$
Phase shift	$\Delta\phi$
Planck constant	$h$
Quantum number	$v_i$
Refractive index at a defined wavelength	$n_\lambda$
Rotational strength	$R$
Speed of light	$c$
Stokes parameters	$S_0, S_1, S_2, S_3$
Transmission	$T$
Vibrational amplitude	$Q$
Vibrational circular dichroism	$\Delta A$
Wavelength	$\lambda$
Wavenumber	$\bar{\nu}$



# 1. Introduction

---

## 1.1 Motivation and scope of the work

The mid-infrared (mid-IR) is an information rich spectral region, containing structural information on nearly all organic molecules. In addition, this information is accessible in a label-free and non-destructive manner through vibrational spectroscopy. This wealth of information can be even further increased by adding a chiral dimension to the analytical workflow, a technique called vibrational circular dichroism (VCD). However, this added dimension also comes with additional challenges, since the low intensity of chiral signals necessitates very low noise floors, corresponding to long measurement times.<sup>1</sup>

Around the same time the first commercial VCD instruments were introduced, the field of vibrational spectroscopy was revolutionized by the development of quantum cascade lasers (QCL). Providing powerful, highly polarized and coherent laser light in the mid-IR range, they opened additional avenues for accessing the vibrational information outside of classical absorption techniques. Besides new techniques, adaptations of already established methods to include laser spectroscopy had the potential of improving sensitivity and time resolution. One of the fields that would obviously improve significantly by the implementation of QCLs is VCD. Since VCD relies on quantifying small differences in the absorption of alternately circular polarized light, a powerful, inherently polarized light source seems to be the perfect fit. Indeed, the first combination of QCL and VCD technology was published in 2011.<sup>2</sup> However, by the time this thesis was started QCL based VCD measurements had yet to outperform commercial instruments and no new developments were reported.<sup>3,4</sup>

The work presented in this thesis was performed in the research group for Process Analytics, internationally known as Chemical Analysis and Vibrational Spectroscopy (CAVS), at TU Wien. This group is headed by Prof. Bernhard Lendl, and its research revolves around solving analytical challenges by vibrational spectroscopy, with an emphasis on developing novel optical systems. Consequently, the aim was to improve upon QCL-VCD spectroscopy and help to realize its potential as an important analytical technique. This endeavor was based on combining the experience present in the research group on low noise laser spectroscopy with the new avenue of QCL-VCD.

## 1.2 Chirality in the chemical world

To better understand the importance of VCD, it needs to be evaluated in the broader context of chirality, its implications for biological organisms and state of the art analytical methods. This will

---

be done in the following, with an emphasis on when which method could prove to be the superior analytical tool to solve a given research question.

### 1.2.1 Definitions and impact of chirality

In the International Union of Pure and Applied Chemistry (IUPAC) Compendium of Chemical Terminology (= "Gold Book") chirality is defined as a "The geometric property of a rigid object (or spatial arrangement of points or atoms) of being non-superposable on its mirror image".<sup>5</sup> Chirality is of interest to a large variety of fields, but for the purposes of the chemical world, the "spatial arrangement of [...]atoms" takes center stage.<sup>5</sup> This characteristic can be found in both inorganic and organic molecules and also be present regardless of the state of matter.<sup>6,7</sup> In the chemical world, the main focus of chiral studies is on organic molecules based on a carbon backbone.<sup>8</sup> The most basic form of chirality in the organic world is the result of a change in rotation at a single carbon atom (called carbon center), resulting in a pair of molecules called enantiomers. An example of this can be seen in Figure 1, which shows the enantiomers of the pharmaceutical active ingredient thalidomide.

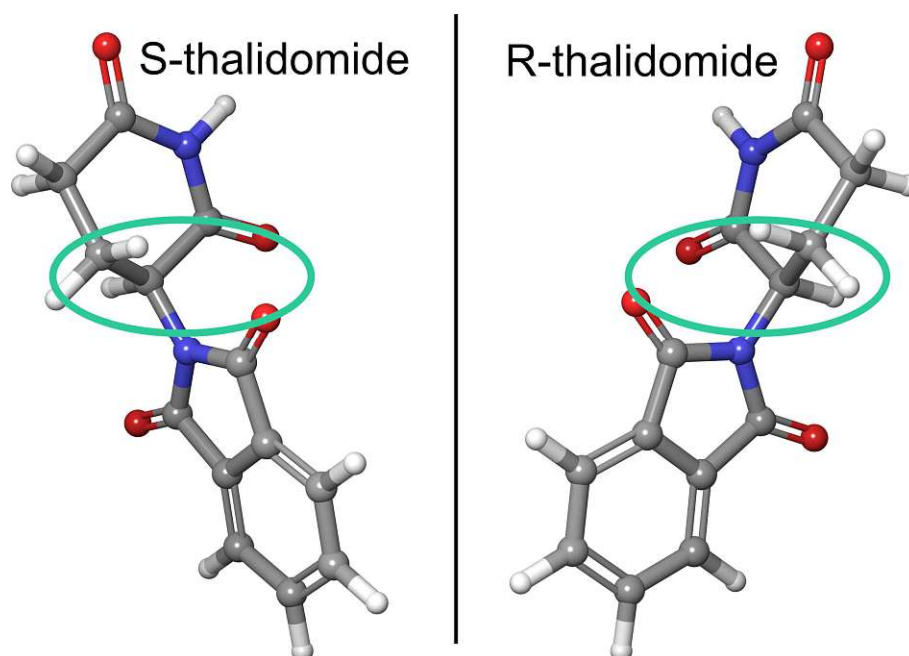


**Figure 1 | The two enantiomers of the pharmaceutical active ingredient thalidomide. The chiral center is marked by the green ellipse.**

Should an equal amount of both enantiomers be present, the mixture would be defined as a racemate, or racemic mixture, and express no sum chirality. In more complex molecules, two or more chiral centers can exist, resulting in several possible stereoisomers. If the molecules differ on more than one, but not all chiral centers, they are called diastereomers, if they differ on all of them they are again classified as enantiomers.<sup>9,10</sup> Quinine is a well-known example of a system of diastereomers, with its multiple conformers exhibiting differences in their chemical activity.<sup>9</sup> However, the most prominent source of chirality is the biological world, including the human body. This aspect begins on the smallest level, with a universal preference in most organisms for the L-form of the proteinogenic amino acids. As a consequence, chemical reactions catalyzed by enzymes (made up of only L-amino acids) show a stereoselectivity.<sup>11</sup> In addition to the chirality of their building blocks, protein exhibit macromolecular chirality as well.<sup>12,13</sup> Due to the different residuals of the amino acids making up a protein and their sequence along the chain, different secondary

structures are formed. The secondary structure is a combination of  $\beta$ -sheets,  $\alpha$ -helices and turns, which then in turn define the proteins tertiary structure.<sup>12,14</sup> Protein chemistry relies heavily on enzymatic reactions, during which the correct reaction partners are brought into close contact as a result of the interaction between the proteins structure and the substrate. It can therefore be reasoned that understanding the chirality involved with proteins forms the basis for understanding their behavior, as the majority of their structure can be directly linked to their chirality.<sup>15,16</sup>

With chirality ingrained in the basic workings of the human body, it stands to reason that the whole organism expresses significant stereoselectivity in its interaction with chemical agents. A benign example of this is the smell of limonene, either reminiscent of lemons or of oranges, depending on the enantiomer present.<sup>12</sup> However, the less then benign ramifications have galvanized the interest in chirality and resulted in regulatory consequences. The text book example for a negative impact of chirality is the thalidomide scandal of the 1950s-1960s.<sup>11,17,18</sup> Thalidomide, see Figure 1, is a pharmaceutical agent possessing one chiral center, resulting in two enantiomers, and was marketed as a sleeping agent or sedative. Since it was effective for this indication, it was also marketed to relieve morning sickness during pregnancy. However, thalidomide, more precisely its S-enantiomer, also possesses teratogenic properties. This characteristic and its specific marketing group lead to thousands of children being born with limb deformities, causing public outrage and judicial consequences for the scientists and officials involved in releasing this drug to the market.<sup>10,11,17</sup> Later research on the drug rebutted the simplification that an enantiomeric pure drug could have prevented the tragedy, as significant *in-vivo* racemization seems to play a role for thalidomide's toxicity.<sup>10,17</sup> Nevertheless, it was made clear that an accurate understanding of a promising drug's chirality is essential to prevent adverse effects and improve efficacy. Indeed, proceedings specifically addressing chiral drug design with an emphasis on enantiopurity have been implemented by the European Medicines Agency (EMA) since 1994.<sup>11</sup>

Consequently, drug design has raced to implement both asymmetric synthetic routes as well as chiral analytics to monitor and control enantiomeric purity during production and product quality control.<sup>19,20</sup>

### 1.2.2 Chiral analytics

Chiral analytics is a diverse field, relying on a number of underlying principles to determine the absolute configuration of an analyte. As is often the case for analytical problems, the choice of method depends on the environment of the analyte, the analyte itself and, especially critical for chiral analytics, the availability of suitable instrumentation.

*Single crystal X-ray diffraction* has been regarded as the gold standard for structure elucidation for decades.<sup>10,19,21</sup> It is based on illuminating a crystal formed from the molecule with X-ray radiation at specified angles. By recording and analyzing the diffraction pattern, a 3-dimensional map of the analyte's electron density can be created and converted to its atomic configuration. The absolute configuration can then be determined based on this data.<sup>19</sup> While a very powerful technique and rightly regarded as the gold standard, X-ray diffraction relies on the presence of a crystal of suitable quality. However, obtaining this crystal is not possible for all analytes, and even if theoretically possible, the practical workflow of crystal growth is everything except straight forward. It's success relies on the experience and skill of the operator and is even in the best case very time consuming.<sup>10,19</sup> It therefore constitutes a bottle neck in a chiral analytical workflow and also the provided information is only a snapshot of the analyte conformation in a non-natural environment. Also, for the purpose of chiral monitoring and process analytical technology (PAT) it is unsuitable due to the time and labor-intensive sample preparation.

While *nuclear magnetic resonance (NMR)* spectroscopy on itself cannot distinguish between enantiomers, it can gain this capability by a dedicated sample pretreatment.<sup>19</sup> In 1973 Dale and Mosher introduced a derivatization of the analyte with both enantiomers of  $\alpha$ -Methoxy- $\alpha$ -trifluoromethylphenylacetic acid, resulting in the formation of diastereomers.<sup>22</sup> By comparing the  $H^1$  spectrum of each produced diastereomer and calculating the differences in chemical shifts between them one can assign the absolute configuration of the analyte.<sup>19,22</sup> The big advantage of this method, which is known after it's inventor as Mosher NMR, is the broad availability of NMR instruments in most chemical labs, However, the obvious disadvantage is the intensive pre-treatment and also the limited applicability, since suitable functional groups (alcohols or amides) must be present on the analyte. The pre-treatment also makes it not suitable for real time process monitoring applications.

*Chiral separation techniques* are mainly composed of liquid chromatography and capillary electrophoresis (CE). Chiral liquid chromatography is an extension of chromatography, commonly known as the workhorse of any modern analytical lab, that is also suitable for chiral analysis.<sup>23–25</sup> This chiral sensitivity is introduced by modifications of the stationary or mobile phase with chiral compounds. Among the most popular compounds are cyclodextrin, poly-saccharides or macrocyclic antibiotics.<sup>23–25</sup> Both cyclodextrin and poly-saccharides form chiral macrostructures, that selectively complex and retain one enantiomer, resulting in differences in retention time for the enantiomers.<sup>24</sup> Macrocyclic antibiotics on the other hand contain multiple chiral centers and functional group, enabling a range of interaction with the analyte. The result is the same, a separation of the two enantiomers in time. The construction of chiral stationary phases based on these materials is a very mature field, and high separation efficiencies can be achieved.

Capillary electrophoresis is generally characterized by a reduced analysis time and buffer volume compared to liquid chromatography.<sup>23,24</sup> In contrast to chromatography, in CE the mobile phase is not actively pumped but instead moved by an electric field between the two ends of the capillary. Chiral CE is for the most part operated in the electrokinetic chromatography mode, in which the selector is directly dissolved in the mobile phase and then forms temporary complexes with the analyte.<sup>23,26,27</sup> These interactions influence the traveling speed as a function of the molecules chiral identity. Like for chromatographic methods, cyclodextrin is also the most used chiral selector for CE applications. Cyclodextrin can also be implemented in micellar electrokinetic CE, in which chiral micelles are formed. In this case the migration of the analyte into the micelle is affected by its absolute configuration, resulting in a chiral separation.<sup>26,27</sup> However, while chiral separation is very efficient, neither chromatography nor CE can assign absolute configuration on its own. This determination can only be achieved by coupling to optical techniques or by comparing the chromatogram to one obtained from a similar compound with known absolute configuration.<sup>28</sup>

One of the optical techniques that can be coupled to chromatographic methods but also employed as a stand-alone method is *optical rotation (OR)*. It relies on the change of rotation linearly polarized light experiences when travelling through an optically active sample.<sup>10,19,28</sup> The fairly simple measurement scheme, only relying on two linear polarizers and a light source has resulted in its broad acceptance and till recently it was the only chiral method accepted by the federal drug administration.<sup>29</sup> Generally it is measured on the Sodium D line (589 nm) and in defined solvents. However, it is heavily influenced by temperature, impurities and solvent interactions which can even result in a reversal of the OR response. Due to this instability, it has not been further expanded for more complex or mixed samples.<sup>10,19</sup>

Another optical technique is *electronic circular dichroism (ECD)* which analyses the differences in absorbance for left and right-handed circularly polarized in the UV-vis region (~190 -900 nm) of the

electromagnetic spectrum. The difference in absorbance between the two polarization states is in most cases minimal, in the order of  $10^{-3}$  less compared to the parent absorbance.<sup>30–32</sup> Due to the broader wavelength range, changes in solvent and temperature, which detrimentally affect OR, can be compensated more easily and do not affect the evaluation of absolute configuration. For two enantiomers of equal concentration, their ECD spectrum would be equal in intensity, but opposite in sign, allowing for an assessment of the absolute configuration.<sup>30–32</sup> Additionally, the analyte can be evaluated in its natural environment, without any pretreatment necessary. However, for a molecule to be ECD active, it needs to contain suitable chromophores providing for example  $\pi$ - $\pi^*$  transitions, restricting its broad applicability. Possible examples of chromophores are double bonds or carbonyl containing functional groups.<sup>10,19</sup>

*Vibrational circular dichroism* and *Raman optical activity* (ROA) are both grouped under the umbrella term *vibrational optical activity* (VOA) and will therefore be discussed together. Like ECD, these techniques analyze the interaction of the analyte with circularly polarized light.<sup>1,13</sup> VCD can be viewed as either the extension of ECD in the infrared (IR) spectral region, or as the chiral counterpart to classical IR spectroscopy. It measures the chiral absorbance differences occurring in vibrational transitions in the chemical bonds of the analyte, resulting in +/- couplets, similar to ECD spectra. ROA on the other hand is also based on vibrational transitions in the analyte, however it evaluates the differences in circularly polarized light components in inelastically scattered photons.<sup>13,33</sup> It is therefore an extension of the classical Raman effect. Since both techniques rely on vibrational transitions, they are not limited in applicability, as all organic molecules express vibrational transitions that are accessible by at least one of these techniques.<sup>10,34</sup> Like ECD, both VCD and ROA are capable of assessing the chirality of an analyte in its natural environment, giving more insight in its actual structure. The consistent challenge of both techniques however is their weak signal intensity, resulting in the necessity of long measurement times, up to one day, to achieve satisfactory signal-noise ratios (SNR).<sup>34–37</sup> This is especially true for ROA, being a derivative of spontaneous Raman, which is characterized by a small cross section and therefore rather weak scattering intensities. In addition, the long exposure of the sample to the high energy laser beam can lead to sample deterioration. While commonly faster than ROA, VCD is challenged by sample interference, especially by water, a commonly used solvent in biological studies. These interferences limit the applicable pathlength, and therefore the signal intensity, for IR and VCD spectroscopy severely.

Table 1 | Overview of the discussed chiral analytical methods.

Method		Requirements	Advantages	Disadvantages
<i>X-ray diffraction</i>		crystal	Absolute determination	Crystal formation is challenging
<i>Mosher NMR</i>		alcohols, amines	Easy accessibility	Derivatization is necessary
<i>Chiral separation</i>		-	High performance, high throughput	No absolute determination, no monitoring capabilities
<i>OR</i>		-	Easy accessibility and measurements	
<i>ECD</i>		chromophores	Good SNR	Limited applicability
<i>VOA</i>	<i>VCD</i>	-	Near universal applicability	Weak signal, solvent absorbance interferences
	<i>ROA</i>	-	Near universal applicability	Weak signal, possible sample deterioration

NMR ... nuclear resonance spectroscopy; OR ... optical rotation; ECD ... electronic circular dichroism; SNR ... signal-noise ratio; VOA ... vibrational optical activity; VCD ... vibrational circular dichroism; ROA ... Raman optical activity

## 2. Vibrational circular dichroism

As already mentioned, vibrational circular dichroism can be viewed as the chiral analysis of vibrational transitions.<sup>1,6,38</sup> Vibrational transitions are commonly assessed in the mid-infrared spectral range, between 2.5 - 25  $\mu\text{m}$  (4000-400  $\text{cm}^{-1}$ ), although for commercial instruments the long wave cut-off for VCD is located around 600  $\text{cm}^{-1}$ .<sup>1</sup> In this part of the spectrum, fundamental vibrations arising from the chemical composition and arrangement of the analytes can be observed. Indeed, as will be shown, analyzing the vibrational transitions allows for the understanding of both the chemical composition and inter- and intramolecular interactions of a given molecule. The theoretical basis for VCD will be built up by way of explaining the fundamentals of light-matter interaction, the origin of vibrational motions, and how the combination of different oscillators in a molecule will affect the observed spectrum both in classical IR spectroscopy as well as in the context of VCD. Following this, the necessary instrumentation for the realization of VCD measurements will be explained. For more detailed information about vibrational spectroscopy, the interested reader

is referred to ref. <sup>39–42</sup>. A more in depth discussion of VCD and VOA in general can be found in ref. <sup>1,43</sup>.

## 2.1 Fundamentals of spectroscopy

Vibrational spectroscopy, like all spectroscopic techniques, relies on measuring the interaction of light and a chosen sample.<sup>40,41</sup> Energy can be stored in molecules in quantized amounts. The electronic, vibrational and rotational energy levels are important for optical spectroscopy. To get a better picture of this interaction first the nature of light needs to be discussed, followed by the energy levels involved in vibrational transitions.

Light can be described as the combination of an electric field and an orthogonally oriented magnetic field component. The defining characteristic of this combination is the distance between two subsequent maxima of the fields, which is called the wavelength  $\lambda$ . Based on the wavelength,  $\bar{\nu}$  and  $\nu$  being the wavenumber and frequency of the light respectively, both further important characteristics can be derived:

$$\bar{\nu} = \frac{1}{\lambda} = \frac{\nu}{\frac{c}{n_\lambda}} \quad (1)$$

with  $c$  being the speed of light in vacuum and  $n_\lambda$  being the refractive index of the medium the light is travelling through at the specified wavelength. The frequency is defined as the cycles per unit of time and is normally expressed in Hz. Wavenumber on the other hand defines the number of wavelengths fitting in a specific distance and is generally expressed as  $\text{cm}^{-1}$ .  $\bar{\nu}$  is also the preferred quantity for vibrational spectroscopy. The wavelength could theoretically be expressed as the SI-unit m, but for the wavelength range interesting for chemical analysis, nm or  $\mu\text{m}$  are more appropriate. Alternatively, the spectral area could also be mapped by the corresponding energy in joule or eV.

The wave characteristics of light can also be used to visualize the polarization of light. A common case for this is to assume that the light beam is propagating along the z-axis, with two electric field vectors of orthogonal (horizontal and vertical) orientation being visualized on the x- and y-axis respectively. The two fields can differ in their amplitude ( $E_x, E_y$ ) and can experience a phase shift ( $\Delta\phi$ ) relative to each other on the z-axis. Their combination, when viewed at the XY-plane (i.e. the detector) is generally described as an ellipse and can be called elliptic polarization. By varying  $\Delta\phi$  one arrives at different special polarization states. If  $\Delta\phi = 0$ , the ellipse shrinks to a line, resulting in linear polarization, with an angle of  $\tan^{-1}(E_y/E_x)$ . If  $E_x = E_y$  and  $\Delta\phi = \pm\frac{\pi}{2}$ , the resulting polarization states are called right-handed (+) and left handed circular polarized light (-). In Figure 2 the different polarization states are depicted.<sup>44</sup>

Most real-life light sources will emit field vectors of various orientations, amplitude and wavelength. The overlap of all these vectors yields no clear orientation and shape at the XY plane, and it is therefore called unpolarized light. Spectrometers relying on specific polarization states throughout the optical train are based on polarization optics. Unpolarized light can be converted to linear polarized light of the desired orientation by a polarizer, which transmits only one orientation of field vectors. Subsequent retarding elements (waveplates, modulators) can introduce the desired  $\Delta\phi$  to produce elliptic or circular polarization of different orientations.

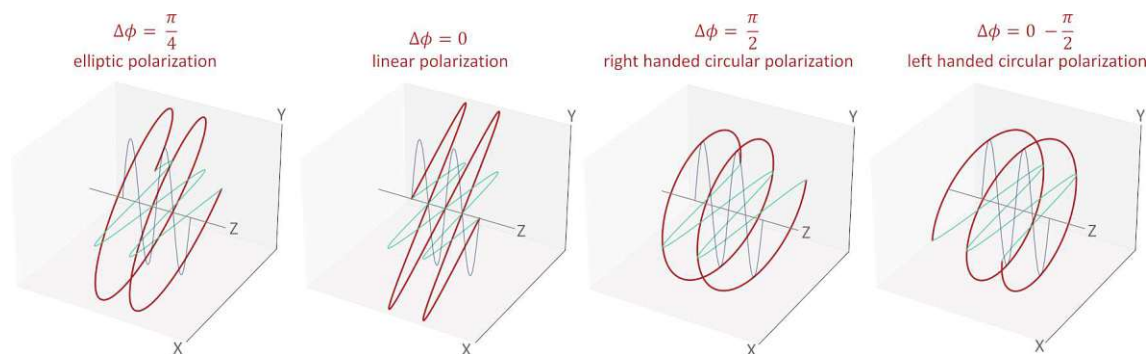


**Figure 2 | Polarized light, achieved by the combination of horizontal and vertical oriented field vectors with different phase shifts relative to each other.**

In addition to describing light as an electromagnetic wave, light can be defined on a particle levels, being made up of photons carrying specific energy packets called quanta.<sup>40,41</sup> The energy transmitted by light is related to its frequency by:

$$E = h\nu \quad (2)$$

This equation combines the already known quantity of frequency and the Planck constant ( $h = 6.626 \times 10^{-34}$  Js). The interaction of light with matter is defined by the transfer of energy. Photons can be absorbed, transferring energy to the molecule, or a photon can be emitted, for example during fluorescence processes, transferring energy from the molecule to the emitted photon. For absorption phenomena, the transfer of energy leads to the elevation of the molecule to a higher energy level.

However, like the energy contained in photons, a molecule has defined discrete levels. The consequences of this can be seen in Figure 3, where light composed of two different frequencies is directed at L-alanine. Since  $E_b$  matches the energy gap  $E_0-E_1$ , it is absorbed, and L-alanine is elevated to  $E_1$ .  $E_a$  matches no energy gap and is therefore fully transmitted.

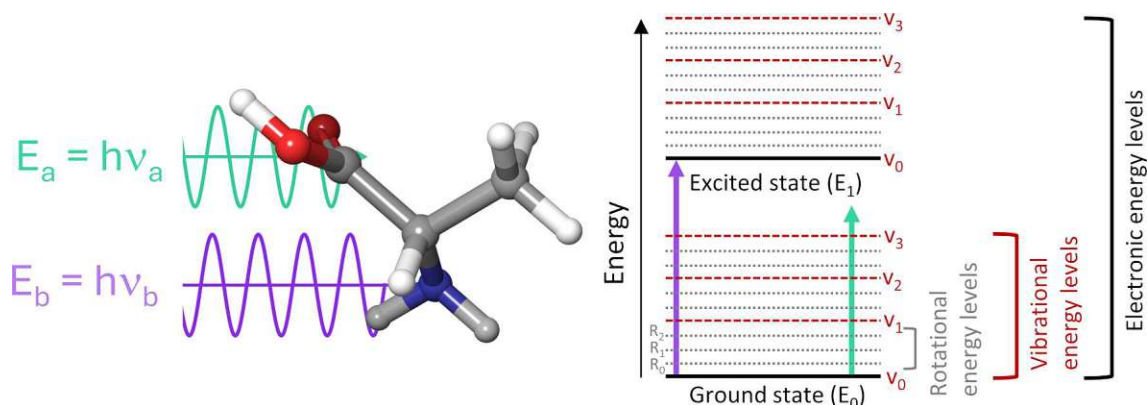


**Figure 3 |** Light of two different frequencies ( $\nu_a$  and  $\nu_b$ ) illuminating L-alanine. Since  $E_b$  matches the electronic energy gap, L-alanine is elevated to  $E_1$ , absorbing  $E_b$ , resulting in no transmission.  $E_a$  does not match any energy gap and is therefore fully transmitted. Besides the electronic levels, also the vibrational and rotational energy levels are depicted.

The depicted energy levels changes of L-alanine can be traced back to several distinct changes in the molecule. High energy light, like the UV-vis spectral range, between  $\sim 190$  and  $800$  nm, can trigger changes in the electronic energy ( $E_{el}$ ) in the molecule. Changes in  $E_{el}$  are characterized by the excitation of electrons in chromophores to higher energy level orbitals.

If incoming light is characterized by lower energy ( $=$  longer  $\lambda$ ) the excitation of electrons is no longer possible. Instead, vibrational ( $E_{vib}$ ) and in some cases rotational transitions ( $E_{rot}$ ) in the molecule are occurring. Several vibrational energy levels are located between the different electronic energy levels, with several rotational energy levels occurring between different vibrational energy levels, see Figure 3. In contrast to  $E_{el}$ , those transitions do not result in changes in the electron distribution but in changes in the relative motions of two or more atoms in a given molecule. However, their occurrence is dependent on two conditions: the energy gap must be equal to the energy of the incoming light and the corresponding movement must lead to a change in the dipole element of the molecule. Due to this characteristic, analyzing vibrational transitions, or vibrational spectroscopy, is sensitive to the structure of a molecule and is also broadly applicable since it does not rely on specific chromophores. As is obvious from the name, vibrational spectroscopy is based on the analysis of these transitions, and the applicable spectral area ranges from  $\sim 800$  nm to  $1$  mm. Due to this broad wavelength area, the energy delivered by the photons varies greatly and correspondingly the effects on the absorbing molecule also vary significantly. In a practical context, the spectral range is divided into the *near-infrared* (NIR), the *mid-infrared* (mid-IR) and the *far-infrared* (FIR) or terahertz spectral areas.

The NIR region,  $12\,500 - 400\text{ cm}^{-1}$ , contains high enough energy to excite overtone and combination vibrations.<sup>39</sup> These transitions are not easily attributable to the different parts of a given molecule, and extensive chemometrics is therefore often necessary for interpretation. Experimentally, it is characterized by the highest source power and highest detector efficiency of the discussed areas.<sup>34,45</sup> It is commercially available as an effortless extension of mid-IR-VCD instruments, with only an exchange of the source being necessary. As a consequence, while not as widespread as MIR, NIR-VCD spectra have been measured and indeed good chiroptical spectral data exist up to  $11\,000\text{ cm}^{-1}$ .<sup>34,45,46</sup>

The mid-IR region,  $4000 - 400\text{ cm}^{-1}$  (or  $600\text{ cm}^{-1}$ ), is home to fundamental vibrations of chemical bonds.<sup>1,41</sup> It is therefore the easiest to interpret the spectral data and directly link it to the chemical composition and arrangement of a given molecule.<sup>39</sup> This characteristic makes it the most used area

for both classical IR spectroscopy, as well as for VCD, being the focus of design for all commercial VCD instruments. All experimental work discussed in this study has been performed in the mid-IR spectral region. Experimentally, it is characterized by short pathlength, and low detector sensitivity at room temperature, resulting in the need for cryogenic cooling.

The FIR region, 400 – 10 cm<sup>-1</sup>, analyses rotational transitions as well as low frequency skeletal vibrations. Due to the hard cut-off at 600 cm<sup>-1</sup> imposed by the optics used for commercial VCD instrument, FIR-VCD is not a common research technique, and any implementations necessitates custom built instruments.<sup>47</sup> Modern realizations mostly focus on utilizing the lower frequency (<50 cm<sup>-1</sup>) radiation for chiral sensing for very specific scenarios.<sup>48,49</sup>

## 2.2 Vibrational transitions

Above the conditions of the incident light and how it is changed by interaction with molecules are discussed. However, also the origin of the fundamental vibrations and an approximation of their location in the spectral frequency domain needs to be discussed.

### 2.2.1 Harmonic vs. anharmonic oscillator

A given molecule can undergo numerous possible vibrations, rotations and translation. The number of possible fundamental vibrations depends on the number of atoms in the molecule and its geometry, and it can be calculated by:

$$DOF (linear) = 3 * N - 6 \quad (3)$$

$$DOF (non - linear) = 3 * N - 5 \quad (4)$$

with DOF referring to the number of possible vibrations (degree of freedom), N being the number atoms in the molecule and a specific loss of DOF being introduced based on the geometry (linear or non-linear) of the molecule.

To visualize these vibrations, the concept of a harmonic oscillator, based on Hooke's law, was borrowed from classical mechanics. The simplest case is depicted in Figure 4 (a), with two atoms of different masses ( $m_1$ ,  $m_2$ ) connected by a spring defined by a force constant ( $k$ , equaling the bond strength in this chemical model). With no external energy applied, the masses are separated by the equilibrium distance  $x_e$ , which is the distance probable at the energy minimum for this molecule. If energy is applied, the masses will begin to oscillate, resulting in a displacement  $x$ . The amplitude of their movement being inversely proportional to their respective mass.<sup>39</sup> The motion of this oscillator can be described by:

$$ma = -kx \text{ or } m\ddot{x} = -kx \quad (5)$$

With  $a$  being the acceleration or the second derivative of the displacement  $x$ . This can be rewritten as:

$$\ddot{x} + \frac{k}{m}x = 0 \quad (6)$$

which can be solved as to describe the position of the oscillator as a function of time as

$$x(t) = A \cos\left(\sqrt{\frac{k}{m}}t + \alpha\right) \quad (7)$$

With  $A$  being the amplitude of the motion,  $\sqrt{\frac{k}{m}}$  being the angular frequency ( $\omega$ ) and  $\alpha$  being the phase. This equation can be used to calculate the frequency of the oscillator depending on the masses of the oscillating atoms ( $m_1, m_2$ ) and the strength of their chemical bond ( $k$ ) according to:

$$\nu = \frac{1}{2\pi} \omega = \frac{1}{2\pi} \sqrt{\frac{k}{m}} = \frac{1}{2\pi} \sqrt{k \left( \frac{1}{m_1} + \frac{1}{m_2} \right)} \quad (8)$$

In the context of vibrational spectroscopy, the wavenumber position,  $\bar{\nu}$ , is more frequently used for the interpretation of spectral data than the classical frequency or the related photon energy. Therefore eq. (8) is adapted according to eq. (1):

$$\bar{\nu} = \frac{1}{2\pi c} \sqrt{k \left( \frac{1}{m_1} + \frac{1}{m_2} \right)} \quad (9)$$

In addition to the wavenumber position of a given vibrational mode, the harmonic oscillator model can be employed to calculate potential energy ( $V$ ) and the kinetic energy ( $T$ ) corresponding to the displacement ( $x$ ) of the spring:

$$T = \frac{1}{2} m \dot{x}^2 \quad (10)$$

$$V = \frac{1}{2} m x^2 \quad (11)$$

In a chemical context, the oscillation always occurs in reference to an equilibrium position ( $x_e$ ), therefore Eq. (11) can be substituted according to  $r = x - x_e$ . The result of this equation as a function of the distance can be seen in Figure 4 (c), which traces a parabolic function.<sup>42</sup>

However, as already mentioned the energy contained in a molecule is portioned in discrete energy packages, so the actual energy levels for the molecule oscillating at the given frequency  $\nu$  are given by:

$$E_i = h\nu(\nu_i + 0.5) \quad (12)$$

with  $E_i$  being the energy level corresponding to the vibrational quantum number  $\nu_i$ , with  $\nu_i$  being an integer non-negative value. The resulting allowed energy levels are depicted as horizontal lines in Figure 4 c, with the minimum occurring for  $\nu_i = 0$  at  $x_e$ .

Based on these energy levels it is possible to calculate the spectral response of a given molecule, as the required energy can be translated to spectral frequencies according to eq. (2).

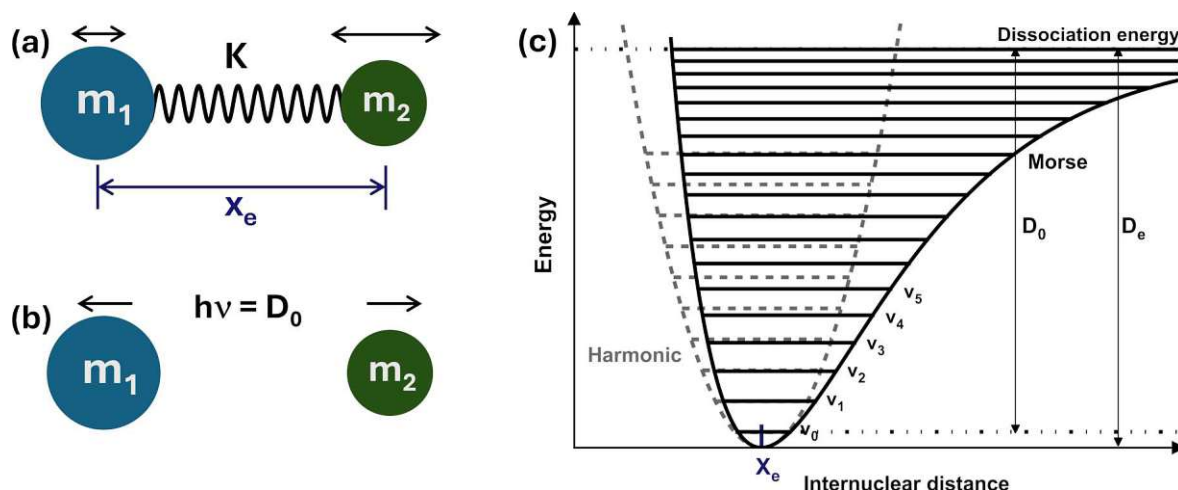


**Figure 4 |** (a) Schematic of a classic harmonic oscillator.  $m_1$  and  $m_2$  are the masses of the involved molecules and  $X_e$  is the distance at the lowest energy level. (b) If the incident light is equal to  $D_0$ , the increased motion will lead to the dissociation of the chemical bond. (c) Comparison of the potential energy of a harmonic and an anharmonic oscillator.  $D_0$  represents the dissociation energy needed to dissolve the bond and  $D_e$  is the depth of well of a given oscillator. Horizontal lines indicate the energy levels possible for integer quantum numbers.

However, while the classical Hooke's model assists in understanding vibrational transitions, does not reflect reality. If the energy is too high and the corresponding oscillation of the molecules too large, the bond will break. In other direction, if the atoms are oscillating too close together, the electric repulsion of the nuclei prevents further decrease of the internuclear distance. Thus the oscillations of atoms can no longer be viewed as a *harmonic* oscillator and instead must be treated as an *anharmonic* oscillator. The first mathematical model for this was introduced by Morse in 1929 and it is still in use today (although for more accurate simulations modifications were introduced in the meantime).<sup>50</sup> The potential energy of an anharmonic oscillator according to Morse is traced by the solid line in Figure 4 c and can be calculated according to:

$$V = D_0 \left( 1 - e^{-r \sqrt{\frac{f_c}{2D_0}}} \right)^2 \quad (13)$$

with  $D_0$  being the dissociation energy, see Figure 4, and  $f_c$  being the force constant at the potential minimum.<sup>42</sup> As a result of the anharmonicity, an increased broadening of the potential with increasing displacement can be observed. An intrinsic limit now appears at the dissociation energy ( $D_0$ ), at which point the energy introduced by incident light leads to the breakage of the chemical bond, see Figure 4 (b). Due to the anharmonicity introduced, an additional term is introduced to eq. 7, resulting in:

$$E_i = h\nu(v_i + 0.5) - h\nu\chi_e(v_i + 0.5)^2 \quad (14)$$

with  $\chi_e$  being the anharmonicity constant specific to the vibration. The calculated allowed energy levels are depicted in Figure 4 c as solid horizontal lines, with the quantum number indicated besides them. As is evident in the plot, the added term results in differences in the spacing for the energy levels with increasing  $v_i$ . While for the harmonic oscillator the spacing between the vibration energy levels is equidistant, the broadening of the anharmonic oscillator with increasing displacement results in parallel narrowing of the spacing for higher energy levels. Accordingly, for the harmonic oscillator model only  $|\Delta v_i| = 1$  transitions, called fundamental

transitions, are allowed. With the onset of anharmonicity, overtone bands ( $|\Delta\nu_i| > 1$ ) and combination of modes at different spectral frequencies are possible, leading to corresponding additional bands in the IR spectrum. However, due to lower probability for those modes, their intensity is reduced compared to the fundamental vibrations.

### 2.2.2 IR absorption processes

By applying the oscillator model, one can calculate the spectral frequency for each possible transition in a given molecule. However, even though a movement is possible, this does not necessarily mean that a corresponding infrared absorption band is observed. According to the selection rules of IR spectroscopy, the occurrence of an IR absorption band depends on two conditions: the light's frequency must match the natural frequency of the oscillator, and the dipole moment of the molecule must change during the transition. For a given molecule with  $i$  atoms the dipole moment  $\mu$  is function of the atoms charge  $e_i$  and their position  $x_i$  according to:

$$\mu = \sum e_i x_i \quad (15)$$

The atomic charge of an atom can be calculated based on molecular orbital calculations, or, as a rough estimate, be based upon the relative electronegativity of the bonded atoms, e.g. for HCl, H would be assigned a positive partial charge and Cl a negative one.

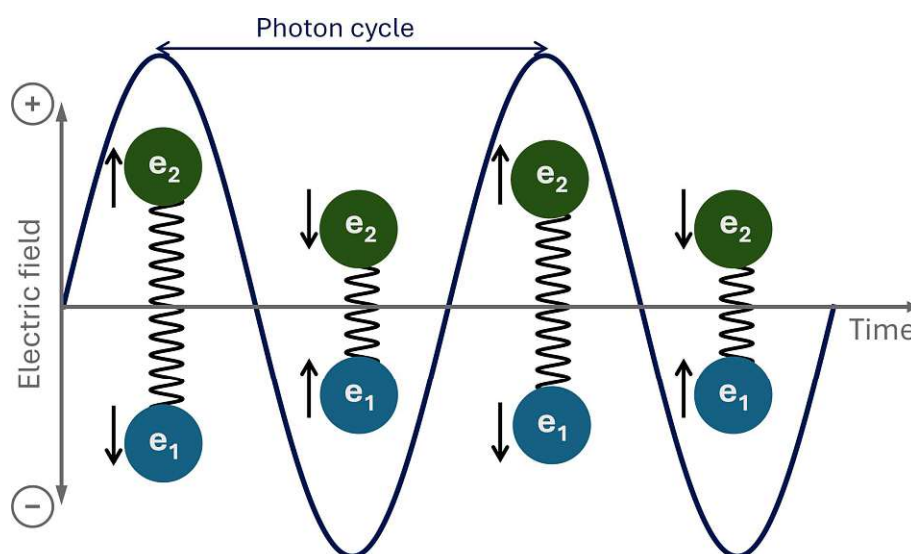


**Figure 5 | Interaction between the electric field component of an incoming photon and a diatomic molecule. In this case the frequency of the light matches the natural frequency of one of the possible motions of the atoms, resulting in an application of force on the atoms by the light. As a result, the chemical bond expands and contracts over the course of one photon cycle.**

The interaction between incoming radiation and a simple molecule can be described as depicted in Figure 5. If the radiation frequency  $\nu$  matches one of the molecule's oscillators natural frequencies (see equation (8)), the electric field component of the light can apply force on the molecule and induce a movement of the involved atoms. This will change the positions  $r_i$  of the atoms, and in combination with an inequality in their atomic charge  $e_i$  (or electronegativity), can lead to a change in the molecule's dipole moment, depending on the relative movement of the atoms. The IR absorption process can consequently occur, if the change in dipole moment relative to the movement of the atoms is nonzero:

$$\left(\frac{\delta\mu}{\delta Q_i}\right)_0 \neq 0 \quad (16)$$

With  $Q_i$  being the vibrational amplitude of the atom  $i$  along the normal coordinate away from its equilibrium position. The normal coordinate is an alternative way of mapping the movement of atoms during a vibrational mode. One can define the position of atoms in a molecule by their locations on a cartesian coordinate system ( $x, y, z$ ) with its origin in the center of mass of a molecule. A vibrational mode can result in the movement of atoms along all 3 axes in reference to its equilibrium position. This movement can also be weighted by the mass of the atoms. Alternatively, this can be described by summing up the movements of the atoms along  $x, y$  and  $z$ , including the correct signs to account for the directions of the movements. This corresponds to the normal coordinate for this vibrational mode. In this way the combined movement of the atoms can be described by one coordinate.<sup>42</sup> The corresponding strength of the IR absorption is proportional to the square of the change in dipole moment  $(\delta\mu)^2$ .

With these limitations in place, the discrepancy between the multitude of possible oscillations according to the equations (3) and (4) and the observable IR absorption bands can be explained. Since homonuclear diatomic molecules, e.g.  $H_2$ , exhibit no change in the dipole moment during their vibrations, they are IR inactive molecules. Also, the relative movement of the atoms can result in IR inactive vibrations, even though the involved atoms possess different atomic charges.

An example for this is  $CO_2$ , a symmetric molecule comparable in geometry to the linear molecule in Figure 6 (a) and (b). For the symmetric movement (b) the molecule's dipole moment remains unchanged, rendering the vibration IR inactive. The anti-symmetric motion (a) however, results in a net shift of the molecules charge, and the consequent dipole moment satisfies eq. (16), qualifying this vibration as IR active.

However, due to the symmetry of the molecule, some of the IR active motions do not result in additional absorption bands. The motion depicted in Figure 6 (a) can occur in both horizontal directions, resulting in the same vibrational frequency. Consequently, although multiple oscillations are occurring, only one vibrational band will be observed.

### 2.2.3 Coupled oscillators

The above models perform very well when considering only simple molecules, with two oscillating atoms. However, when considering larger molecules, which undoubtedly constitute more interesting analytes, oscillators cannot be considered as isolated entities, but instead coupling between them can and will happen. For practicability, these effects will be explained by the example of the simplest pair of coupled oscillators, which is a molecule composed of 3 atoms in a linear orientation.<sup>39,41</sup> An example of this molecule can be seen in Figure 6 (a) and (b).

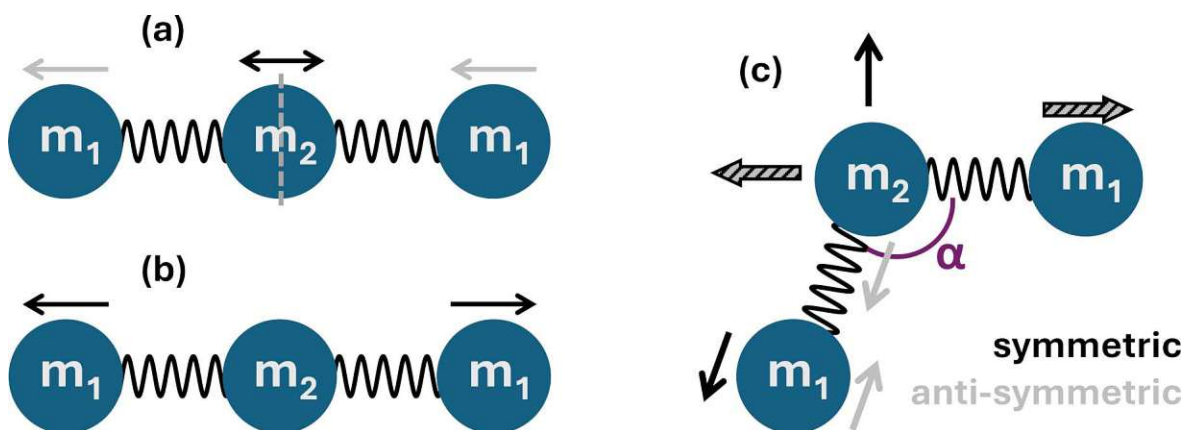


Figure 6 | (a) and (b) depict the out-of-phase (anti-symmetric) and in-phase (symmetric) oscillations of a linear triatomic molecule. (c) Oscillations for a non-linear triatomic molecule with a bond angle of  $\alpha$ . The movement of the symmetric oscillations are indicated in black, the anti-symmetric in grey and movement occurring for both cases are indicated by striped arrows in both colors.

Shown here are the stretch-stretch vibrations possible for this system. The first case (a) is the *out-of-phase* or anti-symmetric stretching vibration, wherein the direction of the vectors for both outer atoms point in the same direction. A result of this movement is that one bond is compressed, while the other is prolonged. The central atom also moves in this case. To calculate the resulting frequency, the center atom is split into two and two separate oscillators are considered according to eq. (5), with  $m_1 = m_2$ :

$$\bar{\nu} = \frac{1}{2\pi c} \sqrt{k \left( \frac{1}{m_1} + \frac{2}{m_2} \right)} = \frac{1}{2\pi c} \sqrt{\frac{k}{m_1}} \sqrt{3} \quad (17)$$

However, if the outer molecules move *in-phase* or symmetrically, as depicted in Figure 6 (b), they both apply the same force to the central atom, but in opposite orientation. Therefore, the central atom does not move, and it can be considered an immovable object, meaning its mass is infinite. eq. (5) is therefore modified to:

$$\bar{\nu} = \frac{1}{2\pi c} \sqrt{k \left( \frac{1}{m_1} + \frac{1}{\infty} \right)} = \frac{1}{2\pi c} \sqrt{\frac{k}{m_1}} \sqrt{1} \quad (18)$$

As is obvious from the above expressions, anti-symmetrically coupled vibrations are located at higher wavenumber locations (and therefore higher energy) than symmetrically coupled vibrations. If the atoms are arranged not in a linear molecule, but in a non-linear (Figure 6 c), the effect of symmetric and anti-symmetric vibrations is not as clearly divided.<sup>41,42</sup> The change in geometry has to be considered by introducing an angle dependence to the vibration, resulting in:

$$\bar{\nu}_{op} = \frac{1}{2\pi c} \sqrt{k \left( \frac{1}{m_1} + \frac{1 - \cos \alpha}{m_2} \right)} \quad (19)$$

$$\bar{\nu}_{ip} = \frac{1}{2\pi c} \sqrt{k \left( \frac{1}{m_1} + \frac{1 + \cos \alpha}{m_2} \right)} \quad (20)$$

With  $\bar{\nu}_{op}$ ,  $\bar{\nu}_{ip}$  being the wavenumber location for the out-of-phase and in-phase oscillation

respectively, and  $\alpha$  being the bond angle. If  $\alpha = 180^\circ$ , which equals a linear molecule, the anti-symmetric and symmetric vibrations can be calculated by (17) and (18). However, these shifts reduce in scope as the angle is reduced, and are reversed in orientation once  $\alpha < 90^\circ$ , as the sign of  $\cos(\alpha)$  changes.

The result of coupled oscillations is the sensitivity of the oscillator frequencies to their neighboring oscillators, which significantly influence the resulting oscillation frequencies and therefore the position of the corresponding absorption band in the IR spectrum. One of the restrictions for this is that the coupled oscillators must be of similar frequencies for effective coupling to happen. If this is the case, those frequencies, called group frequencies, constitute useful tools to identify different molecules, as the shift in e.g. the C=O band can provide information about adjacent atoms.<sup>41,42</sup>

In addition to shifts through coupled oscillators, the frequency of a vibrational mode is also affected by changes in the force constant  $k$ . Neighboring atoms can lead to change the  $e^-$  distribution in a chemical bond, called inductive or mesomeric effects. This in turn changes the strength of the chemical bond and therefore the location of the vibrational band.<sup>42</sup>

While the above definitions are straightforward for small molecules, the complexity increases significantly for each atom added, especially since only fundamental vibrations are counted. As outlined in 2.2.1 for a given vibration frequency, overtones, occurring at integer multiples of the original frequency, can be observed. These overtones can also contribute to coupling processes, e.g. Fermi resonance.<sup>41</sup>

So far, coupling is only described for directly connected oscillators. However, coupling can also happen in longer chain aliphatic or cyclic molecules. Here cooperation or opposition between multiple vibrations can occur over longer distances, involving multiple oscillators. Vibrations like these, which couple over large parts of the molecule are called skeletal vibrations, and the spectral region they are located in is called fingerprint region. Due to the multiple couplings, the resulting vibrations cannot be straightforwardly interpreted. At the same time, they are very specific, enabling the identification of a molecule based on band shifts and band maxima in these vibrations. These circumstances lead to the name convention of the region, as they are akin to a human fingerprint.<sup>40,42</sup>

In the special case of gas analysis, the normal vibrational modes can be superimposed by rotational transitions. For a given vibrational transition, several lower energy rotational transitions are possible, giving rise to a multitude of sharp bands around the vibrational mode. Since the transitions are closely matched, high resolution spectrometers are necessary to be able to differentiate them. Liquid samples in contrast are characterized by broad absorption bands, resulting from overlapping bands originating from the different rotational isomers in the solution and from inter and intramolecular interplay like hydrogen bonding. For solid samples the preparation method and resulting structure, crystalline or amorphous, has a significant impact on the spectra. Amorphous samples will exhibit broadened bands akin to liquid samples, while the limited flexibility of molecules in crystalline samples results in sharp defined bands.

#### 2.2.4 Oscillators in optical active molecules

Coupled oscillators can also be utilized as the basis for one interpretation of vibrational circular dichroism. First described in detail by Kuhn in 1929, and later on extended by Holzwarth and Chabay during the measurement of the first VCD spectrum, this model is called degenerated coupled oscillator model. According to this model, the phenomena of optical activity can be described based on two oscillators in a molecule, i.e. two stretching vibrations as see in Figure 7.<sup>51,52</sup> For the case of

optical activity, those molecules are spaced along the transmission vector of incoming light, and separated by a vector  $\vec{D}$ . The oscillators are oriented perpendicular to the transmission vector (=their separation vector). In addition, the oscillators are not oriented parallel to each other, and move only in the Y and Z direction respectively. The distance between them, due to being on the atomic scale, can be assumed to be significantly smaller than the wavelength of the incoming light. Due to their orientation not parallel to each other, their movement is differently affected by incoming left or right-handed circular polarized light. Therefore they constitute the simplest representation of a chiral vibrational mode.<sup>51–53</sup>

The deductions and utilizable equation resulting from this interpretation are described here briefly, to provide an understanding of the early basis of VCD calculations. For the complete derivation and more in depth discussion an interested reader is referred to ref<sup>52,53</sup>.

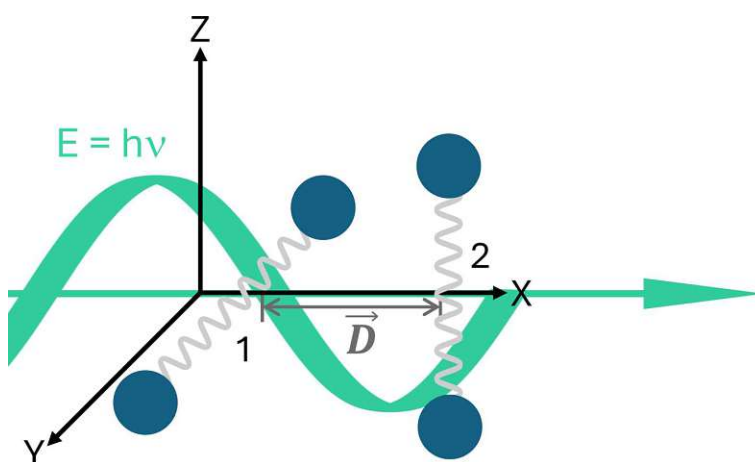


**Figure 7 |** An optical active pair of oscillators (1,2). The two coupled oscillators are arranged orthogonally to each other and to the propagation direction of the electromagnetic wave (sine curve). Furthermore, they are separated from each other by the separation vector  $\vec{D}$  along the propagation direction of the beam.

If  $|\vec{D}|$  is sufficiently small, these two oscillators will couple. Consequently, they can move either in-phase (+) and out-phase (-), generating two vibrational modes, as described in the previous section. The expected VCD intensities of these bands correspond to their respective rotational strength ( $\vec{R}$ ). The general equation for the rotational strength is based on the electronic dipole transition moment ( $\vec{\mu}_T$ ) and the magnetic dipole transition moment ( $\vec{m}_T$ ) according to<sup>52</sup>:

$$\vec{R} = \text{Im}(\vec{\mu}_T \cdot \vec{m}_T) \quad (21)$$

For the stretching modes shown in Figure 7, the magnetic dipole transition moments are 0, and therefore eq. (22) can be rewritten to describe the rotational strength for the in-phase and out of phase according to:

$$\vec{R}^{\pm} = \mp \left( \frac{\pi\nu}{2c} \right) \vec{D} \cdot (\vec{\mu}_{T,1} \times \vec{\mu}_{T,2}) \quad (22)$$

with  $\nu$  being the frequency of the underlying vibrational transition. This equation states that the VCD bands are equal in intensity, but opposite in sign, which is observed in reality for a large share of all VCD bands.<sup>52</sup> The advantage of this interpretation of VCD is that the value of  $\vec{\mu}_T$  for a given vibration transition  $\nu$  can be obtained from the molar absorptivity spectrum. Also, with this interpretation the wavenumber position of the VCD bands can be estimated by treating the system as a dimer, applying the dipolar coupling equation and calculating the band position shift ( $V_{12}$ )

according to:<sup>54,55</sup>

$$V_{12} = \frac{1}{|\vec{D}|^3} \left( \vec{\mu}_{T,1} \cdot \vec{\mu}_{T,2} - \frac{3(\vec{D} \cdot \vec{\mu}_{T,1})(\vec{D} \cdot \vec{\mu}_{T,2})}{|\vec{D}|^2} \right) \quad (23)$$

The expected band positions are then calculated by:

$$\nu^{\pm} = \nu \pm V_{12} \quad (24)$$

Based on these assumptions, the expected VCD spectra can be calculated based on the underlying absorption spectrum and by the distance between the two coupled oscillators on the molecule itself.<sup>54</sup> This interpretation therefore relies on a close understanding of the chemical structure of the molecule in order to identify the correct coupled oscillators and the distance. While very useful as an early approximation of VCD intensities, it relies on finding two near identical vibrational modes in the molecule, restricting its general applicability.<sup>1</sup> In addition, according to eq. (22) the signs above and below the zero line are equal, resulting in VCD bands of equal intensity but opposite sign. This condition is called net zero VCD signal for all modes. Such bands, called couplets, are indeed the most prominent band shape for VCD signals. However, this condition is not general applicable, as prominently demonstrated by the unbalanced C $\alpha$ -H stretching mode of amino acids, with a comparatively intensive positive band being matched by a weak negative band.<sup>56</sup>

The charge flow model and the localized molecular orbital model were developed as a more general description of VCD.<sup>57,58</sup> These models are not built on specific oscillators, but instead are based on the varying distribution of charge during a vibrational mode, making them broadly applicable.

The later developed ring current model was the first non-conservative model, meaning the net zero condition of VCD bands was not applicable, which closer matched the observed reality.<sup>59</sup> This model assumed that a single oscillator induces a current, which in turn generates an oscillating magnetic dipole moment, without an additional movement of any nuclei. The original oscillator is enhanced by the secondary magnetic dipole moment, producing an enhanced monosignate VCD band.<sup>59</sup>

However, while the above models can provide an elucidation of the origin of the observed VCD bands, later developments have resulted in them being replaced for all practical applications outside of teaching.<sup>1</sup> The Born-Oppenheimer approximation does not cover the dynamical response of the electron density in a molecule to nuclear velocity, preventing it from being used to describe VCD.<sup>1</sup> In 1983 this was solved by the theory of vibronic coupling, allowing for a description of the magnetic-dipole transition moment occurring during a vibrational mode.<sup>1</sup> A later development of the magnetic field perturbation formulation built upon this, and reduced the necessary computational efforts significantly.<sup>60</sup> Consequently, it became possible to simulate VCD spectra directly from *ab initio* calculations without underlying approximations.<sup>1</sup> The implementation of these algorithms in commercial software resulted in the current state of the field, in which most VCD spectra are accompanied by the corresponding calculations. This ensures that the conformation of the measured molecule can be evaluated directly by the comparison between experimental data and simulations.<sup>1</sup> In this way it was possible to determine the 3D structure of an molecule in solution without the need to prepare a crystal as required in crystallography.

## 2.3 Instrumentation for vibrational circular dichroism

Having discussed the origins of vibrational transitions, their instrumental accessibility will now be elaborated on. As the focus of this thesis is VCD, this will also be the focus of this part. Similar to classical IR spectrometer, VCD instruments have undergone significant changes and updates since the first proof of concept experiments.<sup>38,61</sup> However, while changes in experimental workflows as well as in the electronic signal path have undoubtedly lead to advances in their performance, the general optical configuration has undergone only small modifications.<sup>1</sup>

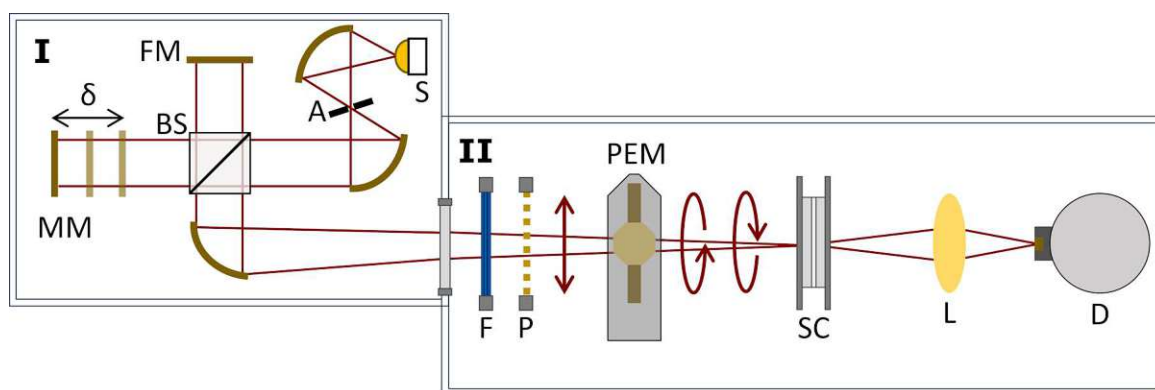


**Figure 8 | General optical configuration of a VCD spectrometer. (I) Spectrometer compartment, containing a Michelson interferometer. It is comprised of a globar IR source (S), an aperture wheel (A), and the actual interferometer part. This consists of a beam splitter (BS), directing the split beams to a fixed mirror (FM) and a moving mirror (MM), moving the distance  $\delta$  along the beam path. After recombination, the light is directed via a focusing mirror through the exit port. (II) VCD optical train, consisting of an optical long pass filter (F), a linear polarizer (P), the photoelastic modulator (PEM), the sample cell (SC), a refocusing lens (L) and the detector (D). The polarization states of the light are indicated by the arrows, undergoing a transition from linear polarized to alternating left and right-handed circular polarized light.**

For commercial and most custom built instruments alike, a globar provides the broadband IR light used for the measurement. In order to provide information on a spectral scale, this broadband light needs to be either divided into monochromatic light, or modulated in a way that the collected detector signal can be related to the spectral profile.<sup>38</sup> In modern VCD instruments, this is achieved by a Michelson interferometer, schematically shown in Figure 8 (I). In this implementation, the light from the globar is collimated and directed onto a beam splitter (commonly made up of thin layers of Ge on KBr). This beam splitter partially transmits and reflects the light, creating two orthogonal beams which are afterwards back reflected by a mirror respectively. One of the mirror is fixed, while the other is constantly moving, creating a path difference between the two returning light beams. As a consequence, upon their recombination, the two beams interfere constructively or destructively, depending on the path difference and the wavelength of the light.<sup>39</sup> Digitizing the detector intensity for the whole traveling range will result in an interferogram, e.g. Figure 9 (left panels), with a characteristic center burst and low intensity components away from it.<sup>39</sup> The centerburst corresponds to equal traveling distances in both arms in the interferometer, leading to constructive interference for the complete wavelength range.

Since the interferogram contains all the spectral components and their intensities as a function of the mirror position, a translation to spectral frequencies is necessary. This is done by applying a Fourier transform during the post processing.<sup>1,39</sup> This process will be covered later in this thesis while discussing the data acquisition in FT-IR.

Following the spectrometer compartment, the modulated light is directed to the optical path necessary for VCD measurements, depicted in Figure 8 (II). Depending on the spectral region of interest, the light may pass an optical long pass filter, designed to transmit only light with longer

wavelengths than the design filter cut-off. This may prove necessary if only a reduced spectral region is of interest and highly absorbing samples/solvents are studied. In this way, saturation of the detector is avoided and the transmitted energy is focused on the spectral area of interest.<sup>38</sup> Following this, a polarizer (normally wire grid based) produces a linear polarized output, cutting off ~50 % of the randomly polarized electric field vectors. This output is directed onto the photoelastic modulator (PEM), with the stress axis of the PEM oriented 45 ° relative to the polarizer's transmission axis. The PEM is the heart of a VCD instrument and is composed of an IR transparent crystal (commonly ZnSe) and two piezo actuators. The piezo actuators are arranged on both sides of the crystal, orthogonal to the light beam. By applying a sine modulated voltage to the actuators, a positive and negative strain can be applied to the crystal, which translates to a positive and negative phase shift for transmitted light. The applied strain is directly proportional to the voltage applied, and the frequency of the modulation is indirectly proportional to the crystal size, but generally varies from 37 kHz to 50 kHz. After the factory side calibration of the voltage, it is possible to precisely set a desired phase shift, i.e.  $\Delta\phi = \frac{\pi}{2}$ , located at any wavenumber position higher than the transmission cut-off of ZnSe at 600 cm<sup>-1</sup> and below the destruction point of the crystal. For VCD operation, the PEM is set to  $\Delta\phi = \pm \frac{\pi}{2}$  at the center of the wavenumber area of interest. With these settings, it acts as a quarter wave retarder, generating a train of alternating right and left-handed circular polarized light at its modulation frequency.

The polarization modulated beam passes the sample, which is commonly placed near the focus point of the incoming light. In most applications of VCD the sample is comprised of an analyte dissolved in a suitable solvent in a cell with a pathlength between ~6 µm and 1 mm. If substantial degrees of birefringence are expected, the sample cell can also be rotated constantly around the light axis during the measurement. As the average of all scans is calculated, the different orientation of the cell will also be averaged, eliminating the birefringence effect on the VCD spectrum. While optional for liquid samples it is essential if solid samples, i.e. KBr pressed pellets, are measured. For these samples this continuing rotation is essential to guarantee an artifact free spectrum. This is due to the intrinsic orientation of solid samples, which generates large artifacts which would otherwise overlap with and distort the actual VCD signal.<sup>6,62</sup>

After the sample the beam is refocused onto the detector element by a lens, commonly made of ZnSe. The usage of lenses is preferred in this case, as upon reflection on a mirror the incoming light undergoes a phase shift dependent on the angle of incidence and the incoming polarization. For a focusing mirror, this angle of incidence varies over the beam diameter. When this light is collected by a polarization sensitive detector, which all detectors are at least to some degree, a bias in the collected intensity is introduced. This bias would then be detected as VCD signal, as it shows a difference for the incoming polarization state, resulting in a non-zero baseline.<sup>38,63</sup>

While for classical FT-IR measurements also room temperature pyro detectors are viable alternatives, the low intensity of VCD signals necessitates high sensitivity, low noise detectors. This is only possible by the utilization of mercury-cadmium-telluride (MCT) elements. For FT-IR applications, those detectors are cooled to cryogenic temperatures by liquid nitrogen. In modern instruments, the detector intensity is digitized, and a digital lock-in amplifier routine is applied: The detector intensity is lowpass filtered to extract the  $I_{DC}(\bar{\nu})$  interferogram. In parallel, the data stream is high pass filtered, mixed with the reference signal obtained from the PEM and again lowpass filtered. This results in the  $I_{AC}(\bar{\nu})$  interferogram. Older instruments or custom made optical setups employ an external lock-in amplifier to obtain the same results.<sup>38</sup>

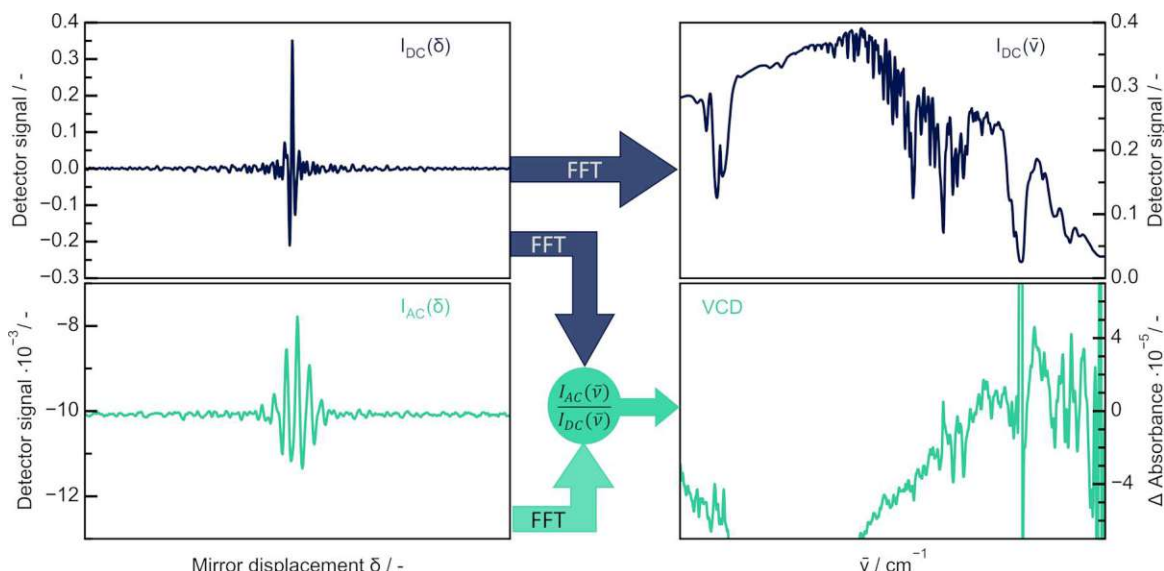


**Figure 9 | Interferograms obtained from a FT-IR VCD instrument equipped with a broadband source. The upper part depicts the interferogram and the calculated IR spectrum, corresponding to the “classical” FT-IR signal. The lower panels depict the high frequency interferogram, extracted based on the PEM frequency, and the calculated VCD spectrum, shown as a ratio of  $I_{AC}$  and  $I_{DC}$ .**

As mentioned, this information is a function of the mirror position, and needs to be converted to the wavenumber scale for interpretation. This can be done by applying the following expression:

$$I_{DC}(\bar{\nu}) = FT[I_{DC}(\delta)] = \frac{1}{2\pi} \int_0^{\infty} I_{DC}(\delta) \cos(2\pi\delta\bar{\nu}) d\delta \quad (25)$$

with  $I_{DC}$  being the intensity arriving at the detector corresponding to the “classical” FT-IR single channel spectrum and  $\delta$  being the optical path difference between the two mirrors.<sup>1</sup> In Figure 9 this transformation is depicted in the upper panels, showing  $I_{DC}$  as a function of both  $\delta$  and  $\bar{\nu}$ .

The high pass filtered component of the detector intensity also needs to be converted to the wavenumber scale, and the same equation can be applied, just with  $I_{DC}$  being replaced with  $I_{AC}$ . The main difference between these two conversions is the phase correction used. While for the  $I_{DC}$  the automatic phase correction can easily identify the correct phase, the  $I_{AC}$  interferogram is more complicated since the resulting VCD spectrum will contain both positive and negative intensities. Modern instruments are calibrated by an artificial all positive VCD signal generated by a birefringent plate, which is done at the manufacturing site and then stored in the instrument software.<sup>1</sup>

For the IR absorption information, the  $I_{DC,S}(\bar{\nu})$  of the sample needs to be corrected by the  $I_{DC,B}(\bar{\nu})$  of the background to yield either the transmission spectrum,  $T(\bar{\nu})$ , or the absorbance spectrum,  $A(\bar{\nu})$ , according to:

$$T(\bar{\nu}) = \frac{I_{DC,S}(\bar{\nu})}{I_{DC,B}(\bar{\nu})} \quad (26)$$

$$A(\bar{\nu}) = -\log_{10} \left( \frac{I_{DC,S}(\bar{\nu})}{I_{DC,B}(\bar{\nu})} \right) \quad (27)$$

Those spectra can be used for the qualitative and quantitative evaluation of the sample.

VCD spectra acquisition on the other hand is in theory a baseline free technique, as a perfectly aligned VCD baseline should be a true zero line throughout the spectral range. The definition for

$I_{AC}(\bar{\nu})$  and  $I_{DC}(\bar{\nu})$  are as follows:

$$I_{AC}(\bar{\nu}) = 0.5[I_R(\bar{\nu}) - I_L(\bar{\nu})] \sin[\alpha_M^0(\bar{\nu})] \quad (28)$$

$$I_{DC}(\bar{\nu}) = 0.5[I_R(\bar{\nu}) + I_L(\bar{\nu})] \quad (29)$$

With  $\alpha_M^0(\bar{\nu})$  being the phase shift applied by the PEM as a function of the wavenumber and  $I_R(\bar{\nu})$  and  $I_L(\bar{\nu})$  are the intensities for right and left-handed circularly polarized light. For the acquisition of a VCD signal the difference in intensity between left and right-handed circularly polarized light is normalized by the total intensity. Therefore, the  $I_{AC}(\bar{\nu})$  and  $I_{DC}(\bar{\nu})$  spectra of a given analyte should be sufficient to obtain a VCD spectrum,  $\Delta A(\bar{\nu})$ , according to:

$$\Delta A(\bar{\nu}) = \frac{1}{2J_1[\alpha_M^0(\bar{\nu})]1.1513} \left[ \frac{FT[I_{AC}(\delta)]}{FT[I_{DC}(\delta)]} \right] \quad (30)$$

with  $J_1[\alpha_M^0(\bar{\nu})]$  being the first order Bessel function of the phase shift applied by the PEM for each wavenumber in radians.<sup>1</sup> The factor  $2J_1[\alpha_M^0(\bar{\nu})]$  can be traced back to the modulation cycle of the PEM, the introduced phase shift and the detection system. A modern PEM is operated by a sinusoidal voltage signal, imposing a modulation of the phase shift, at the angular frequency  $\omega_m$ . The modulation imposed upon  $I_{AC}$  according to eq. (28) to can therefore be defined as function of time ( $t$ ) according to:

$$\sin[\alpha_M^0(\bar{\nu})] = \sin[\alpha_M^0(\bar{\nu}) \sin \omega_M t] \quad (31)$$

This can be rewritten according to trigonometric identities as:

$$\sin[\alpha_M^0(\bar{\nu}) \sin \omega_M t] = \sum_{n=odd} 2J_n[\alpha_M^0(\bar{\nu})] \sin n\omega_M t \quad (32)$$

The resulting signal is demodulated at the fundamental PEM frequency ( $n=1$ ) by a lock-in amplifier or a corresponding digital modulation scheme, extracting the amplitude of  $\sin \omega_M t$ . Consequently, the above equation imposes the PEM efficiency parameter of  $2J_1[\alpha_M^0(\bar{\nu})]$  on the measured CD signal.<sup>1</sup>

Since  $J_1[\alpha_M^0(\bar{\nu})]$  is dependent on the retardation angle set during PEM operation and the optical alignment in the VCD train, but not on the sample measured, it can be calibrated for and applied to each new sample measurement.<sup>64-66</sup> For this calibration measurement, a birefringent plate is placed at the sample position with its fast axis at  $\pm 45^\circ$  relative to the horizontal axis, followed by a polarizer set to either vertical or horizontal orientation. Two of the possible configurations are measured, their absolute spectra are plotted and the crossing points between them are noted. A line directly connecting these crossing points traces out the function  $2J_1[\alpha_M^0(\bar{\nu})]$ . While this value can also be calculated, the experimental procedure is the preferred option as it also accounts for possible effects of the optical alignment and instrument specific scaling effects.<sup>38</sup> This curve is stable enough to not need frequent remeasurement and the intensity corrected VCD spectrum can be calculated according to:

$$\Delta A(\bar{\nu}) = \frac{1}{1.1513} \left[ \frac{I_{AC}(\bar{\nu})}{I_{DC}(\bar{\nu})} \right] \left[ \frac{I_{AC}(\bar{\nu})}{I_{DC}(\bar{\nu})} \right]_{cal}^{-1} \quad (33)$$

with  $\left[ \frac{I_{AC}(\bar{\nu})}{I_{DC}(\bar{\nu})} \right]_{cal}$  being the curve resulting from connecting the crossing points.

With the calibration spectrum obtained, the VCD spectrum can be calculated, with a possible result

seen in Figure 9, lower right. It is obvious, that while in theory VCD is a baseline free technique, in practice the numerous artifacts and noise sources in the optical train result in often significant deviation from the true zero line. Therefore, the VCD spectrum needs to be corrected by a baseline as well. This can be done by subtracting a spectrum obtained for the solvent or, if available, the racemic mixture. Alternatively, a spectrum collected for the opposite enantiomer could be subtracted and the result divided by 2.

The solvent baseline also contains the artifacts in the optical train, and therefore they are cancelled by subtraction. The advantage of using the racemic mixture or the opposite enantiomer, is that this represents the artifacts in the optical train as well as absorbance artifacts arising from the sample itself. A correction with these will therefore always yield the correct VCD spectrum, even if the instrument is not perfectly aligned. However, since pure enantiomers are often difficult to acquire, or in the case of biomolecules impossible to be obtain, a well aligned instrument should acquire baselines of sufficient quality for the solvent correction to be adequate.<sup>38,67,68</sup>

The need for a well aligned, flat zero baseline can offset some of the advantages of FT-IR spectroscopy compared to classical dispersive spectroscopy. There are three main advantages of using FT-IR spectrometer compared to dispersive spectrometer:<sup>39</sup>

- Fellgett's advantage, which states that the increased SNR of FT-IR is equal to  $\sqrt{m}$  with  $m$  being the number of resolution elements  $m = \frac{\bar{\nu}_{max} - \bar{\nu}_{min}}{\Delta\bar{\nu}}$ . This advantage scales with an increase in spectral coverage.
- Jacquinot's advantage, which arises from the fact that the resolution of a dispersive spectrometer is defined by the slit width, and therefore inversely proportional to the throughput. In contrast the resolution of an FT-IR spectrometer is solely defined by the optical path difference. Also, FT-IR spectrometers allow the use of circular apertures, allowing for a higher throughput. Consequently, an FT-IR instrument retains a high throughput, even at high resolutions. In a first approximation this advantage scales with higher resolutions.
- Connes advantage, originating from the parallel modulation of a HeNe laser by the interferometer. The intensity of this laser can be collected by a diode and will be digitized on the same time resolution as the IR interferogram. Since the wavelength of the HeNe laser is known, this interferogram can be utilized to calculate the exact optical path difference  $\delta$  for each sampling point of the IR interferogram. This results in an increased accuracy of the calculated wavenumber axis.

Consequently, an FT-IR instrument is vastly superior to dispersive instruments if broad coverage with high resolution is needed, which makes it the instrument of choice for routine and high-end IR spectroscopy. However, for VCD applications the typical resolutions are  $4\text{ cm}^{-1}$  for small molecules in organic solvents and  $8\text{ cm}^{-1}$  for biomolecules in aqueous solution.<sup>37,37,69-73</sup> As a consequence, the Jacquinot's advantage, while still present, is limited as further resolution enhancement is not desirable, due to a resulting increase in measurement time.

The increased spectral coverage offered by FT-IR spectrometers is of course relevant and advantageous also for VCD experiments. However, again there is a limit to its effectiveness, due to the inherent characteristics of VCD. These limitations relate back to the PEM. Since the PEM is only a perfect quarter wave retarder at one spectral position, the resulting polarization states change significantly when moving away from this position.

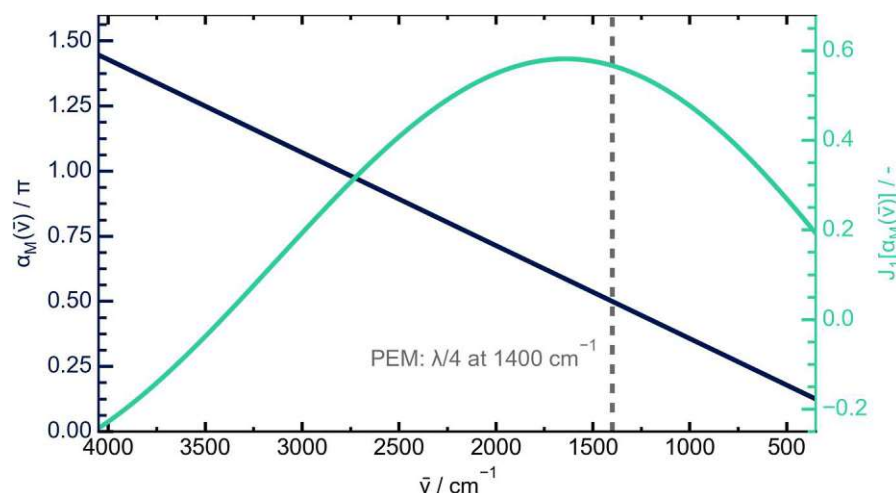


**Figure 10 |** Phase shift in multiples of  $\pi$  and the  $J_1(\bar{\nu})$  of the PEM retardation, calculated for the mid-IR range for a PEM set to quarter wave retardation at  $1400\text{ cm}^{-1}$ .

This is visualized in Figure 10, where for a PEM set to quarter wave setting at  $1400\text{ cm}^{-1}$  the phase shift changes from nearly  $\frac{3}{2}\pi$  at  $4000\text{ cm}^{-1}$  to  $\frac{1}{8}\pi$  at  $400\text{ cm}^{-1}$ . Over the same range, the efficiency of the PEM ( $J_1[\alpha_M^0(\bar{\nu})]$ ) also varies significantly, including a reversal of its sign and therefore the orientation of the VCD bands around  $3400\text{ cm}^{-1}$ . These changes constitute challenges for the attainment of a correct baseline and for the measurement of accurate VCD bands over broader spectral ranges. A possible remedy is the collection of the VCD spectrum in snippets of  $<2000\text{ cm}^{-1}$  each, adjusting the PEM retardation accordingly, a time consuming approach due to the long measurement times necessary when aiming for low noise VCD spectral acquisition.<sup>1</sup> Nevertheless, this approach is indeed used when i.e. both NIR and mid-IR spectral information is required.<sup>34,45</sup>

Most studies take the opposite approach, analyzing only a small spectral area, often adding the already mentioned optical filters to increase the throughput in the area of interest.<sup>37,62,71,72,74,75</sup> In this way the optical alignment is simplified and artifacts can be reduced more effectively, since wavelength dependent shifts in PEM efficiency and polarization states are less disruptive.

The above detailed challenges of VCD spectra acquisition lead to the curious persistence of dispersive VCD instruments as competitive alternatives to FT-IR instruments, albeit only as custom built research instruments.<sup>62,76–78</sup> The low resolution customary for VCD spectra allows for the use of relatively broad slit apertures, increasing the optical throughput. Dispersive instruments collect the spectral data as a function of the angle of the internal grating, which is moved over the course of the data acquisition. This sequential scanning can be slowed down enough to enable the adjustment of the PEM in accordance with the transmitted wavelength, providing perfect polarization states for each collected data point.<sup>61</sup> This is of course not possible for FT-IR instruments, where all spectral elements are transmitted simultaneously, with all existing advantages and disadvantages.

Nevertheless, while the profits gained from FT-IR VCD are less overwhelming than for classical FT-IR spectroscopy, they are still substantial. The most compelling evidence for this is that all modern commercial VCD instruments are built around FT-IR technology.<sup>79–81</sup>

However, the challenges FT-IR VCD faces regarding polarization purity and PEM efficiency are obvious starting points for academic research. Further optical development, based on newer inventions regarding light source or polarization modulation technology could manage to counter the monopoly FT-IR spectroscopy currently enjoys.

## 2.4 Mid-IR laser technology

When discussing possible optimization opportunities in a typical IR spectrometer, the light source is the first and most obvious candidate. As mentioned, commercial IR spectrometers rely on a globar to provide the necessary radiation. Globars are silicon carbide rods that are resistively heated to around 1400 K, providing broadband blackbody IR emission between 2 to 25  $\mu\text{m}$ .<sup>82,83</sup> They are inexpensive and fairly stable, and their broad emission makes them ideal sources for FT-IR spectrometer. However, while they provide radiant power of  $\sim 40$  mW in the sample compartment of an FT-IR spectrometer, this power is spread out over the emission range, resulting in only a few  $\mu\text{W}$  of power at each wavenumber.<sup>84</sup> In addition, their emission spectrum can only roughly be changed by modulating their temperature, which also changes the overall spectral power density, and the light they provide is spatially incoherent and not polarised.<sup>82,85</sup> In the UV-vis spectral region, the realization of ruby lasers (light amplification by stimulated emission of radiation) offered the first opportunity for a light source characterized by high brilliance and spatial coherence, leading to significant advancements in spectroscopy.<sup>83,86</sup>

The first mid-IR laser sources did not lag far behind and were realized in 1964 for 6.7  $\mu\text{m}$  and 8.5  $\mu\text{m}$ .<sup>87,88</sup> These lasers relied on gain material composed of lead salts, PbTe and PbSe respectively, and were in use for several decades after their introduction. However, in contrast to their UV-vis counterparts, they were never in general use as they suffered from significant drawbacks. Due to the very low thermal conductivity of both the gain medium and the substrates ( $\text{BaF}_2$ ), lasing operating leads to significant self-heating of the instrument. As a result of the complicated cooling necessary, lead salt laser were restricted to research use.<sup>83</sup>

With the advent of commercial non-linear crystal manufacturing, difference-frequency generation (DFG) and optical parametric oscillators (OPO) enabled the mid-IR community to take advantage of the developments made in the UV-vis and NIR laser technology. A NIR pump and a NIR signal beam, for DFG, or a single pump laser in an optical resonator configuration, for OPO, are directed through a non-linear crystal, resulting in the generation of an idler photon at  $\nu_i = \nu_p - \nu_s$ .<sup>89</sup> By changing the non-linear crystal temperature, or by phase shift and angle modulation the idler emission can be tuned broadband in the IR range. While these technologies proved to be easier to commercialize than lead salt diode lasers, their implementation requires challenging optical engineering, also limiting their application to carefully controlled laboratory conditions.

Although the above-mentioned technologies have provided useful alternatives to classical globars, an actual equivalent to UV-vis laser technology in terms of applicability was not developed till the middle of the 1990s. In 1994 Faist et al. published the first implementation of quantum cascade technology in the form of a quantum cascade laser operating at 4.26  $\mu\text{m}$ .<sup>90</sup> Their approach constitutes a radical divergence from the classical semiconductor laser design and was dubbed quantum cascade laser (QCL) by them.

When one disregards the materials used, the aforementioned lead salt diode lasers and their counterparts in the UV-vis and NIR region rely on the same physical principle, interband transitions.<sup>85,91</sup> During interband transitions electrons from the conduction band recombine with holes in the valence band, leading to a transition of the electron to a lower energy state. This difference in energy is compensated by a radiative process according to  $E = h\nu$ , leading to the emission of light at  $\nu$ , see also Figure 11 (a). This process requires a constant supply of energy to maintain population inversion. This energy is provided by an electric current or an external light source and an optical resonator for stimulated emission.<sup>83,91,92</sup>

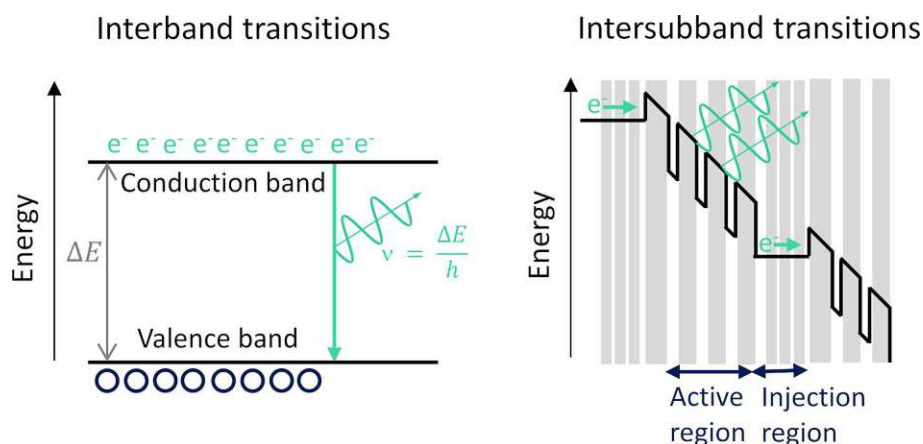
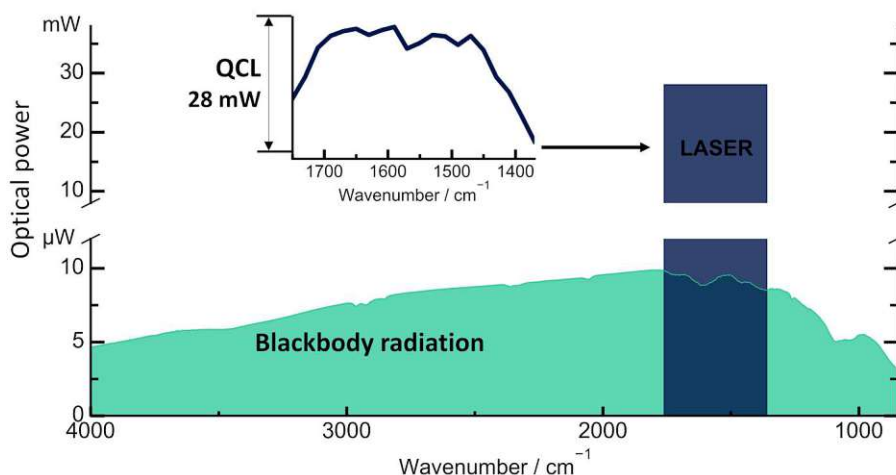


Figure 11 | Electron transitions and radiative processes for interband and inter-subband transitions.

In a standard semiconductor laser, the wavelength of the emission can be set by changing the bandgap in the semiconductor material. This can be achieved by combination of different materials in an alloy.<sup>83</sup> However, achieving the necessary bandgaps in the mid-IR is non-trivial and comes with drawbacks, e.g. as observed for lead salt diodes.

A QCL in contrast does not rely on interband transitions but rather on inter-subband (ISB) transitions in the conduction band. These transitions are achieved by complex heterostructures, comprised of layers of different semiconductor materials of varying but precisely defined bandgaps and thickness, see Figure 11 (b). When a current is applied, an electron is injected at the highest energy level, starting in a so-called “active region”. In this region, the electron transitions to a lower ISB energy level, again compensated for by emission of radiation. The frequency of this radiation corresponds to the energy difference between the ISB levels, which can be tailored by adapting the thickness of the involved layers. This characteristic decouples the emission properties from the bandgap of the involved material, enabling the construction of suitable gain medium over the entire mid-IR spectral region while only relying on a few material combinations (mostly InGaAs/AlInAs). While the layer thickness defines the emission profile of a QCL, its emission is further characterized by an inherent polarization bias. According to the selection rule of optical transitions, only light with electrical field vectors parallel to the growth direction is emitted during the lasing scheme. This leads to a near perfect linearly polarized emission. This emission is only reduced in purity by birefringence in the collimating lenses or the waveguides.<sup>82,83,90,93</sup>

In addition to the active region, a QCL also comprises a subsequent “injection region”, depicted as narrow layers in the schematics. This region allows for non-radiant resonant tunneling, extracting electrons from the lower ISB energy level, ensuring population inversion persists. This tunneling occurs with a time constant of  $\sim 0.5$  ps, significantly quicker than the radiant relaxing (time constant  $\sim 4.3$  ps), leading to electrons accumulating in the injection region.<sup>90</sup> The injection region borders another active region, in which the radiative transitions start anew. This constitutes another advantage of QCLs, as each chip encompasses 40 or more active/injection region pairs, permitting the recycling of already transitioned electrons. Since the layers are constructed equal, this leads to the emission of multiple identical photons for each electron, increasing the efficiency of the lasing scheme dramatically.<sup>82,83,90</sup> Indeed, the wall plug efficiency, which is the conversion rate of supplied electronical energy to radiative energy, for QCLs can reach  $\sim 20\%$  and  $\sim 16\%$  for CW and pulsed operation respectively.<sup>94,95</sup>



**Figure 12 | Comparison of the typical optical power of a globar (=blackbody radiation) with the spectral density of one of the EC-QCLs (pulsed mode, 5 % duty cycle) used in this study. Adapted from ref <sup>84</sup>.**

As a result, QCLs emit highly brilliant light with a comparatively low energy consumption, evidenced by the optical power of modern QCLs reaching several hundred milliwatt in optical power at each wavenumber when operated in continuous wave (CW) mode. Even pulsed operation QCLs, e.g. Figure 12, vastly outperform the spectral power density of thermal emitters.

**QCL resonator design:** Since its first development, QCLs have been extensively improved upon, both in the design of the gain medium and equally importantly also in the construction of the resonator. The fabrication process of QCLs allows not only for the choice of its center wavelength, but also for the adaption of its gain curve, enabling ever extending wavelength ranges accessible by newer chips.<sup>82,91</sup> As for the resonator design, three models have emerged as the most commonly used ones, see Figure 13:

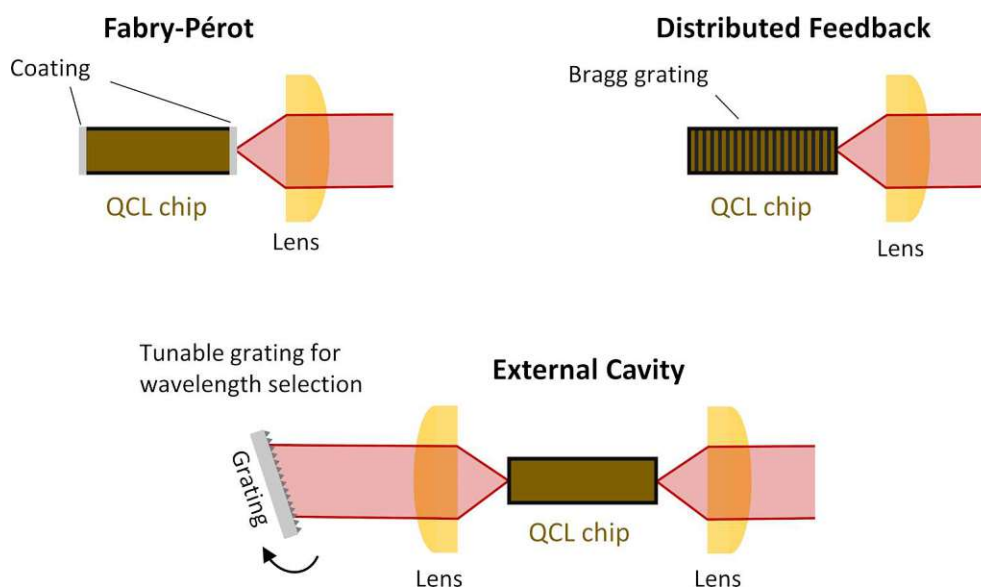


**Figure 13 | The three most common configuration for QCL resonator design. Adapted from ref<sup>91</sup> under creative commons 3.0.**

A *Fabry-Pérot* (FP) design constitutes of the QCL chip with high reflectivity coating applied to both end facets, with the emission wavelength dependent on the gain medium and the cavity length of the chip. This is due to the reliance of constructive interference for wavelength selection. Since

those conditions are met several times over a broader spectral range, FP-QCLs provide multimodal emission covering a comparatively large spectral area. Consequently, they did find use in the analysis of the broad spectral bands of liquid samples. However, for liquid sensing they have been mainly replaced by tailored devices relying on an external cavity.<sup>91</sup>

*Distributed feedback* lasers (DFB) lasers on the other hand are used for gas-phase analytics, which comprises to date the biggest market for QCLs for scientific use. They are manufactured by fabricating a Bragg grating into the laser waveguide, acting as a filter for the modes selected by the gain medium. This grating eliminates all modes except the one it was designed for, providing highly monochromatic light, suitable for high resolution gas measurements. This design wavelength can be slightly tuned ( $\sim 5 \text{ cm}^{-1}$ ), through modulating the current or the temperature of the laser and the waveguide. These modulations lead to changes in the refractive index and it also slightly affects the dimensions of the waveguide material, shifting the resonance conditions for the grating.

The last resonator design is at the same time the most complex, as it relies on external manipulation of the emission spectrum. For the construction of an *external cavity QCL* (EC-QCL) a broad gain QCL waveguide is combined with an external turnable grating. The movement of the grating enables the selection of the laser's emission wavelength, and the spectral area is constrained by the gain curve of the QCL-waveguide and the wavelength dependent efficiency of the grating. The consequence is a broadly tunable emission spectrum, with a characteristically structured emission profile, see Figure 14.

This design allows for sequential scanning of the spectral range, fast sweeps over the spectral range or single mode emission by fixing the grating in position. Modern EC-QCLs are capable of covering several hundred wavenumbers with one chip, lending themselves well to the analysis of broad liquid sample absorption bands. In addition, it is possible to combine several chips with overlapping beam outputs in one instrument, covering up to several hundred wavenumbers. Such instruments and also single chip lasers are commercially available, bringing mid-IR laser technology from a niche technique into the scientific mainstream.<sup>91</sup>

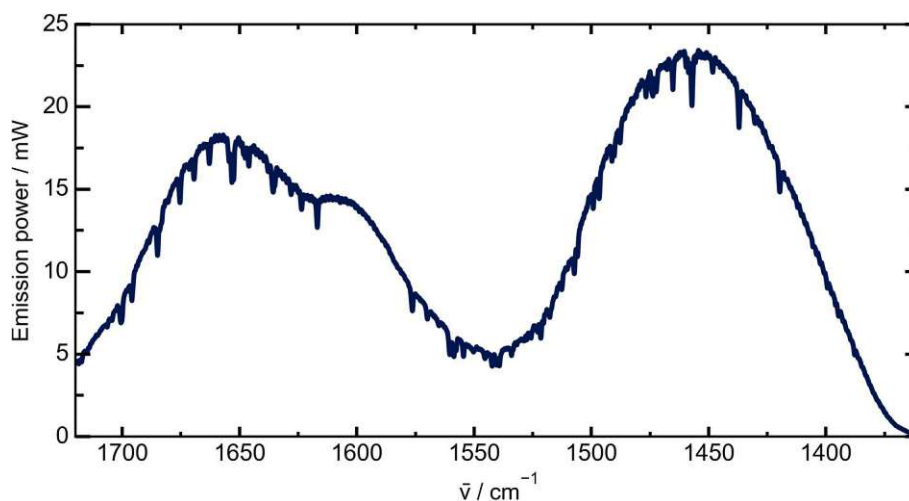


Figure 14 | Emission spectrum of one of the EC-QCLs used for this study.

**Selection of QCL applications:** The qualities of QCL and their increasing availability and refinement have led to improvements upon already existing thermal emitter based techniques or the implementation of new spectroscopic techniques.

In the field of classical transmission absorption spectroscopy, the high brilliance of QCL's enabled the switch to longer pathlengths for the transmission cell. This resulted in an increase of the absorbance and therefore an increase in the sensitivity of the system. This also facilitated liquid

handling, since the back pressure of the flow cells was reduced significantly.<sup>91,96,97</sup> It was for example possible to revolutionize the field of protein analytics through the utilization of EC-QCLs in the 1800-1400  $\text{cm}^{-1}$  spectral region. This region is home to the amide I band (1700-1600  $\text{cm}^{-1}$ ), corresponding to the C=O stretching and N-H in-phase bending vibrations, and the amide II band (1600-1500  $\text{cm}^{-1}$ ), corresponding to the N-H bending and C-N stretching vibrations, of proteins.<sup>97</sup> These bands carry important structural information about proteins, however, especially the amide I band overlaps with the H-O-H bending vibration of water, located at 1643  $\text{cm}^{-1}$ . With the high power density offered by modern EC-QCLs the useable pathlength could be extended up to 38  $\mu\text{m}$  from the previous <10  $\mu\text{m}$  applicable for FT-IR instruments.<sup>98</sup> Further optimization of the optical setup by balanced detection and emission profile shaping enabled limits of detection (LOD) as low as 4.3  $\mu\text{g/mL}$ .<sup>99</sup> Commercialization of QCL-spectrometer (available from Daylight Solutions Inc., Redshift Bio) for the liquid phase enabled the further investigation of QCLs for portable analytics by coupling with liquid chromatography instruments. It was shown that the structural information provided by the IR spectrum increased the resolving power of the chromatography run, outperforming the classical UV-vis detector commonly used in these applications.<sup>100,101</sup>

Besides improving the classical applications of IR spectroscopy, the high power laser light allows the exploration of alternative spectroscopic techniques. When light is absorbed by the analyte, this decreases the transmitted intensity, which is probed in absorption spectroscopy. At the same time, this absorption leads to heating of the sample. By modulating the incoming light beam, the sample temperature heating is also modulated, and a wave is generated. This temperature wave can lead to changes in the refractive index or density of the sample, which are the basis for photothermal spectroscopy. Also this temperature wave leads to a pressure wave due to the expansion of the sample upon heating, creating an acoustic wave which constitutes the basis for photoacoustic spectroscopy.<sup>102-104</sup>

These spectroscopic techniques are called indirect spectroscopy, since an effect of the absorption of the is measured, not the absorption itself. They profit from the application of QCLs in two ways, firstly by utilizing mid-IR light the sensitivity is increased as specific vibrations can be targeted, and secondly since for these techniques the signal scales directly with the power of the light source and inversely with the beam diameter, the high power, highly focused QCLs can bring substantial SNR profits.<sup>102,105-108</sup> While photoacoustic phenomena are probed by microphones, photothermal spectroscopy relies on interferometer to directly measure the phase shift caused by the heating or on the formation of thermal lensing, which changes the focus point of a visible probe laser which in turn can be related to the absorption.<sup>102,105-108</sup> With the availability of comparatively low cost DFB-QCL, photothermal and photoacoustic principles have galvanized the construction of robust, sensitive gas sensors capable of vastly outperforming FT-IR based instruments.<sup>107-111</sup>

Beyond the construction of sensors, photothermal spectroscopy also enables chemical imaging beyond the quite high diffraction limit for IR light.<sup>112-114</sup> This is possible by utilizing an atomic force microscope (AFM) to detect the effects of absorption on the sample. The expansion generated by absorption of the pulsed QCL light source can be probed with nm resolution by the AFM, decoupling the achievable spatial resolution from the wavelength of the incoming light.<sup>114-117</sup>

MIR dispersion spectroscopy is another field which profited from the popularization of QCLs.<sup>118-122</sup> It is also singular in the sense that it profits from not only the high power provided by the laser, but also from its inherently polarized emission and its coherence.<sup>118</sup> Like photothermal spectroscopy, dispersion spectroscopy takes a different approach to the collection of vibrational information than classical IR spectroscopy. In parallel to the absorption of the electro-magnetic wave, transmitted light also undergoes a phase shift as a consequence of the interaction with the analyte. This phase

shift can be measured, e.g. by a Mach-Zehnder interferometer, and is linearly dependent on the oscillator strength of the analyte, its concentration and the pathlength of the cell.<sup>118–124</sup> This linear dependency is true even for highly absorbing samples, where the assumed linearity of classical absorbance spectroscopy breaks down.<sup>118,123</sup> This improved working range can prove useful for sensor design, since real life applications seldom keep to the constraints set by model studies in a laboratory environment.

It can therefore be said that the implementation of QCLs and their broad commercial availability has revolutionized the field of IR spectroscopy significantly. New techniques have been developed as well as already existing ones refined and improved upon.

### 3. Laser based Vibrational Circular Dichroism

---

Chiroptical spectroscopy as a field operates in a constant struggle against the low intensities of the analyte signals and the comparatively high artifact background in addition to omnipresent matrix absorption interfering with correct spectra evaluation.<sup>13,125</sup> Accordingly, constant optimization and the adaption of technological progress was a constant during the early development phase, to render the techniques practical in a real life environment.<sup>126–129</sup> A lot of the early work on VCD focused on the understanding of polarization artifacts and how to avoid or address them.<sup>63,67,68</sup> In parallel, alternative sources of introducing modulated polarization into the measurement system were explored. Besides the now ubiquitous PEM, rotating quarter wave retarders, rotating polarizers in combination with a Fresnel retarder or also polarizing interferometer designs were discussed and tested regarding their effectiveness for VCD spectral acquisition.<sup>47,66,130–132</sup> Once the combination FT-IR + PEM was established as state of the art, constant effort was undertaken to optimize the signal to noise ratio and decrease the artifact levels. Dual source interferometer, constructively interfering for the  $I_{AC}$  channel and destructively interfering for the  $I_{DC}$  channel boosted VCDs signals without overloading the detector.<sup>133</sup> The implementation of a second PEM after the sample position facilitating the alignment process by cancelling out most of the optical artifacts.<sup>65,126</sup> With the advancements of modern computers completely digital signal processing eliminated the need for external lock-in detection and further simplified spectra acquisitions. It stands to reason that VCD can also profit from the implementation of a high power, linearly polarized light source like QCLs.<sup>2,134</sup>

### 3.1 Synergies between quantum cascade lasers and vibrational circular dichroism

As already elaborated on, the spectral frequency dependency of the phase shift introduced by the PEM and its efficiency curve counteract the multiplex advantages of classical FT-IR instruments.<sup>14,38,61</sup> This opens up niche applications for both dispersive instruments, but also for state of the art QCL based instruments. The maximum tunability of the EC-QCLs used in this study covers 400 cm<sup>-1</sup>, between 1760 and 1360 cm<sup>-1</sup>. For this range, the PEM phase shift varies a maximum of  $\pm 12\%$  around perfect  $\frac{\lambda}{4}$  retardation, and  $J_1[\alpha_M^0(\bar{\nu})]$  changes from 0.54 to 0.58, both much smaller discrepancies to be handled than the ones prevalent for broad band FT-IR experiments (see Figure 10). Besides the stepwise coverage of the spectral range, a characteristic QCLs share with dispersive instruments, QCL have other inherent advantages for VCD measurements.

In order to generate the alternating trains of left and right handed circular polarized light, the beam impacting the PEM needs to be linearly polarized, with 45 °angle relative to the stress axis of the PEM.<sup>1,38</sup> Since globars emit randomly polarized light they necessitate the implementation of a polarizer, commonly based on a wire grid design, before the PEM in order to condition the light's polarization properly. However, due to its selective transmission a polarizer reduces the spectral throughput of unpolarized light by 50 %, a loss that may prove problematic for highly absorbing sample-solvent system. QCL chips in contrast provide inherently polarized light due to the selection rule allowing only for specific electric field vectors to be emitted. For practical purposes, the quality of this polarization will be slightly diminished due to birefringence in the laser cavity and the beam steering optics, possibly necessitating the implementation of a wire grid polarizer for polarization quality improvement on a case-to-case basis. However, in this case the errors introduced are small enough that a polarizer will transmit >99 % of the laser intensity, a dramatically improved throughput compared to thermal emitters.<sup>135</sup> Besides the inherent polarization, the high brilliance of QCLs can be utilized similarly to classical IR spectroscopy to enable longer pathlengths and consequently higher signal intensities in the resulting VCD spectra.

**Early implementations of QCL-VCD:** Lüdeke et al. published the first VCD spectra obtained by EC-QCL-VCD spectroscopy in 2011.<sup>2</sup> In this application the laser was operated in CW mode, modulated by a chopper and tuned to cover the spectral region between 1320 and 1220 cm<sup>-1</sup>. Akin to FT-IR VCD the polarization was improved by a polarizer and modulated by a ZnSe PEM (37 kHz). At the PEM the first differences to a FT-IR system occurred, since the PEM was tilted and followed by an aperture. The reason for this is the occurrence of interference effects, reflections between the two planar surfaces of the PEM crystal, which overlap and distort VCD bands originating from the analyte.<sup>136,137</sup> The intensity of these interferences is directly proportional to the coherence of the light source, which in the case of a (QC) laser leads to significant problems. The tilted PEM allows for the spatial separation of the reflected beam from the transmitted one, and the subsequent aperture blocks the reflected part, preventing the occurrence of interferences.

After passing the sample and being focused by a ZnSe lens, the modulated laser intensity is recorded by a thermoelectrically cooled MCT detector. This is another change to classical FT-IR spectroscopy, as the high intensity of the laser negates the need for low noise cryogenically cooled detectors. This setup was employed to collect VCD spectra of Ni(sp)Cl<sub>2</sub>, (R)-(+)-limonene in CDCl<sub>3</sub> and L- and D-proline in H<sub>2</sub>O.<sup>2</sup> The high power of the QCL allowed for significantly longer pathlengths (up to 1 mm) and its applicability was shown in subsequent publications.<sup>3,4,138</sup> However, while the developments were substantial, the laser based system failed to outperform conventional FT-IR VCD systems.

Further developments of QCL based VCD focused on combining VCD with spatially resolved measurements. One of the instruments built for this purpose by Sato et al. combined an EC-QCL with a commercial FT-IR VCD instrument, allowing for an easy switch between the two techniques.<sup>134</sup> It was utilized for mapping of solid state protein samples as well as organic samples, but still the spectral quality comparison between FT-IR and QCL-VCD attested a near equal performance.<sup>134,139</sup> A further QCL-VCD microscope was developed by Phal et al. as a standalone instrument.<sup>135</sup> It performed well for mapping of solid state protein samples and the analysis of human derived tissue samples, but a direct comparison in terms of noise level and measurement time with FT-IR VCD instruments was not reported.

Overall the development of QCL-VCD spectroscopy so far have shown the great potential of the technique. Especially the combination with highly absorbing solvents ( $\text{H}_2\text{O}$ ) or spatially resolved measurements has proven to be a successful endeavor. Nevertheless, the years spent in optimizing FT-IR VCD have offset the disadvantages of its low power light source and QCL-VCD has failed to surpass it consistently so far.

### 3.2 Laser based vibrational circular dichroism

To explain why outperforming FT-IR VCD is a non-trivial goal, the setbacks faced by QCL-VCD need to be elaborated on. To do this, some of the challenges for laser based VCD will be discussed below. Subsequently, some possible solutions developed in this thesis for these problems will be outlined.

#### 3.2.1 Challenges of laser based vibrational circular dichroism

**Interference effects:** As already mentioned, coherent light sources like QCLs can introduce detrimental artifacts to spectroscopic measurements. With the high coherence, intense interference effects can occur, overlapping the actual analyte information. While above, these effects were only discussed in regard to the PEM, they can arise from all optical elements containing two parallel planar surfaces in the system. An example can be seen in the right panel of Figure 15, which depicts a raw VCD spectrum of an empty sample compartment, with no optical element between the PEM and the detector. The spectra are overlaid with an interference pattern originating from a KRS-5 wire grid polarizer. Due to the low intensity of the VCD signals, interference fringes are extremely problematic.

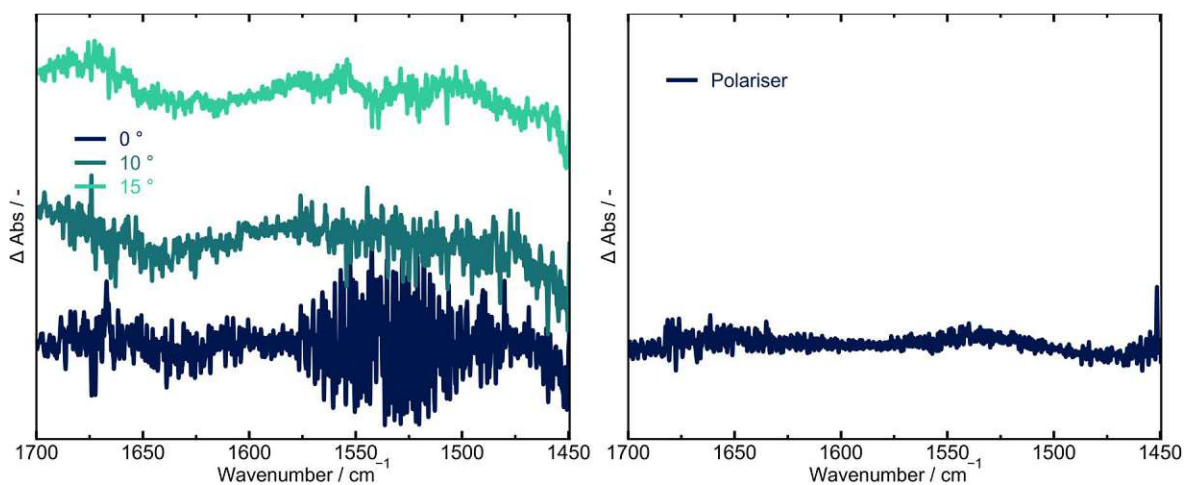


**Figure 15 |** (left) Raw VCD spectra of an empty compartment collected for different PEM tilting angles. The spectra are offset for clarity. (right) A raw VCD spectrum showing the interference effects occurring when placing a polarizer in the optical train. The y-axes are scaled equal.

In addition, due to the involvement of different states of polarization, the spacing of the pattern may vary between  $I_{AC}(\bar{\nu})$  and  $I_{DC}(\bar{\nu})$  resulting in a difference frequency pattern after the calculation of the raw VCD spectrum. When working with lasers and especially in the context of chiroptical spectroscopy an understanding of interference phenomena is therefore crucial.

This understanding can be provided by viewing the optical elements as (inefficient) Fabry-Pérot interferometers. Following this method, the frequency of the interference pattern can be approximated by:

$$\Delta\omega_r = \frac{c\pi}{n_\lambda d \cos \theta_i} \quad (34)$$

with  $\Delta\omega_r$  being the free spectral range in angular frequencies,  $n_\lambda$  and  $d$  being the refractive index at  $\lambda$  and thickness of the optical element respectively and  $\theta_i$  being the angle of incidence. Continuing, the intensity of the fringes can be calculated by:

$$I_t(\omega) = \frac{I_0(\omega)}{1 + \left(\frac{2F}{\pi}\right)^2 \sin^2\left(\frac{\pi\omega}{\Delta\omega_r}\right)} \quad (35)$$

with  $I_0(\omega)$  and  $I_t(\omega)$  being the incoming and transmitted intensity as a function of the angular frequency  $\omega$  respectively and  $F$  being the Finesse, which is directly proportional to the reflectivity of the optical element<sup>44</sup>.

When operating in the context of optical elements like lenses or windows, the most important parameters are the thickness and the refractive index of the element. Since the free spectral range refers to the spacing of the interference pattern, it can be retrieved from the transmitted intensity spectrum. By noting the refractive indices and thicknesses of the involved optical elements, the most probable origin of the pattern can be identified.

Interference phenomena arising from the PEM on the other hand are a special case, as during the modulation cycle the refractive index of the crystal varies slightly due to the applied stress. This modulation shows itself in an additional modulated interference pattern at the PEM frequency in addition to the static interference pattern arising from the ZnSe crystal in general. Consequently, the interference pattern observed in a VCD spectrum for an orthogonal PEM, see Figure 15 left, is more intense by a factor of  $\sim 5$  than the one observed for the polarizer, see Figure 15 right.

Having discussed the adverse effects of interference phenomena, possible remedies have to be elaborated. One option is to reduce the finesse of the optical element, either by choosing a low refractive index material, like  $\text{CaF}_2$  or by applying an anti-reflection coating.<sup>136</sup> While easily done for windows or lenses, this option can be impossible for more specialized optics. This is especially true for polarization optics, like retarders for which the principle of operation is based on the use of birefringent material and a change of material is not possible.

If the problematic optical element has to be used, another option is to tilt the element relative to the propagating light. Depending on the resulting angle of incidence, the reflected beam can be displaced away from the transmitted beam. If the displacement is large enough to ensure no overlap of the beams on the detector, no interference pattern will be observed.<sup>136</sup> The displacement ( $\Delta d$ ) is dependent on a number of variables and can be calculated according to:

$$\Delta d = d \sin 2\theta_i \frac{n_{1,\lambda}}{n_{2,\lambda}} \quad (36)$$

with  $d$  being the thickness of the element,  $\theta_i$  being the angle of incidence and  $n_{1,\lambda}$  and  $n_{2,\lambda}$  being the refractive index of air and the optical element at  $\lambda$  respectively.

This option is the method of choice for removing interference fringes originating from the PEM crystal. As can be seen in Figure 15 left, for increasing angles of incidence the interference effects are decreased significantly, until they approach manageable levels for  $\theta_i = 15^\circ$ . According to (36)

for this angle and assuming an refractive index of 2.41 and a thickness of 9.53 mm for the ZnSe crystal, the separation of the two beams is 1.98 mm, which is sufficient for a laser beam diameter  $< 2$  mm.<sup>140</sup> Since  $\Delta d$  is directly proportional the thickness of the optical element, a complete separation is not possible for thin optics like the polarizer mentioned above. This can be offset by reducing the beam diameter, e.g. with a telescope, reducing the necessary  $\Delta d$ . Since large angle of incidences also reduce the modulation efficiency of a PEM, a decrease in beam diameter is also warranted when dealing with interference effects arising from the modulator.

**Laser noise:** Besides challenges emerging from an interaction between the laser light and optical elements, the light source itself can have negative effects. For FT-IR VCD measurements, the used globar constitutes an extremely stable light source, with the detector and the interferometer mainly contributing to the noise floor. Laser sources on the other hand may also be affected by power fluctuations, long term thermal drifts and  $1/f$  noise.<sup>141,142</sup> Whereas frequency noise is often negligible for condensed phase applications, intensity noise is often problematic. This is especially true for QCLs operated in pulsed mode, as they are additionally affected by pulse-to-pulse intensity fluctuations. For modern systems, those fluctuations amount to  $\sim 2\%$ , constituting a significant part of the noise floor. Since chiroptical signals normally account for about  $10^{-5}$  of the total signal change, fluctuations of  $2\%$  can offset the advantages of QCLs substantially.

While CW lasers do not suffer from such fluctuations, the thermal drifts and  $1/f$  noise are still present. Since CW lasers are commonly modulated by a chopper at a few Hz, the  $1/f$  noise is comparatively high. In addition, this mode of operation requires extensive cooling and the data acquisition via a lock-in amplifier is less efficient than for high frequency laser pulses. Overall, this noise is one of the main reasons that QCL based VCD instruments have not significantly outpaced their FT-IR counterparts. Dedicated optical design is needed to counter these adverse laser properties.

**Laser emission characteristics:** The laser noise described above is inherent to all lasers, regardless of the chip material or resonator design. There are some other unique challenges that are specific to EC-QCLs. For one, the reproducible turning of the grating and therefore the spectral scanning was a parameter that underwent continuous improvement over the years. This led to wavelength shifts between subsequent scans, which had decreased the noise reduction normally afforded by scan averaging. Possible remedies explored were automatic alignment of the scans against each other, or the removal of shifted scans by an automatic similarity index evaluation.<sup>97,98,143,144</sup> Fortunately, further engineering by the laser manufacturer perfected the laser design sufficiently enough to correct this error in the latest generations of QCLs.<sup>118,145,146</sup>

In addition to its reproducibility, the grating also affects the beam pointing stability of the QCL over its tuning range. In parallel to the change of the emitted wavelength, the angle of the beam emitted by the laser changes slightly, which results in a laser pointing instability over the wavelength range. The magnitude of this change can be monitored by an IR camera as seen in Figure 16. The data collected for both QCLs used in this thesis is plotted for both vertical and horizontal deviation. For the vertical direction, no pointing change over the tuning ranges is observed. One outlier can be attributed to interference from water vapor, which affects the centroid assignment by the camera due to low laser intensity. In contrast, the horizontal centroid positions, in which plane the grating seems to move, change quite substantially. For the two laser at a distance of 50 cm changes  $\pm 100 \mu\text{m}$  ( $\pm 0.4$  mrad) relative to the average beam position of the respective tuning ranges can be observed.

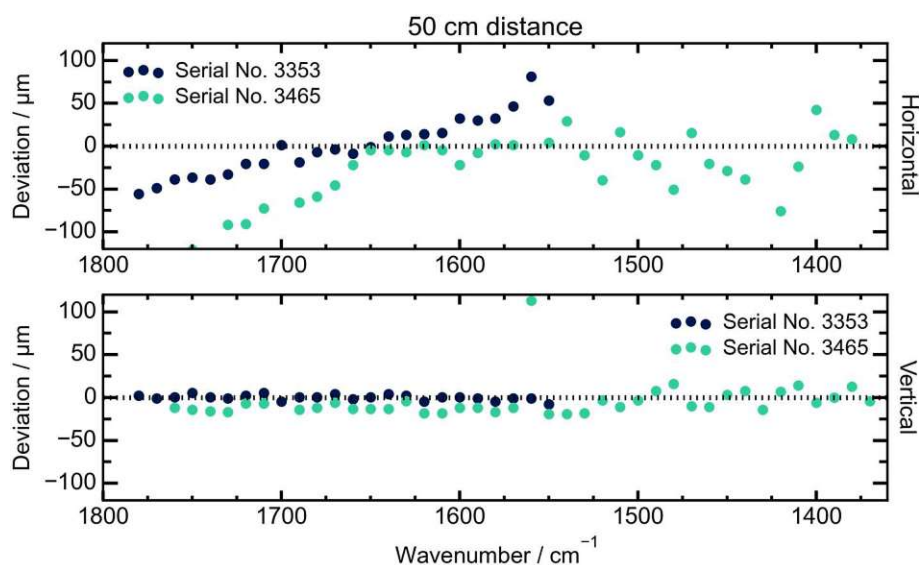


**Figure 16 | Change of the centroid position in  $\mu\text{m}$  measured at 50 cm distance between laser and camera. The data is plotted for both horizontal and vertical deviation, for both QCLs used in this thesis and relative to the mean position of each laser respectively.**

While small, such changes in position can be detrimental when high spatial resolution is needed or in combination with the interference effects above. When a tilted optical element, like the PEM, is combined with a blockage or aperture slight changes in the beam position can affect the transmitted intensity. Depending on the specific situation, an aperture can impose a wavelength dependent attenuation on the laser emission, or the beam may be partly clipped by the blockage. In order to both eliminate interference fringes and avoid a deviation from the gaussian beam profile, the beam pointing stability needs to be assessed before the implementation of a QCL-VCD setup. As part of the optical design, this information needs to be paid attention to and compensated for if necessary.

### 3.2.2 Balanced detection for laser spectroscopy

With the limitations and specific challenges of QCL in mind, the goal of this thesis was the implementation of a QCL-VCD instrument for the analysis of liquid samples. It was expected that the high laser brilliance and the broad tunability of modern EC-QCLs could be leveraged to achieve lower LODs and shorter measurement times compared to classical FT-IR systems. The first aspect to be considered was the aforementioned laser noise, which was expected to significantly influence the achievable noise floor.

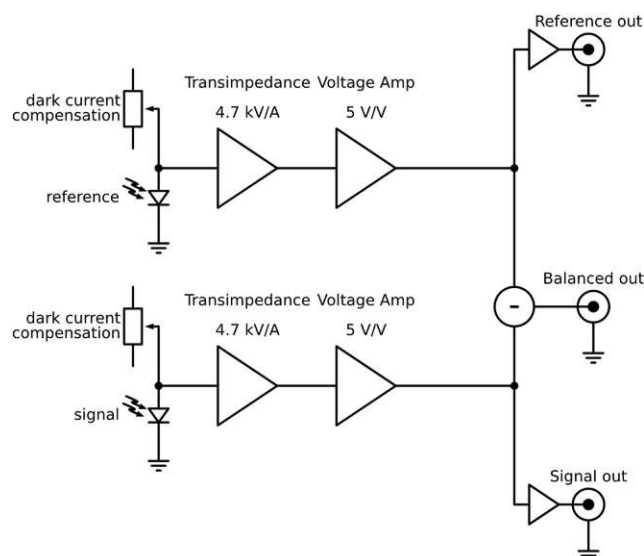


Figure 17 |Electrical configuration for the balanced detector used in this thesis.

Noise originating from laser sources has been known for some time now, and several methods have been explored to counter it. The most common one, and also the one employed in this thesis is balanced detection. First proposed in 1991 by Hobbs, this scheme combines careful optical alignment with an electronical noise cancellation.<sup>141</sup> The laser beam is split into two paths, with their respective intensities being as close to equal as possible. Each path is directed onto a separate detector. One of the paths, commonly called signal path, contains the sample, while the other path is referred to as reference path.<sup>147</sup>

After the intensity of the laser is recorded on both detectors, the voltages are amplified, and analog subtracted as seen in Figure 17. As both paths contain the noise originating from the light source, this noise gets cancelled, dramatically reducing the measurement noise. However, since the sample is only present in one path, its absorption is still accessible.

The efficiency of this noise rejection is dependent on a number of parameters. A characterization of the frequency response of both detectors and their respective amplifiers is normally performed at the factory. This is done to avoid operating the laser at frequencies which offer low noise rejection performance. In addition, optical engineering is essential, as the efficiency of this rejection is dependent on the ratio between the two detector signals, which should lie as close to 1 as possible. Achieving this equal intensity is non-trivial and may require additional attenuators in one of the channels.<sup>99,141,148</sup>

During previous studies performed in the research group, balanced detection was successfully applied for gas analytics and also protein absorption measurements in aqueous solution.<sup>99,142</sup> The latter was foremost the inspiration for applying balanced detection also to vibrational circular dichroism, as it showcased the potential of this scheme even for broadband spectra of liquid samples. The development and characterization of this setup is described in **Publication I**.<sup>145</sup>

### 3.2.3 Development of low noise laser based vibrational circular dichroism

**Optical setup:** The laser used as light source for the first iteration of balanced detection was an EC-QCL (Daylight Solutions, Serial No. 3353) tunable between 1781.90-1549.91  $\text{cm}^{-1}$ . It offers both CW and pulsed operation, but in order to reduce  $1/f$  noise and facilitate lock-in detection, the laser was set to 1 MHz, 200 ns pulse (= 20 % duty cycle) operation. To avoid a subsequent reduction in spectral coverage, the laser current was kept above the lasing threshold for the whole gain curve.

The resulting highly intense vertically polarized (1:100) laser beam was attenuated by a beam splitter and subsequent reflective attenuators in the beam path of the reference and signal channel respectively. This configuration allowed the use of a high current, enabling broad spectral coverage, while reducing the intensity reaching the detectors to ensure staying in their linear range.

A second beam splitter was used to obtain the two beam geometry inherent to a balanced detection scheme. The reflected beam was deemed the reference beam, and after passing a reflective attenuator it was focused by a 200 mm ZnSe lens through a reference transmission cell at the reference detector. Careful adjustment of the attenuator and the alignment was performed in order to keep the ratio between the two detectors as close to 1 as possible over the whole wavelength range.

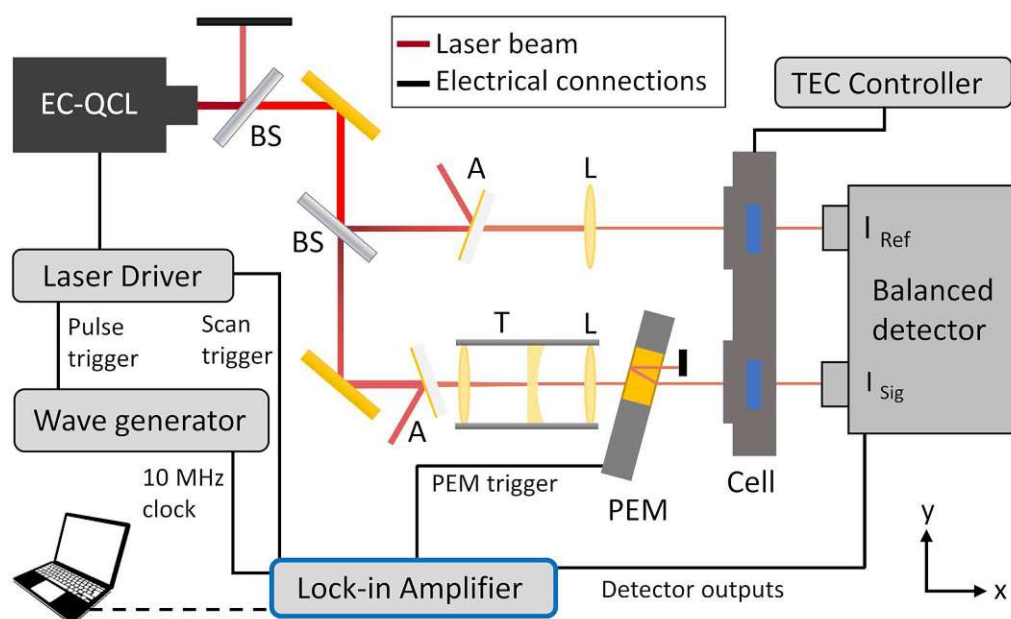


**Figure 18 | Setup built to explore the applicability of balanced detection for low noise VCD measurements. Sourced under the terms of CC-BY-4.0 from ref <sup>145</sup>.**

The transmitted beam path was deemed the sample path and was sent through a more substantial amount of optical elements. Besides a reflective attenuator, a cage system incorporating a Galilean telescope and a 200 mm ZnSe lens was placed in the light path. At the laser's original beam diameter of 2.5 mm, the removal of interference effects from the subsequently placed PEM would require a tilt angle of  $\sim 19^\circ$  according to eq. (36). This is without accounting for the beam deviation measured in Figure 16. Consequently, the beam diameter was reduced by a factor of 3 by the telescope to below 1 mm. In combination with a tilt angle of  $15^\circ$  this ensured that the reflected beam could be blocked without clipping the transmitted beam. Afterwards the beam passed a sample transmission cell and was collected by the sample detector. Due to the wavelength area covered by the laser, the optical setup was enclosed in an acrylic glass housing and flushed continuously with dry air to reduce interference from water vapor.

**Electronical configuration:** The laser intensity is doubly modulated, at the laser pulsing frequency and at the PEM frequency (42 kHz). To extract the relevant information a multi-channel lock-in amplifier (MFLI, Zurich Instruments) was connected to the balanced and reference channel outputs. The reference signal from the PEM was directly fed to the MFLI, while a waveform generator was in turn synchronized to the MFLI by means of its 10 MHz clock. This waveform generator was employed to control the pulsing scheme of the EC-QCL, with the synchronization ensuring the

correct demodulation of the laser intensity by the MFLI. The laser was set to continuously sweep over the wavelength area at a speed of  $640 \text{ cm}^{-1}/\text{s}$ , and a sampling interval of 10 samples per  $\text{cm}^{-1}$  was chosen. Since the sampling rates of the MFLI can only be set to a discrete number of options, the scan rate of the laser was chosen in a manner that the 10 sample/ $\text{cm}^{-1}$  criterion is satisfied. Noise evaluation was performed for the different settings, and a relatively slow scanning speed of  $640 \text{ cm}^{-1}$  resulted in the best performance in regard to the VCD signal. This can be attributed by the comparatively slow modulation imposed by the PEM, which can be better resolved by longer time constants. Since the time constant was set relative to the scan rate of the laser, the lower sweep rates performed superior. The start of the sweep was characterized by a high transistor-transistor logic (TTL) signal, which was picked up by the MFLI and used to synchronize the data acquisition to the process of the wavelength sweep. Since the balanced signal output only describes the difference between the two channels, an offset reference spectrum had to be collected once and could be reused as long as the same measurement conditions and solvents were used. Substituting eq. (30) with the corresponding values for this setup yields:

$$\Delta A(\bar{\nu}) = \frac{1}{2J_1[\alpha_M^0(\bar{\nu})]1.1513} \left[ \frac{I_{AC}^b(\bar{\nu})}{I_{DC}^b(\bar{\nu}) + I_{DC}^r(\bar{\nu})} \right] \quad (37)$$

with the subscripts AC and DC referring to the already established convention of PEM and classical IR respectively, while the superscripts r and b refer to the reference and balanced detector respectively. The resulting spectra were filtered by a finite impulse response filter to a final resolution of  $1.6 \text{ cm}^{-1}$ .

**Application:** While the overall design of the balanced detection VCD setup had the potential to significantly reduce the measurement noise, the first application was to evaluate the performance and judge possible improvements. For this reason, the transmission cells were filled with the chosen solvent  $\text{CHCl}_3$  and up to 3000 scans (= 20 min measurement time) were collected in 5 replicates for either single detector or balanced detector operation. The dataset was split in half and 1500 scans were averaged each to produce a background and a “sample” VCD spectrum, which were subsequently subtracted. The resulting 100 % lines can be seen in Figure 19 A, with the resulting root mean square (RMS) noise being plotted as well. A more complete assessment of the noise level can be achieved by plotting the change of noise as a function of averaging time (akin to the Allan variance), which can be seen in Figure 19 B. Even for short averaging periods, the balanced detector outperforms single detector operation significantly and this continues to be the case with increasing averaging time. This showcases the improvement and stabilization achievable by balanced detection even for VCD measurements.

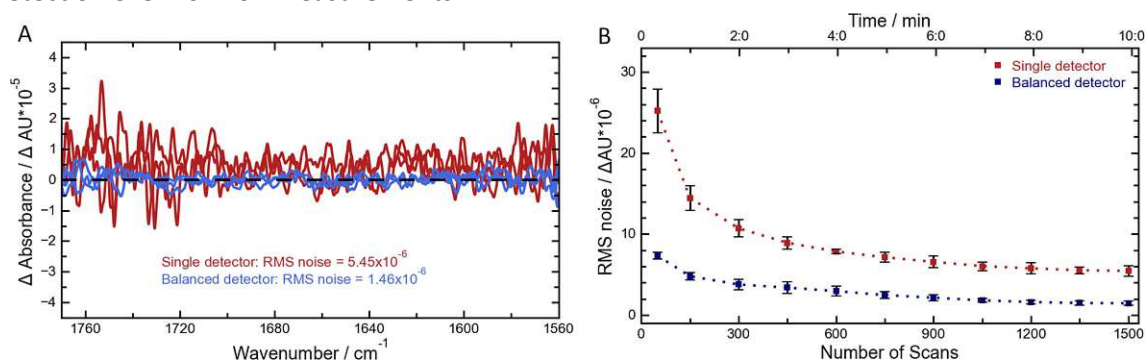


**Figure 19 | Results of the noise comparison between single detector and balanced detector QCL-VCD measurements.** The shown spectra are the results of a scan averaging 1500 scans (A), and the noise decrease as a function of the measurement time is plotted for both detection schemes (B). Adapted under the terms of CC-BY-4.0 from ref. 145

While the above results showed a decrease of the noise floor by a factor of 3, this is a less striking

improvement than previously reported for balanced detection in absorbance QCL spectroscopy. For comparative balanced detection systems in classical IR absorbance spectroscopy 20-fold improvements in terms of noise were reported.<sup>99</sup> An explanation for this difference can be found in eq. (37), in which the  $I_{AC}^b(\bar{\nu})$  component is normalized by division through the  $I_{DC}^{b+r}(\bar{\nu})$  component. Both intensities are collected in parallel, and through the normalization process the VCD signal becomes less influenced by laser power fluctuations. Therefore, the inherent data acquisition process of VCD signals offsets the gains provided by balanced detection to some degree. Still, from the data it can be seen that this process is not perfect and balanced detection achieves further decoupling of VCD signals from measurement noise.

Besides the comparison with a single detector system, balanced detection VCD needs to be benchmarked against the gold standard FT-IR VCD. For this in addition to the RMS noise, the maximum deviation from zero or noise height was also calculated and compared to literature values for FT-IR VCD which can be seen in Table 2. While single detector performance fails to outperform classical FT-IR VCD, balanced detector QCL-VCD achieves this easily, even for measurement times shorter by at least a factor of 3.

**Table 2 | Noise characteristics comparison between single detector QCL-VCD, balanced detector QCL-VCD and FT-IR VCD. Sourced under the terms of CC-BY-4.0 from ref<sup>145</sup>.**

	RMS noise [10 <sup>-6</sup> ΔAU]	Time [min]	Noise height [10 <sup>-6</sup> ΔAU]	Time [min]
<i>Single detector</i>	5.45	10	15.2	10
<i>Balanced detector</i>	1.46	10	3.83	10
<i>FT-IR VCD</i> <sup>149,150</sup>	2.8	30	50	60

For further reading on the development of balanced detection VCD the reader is referred to ref<sup>145</sup>.

### 3.2.4 Steps towards chiral monitoring

With the benefits of balanced detection QCL-VCD established, further work focused on advancing the technique towards chiral monitoring. This goal can be located in the broader context of process analytical technology (PAT). PAT is an advocated concept to facilitate innovations and improve quality and yield mainly in the pharmaceutical industry and was given out by the Federal drug administration (FDA) in 2004.<sup>151</sup> The main scope of this directive is the pharmaceutical industry, which overlaps with the foremost field of application of chiral analytics.<sup>26,152</sup> As can be derived from the name, PAT concerns itself primarily with the progress and only in passing with the finished product. In brief, the process of PAT can be described as follows:<sup>151,153</sup>

- 1. Understand the process:** Based on previous experiments, theoretical understanding and expert knowledge, the critical process parameters are identified and their influence on the variations of the finished product are mapped out.
- 2. Monitor the process:** Building upon the information gained in step 1 an adequate monitoring system can be designed. The aim is to assure reaching defined critical quality attributes (CQA) in the finished product by determining critical process parameters (CPP)s. This is achieved by applying numerous, often orthogonal, analytical techniques to monitor the process under investigation. The analytical chemical data is often combined with process data to derive relevant conclusions. This step can also involve soft sensors, which take information from multiple measurement techniques to predict not easily accessible process variables.<sup>154</sup>

3. **Control the process:** By combining the knowledge about the process with near real time monitoring, deviations from the correct course of a process can be identified early on. As a consequence, the deviations can be addressed and rectified through adjustment of the relevant CCPs, preserving the quality of the finished product, i.e. assuring high CQAs.

Spectroscopic methods, able to gather information in a non-invasive manner, have been at the forefront of PAT developments. Indeed, both FT-IR spectroscopy and ECD have been successfully applied as monitoring tools for protein stability studies or aggregation behavior in monoclonal antibodies.<sup>101,154–156</sup> However, VCD has so far been excluded from PAT designs by its low time resolution and weak sensitivity. That is not to say that VCD is not an essential part of modern pharmaceutical workflows. On the contrary, it can be viewed as the gold standard for absolute configuration assignment of finished chiral pharmaceuticals, as outlined in the US pharmacopeia.<sup>18,150,157</sup> It stands to reason that the opportunities offered by balanced detection QCL-VCD can extend its useability from an end of the line to a PAT technique broadly used in process monitoring.

**Spectral coverage vs time resolution** As discussed above, the broad tunability provided by modern EC-QCL systems enables the measurement of liquid samples, which constitute the most common state of matter during pharmaceutical manufacturing. However, as is also the case for FT-IR spectroscopy, the spectrum often contains only a small percentage of actual bands, with the rest corresponding just to an empty baseline. In contrast to FT-IR spectroscopy however, in EC-QCL spectroscopy, and in dispersive spectroscopy, the scan area can be amended to avoid collecting empty spectral areas. Since for EC-QCL spectroscopy this directly translates into reduced measurement time, it is an interesting opportunity for sensor design. Since the foundation of PAT is understanding the process, one can also predict the useful spectral area for process monitoring. This can be then used to specifically tailor QCL emission to the area of interest without wasting measurement time on empty spectral areas.

To test the possible gains offered by these considerations, chiral molecules with characteristic bands in different areas of the available EC-QCL were considered. One easily available analyte pair were the diastereomers quinine/quinidine, with bands between 1550 and 1670  $\text{cm}^{-1}$ .<sup>9</sup> For the higher wavenumber area, the search proved to be more difficult, and only one suitable and easily accessible analyte was found. This analyte was  $\alpha$ -D-galactose-pentaacetate, a modified chiral carbohydrate, with the pentaacetate group adding absorption and corresponding VCD bands in the carbonyl spectral region, 1665-1780  $\text{cm}^{-1}$  accessible by the laser.<sup>158</sup> The modification of  $\alpha$ -D-galactose-pentaacetate was done to introduce less rotational ambiguity into the carbohydrate analyte, enhancing its VCD signals.<sup>158</sup> All analytes were readily soluble in  $\text{CHCl}_3$  and the chosen concentrations were 20 mM for  $\alpha$ -D-galactose-pentaacetate and 144 mM for Quinine and Quinidine. At the used pathlength of 160  $\mu\text{m}$ , these concentrations result in a maximum absorbance  $>0.6$  AU, ensuring appropriate signal heights for the VCD spectra.<sup>38</sup> Consequently, the laser was set to sweep only over the spectral area useful for the respective analyte and 700 scans were averaged for each spectrum, amounting to  $< 3$  min of acquisition time. The resulting single channel spectra can be seen in Figure 20, with each sweep area covering the respective absorption bands, yielding the necessary information. The slight difference in intensity can be attributed to the change in current for the 1670-1550  $\text{cm}^{-1}$  area. This change was possible due to the maximum of the laser lying outside of the scanned area, allowing for a higher current without risking saturating the detector.

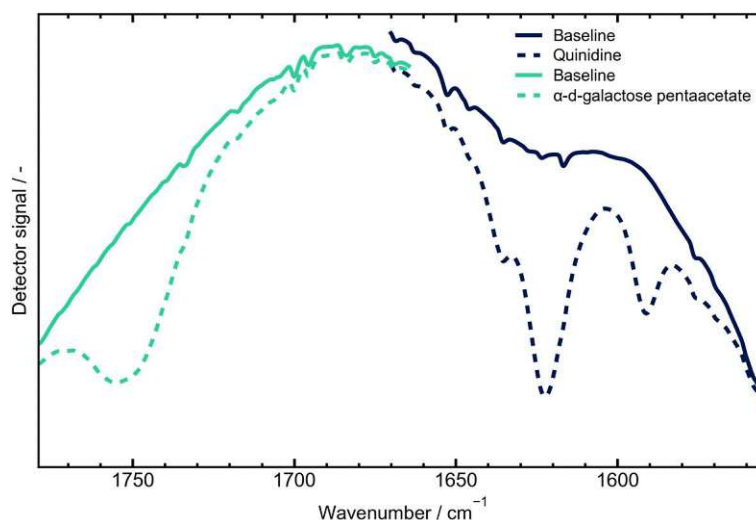


**Figure 20 |** Baseline and sample spectra collected for different analytes and spectral areas of the tuning range offered by one of the EC-QCL used for this thesis.

The calculated IR absorbance and VCD spectra can be seen in Figure 21 with a filtered resolution of  $5\text{ cm}^{-1}$ . The IR absorbance spectrum of  $\alpha$ -D-galactose-pentaacetate in the area accessible by the laser is dominated by a strong absorbance band at  $1751\text{ cm}^{-1}$ , which translates to a well resolved positive couplet in the VCD spectrum. This vibration can be attributed to the C=O stretch vibration occurring in the ester bond between the acetate residual and the galactose. The location of this band at the higher frequency limit of such bands can tentatively be attributed to the ether group connected to the alcoholic O of the ester group.<sup>158,159</sup> The couplet extends from the minimum at  $1755\text{ cm}^{-1}$  to a maximum at  $1747\text{ cm}^{-1}$ , which corresponds well to the location reported in literature.<sup>158</sup>

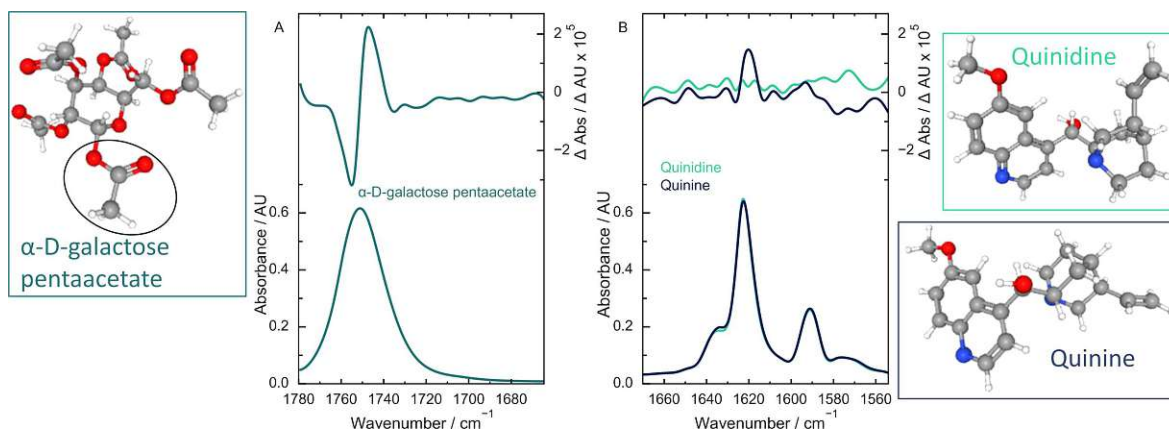


**Figure 21 |** IR absorbance and VCD spectra for  $\alpha$ -D-galactose pentaacetate (A) and quinine/quinidine (B). The corresponding 3D-structures are placed next to the spectra. For  $\alpha$ -D-galactose-pentaacetate one of the acetate residuals is marked with a black ellipse.

As for quinine and quinidine, their IR spectra are virtually identical, as expected for diastereomers, with a strong absorption band at  $1620\text{ cm}^{-1}$  and a weaker one at  $1590\text{ cm}^{-1}$ , corresponding to the C=N vibration of the quinoline ring.<sup>9,160</sup> The corresponding VCD spectra are not as resolved as the  $\alpha$ -D-galactose-pentaacetate one, with one weak band at  $\sim 1575\text{ cm}^{-1}$  and one artifact mirroring the absorbance band at  $1620\text{ cm}^{-1}$ . The weak signals were expected from the literature, as only weak VCD bands have been found for Quinine/Quinidine in the spectral area accessible by the laser.

Nevertheless, the orientation of the band around  $\sim 1575\text{ cm}^{-1}$  exhibits the typical mirror image expected for the molecule pair and matches the peak positions reported in literature quite well.<sup>9</sup> Accordingly, it can be concluded that even for challenging analytes like these, the adjusted QCL-VCD setup performs satisfactory at measurement times of below 3 minutes.

**Fast monitoring** With the additional speed advantage of tailored coverage, a more dynamic study was carried out, which was the basis for **publication II**. As mentioned for the quinine/quinidine measurements, strong VCD bands are generally located between  $1500\text{--}900\text{ cm}^{-1}$ , with terpenes being prominent examples. These molecules are often used as benchmark samples to showcase instrumental improvements.<sup>9,149,161–163</sup> Due to the restrictions imposed by the laser coverage these samples were not accessible by our system. The laser's spectral range is mostly home to biological samples like proteins or nucleic acids.<sup>14,158</sup>

Biological samples constitute meaningful analytes and are indeed part of this thesis, but for the application of chiral monitoring small molecules in organic solvents were considered more appropriate analytes. With the restrictions imposed by the accessible spectral area, the enantiomeric pair R/S-(±)-1,1'-bi-2-naphthol (BINOL) was selected. As can be seen in Figure 22, these molecules have two strong bands and corresponding VCD couplets in the region between  $1650$  and  $1580\text{ cm}^{-1}$ . The doublet peaks in the absorbance spectra and their matching VCD bands can be attributed to C=C stretch vibrations in the naphthalene backbone.<sup>159</sup> In addition to the presence of absorption bands in the accessible area, see, these molecules have industrial relevance. Due their very stable confirmation, they are used as chiral motifs of polymers and their derivatives are important reactants for asymmetric chemical reactions.<sup>164,165</sup> Besides their relevance for industry, the signals arising from the BINOL in this area are  $< 5 \cdot 10^{-5}\text{ ΔAU}$ , which is also a level relevant for applications in biological systems or chiral synthesis. In comparison similar studies, which also aimed studying dynamic systems, were performed with model molecules, e.g. terpenes, with VCD signal intensities higher than  $10^{-4}\text{ ΔAU}$ . It is important to note that these studies using state of the art FT-IR VCD spectrometer were carried out at a much lower time resolution of between 20 to 60 minutes.<sup>149,166</sup>

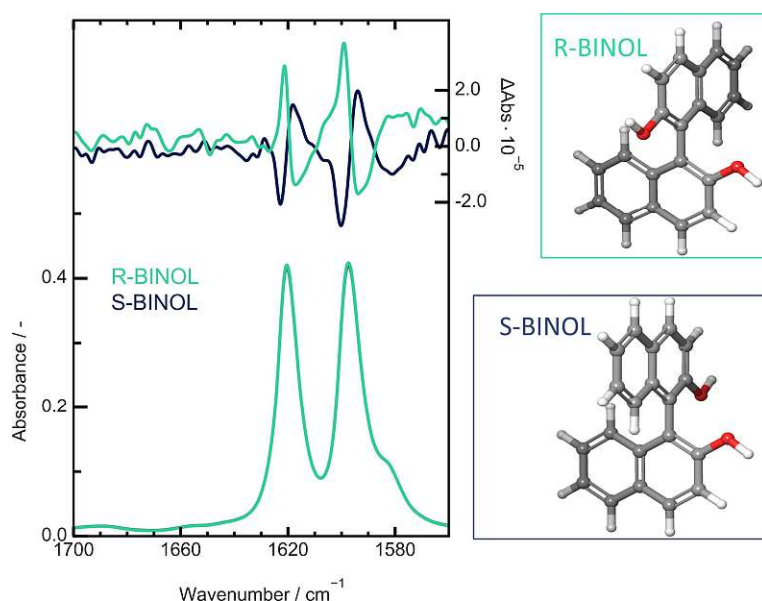
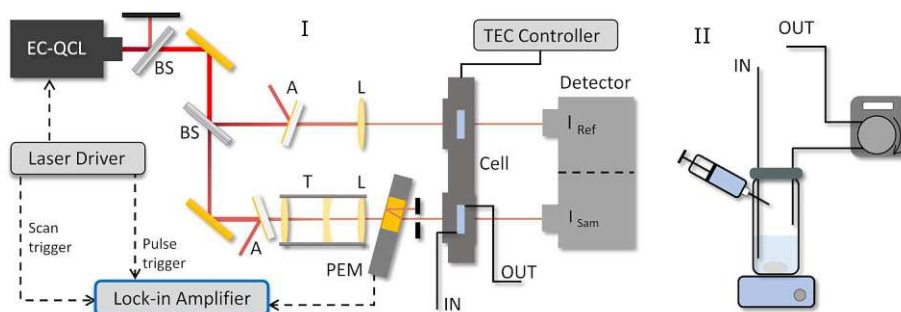


Figure 22 | (left) IR and VCD spectra of R- and S-BINOL. (right) 3D-structure of the molecules.

A common problem for storage of chiral substances is racemization, which refers to decrease in enantiomeric purity of a substance till the equilibrium, a 50:50 R:S mixture, is reached.<sup>165</sup> We

decided to simulate this process by the time dependent mixing of the two BINOL-enantiomers. The optical setup used for this study can be seen in Figure 23. It is a slight modification of the one presented in **publication I**, with a simplified electronic configuration and a closed loop pump system attached to the sample cell.<sup>146</sup> This pump system is used to represent an on-line sampling configuration, with a small stream of a reactor diverted through the analysis system (the QCL-VCD system) and afterwards rejoining the original reaction mixture.



**Figure 23 |** Optical setup (I) and fluid handling system (II) used for the simulated monitoring study. The fluid handling system was connected to the sample system as indicated by IN and OUT, resulting in a closed loop. Sourced from ref.<sup>146</sup>.

For the simulated racemization, a solution of S-BINOL was left to circulate in the closed loop through the sample cell and small amounts of R-BINOL were added every 6 min. These intervals were portioned into a waiting period, 3:16 min, to ensure proper mixing, and a spectral acquisition of 2:44 min. After 60 minutes the racemic mixture was reached, and the process was stopped. To be able to better assess the performance of QCL-VCD for this purpose, the process was repeated for three concentrations (20, 40 and 80 mM). The dataset was therefore comprised of 11 different ratios of the enantiomers, corresponding to enantiomeric excess (EE), and 3 different concentrations. Another analytical value, the differences in molar concentration, was implemented to combine the data in a meaningful way:

$$difM [mM] = \frac{EE [\%]}{100} c_{BINOL} [mM] \quad (38)$$

with  $c_{BINOL}$  being the concentration of BINOL regardless of its chiral identity. This value can be used similarly to LOD, as it defines the minimum difference in concentration between the two enantiomers that can be resolved. The spectra obtained from these experiments can be seen in Figure 24.

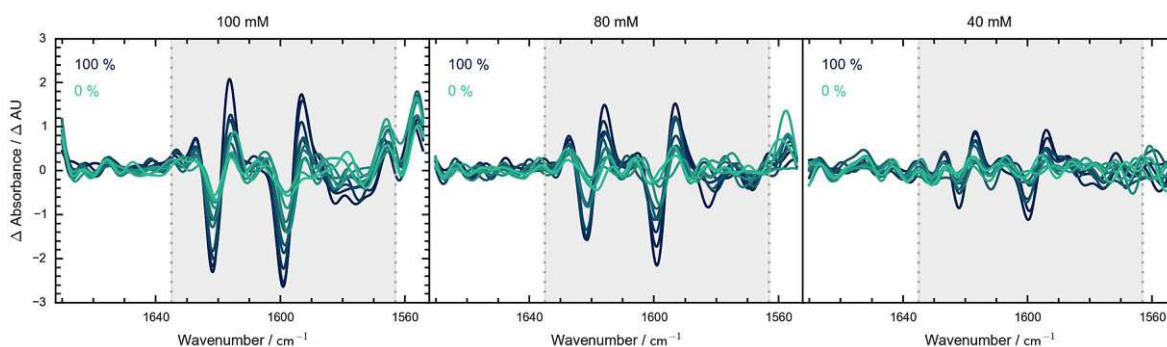


**Figure 24 |** VCD spectra obtained from the different racemization simulation as a function of concentration and EE levels. All subplots are scaled to the same y-axis. Adapted from ref.<sup>146</sup>.

The spectra show the typical couplets expected from BINOL in this spectral area, arising from the C=C deformation vibrations in the naphthalene backbone, see also Figure 22.<sup>159,164</sup> Also as expected, the signal intensity decreases along the decreasing EE levels, which can be observed even for the lowest tested concentration.

While monitoring could be done by plotting the relative size of the couplets, better and more stable results are normally achieved by applying chemometric evaluations. For quantitative evaluations, the first algorithm that comes to mind is partial least squares regression (PLSR). This method deconstructs the data into a number of orthogonal latent variables (LV), building a prediction model based on them, not on the underlying spectra. This counters the influence of collinearity which is an inherent challenge for spectral data.<sup>167</sup> By doing this, one can leverage the entire information contained in a VCD (or IR) spectrum, while avoiding overfitting of the data.

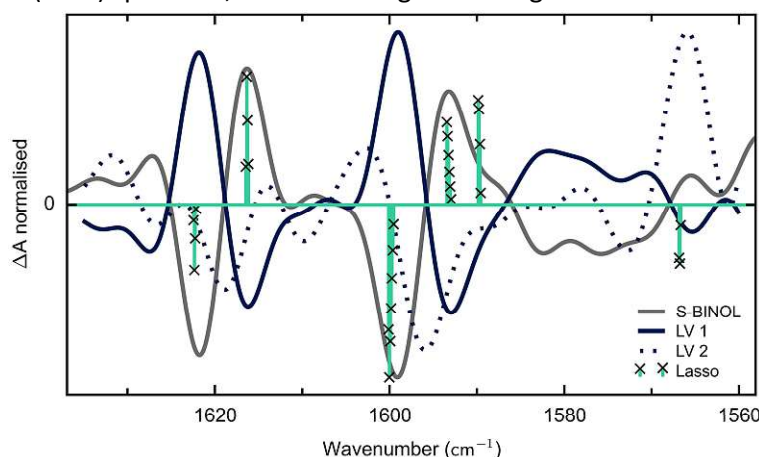


**Figure 25 | Coefficients obtained for the used models, plotted against a typical S-BINOL spectrum. Adapted from ref.<sup>146</sup>.**

PLSR evaluation of the data was set as benchmark, due to the above mentioned advantages, and also because it is commonly used for FT-IR VCD spectra evaluations.<sup>70,166</sup> The competing evaluation method was least absolute shrinkage and selection operator (lasso), which does automatic feature selection instead of transforming the spectral data.<sup>168</sup> It can be viewed as a modified multiple linear regression, with an automatic weighting of the variables (=wavenumbers). During the lasso algorithm, this weighting can lead to the omission of variables from the model building. Consequently, the model is only built upon the most information rich spectral areas. This concept is easily understood when looking at the coefficients which are the results of the respective models, as seen in Figure 25. PLSR relies on LV1 and LV2, which correspond perfectly to the normalized S-BINOL VCD spectrum. Lasso in contrast relies only on a few wavenumber positions, which however again correspond well to the strong bands of the S-BINOL spectrum. For assessing the overall performance of the model, the root mean square error of cross validation and of prediction (RMSECV and RMSEP) were calculated according to:

$$RMSE = \sqrt{\frac{\sum_{i=1}^n (y_i - \hat{y}_i)^2}{n}} \quad (39)$$

with  $y_i$  and  $\hat{y}_i$  being the real and predicted *difM* value of sample  $i$  and  $n$  being the number of samples. For the RMSECV a leave one out cross validation was applied, while the RMSEP value was based on a validation set corresponding to 20 % of the samples.

As can be seen in Table 3 PLSR remains slightly superior due to the broad spectral dataset it is based on. However, it does not offer much insight into improving the system to provide better monitoring capabilities. Also lasso appears to be more stable against overfitting, as the performance does not

decrease significantly between the cross validation and the prediction set.

**Table 3 | Figures of merit for the used chemometric methods.**

		PLS	Lasso
<i>RMSECV</i>	mM	2.8	3.4
	%EE	(2.8-7.0)	(3.4-8.4)
<i>RMSEP</i>	mM	3.5	3.6
	%EE	(3.5-8.8)	(3.6-9.0)

RMSECV: root mean error of cross validation

RMSEP: root mean error of prediction

In contrast, the automatic feature selection performed by lasso can be leveraged to in turn improve the optical design. Since the emission profile of an EC-QCL is adaptable, it can be set to only emit at the wavelengths selected by the algorithm. While only a small fraction of the spectral range is sampled, the prediction accuracy would remain the same. By applying such a regime, high quality prediction can be achieved at even higher time resolution as the one presented here. In the context of PAT systems, outlined previously, a reduced response time is crucial to ensure correct process control mechanisms. The combination of lasso and tunable EC-QCL VCD can be seen as the logical extension of the adapted spectral coverage which comprised the basis for this study, replacing human decision making by automatic objective feature selection.

In conclusion, it can be said that QCL-VCD technology has high potential for monitoring applications and PAT schemes. Based on the differences to classical FT-IR systems, mainly tunability and high power, fast and precise acquisition of chiral information is possible and can potentially be used to streamline asymmetrical reaction processes.

### 3.2.5 Proteins – Chirality in macromolecules studied by QCL-VCD

Besides chiral small molecules, the other prominent group of analytes for VCD is comprised of biomolecules, mainly proteins, peptides or short strands of nucleic acids. Since for those biopolymers their function is intrinsically linked to their structure, the added information gained by chiroptical methods can enhance the understanding of them. For the purpose of this thesis, the focus will be on protein studies, since it is also the most prominent field overall.<sup>14,71,78,169,170</sup> Before moving on to VCD spectral acquisitions of proteins however, the basis of protein analytics by vibrational techniques should be discussed.

The most prominent IR active bands of proteins are the amide I-III bands, located between 1300 and 1700 cm<sup>-1</sup>.<sup>99,171</sup> Most analysis focus on the amide I and II for structure analytics, as they can be correlated straightforward to secondary structure changes.<sup>14,101</sup> They originate in the backbone of proteins, i.e. in the peptide bonds between the amino acids comprising the primary structure of proteins, as can be seen in Figure 26 A. The amide I vibration is dominated by C=O stretching vibration of the carbonyl moiety, with contributions from the N-H in phase bending of the amide group. The amide II vibration in contrast is a combination vibration originating from the N-H bending and C-N stretching vibrations.<sup>97,171</sup> Both vibrations are susceptible to peak maxima shifts and shape changes upon secondary structure changes, a characteristic which can be utilized for getting information on protein structures. These shifts can be attributed to changes in the hydrogen bonds and angle dependent coupling occurring between the amide groups.<sup>172</sup> In general, the amide I band is recognized as being the most sensitive to those changes and therefore is the

focus of most studies.<sup>97,173</sup>

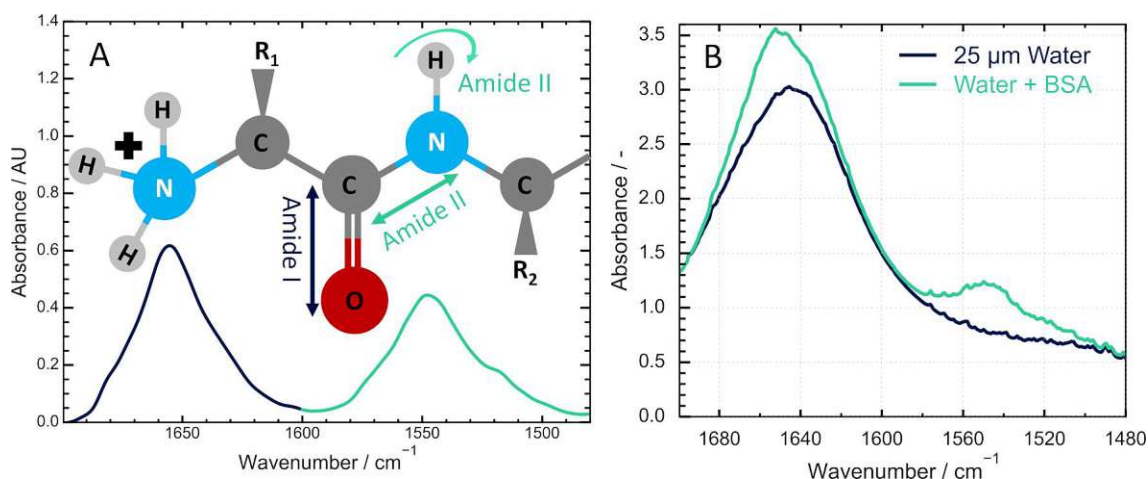


**Figure 26 | (A) Amide I and amide II of BSA in water. (inset): Movement of the peptide backbone responsible for the amide vibrations. (B) Uncorrected absorbance spectrum of water and BSA in water.**

Unfortunately, the amide I vibration is also the most challenging to resolve, as it overlaps with the strong H-O-H bending vibration of water at 1643 cm<sup>-1</sup>, as can be seen in Figure 26 B. Since water based solvent systems are the natural environment of proteins, this severely restricts the pathlength and therefore the concentration range applicable for IR protein studies.<sup>99</sup> The last band, the amide III band is the weakest one of the amide bands and is seldom used for structure analytics, although promising results have been reported for its dihedral angle sensitivity.<sup>174</sup>

As for their classical IR absorbance counterpart, protein VCD bands can be organized in different areas corresponding to the amide bands. However, the broad bands common for classical IR are resolved into a pattern of narrow  $\pm$  bands. Due to the inherent weak intensity of VCD spectra, the challenges of IR protein measurements are amplified, with even shorter pathlength (<6  $\mu$ m) being necessary to provide a high enough light flux. According to the general rule of thumb for VCD instrumentation, absorbance values between 0.4 and 0.8 are desired, resulting in concentrations between 100-200 mg/mL for the measurements.<sup>45,175,176</sup> Even at these high concentrations, low noise spectra are commonly collected over at least 6 h of measurement time, severely restricting the experimental throughput.<sup>45,76,177</sup>

### 3.2.5.1 Proteins in aqueous solutions

As part of this thesis, it was planned to utilize the high brilliance of the available EC-QCL to facilitate protein VCD studies in aqueous solutions. This necessitated several changes in the optical setup to account for the specific challenges of protein VCD studies. The finished optical setup used for this purpose can be seen in Figure 27. Below, the development process will be explained.

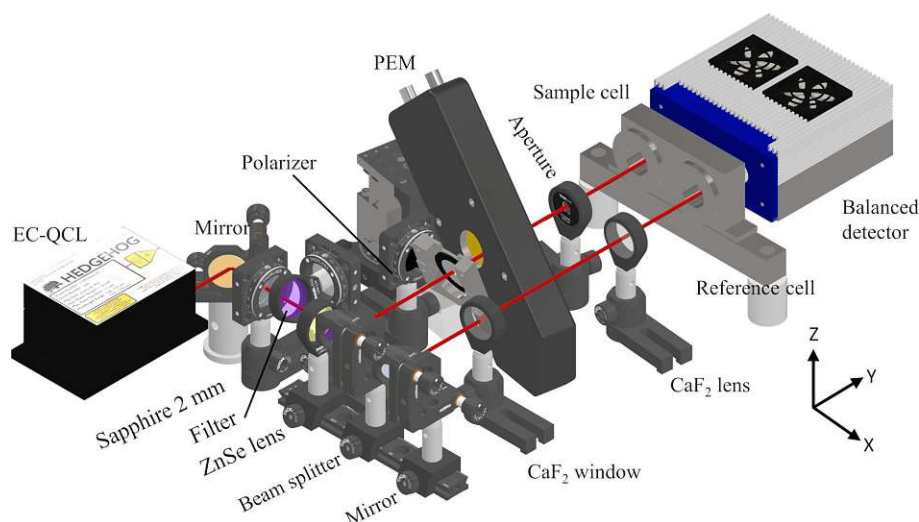
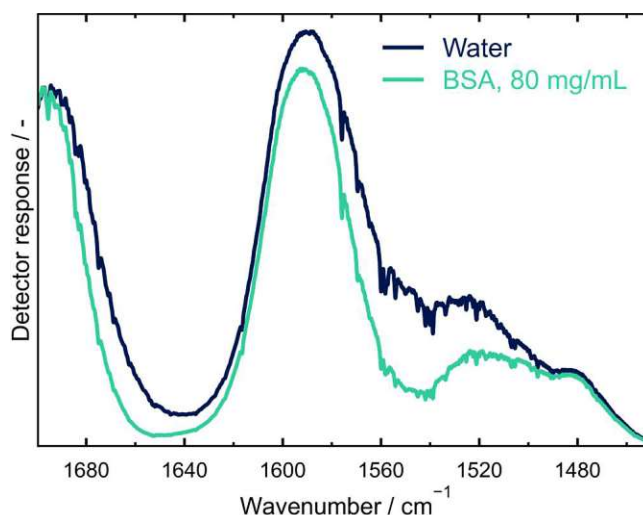


Figure 27 | Optical setup used for the VCD measurements of aqueous solutions.

**Setup development:** Due to the broader spectral coverage necessary for protein studies, a different EC-QCL (Daylight Solutions, Serial No. 3465) was used for the experimental setup. This model was tunable between 1360 and 1760  $\text{cm}^{-1}$  and able to operate at a duty cycle up to 30 %. For the spectra acquisition, the laser was set to pulsed mode at 600 kHz with 500 ns pulse length. The laser was swept between 1450 and 1700  $\text{cm}^{-1}$  at a speed of 80  $\text{cm}^{-1}/\text{s}$ , and 4 spectra of 141 scans each were collected for a typical measurement. This corresponds to an acquisition speed of 40 min per sample. The electronic configuration was left as in Figure 23, with the lock-in directly referenced to the laser and the PEM and spectra were collected at 20 samples/wavenumber. The spectra were then corrected for baseline shifts and were smoothed by fitting a 3<sup>rd</sup> degree spline with knots spaced 8  $\text{cm}^{-1}$  apart. This achieved an 8  $\text{cm}^{-1}$  resolution, verified by comparing a filtered  $\text{H}_2\text{O}$  vapor spectrum to FT-IR vapor spectra of the chosen solution.

The high absorption of water necessitated an adjustment of the intensity profile of the EC-QCL. At the high current necessary to ensure adequate transmission through the water band, the high power of the laser would lead to detector saturation in the area outside of this band. The lower wavenumber area was attenuated by a 2 mm sapphire window, the thickness selected to provide transmission down to 1450  $\text{cm}^{-1}$ . As sapphire is a birefringent material, the window was set into a rotational mount and the optical axis was oriented parallel to the laser polarization. This was done to minimize the degradation of the inherent laser polarization. Afterwards the higher wavenumber area was attenuated by a silicon based long pass filter. To reduce the interference fringes originating from this optical element, the laser was rotated around the Y-axis (Figure 27) by 20°. This axis was chosen, as according to the Fresnel equation the reflection of the laser light (p-polarized) at the filter surfaces should be reduced at this orientation.

A further increase of the angle was not possible, as this would have reduced the filter efficacy too much to provide adequate attenuation.



**Figure 28|** Detector response for a 25  $\mu\text{m}$  pathlength cell filled with water and for the same cell with BSA in water at 80 mg/mL.

As can be seen in Figure 28 the selective attenuation of the window-filter combination ensured a relative high throughput in the water band area. The maximum intensity was set to be in the linear range of the detector by observing single pulse intensities. After the attenuators the laser was focused by a 200 mm ZnSe lens and directed at a beam splitter. The reflected beam was chosen as sample beam since it contained 60 % of the laser intensity. The further additions to this beam path, i.e. PEM and polarizer, reduced the overall transmission, therefore the placement in the more intense beam path partly compensated these losses. In the end, almost equal intensities of both beam paths could be achieved, which is necessary for effective balanced detection operation. The PEM, a 50 kHz model, was placed in it at an angle of  $10^\circ$  around the Z-axis, with a 1 mm aperture placed to remove the diverted reflected beam. A KRS-5 polarizer (1:300 extinction ratio) was placed before the PEM.

This was done, since the rotational adjustment of the sapphire window described above relies on the assumption that the laser emission is highly polarized and stable. However, at least for DFB-QCLs, also the emission of circular or differently oriented vertically polarization states were reported.<sup>93</sup>

Consequently, the inherent polarization of the laser was investigated by means of a polarizer, operating as an analyzer, and a zero order quarter waveplate centered on 6  $\mu\text{m}$ . The waveplate was placed in a rotational mount, followed by the polarizer also in a rotational mount and the intensity was collected by the sample detector. The intensity at the detector can be calculated according to:

$$I(\alpha, \beta, \phi) = \frac{1}{2} * \{S_0 + (S_1 \cos 2\beta + S_2 \sin 2\beta) * \cos 2(\alpha - \beta) + [(S_2 \cos 2\beta - S_1 \sin 2\beta) * \cos \phi + S_3 \sin \phi] \sin 2(\alpha - \beta)\} \quad (40)$$

with  $\alpha$ ,  $\beta$ ,  $\phi$  being the angle of the analyzer, angle of the waveplate and the phase shift applied by the waveplate respectively and  $S_0$  to  $S_3$  being the stokes parameter of the incoming laser light.<sup>178</sup>

All angles are measured against the horizontal axis. By changing  $\alpha$  and  $\beta$  and collecting the corresponding intensity at the detector, the stokes parameter and therefore the polarization composition can be calculated. The used combinations are listed in Table 4.

**Table 4 |** Different settings for the angles of the polarizer ( $\alpha$ ) and the waveplate ( $\beta$ ) used during the characterization of the laser.

	1	2	3	4	5
$\alpha$	0 °	90 °	45 °	45 °	45 °
$\beta$	0 °	0 °	0 °	45 °	90 °

Option 4 was added since the typical application of this method aims to characterize a monochromatic laser, where the phase shift  $\phi$  introduced by the waveplate corresponds to 90 °. This leads to the elimination of  $S_1$  and  $S_2$  from option 5, simplifying the equation system. Since  $\phi$  corresponds to 90 ° only at one point in the wavelength range of the laser, one additional equation had to be added to facilitate the calculations.

For a given light source,  $S_0$  corresponds to the total intensity,  $S_1$  to the linear polarization in vertical or horizontal direction,  $S_2$  to the linear polarization at  $\pm 45^\circ$  orientation and  $S_3$  to the left or right-handed circular polarized component. In Figure 29 the values for  $S_1$ - $S_3$  normalized to  $S_0$  are plotted against the wavenumber range. As expected,  $S_1$  stays at around -1 for the spectral range, which

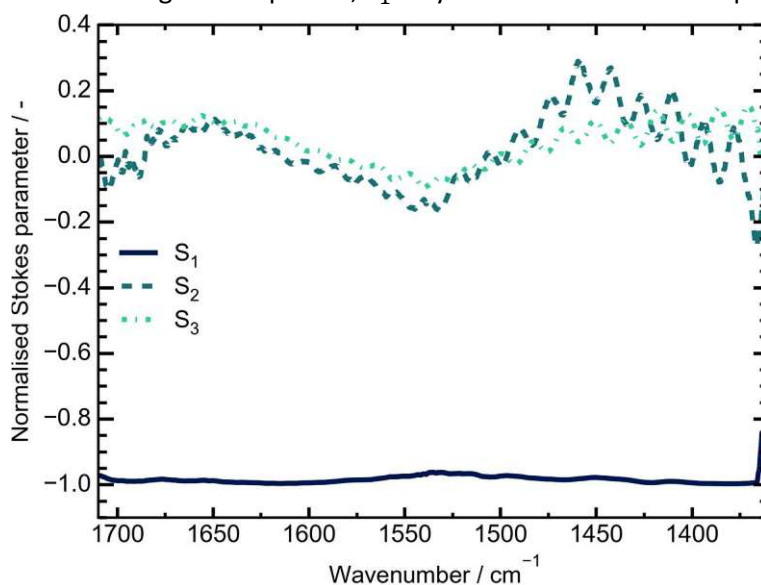


**Figure 29 |** Normalized stokes parameter collected for the used laser source.

corresponds to vertical polarization. Unfortunately, the laser emission also contains non-trivial  $S_2$  and  $S_3$  components, probably arising from birefringence in the chip and the window materials. The fringes at a frequency of  $\sim 10 \text{ cm}^{-1}$  in the characterization measurements originate from the used quarter waveplate. This optical element was not present during the actual measurements. Consequently, the mentioned polarizer was placed in the optical path to remove these components and increase the purity of the laser polarization. Since the polarizer also gave rise to significant interference effects, it was tilted by an angle of 40 ° (around the X-axis). With the rotational axis being oriented at 90 ° to the transmission axis, no reduction of the polarizer performance was observed.<sup>179</sup>

The transmitted beam passing the beam splitter was set to be the reference beam and was directed through a  $\text{CaF}_2$  window and refocused by a 200 mm  $\text{CaF}_2$  lens. The focus point of the 200 mm ZnSe lens was set to the back surface of the PEM, and the beam only slightly diverged till it was collected by the sample detector. In contrast, for the reference channel the refocusing steps were necessary to ensure enough intensity was reaching the detector for adequate signal balancing. Both beams

passed a respective 26  $\mu\text{m}$  pathlength cell in a double pathlength transmission cell, which was set to 25 °C. The complete setup was placed on a temperature-controlled breadboard set to 22 °C (approx. room temperature) and enclosed in acrylic glass housing for further stabilization and to facilitate flushing with dry air.

**Concentration range:** To evaluate the performance of the instrument, a calibration curve of bovine serum albumin (BSA) spanning from 10 - 100 mg/mL was prepared in ultrapure water (resistivity: 18 m $\Omega\text{cm}$ ). BSA is a small protein mainly composed of  $\alpha$ -helical structures, easy to acquire and broadly soluble in water even at high concentrations.<sup>45</sup> As can be seen in Figure 30 (A) the resulting IR absorbance spectra exhibit the expected gradual increase in intensity for the amide I and II bands. Also the band maxima, 1654  $\text{cm}^{-1}$  and 1546  $\text{cm}^{-1}$  for the amide I and II respectively, correspond to values found in literature. The corresponding VCD spectra on the other hand are not so easily interpretable. Despite the measures described above, the spectra are heavily distorted by high frequency interference fringes. A Fourier transform analysis of the spectra revealed frequencies of 3  $\text{cm}^{-1}$  and 1  $\text{cm}^{-1}$ , which could be attributed to the long pass filter and the polarizer respectively. Consequently, the spectra, originally collected at 0.5  $\text{cm}^{-1}$  resolution, were smoothed to 8  $\text{cm}^{-1}$  resolution as already described. The spectra are shown in Figure 30 (B). This resolution was chosen, since most VCD spectra of biomolecules are presented at 8  $\text{cm}^{-1}$ . At this resolution, the VCD spectra can be interpreted and indeed show the expected trend in intensity.

The amide I area is composed of the well resolved positive couplet expected for mostly  $\alpha$ -helical proteins, spanning from 1662 to 1642  $\text{cm}^{-1}$ , which again corresponds well with literature values. In the amide I area, one would expect a negative band at  $\sim 1515 \text{ cm}^{-1}$ , which indeed is present in the collected spectra. What is not expected is the positive band around 1548  $\text{cm}^{-1}$ , corresponding well to the amide II band, which in combination with the 1515  $\text{cm}^{-1}$  band mimics a couplet. Based on the band maximum position this peak can be deduced to be an absorbance artifact and is an indicator that the baseline adjustment was not entirely successful. Subsequent alignment was performed, but it was not possible to reduce all artifacts over the wavelength range to an acceptable level.

The process was greatly hindered by the strong fringes, as they distorted the baseline and reduced the SNR significantly. For further progress in this experiment alternative attenuators will be necessary, or as a first step it may help to reduce the pathlength significantly. Alternatively, methods could be implemented to reduce the coherence of the laser, as already proposed in the literature for visible laser systems.<sup>180,181</sup> It might also be sensible to reduce the spectral coverage and focus only on the amide I region. This should facilitate the alignment process and the amide I band alone can contain enough information for most applications.<sup>182,183</sup>

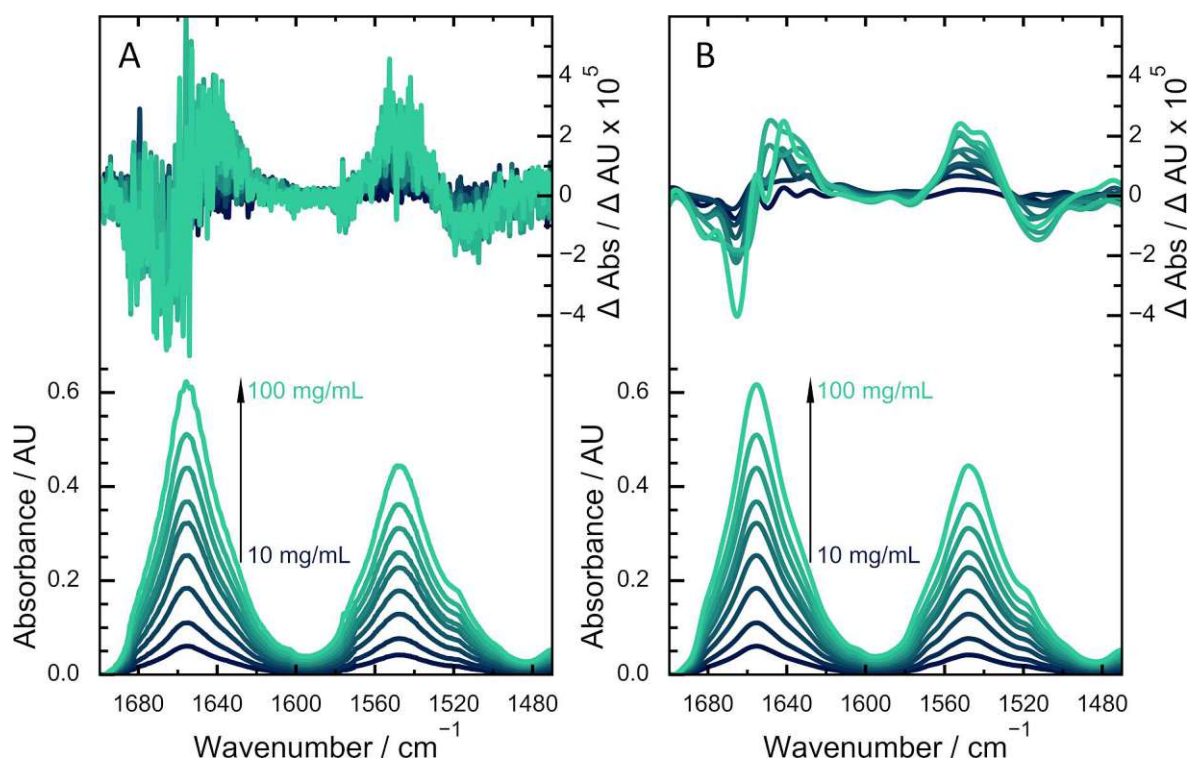


**Figure 30 | (A)** IR absorbance and VCD spectra of BSA in different concentrations. The spectra are unfiltered and presented at a resolution of  $0.5\text{ cm}^{-1}$ . **(B)** The IR absorbance and VCD spectra shown in (A) after applying a lowpass filter with a cut-off of  $8\text{ cm}^{-1}$ .

Nevertheless, even though the spectra are not perfectly artifact free, the data shows the potential of QCL-VCD for aqueous protein solutions. The amide bands were well resolved, even against a water background absorbance of 3.0. The overall level noise levels were satisfactory, and the increased pathlength of  $26\text{ }\mu\text{m}$  extends VCD measurements of proteins to significantly lower concentration regimes. The presented data can be seen as an important step towards fast and sensitive VCD spectra acquisitions, and the author is convinced that further improvements will allow VCD to be used for dynamic studies in the future.

### 3.2.5.2 Low concentration VCD – proteins in $\text{D}_2\text{O}$

Besides exchanging the light source for a laser, one can also enable lower concentration protein studies by exchanging the solvent system. FT-IR VCD protein studies have been performed at pathlengths between  $25\text{--}50\text{ }\mu\text{m}$  by switching to  $\text{D}_2\text{O}$  based solvent systems.<sup>75,183,184</sup> The replacement of H by D leads to an increase in mass of the oscillator, which according to eq. (9) leads to a shift of the vibrations to lower frequencies. Consequently, the D-O-D bending vibration is found around  $1200\text{ cm}^{-1}$  leaving the amide bands unobstructed. This method has been routinely used if the effect of external changes, like temperature or pH changes, are to be studied without the possibly detrimental influence of the high concentrations normally associated with VCD protein studies.<sup>16,73,76,183,185</sup>

While this procedure is used to make larger pathlengths accessible for FT-IR experiments, laser-based studies can also profit from it: The high brilliance of QCLs and the low absorption of  $\text{D}_2\text{O}$  in the amide regions allow for pathlengths of up to  $478\text{ }\mu\text{m}$  and  $270\text{ }\mu\text{m}$  for transmission and dispersion analytics respectively.<sup>173,184</sup>

The goal of the work presented in this chapter was to extend this combination to QCL-VCD spectroscopy, improving the sensitivity and time resolution of the technique in the application of

protein analytics. The results of this can be found in **Publication III**.

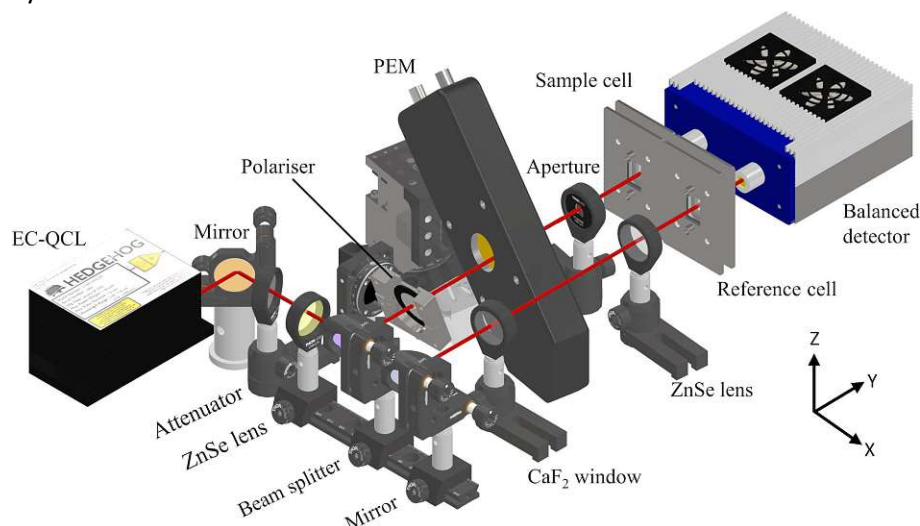


**Figure 31 | Optical setup used for the protein studies in D<sub>2</sub>O solutions.**

For this purpose, the setup presented before was adapted to be better suited for protein measurements in D<sub>2</sub>O, see Figure 31. The emission profile shaping done by the sapphire window and the long pass filter was not necessary anymore, as the high absorption of H<sub>2</sub>O did not need to be compensated. A reflective broadband attenuator, akin to the one used in publication I and II, was implemented instead. In addition, the double pathlength cell was replaced by two separate transmission cells. These cells were the same model used in our FT-IR instruments, and the sample could be directly injected into the cell, with minimal tubing involved. This was done to keep sample consumption at a minimum.

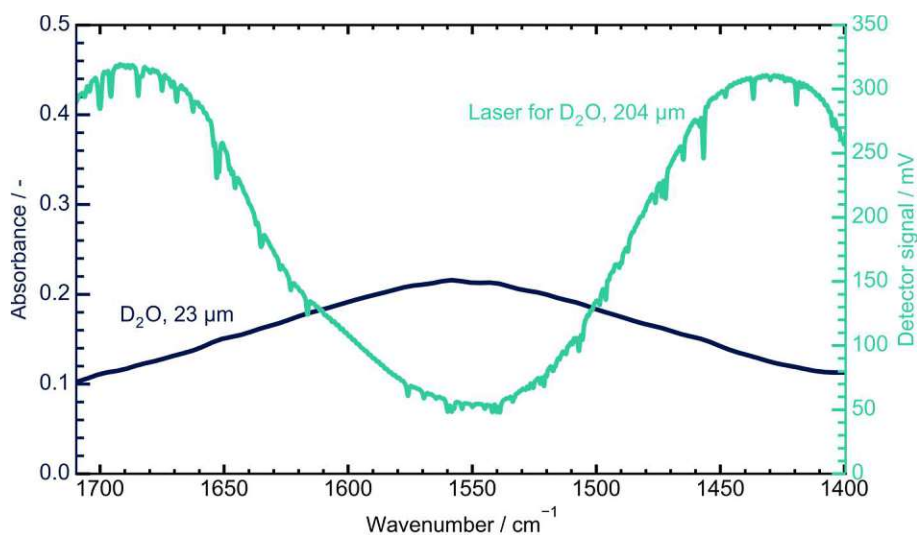


**Figure 32 | FT-IR absorbance spectrum of D<sub>2</sub>O in a 23 μm cell and transmission profile of the used EC-QCL setup for a pathlength of 204 μm.**

In addition, the sample cell could be placed at different positions and orientations with ease, independently from the reference beam. This provided another degree of freedom for the baseline adjustment before VCD measurements. The used pathlength was 204 μm, which is longer than the ones previously used on FT-IR instruments, but shorter than for other QCL-IR transmission setups reported elsewhere.<sup>75,173,184</sup> This is in part due to the expected lower signal for VCD measurements,

and therefore a more conservative adjustment to preserve a high spectral throughput. Another reason is a slight absorption band of  $D_2O$  at around  $1550\text{ cm}^{-1}$ , which in combination with the gain curve of our EC-QCL lead to a very uneven transmission profile, see Figure 32. While higher pathlength are indeed possible, this configuration was chosen to keep the noise levels low and facilitate alignment.

Besides the optical setup, also the laser pulsing scheme was adapted. While in the previous iterations the laser was operating independently of the PEM, in this configuration the laser pulsing scheme was modulated in reference to the PEM's modulation cycle. The PEM reference frequency (50 kHz) was fed to the lock-in amplifier and one demodulator was set to the 8<sup>th</sup> harmonic (400 kHz), outputting a TTL signal at this frequency. This signal was connected to the laser controller to set the modulation frequency and the pulse length was set to 700 ns, resulting in a duty cycle of 28 %.

For the adjustment of the pulsing scheme, a polarizer oriented horizontally was placed in the sample channel after the PEM. This created a crossed configuration, and the lock-in amplifier phase was adjusted until 2 of the 8 laser pulses occurring during the modulation cycle ( $20\text{ }\mu\text{s}$ ) were maximized. Due to the crossed configuration, 2 other pulses should exhibit minimum intensity. This is indeed what was observed. Figure 33, which depicts the digitized detector intensity as a function of time. This reference configuration was deemed stable over at least several months according to frequent control measurements.

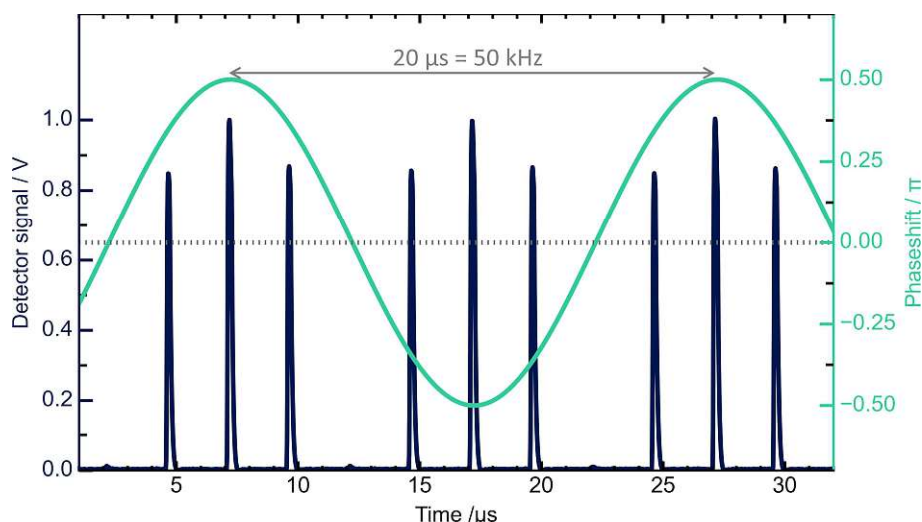


**Figure 33 |** Detector signal for the transmission of the laser through a crossed polarizer configuration. The correct referencing of the laser can be seen, as during the modulation cycle two laser pulses are maximized and 2 are minimized.

The motivation for switching to this modulation scheme was to apply the most efficient use of the laser intensity, while still keeping a relatively high duty cycle of 28 %, crucial for good lock-in amplifier sensitivity. With this configuration 25 % of the laser energy passed the PEM at the highest modulation points. In the future, this scheme could be combined with a different data acquisition scheme, based on digitizing singular pulses. In this case, the laser could be set to the PEM's 2<sup>nd</sup> harmonic, allowing for 100 % of the laser intensity being used for VCD signal generation. This could allow for high performance in terms of SNR at a dramatically reduced duty cycle.

Of course, by referencing the two systems, there was also the possibility of the laser pulse intensity variations being imposed upon the VCD signal as deviations from the baseline. However, direct comparison between VCD spectra acquired at different modulation schemes verified that this was

not the case. In addition, the VCD signal could also be more affected by interference effects occurring at even harmonics, with the laser operating at one of these.<sup>136</sup> Fortunately, the interference reduction by an angled PEM also reduces these interference effects, eliminating this problem.

With the laser pulsing scheme established, the laser was set to continuously sweep at a speed of 40 cm<sup>-1</sup>/s in the ranges of 1400-1710 cm<sup>-1</sup> and 1580-1710 cm<sup>-1</sup>. For each measurement, either 38 (1400-1710 cm<sup>-1</sup>) or 90 (1580-1710 cm<sup>-1</sup>) sweeps were collected for one scan of 5 minutes, and several of these scans were averaged to collect one spectrum. The spectra were smoothed as described in 3.2.5.1 and corrected for baseline shifts.

Reference measurements for proteins in D<sub>2</sub>O were performed on a Bruker Vertex 70v spectrometer, equipped with a PMA50 accessory. A long pass filter (cut-off: ~1828 cm<sup>-1</sup>) was introduced before the polarizer to increase the relative spectral throughput in the area of interest and the samples were placed in a 23 μm pathlength cell. The spectra were collected at a total measurement time of 1 h with a resolution of 8 cm<sup>-1</sup>.

**FT-IR-VCD vs QCL-VCD:** A set of three proteins was selected for the evaluation, representing different combinations of secondary structures. As already mentioned, BSA is composed mainly of α-helical structures. In contrast, lysozyme is comprised of mixture of α-helical structures and turn structures, while β-lactoglobulin features a comparatively high percentage of β-sheets in addition to α-helices and turns. To compare the FT-IR and QCL systems, solutions of the proteins at 60 mg/mL (FT-IR) and 8 mg/mL (QCL) respectively were placed in the appropriate transmission cells and spectra were collected for 1 h. Noise comparisons revealed a near identical noise at this measurement time for the systems.

As can be seen in Figure 34 the IR absorbance and VCD spectra of both instruments agree very well in regard to band positions and maxima. While the different secondary structures are less obviously reflected in the absorbance spectra, the VCD spectra show substantial differences in the amide I' bands, with the “ ‘ ” denoting measurements in D<sub>2</sub>O. This is especially true for the comparison between BSA and lysozyme which for the IR absorbance spectra only differ in their intensity. Their VCD amide I' band on the other hand exhibit a clear difference, with a strong couplet for BSA and 2 negative peaks for lysozyme. As was reported before, the added chiral dimension of VCD provides improved insight into the composition of proteins when compared to classical IR absorbance spectra.<sup>14,182</sup>

Further evaluation of the accessible concentration range with BSA (similar to the one performed for BSA in H<sub>2</sub>O) was also conducted. For BSA concentrations between 2 to 14 mg/mL were measured at 1 h of measurement time. Well resolved VCD bands could be identified for the whole concentration range. For an evaluation of the performance, the LOD was calculated by:

$$LOD = \frac{3 * m}{RMS\ noise} \quad (41)$$

with *m* being the slope of the linear calibration line fitted to the VCD amide I' bands. This resulted in a LOD value of 0.3 mg/mL.

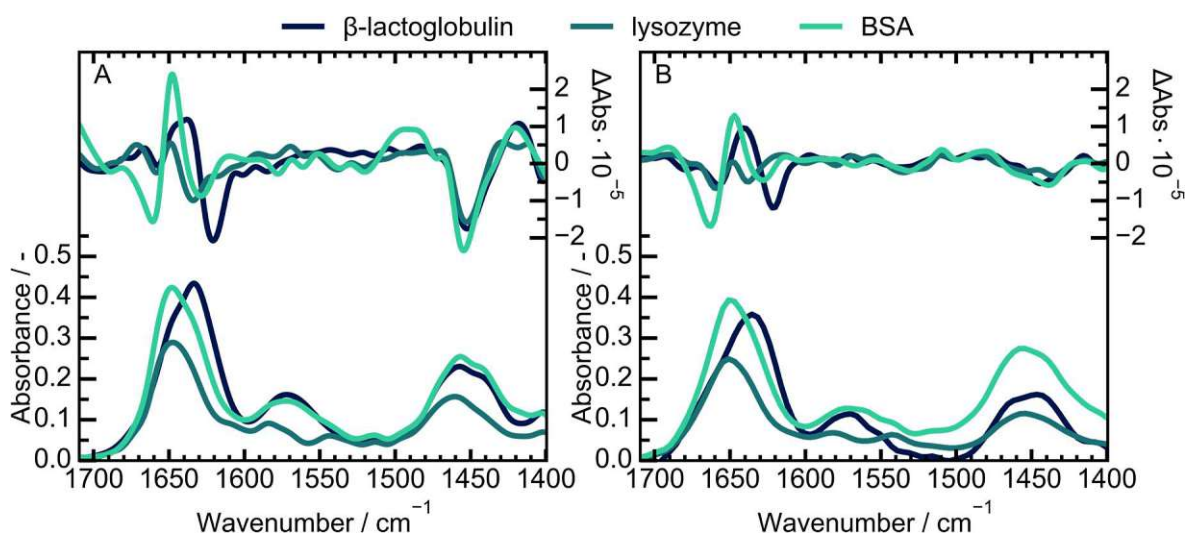


**Figure 34** | IR absorbance and VCD spectra of different proteins in  $D_2O$ , collected after 1 h of measurement time. The spectra were collected on a commercial FT-IR instrument (B, 60 mg/mL) and the self-built QCL-VCD instrument (A, 8 mg/mL).

**High time resolution:** For protein study, more often than not the amide I band carries sufficient structure information. This can be leveraged for QCL systems, as it allows to implement faster monitoring by reducing the spectral range. Consequently, the laser was set to sweep between  $1580$  and  $1710\text{ cm}^{-1}$ , and spectra were collected at a measurement time of 5 min.

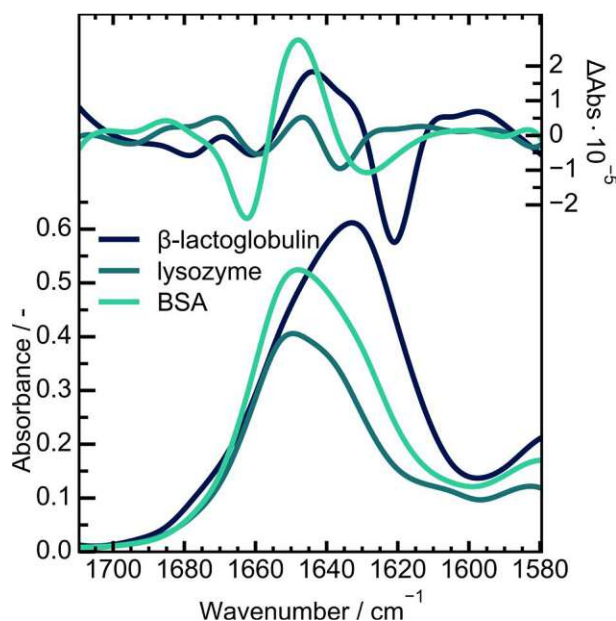


**Figure 35** | Amide I' absorbance and VCD band for different proteins. The data was collected with our QCL-VCD system at a concentration of 10 mg/mL and 5 min measurement time.

While a further decrease in noise could be achieved with increased averaging, the noise level ( $8.2 \cdot 10^{-7}$ ) achieved after 5 minutes of averaging were sufficient, considering an expected VCD signal height of  $>1 \cdot 10^{-5}$ . For reference, the corresponding measurement time to reach similar noise levels ( $8.3 \cdot 10^{-7}$ ) at an FT-IR instrument is 40 min. The three already described proteins were measured, at a concentration of 10 mg/mL. As can be seen in Figure 35 the resulting VCD spectra are of high quality and the characteristic bandshapes can be identified. This constitutes the first report of VCD spectra of proteins at such a short measurement time, while still yielding well resolved bands.

Based on these results, it can be concluded that high sampling rate monitoring of protein refolding process or thermal denaturation studies are within the realm of possibilities for QCL-VCD. With an improved system, incorporating even longer pathlengths QCL-VCD can encroach on concentration ranges normally reserved for ECD measurements. Since with the current system, the classical IR absorbance information is also available a combination of the two techniques at similar time resolution is possible and has the potential to improve our understanding of the molecular processes involved in protein folding.

### 3.3 Further opportunities for QCL-VCD technology

In the chapters so far, the combination of QCL-VCD with balanced detection was described. This configuration achieved quite substantial results and led to advances in both time resolution and sensitivity. The overall design was improved, and it was characterized against the state of the art. However, the basic principle of the measurement techniques and the optical elements did not change significantly compared to the classical FT-IR systems. In this part, which can be viewed as an outlook for further improvements, optical improvements are described which are more closely tailored to the properties of QCL technology.

#### 3.3.1 High frequency polarization modulation

The implementation of PEMs for polarization modulation devices for VCD instruments provided kHz modulation over the IR range for the first time, a significant improvement over e.g. spinning waveplates.<sup>66,186</sup> Consequently, the intensity modulation imposed by a PEM is denoted as  $I_{AC}(\tilde{\nu})$ . Compared to the chopper frequencies of dispersive instruments or the mirror movement of early FT-IR instruments it occurs at significantly higher modulation frequencies.

In contrast, for the data presented here the PEM frequency modulation is slow compared to the laser pulsing scheme. Modern EC-QCL support modulation frequencies in the MHz domain, and can sweep over the spectral range at several thousand wavenumbers per second.<sup>99,144</sup> Indeed, the comparatively slow scan speeds used in this thesis were chosen to allow for collecting several PEM cycles per wavenumber step.

An alternative approach to polarization modulation can be provided by relying on an electro-optical modulator (EOM) based on the Pockels effect. For the operation of a PEM an external voltage modulation dictates the strain imposed on the optical element by piezo actuators. In contrast during EOM operation this external voltage is directly applied to the optical element, which reacts by a modulation of its refractive index, applying a phase shift to transmitted light. By miniaturizing the devices, it is possible for EOMs to impose polarization modulation in the GHz domain.<sup>44,187,188</sup> However, in contrast to PEMs, the optical material useable for EOMs is limited to suitable crystals like  $\text{KH}_2\text{PO}_4$  (KDP), limiting its applicability for some wavelengths regions. In addition, the phase shift in EOMs is directly proportional to the applied voltage, necessitating high voltage modulation signals for use in the mid-IR region.<sup>44</sup>

Fortunately, ongoing developments have provided remedies for these challenges, and there now exist EOMs comprised of IR transparent materials (GaAs) operated in a resonance scheme. This resonance scheme leads to a significant decrease in necessary voltage, enabling modulation in the mid-IR range at amplitudes of a few volts. One of these is the AM-0.5G3\_IR4 (Qubig, Germany) which was used to test high frequency modulation for VCD measurements. Its characteristics are listed in Table 1.

Table 5 | Characteristics of the used EOM model.

	Value
Resonance frequency [kHz]	518
Quality factor Q	247
Extinction ratio	> 200:1
Crystal material	GaAs
Aperture [mm <sup>2</sup> ]	2.5
AR coating (R<1 %) [μm]	5.4-7.6

The device was AR coated to match the emission spectrum of the used laser. Figure 36 shows pictures of the device, which is a compact cube with 40 mm side length. This is a significant improvement over the comparable bulky PEM.

The external modulation voltage is applied by the SMA connector shown on the side of the left picture. The white marker indicates the optical axis of the EOM. What is obvious at first glance is that the EOM crystal does not completely fill the aperture, allowing for the passage of unmodulated light. This was prevented by fixing black construction hardboard to the entrance and exit aperture. Since the aperture was small when compared to the laser diameter of 2.5 mm, correct focusing of the laser as well as careful alignment was deemed essential.

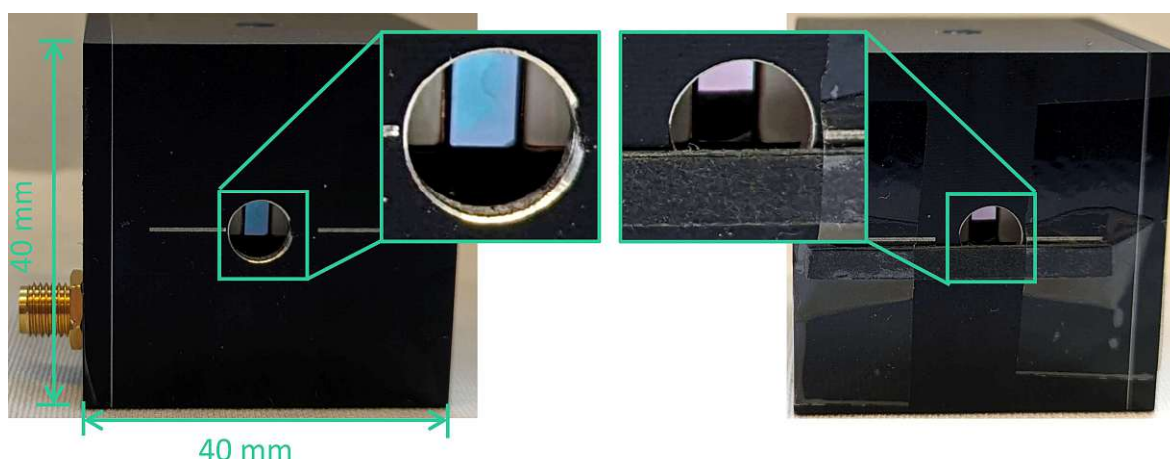


Figure 36 | Pictures of the used EOM. The insets are magnified views of the aperture, with the attachment of laser resistant cardboard on the right.

The alignment was solved by placing a rotational stage on the breadboard, providing rotational movement. On this rotational stage, a XYZ stage was placed for precise movement in the specified dimensions. On this stage a combination of a 90 ° and a 45 ° angled bracket was placed. A 5-axis stage was placed on the angled bracket, providing pitch and yaw movements for the EOM which was subsequently placed on the stage. The orientation at 45 ° relative to the vertical ensured that the axis of the EOM was set at 45 ° to the predominant polarization axis of the laser. This configuration was necessary to convert the incoming light's polarization to circular polarized light. The resulting arrangement can be seen in Figure 37.

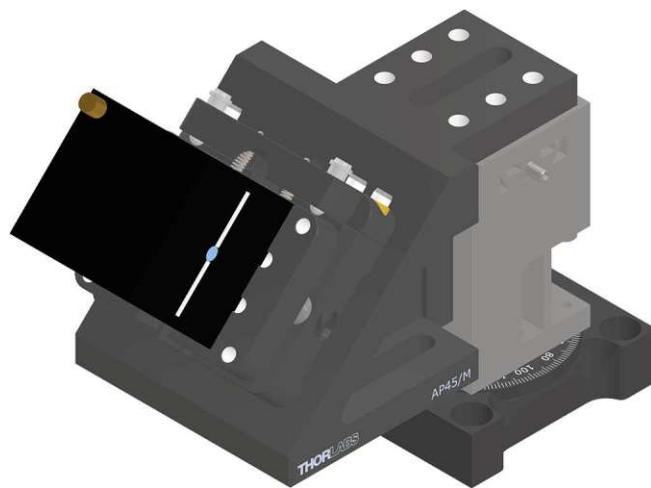


Figure 37 | Optical stage for the EOM measurements.

To adjust the laser diameter to better correspond the EOM aperture, the diameter was reduced by a factor of 3 by the Galilean telescope already used in publication I and II. The laser beam was oriented parallel to the holes of the breadboard and the EOM was placed in the beam path. Relying on the XYZ stage the EOM was adjusted for maximum throughput with no voltage applied. Following this step, an external sinusoidal modulation voltage at 517.5 kHz was applied by means of a waveform generator. This frequency was chosen, as a scanning of the frequency range around 518 kHz revealed this to perform best in regards to the applied phase shift.

The laser was set to pulsed mode with a modulation frequency of 1.035 MHz and a pulse length of 200 ns, combined with external triggering mode. This scheme was chosen since this frequency corresponds to the 2<sup>nd</sup> harmonic of the EOM frequency, and the pulses could be referenced to the modulation cycle similar to the configuration shown in Figure 33. However, in contrast to the previously shown system, the high frequency of the EOM allowed high duty cycle operation of the laser at 20 % already at the 2<sup>nd</sup> harmonic. This resulted in 100 % of the laser power passing the EOM at the highest modulation values while still maintaining efficient detection by a lock-in amplifier.

For alignment purposes the laser was set to one wavenumber in the middle of the spectral region of interest and a linear polarizer was placed behind the EOM in a crossed configuration. The position of the EOM was adjusted taking advantage of all degrees of freedom offered by the combination of multiple stages. This was done until the difference in intensity between the two pulses during one modulation cycle was as close to zero as possible.

When this was achieved the applied voltage was increased and the intensity at the detector monitored. When a further voltage increase did not lead to an increase in intensity and instead the intensity decreased, the halfwave voltage was found. At this voltage, the laser polarization was shifted by  $\pi$ , converting it to horizontally polarized light which could pass the polarizer unhindered. For this alignment a wavelength of 6.309  $\mu\text{m}$  was chosen. This wavelength was located in the middle of the spectral range and also showed no interference from water vapor. At this wavelength, the halfwave voltage was found to be 5.425 Vpp, and the corresponding quarter wave retardation (phases hift of  $\frac{\pi}{2}$ ) was reached at 2.7125 Vpp. This was verified by rotating the polarizer and observing the intensity. At perfect quarter wave retardation the intensity should be independent of the polarizer angle.

With these settings, the polarizer was removed and broadband spectra were collected. For these the detector intensity was demodulated at the EOM frequency and the 2<sup>nd</sup> harmonic and the laser was swept between 1700 and 1500  $\text{cm}^{-1}$ . The resulting baseline corrected VCD spectrum can be

seen in Figure 38, denoted as “referenced laser”.

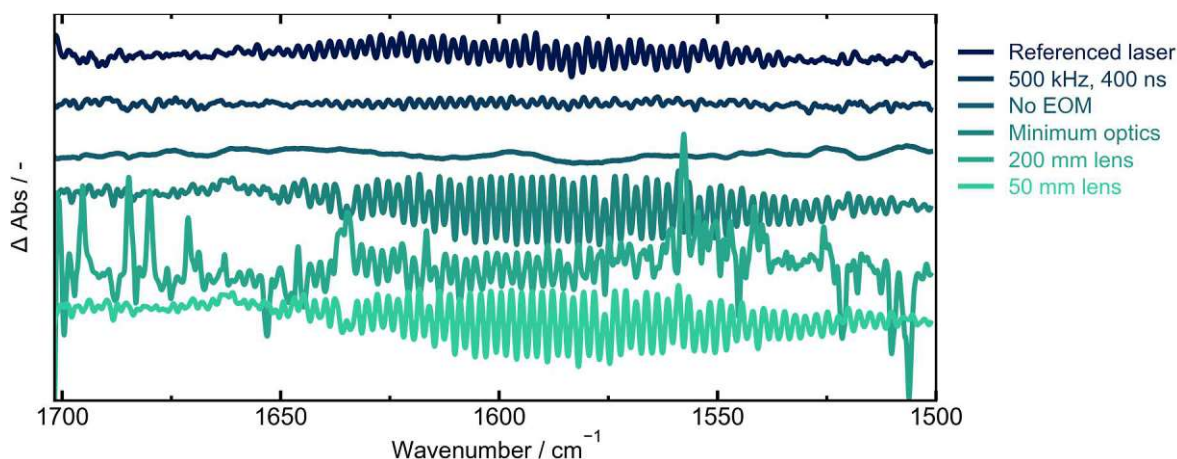


**Figure 38 |** Baseline corrected VCD spectra of different optical configuration, collected for the EOM setup. The spectra are offset and plotted in the sequence set by the legend.

The spectra is overlaid by strong interference fringes at a frequency of  $\sim 2.5 \text{ cm}^{-1}$ . One origin for this could be differences in phase for the two pulses due to the applied retardation, and therefore the laser was set to 500 kHz with 400 ns pulse length, with no referencing to the EOM. While this helped to decrease the interference effects, they were still present at the same frequency. A subsequent removal of the EOM resulted in the elimination of the interference fringes. It could be therefore assumed that the fringes originate from the parallel surfaces of the EOM. However, the frequency was lower than expected for the 40 mm EOM crystal, so the presence of reflection between the optical elements was also investigated. This was done by removing the Galilean telescope and operating the setup at the native laser beam diameter. Unfortunately, this did not lead to a removal of the interference fringes, and therefore it was assumed that the EOM itself was the origin of the effects.

Subsequently, different methods of reducing the beam diameter were explored. Convex ZnSe lens with different focal lengths were employed to change the spot size at the entrance aperture of the EOM. The tested lenses should provide smaller beam diameters than the Galilean telescope and reduce the parallelism of the laser beam. However, this also did not lead to a removal of the effects, as can be seen in Figure 38.

It was concluded that a removal of the coherence of the QCL was the most promising path to make use of the high polarization modulation of the EOM. There are some designs reported for this purpose. For example a lens could be moved small distances orthogonal to the laser beam, leading to a slight change in the beam focus.<sup>181</sup> Alternatively, a rotating diffuser could be introduced into the optical path.<sup>180</sup>

With the coherence reduced, the stability of the EOM would also be an avenue for improvement. Over the course of this thesis, a complete evaluation of the long-term stability of the EOM was not possible. However, according to advice from the manufacturer, this model has the option to be outfitted with a temperature control system, as is already available for other models. This should stabilize the resonance frequency even over longer time periods.

However, these changes were outside the scope of this thesis, and only offer possible starting point for work building upon this thesis. In conclusion, while the high frequency modulation of EOMs constitutes immense potential to improve QCL based VCD measurements, the complicated alignment and especially the occurrence of interference fringes render its implementation a non-

trivial matter.

## 4. Conclusions and outlook

This thesis was focused on establishing QCL-VCD systems as valid alternatives to classical FT-IR VCD spectrometers. This goal was based on the implementation of a balanced detection scheme to compensate for the intensity noise introduced by the pulsed light source. This combination in itself proved to be non-trivial, with the tradeoff between correct VCD baselines and adequate balancing providing constant challenges. The achieved findings were submitted for review by the broader scientific community and resulted in three manuscripts, two of which were already published and the third submitted for publication. (**publications I-III**)

The first stage of the thesis comprised the construction of a quantum cascade laser based vibrational circular dichroism setup. This constituted the first iteration of balanced detection QCL-VCD, the first VCD study performed in the research group and, at that time, one of four QCL-VCD systems existing worldwide.

The work combined the knowledge on laser spectroscopy already present in the group with new avenues of QCL-VCD design to compensate the challenges inherent to laser-based spectrometers. It was proven that the constructed balanced detection system offered stabilization advantages over the one introduced by the VCD normalization scheme alone. Noise decreases by a factor of 3 compared to single detector QCL-VCD could be reported and FT-IR VCD instruments noise levels were outperformed by a factor of 2, while keeping the acquisition time on the scale of a few minutes.

The noise reduction was utilized to evaluate the suitability of QCL-VCD in the context of PAT and process monitoring. It was shown that QCL-VCD can track chiral changes at a time resolution of 3 minutes, even for low concentrations of 40 mM chiral molecules in organic solvents. Subsequent statistical evaluation was implemented to enable an informed sensor design. This provided an avenue to develop laser-based sensors, able to provide chiral information at a time scale relevant for PAT applications. Building upon these results further increases in the time resolution can be envisioned, and the adjustable emission range of QCLs can provide a solid base for high-speed dedicated sensor design.

The flexibility of QCL-VCD was explored by deviating from small chiral molecules in organic solvents to the study of proteins in H<sub>2</sub>O and D<sub>2</sub>O. The high brilliance of QCLs could be leveraged to allow for longer pathlengths even for such high absorbing solvents. As a consequence, the measurements presented in this thesis constitute substantial improvements in terms of sensitivity and also time

resolution. Well resolved spectra of proteins were accessible for 10 mg/mL and 2 mg/mL in H<sub>2</sub>O and D<sub>2</sub>O respectively. Indeed, it was possible to perform secondary structure evaluation of proteins in D<sub>2</sub>O at a time resolution of 5 minutes for 10 mg/mL. With this high time resolutions, dynamic studies, e.g. protein denaturation or enzyme kinetics, can be considered realistic applications, which is not the case for FT-IR VCD.

Presentations of these results at international conferences achieved consistently positive feedback from the VOA community. Indeed, as a consequence of these events, two guest researchers could be hosted at the group. These cooperations extended the application of QCL-VCD to blood serum analytics and furthering our understanding of self-assembling macromolecules. The results obtained during these visits are in the process of evaluation and subsequent publication is planned. This thesis implemented QCL-VCD and VCD in general as valid analytical tool in the research group. The result of the work is a versatile setup, which can be quickly adapted for the measurement of different analytes. This will allow for the combination with additional QCLs available in the research group, covering even broader spectral ranges. By this combination, one of the main problems during this thesis, the limited spectral range for small molecule evaluation can be solved. Furthermore, currently non-accessible spectral ranges of interest for the analysis of biomolecules are to be investigated. It is reasonable to assume that the advantages of QCL-VCD, i.e. high sensitivity and short measurement times, will open new avenues for VCD analytics.

Besides the adaptation of the constructed system, another system based on the mentioned high frequency EOM could provide even higher acquisition speed than the data presented here. If the effect of interference effect can be reduced, this modulator constitutes a valid alternative to classical PEM polarization modulation schematics. Any additional studies can now be referenced directly by the in-house available FT-IR VCD system, providing an easy benchmark. It is expected that QCL-VCD will help advance both the analytical workflow as well as our understanding of processes ranging from protein folding to catalysis.

## Bibliography

- (1) Nafie, L. A. *Vibrational Optical Activity: Principles and Applications*, 1st ed.; Wiley, 2011. <https://doi.org/10.1002/9781119976516>.
- (2) Lüdeke, S.; Pfeifer, M.; Fischer, P. Quantum-Cascade Laser-Based Vibrational Circular Dichroism. *J. Am. Chem. Soc.* **2011**, *133* (15), 5704–5707. <https://doi.org/10.1021/ja200539d>.
- (3) Rütther, A.; Pfeifer, M.; Lórenz-Fonfría, V. A.; Lüdeke, S. Reaction Monitoring Using Mid-Infrared Laser-Based Vibrational Circular Dichroism: REACTION MONITORING USING LASER-BASED VCD. *Chirality* **2014**, *26* (9), 490–496. <https://doi.org/10.1002/chir.22307>.
- (4) Rütther, A.; Pfeifer, M.; Lórenz-Fonfría, V. A.; Lüdeke, S. pH Titration Monitored by Quantum Cascade Laser-Based Vibrational Circular Dichroism. *J. Phys. Chem. B* **2014**, *118* (14), 3941–3949. <https://doi.org/10.1021/jp4122886>.
- (5) *The IUPAC Compendium of Chemical Terminology: The Gold Book*, 4th ed.; Gold, V., Ed.; International Union of Pure and Applied Chemistry (IUPAC): Research Triangle Park, NC, 2019. <https://doi.org/10.1351/goldbook>.
- (6) Jähnigen, S. Vibrational Circular Dichroism Spectroscopy of Chiral Molecular Crystals: Insights from Theory. *Angew. Chem. Int. Ed.* **2023**, e202303595. <https://doi.org/10.1002/anie.202303595>.
- (7) Valentín-Pérez, Á.; Rosa, P.; Hillard, E. A.; Giorgi, M. Chirality Determination in Crystals. *Chirality* **2022**, *34* (2), 163–181. <https://doi.org/10.1002/chir.23377>.
- (8) Ranjbar, B.; Gill, P. Circular Dichroism Techniques: Biomolecular and Nanostructural Analyses-A Review. *Chem. Biol. Drug Des.* **2009**, *74* (2), 101–120. <https://doi.org/10.1111/j.1747-0285.2009.00847.x>.
- (9) Sen, A.; Bouchet, A.; Lepère, V.; Le Barbu-Debus, K.; Scuderi, D.; Piuze, F.; Zehnacker-Rentien, A. Conformational Analysis of Quinine and Its Pseudo Enantiomer Quinidine: A Combined Jet-Cooled Spectroscopy and Vibrational Circular Dichroism Study. *J. Phys. Chem. A* **2012**, *116* (32), 8334–8344. <https://doi.org/10.1021/jp3047888>.
- (10) Bogaerts, J.; Aerts, R.; Vermeyen, T.; Johannessen, C.; Herrebout, W.; Batista, J. Tackling Stereochemistry in Drug Molecules with Vibrational Optical Activity. *Pharmaceuticals* **2021**, *14* (9), 877. <https://doi.org/10.3390/ph14090877>.
- (11) Hancu, G.; Modroiu, A. Chiral Switch: Between Therapeutical Benefit and Marketing Strategy. *Pharmaceuticals* **2022**, *15* (2), 240. <https://doi.org/10.3390/ph15020240>.
- (12) Kuroski, D. Advances of Vibrational Circular Dichroism (VCD) in Bioanalytical Chemistry. A Review. *Anal. Chim. Acta* **2017**, *990*, 54–66. <https://doi.org/10.1016/j.aca.2017.08.014>.
- (13) Barron, L. D. The Development of Biomolecular Raman Optical Activity Spectroscopy. *Biomed. Spectrosc. Imaging* **2015**, *4* (3), 223–253. <https://doi.org/10.3233/BSI-150113>.
- (14) Hilario, J.; Kubelka, J.; Keiderling, T. Vibrational Circular Dichroism of Biopolymers: Summary of Methods and Applications. In *Vibrational Spectroscopy of Biological and Polymeric Materials*; Braiman, M., Gregoriou, V., Eds.; CRC Press, 2005; pp 253–324. <https://doi.org/10.1201/9781420027549.ch6>.
- (15) Keiderling, T. A. Protein and Peptide Secondary Structure and Conformational Determination with Vibrational Circular Dichroism. *Curr. Opin. Chem. Biol.* **2002**, *6* (5), 682–688. [https://doi.org/10.1016/S1367-5931\(02\)00369-1](https://doi.org/10.1016/S1367-5931(02)00369-1).
- (16) Urbanová, M.; Keiderling, T. A.; Pančoška, P. Conformational Study of Some Milk Proteins. Comparison of the Results of Electronic Circular Dichroism and Vibrational Circular Dichroism. *Bioelectrochem. Bioenerg.* **1996**, *41* (1), 77–80. [https://doi.org/10.1016/0302-4598\(96\)01932-0](https://doi.org/10.1016/0302-4598(96)01932-0).
- (17) Tokunaga, E.; Yamamoto, T.; Ito, E.; Shibata, N. Understanding the Thalidomide Chirality in Biological Processes by the Self-Disproportionation of Enantiomers. *Sci. Rep.* **2018**, *8* (1), 17131. <https://doi.org/10.1038/s41598-018-35457-6>.
- (18) D'Acquarica, I.; Agranat, I. The Quest for Secondary Pharmaceuticals: Drug Repurposing/Chiral-Switches Combination Strategy. *ACS Pharmacol. Transl. Sci.* **2023**, *6* (2), 201–219.

- <https://doi.org/10.1021/acsptsci.2c00151>.
- (19) Saito, F.; Schreiner, P. R. Determination of the Absolute Configurations of Chiral Alkanes – An Analysis of the Available Tools. *Eur. J. Org. Chem.* **2020**, 2020 (40), 6328–6339. <https://doi.org/10.1002/ejoc.202000711>.
  - (20) H. Brooks, W.; C. Guida, W.; G. Daniel, K. The Significance of Chirality in Drug Design and Development. *Curr. Top. Med. Chem.* **2011**, 11 (7), 760–770. <https://doi.org/10.2174/156802611795165098>.
  - (21) Wesolowski, S. S.; Pivonka, D. E. A Rapid Alternative to X-Ray Crystallography for Chiral Determination: Case Studies of Vibrational Circular Dichroism (VCD) to Advance Drug Discovery Projects. *Bioorg. Med. Chem. Lett.* **2013**, 23 (14), 4019–4025. <https://doi.org/10.1016/j.bmcl.2013.05.005>.
  - (22) Dale, J. A.; Mosher, H. S. Nuclear Magnetic Resonance Enantiomer Regents. Configurational Correlations via Nuclear Magnetic Resonance Chemical Shifts of Diastereomeric Mandelate, O-Methylmandelate, and .Alpha.-Methoxy-.Alpha.-Trifluoromethylphenylacetate (MTPA) Esters. *J. Am. Chem. Soc.* **1973**, 95 (2), 512–519. <https://doi.org/10.1021/ja00783a034>.
  - (23) Ward, T. J.; Ward, K. D. Chiral Separations: A Review of Current Topics and Trends. *Anal. Chem.* **2012**, 84 (2), 626–635. <https://doi.org/10.1021/ac202892w>.
  - (24) Alvarez-Rivera, G.; Bueno, M.; Ballesteros-Vivas, D.; Cifuentes, A. Chiral Analysis in Food Science. *TrAC Trends Anal. Chem.* **2020**, 123, 115761. <https://doi.org/10.1016/j.trac.2019.115761>.
  - (25) Ribeiro, A. R. L.; Maia, A. S.; Ribeiro, C.; Tiritan, M. E. Analysis of Chiral Drugs in Environmental Matrices: Current Knowledge and Trends in Environmental, Biodegradation and Forensic Fields. *TrAC Trends Anal. Chem.* **2020**, 124, 115783. <https://doi.org/10.1016/j.trac.2019.115783>.
  - (26) Orlandini, S.; Hancu, G.; Szabó, Z.-I.; Modroiu, A.; Papp, L.-A.; Gotti, R.; Furlanetto, S. New Trends in the Quality Control of Enantiomeric Drugs: Quality by Design-Compliant Development of Chiral Capillary Electrophoresis Methods. *Molecules* **2022**, 27 (20), 7058. <https://doi.org/10.3390/molecules27207058>.
  - (27) Bernardo-Bermejo, S.; Sánchez-López, E.; Castro-Puyana, M.; Marina, M. L. Chiral Capillary Electrophoresis. *TrAC Trends Anal. Chem.* **2020**, 124, 115807. <https://doi.org/10.1016/j.trac.2020.115807>.
  - (28) Roussel, C.; Rio, A. D.; Pierrot-Sanders, J.; Piras, P.; Vanthuyne, N. Chiral Liquid Chromatography Contribution to the Determination of the Absolute Configuration of Enantiomers. *J. Chromatogr. A* **2004**, 1037 (1–2), 311–328. <https://doi.org/10.1016/j.chroma.2004.01.065>.
  - (29) Nafie, L. A. ChemInform Abstract: Vibrational Circular Dichroism - A New Tool for the Solution-State Determination of the Structure and Absolute Configuration of Chiral Natural Product Molecules. *ChemInform* **2009**, 40 (14). <https://doi.org/10.1002/chin.200914279>.
  - (30) Slade, D.; Ferreira, D.; Marais, J. P. J. Circular Dichroism, a Powerful Tool for the Assessment of Absolute Configuration of Flavonoids. *Phytochemistry* **2005**, 66 (18), 2177–2215. <https://doi.org/10.1016/j.phytochem.2005.02.002>.
  - (31) Rogers, D. M.; Jasim, S. B.; Dyer, N. T.; Auvray, F.; Réfrégiers, M.; Hirst, J. D. Electronic Circular Dichroism Spectroscopy of Proteins. *Chem* **2019**, 5 (11), 2751–2774. <https://doi.org/10.1016/j.chempr.2019.07.008>.
  - (32) Shindo, Y.; Nakagawa, M. Circular Dichroism Measurements. I. Calibration of a Circular Dichroism Spectrometer. *Rev. Sci. Instrum.* **1985**, 56 (1), 32–39. <https://doi.org/10.1063/1.1138467>.
  - (33) Kapitán, J.; Barron, L. D.; Hecht, L. A Novel Raman Optical Activity Instrument Operating in the Deep Ultraviolet Spectral Region: Raman Optical Activity Instrument Operating in DUV Spectral Region. *J. Raman Spectrosc.* **2015**, 46 (4), 392–399. <https://doi.org/10.1002/jrs.4665>.
  - (34) Guo, C.; Shah, R. D.; Dukor, R. K.; Freedman, T. B.; Cao, X.; Nafie, L. A. Fourier Transform Vibrational Circular Dichroism from 800 to 10,000cm<sup>-1</sup>: Near-IR-VCD Spectral Standards for Terpenes and Related Molecules. *Vib. Spectrosc.* **2006**, 42 (2), 254–272. <https://doi.org/10.1016/j.vibspec.2006.05.013>.
  - (35) Bogaerts, J.; Desmet, F.; Aerts, R.; Bultinck, P.; Herrebout, W.; Johannessen, C. A Combined

- Raman Optical Activity and Vibrational Circular Dichroism Study on Artemisinin-Type Products. *Phys. Chem. Chem. Phys.* <https://doi.org/10.1039/d0cp03257c>.
- (36) Baumruckt, Vi.; Keiderling', T. A. Vibrational Circular Dichroism of Proteins in H<sub>2</sub>O Solution. 4.
- (37) Bünnemann, K.; Pollok, C. H.; Merten, C. Explicit Solvation of Carboxylic Acids for Vibrational Circular Dichroism Studies: Limiting the Computational Efforts without Losing Accuracy. *J. Phys. Chem. B* **2018**, 122 (33), 8056–8064. <https://doi.org/10.1021/acs.jpcc.8b05928>.
- (38) Keiderling, T. Instrumentation for Vibrational Circular Dichroism Spectroscopy: Method Comparison and Newer Developments. *Molecules* **2018**, 23 (9), 2404. <https://doi.org/10.3390/molecules23092404>.
- (39) Griffiths, P. R.; De Haseth, J. A. *Fourier Transform Infrared Spectrometry*, 1st ed.; Wiley, 2007. <https://doi.org/10.1002/047010631X>.
- (40) Stuart, B. H. *Infrared Spectroscopy: Fundamentals and Applications: Stuart/Infrared Spectroscopy: Fundamentals and Applications*; Analytical Techniques in the Sciences; John Wiley & Sons, Ltd: Chichester, UK, 2004. <https://doi.org/10.1002/0470011149>.
- (41) Larkin, P. *Infrared and Raman Spectroscopy: Principles and Spectral Interpretation*, Second edition.; Elsevier: Amsterdam, Netherlands ; Oxford, United Kingdom ; Cambridge, MA, United States, 2018.
- (42) *Infrared and Raman Spectroscopy: Methods and Applications*, 1st ed.; Schrader, B., Ed.; Wiley, 1995. <https://doi.org/10.1002/9783527615438>.
- (43) Berova, N. *Comprehensive Chiroptical Spectroscopy*; John Wiley & Sons: New York, 2012.
- (44) Reider, G. A. *Photonik: Eine Einführung in die Grundlagen*; Springer Vienna: Vienna, 2012. <https://doi.org/10.1007/978-3-7091-1521-3>.
- (45) Ma, S.; Freedman, T. B.; Dukor, R. K.; Nafie, L. A. Near-Infrared and Mid-Infrared Fourier Transform Vibrational Circular Dichroism of Proteins in Aqueous Solution. *Appl. Spectrosc.* **2010**, 64 (6), 615–626. <https://doi.org/10.1366/000370210791414434>.
- (46) Fusè, M.; Longhi, G.; Mazzeo, G.; Stranges, S.; Leonelli, F.; Aquila, G.; Bodo, E.; Brunetti, B.; Bicchi, C.; Cagliero, C.; Bloino, J.; Abbate, S. Anharmonic Aspects in Vibrational Circular Dichroism Spectra from 900 to 9000 Cm<sup>-1</sup> for Methyloxirane and Methylthiirane. *J. Phys. Chem. A* **2022**, 126 (38), 6719–6733. <https://doi.org/10.1021/acs.jpca.2c05332>.
- (47) Polavarapu, P. L.; Chen, G.-C. Polarization-Division Interferometry: Far-Infrared Dichroism. *Appl. Spectrosc.* **1994**, 48 (11), 1410–1418. <https://doi.org/10.1366/0003702944028119>.
- (48) Choi, W. J.; Cheng, G.; Huang, Z.; Zhang, S.; Norris, T. B.; Kotov, N. A. Terahertz Circular Dichroism Spectroscopy of Biomaterials Enabled by Kirigami Polarization Modulators. *Nat. Mater.* **2019**, 18 (8), 820–826. <https://doi.org/10.1038/s41563-019-0404-6>.
- (49) Zhang, Z.; Yang, G.; Fan, F.; Zhong, C.; Yuan, Y.; Zhang, X.; Chang, S. Terahertz Circular Dichroism Sensing of Living Cancer Cells Based on Microstructure Sensor. *Anal. Chim. Acta* **2021**, 1180, 338871. <https://doi.org/10.1016/j.aca.2021.338871>.
- (50) Morse, P. M. Diatomic Molecules According to the Wave Mechanics. II. Vibrational Levels. *Phys. Rev.* **1929**, 34 (1), 57–64. <https://doi.org/10.1103/PhysRev.34.57>.
- (51) Kuhn, W. Quantitative Verhältnisse Und Beziehungen Bei Der Natürlichen Optischen Aktivität. *Z. Für Phys. Chem.* **1929**, 4B (1), 14–36. <https://doi.org/10.1515/zpch-1929-0403>.
- (52) Holzwarth, G.; Chabay, I. Optical Activity of Vibrational Transitions: A Coupled Oscillator Model. *J. Chem. Phys.* **1972**, 57 (4), 1632–1635. <https://doi.org/10.1063/1.1678447>.
- (53) Kuhn, W. Optical Rotatory Power. *Annu. Rev. Phys. Chem.* **1958**, 9 (1), 417–438. <https://doi.org/10.1146/annurev.pc.09.100158.002221>.
- (54) Buffeteau, T.; Ducasse, L.; Brizard, A.; Huc, I.; Oda, R. Density Functional Theory Calculations of Vibrational Absorption and Circular Dichroism Spectra of Dimethyl- L -Tartrate. *J. Phys. Chem. A* **2004**, 108 (18), 4080–4086. <https://doi.org/10.1021/jp037698y>.
- (55) Tinoco, I. The Exciton Contribution to the Optical Rotation of Polymers. *Radiat. Res.* **1963**, 20 (1), 133. <https://doi.org/10.2307/3571340>.
- (56) Nafie, L. A.; Oboodi, M. R.; Freedman, T. B. Vibrational Circular Dichroism in Amino Acids and Peptides. 8. A Chirality Rule for Methine C\*.Alpha.-H Stretching Modes. *J. Am. Chem. Soc.* **1983**, 105 (25), 7449–7450. <https://doi.org/10.1021/ja00363a044>.

- (57) Abbate, S.; Laux, L.; Overend, J.; Moscovitz, A. A Charge Flow Model for Vibrational Rotational Strengths. *J. Chem. Phys.* **1981**, *75* (7), 3161–3164. <https://doi.org/10.1063/1.442488>.
- (58) Nafie, L. A.; Walnut, T. H. Vibrational Circular Dichroism Theory: A Localized Molecular Orbital Model. *Chem. Phys. Lett.* **1977**, *49* (3), 441–446. [https://doi.org/10.1016/0009-2614\(77\)87010-3](https://doi.org/10.1016/0009-2614(77)87010-3).
- (59) Nafie, L. A.; Freedman, T. B. Ring Current Mechanism of Vibrational Circular Dichroism. *J. Phys. Chem.* **1986**, *90* (5), 763–767. <https://doi.org/10.1021/j100277a013>.
- (60) Stephens, P. J. Theory of Vibrational Circular Dichroism. *J. Phys. Chem.* **1985**, *89* (5), 748–752. <https://doi.org/10.1021/j100251a006>.
- (61) Keiderling, T. A.; Lakhani, A. Mini Review: Instrumentation for Vibrational Circular Dichroism Spectroscopy, Still a Role for Dispersive Instruments. *Chirality* **2018**, *30* (3), 238–253. <https://doi.org/10.1002/chir.22799>.
- (62) Keiderling, T. A. Structure of Condensed Phase Peptides: Insights from Vibrational Circular Dichroism and Raman Optical Activity Techniques. *Chem. Rev.* **2020**, *120* (7), 3381–3419. <https://doi.org/10.1021/acs.chemrev.9b00636>.
- (63) Malon, P.; Keiderling, T. A. A Solution to the Artifact Problem in Fourier Transform Vibrational Circular Dichroism. *Appl. Spectrosc.* **1988**, *42* (1), 32–38. <https://doi.org/10.1366/0003702884428716>.
- (64) Nafie, L. A.; Keiderling, T. A.; Stephens, P. J. Vibrational Circular Dichroism. *J. Am. Chem. Soc.* **1976**, *98*, 9.
- (65) Lipp, E. D.; Zimba, C. G.; Nafie, L. A.; Vidrine, D. W. Polarization Demodulation: A New Approach to the Reduction of Polarization Artifacts from Vibrational Circular Dichroism Spectra. *Appl. Spectrosc.* **1982**, *36* (5), 496–498. <https://doi.org/10.1366/0003702824639484>.
- (66) Malon, P.; Keiderling, T. A. Spinning Quarter-Wave Plate Polarization Modulator: Test of Feasibility for Vibrational Circular Dichroism Measurements. *Appl. Spectrosc.* **1996**, *50* (5), 669–674. <https://doi.org/10.1366/0003702963905844>.
- (67) Cao, X.; Dukor, R. K.; Nafie, L. A. Reduction of Linear Birefringence in Vibrational Circular Dichroism Measurement: Use of a Rotating Half-Wave Plate. *Theor. Chem. Acc.* **2008**, *119* (1–3), 69–79. <https://doi.org/10.1007/s00214-007-0284-8>.
- (68) Xie, P.; Diem, M. Measurement of Dispersive Vibrational Circular Dichroism: Signal Optimization and Artifact Reduction. *Appl. Spectrosc.* **1996**, *50* (5), 675–680. <https://doi.org/10.1366/0003702963905925>.
- (69) Rodríguez-Ortega, P. G.; Sánchez-Valera, M.; López-González, J. J.; Montejo, M. Fourier Transform Infrared Spectroscopy and Vibrational Circular Dichroism Assisted Elucidation of the Solution-State Supramolecular Speciation in Racemic and Enantiopure Ketoprofen. *Appl. Spectrosc.* **2022**, *76* (2), 216–227. <https://doi.org/10.1177/00037028211060073>.
- (70) Kott, L.; Petrovic, J.; Phelps, D.; Roginski, R.; Schubert, J. Determination of a Low-Level Percent Enantiomer of a Compound with No Ultraviolet Chromophore Using Vibrational Circular Dichroism (VCD): Enantiomeric Purity by VCD of a Compound with Three Chiral Centers. *Appl. Spectrosc.* **2014**, *68* (10), 1108–1115. <https://doi.org/10.1366/13-07112>.
- (71) Vrtělka, O.; Králová, K.; Fousková, M.; Habartová, L.; Hříbek, P.; Urbánek, P.; Setnička, V. Vibrational and Chiroptical Analysis of Blood Plasma for Hepatocellular Carcinoma Diagnostics. *The Analyst* **2023**, *148* (12), 2793–2800. <https://doi.org/10.1039/D3AN00164D>.
- (72) Sgammato, R.; Van Bremp, N.; Aerts, R.; Van Doorslaer, S.; Dewilde, S.; Herrebout, W.; Johannessen, C. Interaction of Nitrite with Ferric Protoglobin from *Methanosarcina Acetivorans* – an Interesting Model for Spectroscopic Studies of the Haem–Ligand Interaction. *Dalton Trans.* **2023**, *52* (10), 2976–2987. <https://doi.org/10.1039/D2DT03252J>.
- (73) Pazderková, M.; Pazderka, T.; Shanmugasundaram, M.; Dukor, R. K.; Lednev, I. K.; Nafie, L. A. Origin of Enhanced VCD in Amyloid Fibril Spectra: Effect of Deuteration and pH. *Chirality* **2017**, *29* (9), 469–475. <https://doi.org/10.1002/chir.22722>.
- (74) Poopari, M. R.; Dezhahang, Z.; Xu, Y. Identifying Dominant Conformations of N-Acetyl-L-Cysteine Methyl Ester and N-Acetyl-L-Cysteine in Water: VCD Signatures of the Amide I and the CO Stretching Bands. *Spectrochim. Acta. A. Mol. Biomol. Spectrosc.* **2015**, *136*, 131–140.

- <https://doi.org/10.1016/j.saa.2013.08.118>.
- (75) Synytsya, A.; Judexová, M.; Hrubý, T.; Tatarkovič, M.; Miškovičová, M.; Petruželka, L.; Setnička, V. Analysis of Human Blood Plasma and Hen Egg White by Chiroptical Spectroscopic Methods (ECD, VCD, ROA). *Anal. Bioanal. Chem.* **2013**, *405* (16), 5441–5453. <https://doi.org/10.1007/s00216-013-6946-6>.
- (76) Niederhafner, P.; Šafařík, M.; Neburková, J.; Keiderling, T. A.; Bouř, P.; Šebestík, J. Monitoring Peptide Tyrosine Nitration by Spectroscopic Methods. *Amino Acids* **2021**, *53* (4), 517–532. <https://doi.org/10.1007/s00726-020-02911-7>.
- (77) Welch, W. R. W.; Kubelka, J.; Keiderling, T. A. Infrared, Vibrational Circular Dichroism, and Raman Spectral Simulations for  $\beta$ -Sheet Structures with Various Isotopic Labels, Interstrand, and Stacking Arrangements Using Density Functional Theory. *J. Phys. Chem. B* **2013**, *117* (36), 10343–10358. <https://doi.org/10.1021/jp4056126>.
- (78) Cheeseman, J. R.; Frisch, M. J.; Keiderling, T. A. Increased Accuracy of Vibrational Circular Dichroism Calculations for Isotopically Labeled Helical Peptides. *Spectrochim. Acta. A. Mol. Biomol. Spectrosc.* **2024**, *313*, 124097. <https://doi.org/10.1016/j.saa.2024.124097>.
- (79) PMA50 *Polarisations-Modulations-Modul*. <https://www.bruker.com/de/products-and-solutions/infrared-and-raman/ft-ir-research-spectrometers/pma50-polarization-modulation-module.html> (accessed 2024-05-19).
- (80) *ChiralIR-2X*. BioTools. <https://biotools.us/chiralir-2x/> (accessed 2024-05-19).
- (81) *Vibrational CD*. JASCO Inc. <https://jascoinc.com/products/spectroscopy/vibrational-circular-dichroism/> (accessed 2024-05-19).
- (82) Hlavatsch, M.; Mizaikoff, B. Advanced Mid-Infrared Lightsources above and beyond Lasers and Their Analytical Utility. *Anal. Sci.* **2022**, *38* (9), 1125–1139. <https://doi.org/10.1007/s44211-022-00133-3>.
- (83) Jung, D.; Bank, S.; Lee, M. L.; Wasserman, D. Next-Generation Mid-Infrared Sources. *J. Opt.* **2017**, *19* (12), 123001. <https://doi.org/10.1088/2040-8986/aa939b>.
- (84) Brandstetter, M.; Genner, A.; Anic, K.; Lendl, B. Tunable External Cavity Quantum Cascade Laser for the Simultaneous Determination of Glucose and Lactate in Aqueous Phase. *Analyst* **2010**, *135* (12), 3260–3265. <https://doi.org/10.1039/c0an00532k>.
- (85) Mizaikoff, B. Waveguide-Enhanced Mid-Infrared Chem/Bio Sensors. *Chem. Soc. Rev.* **2013**, *42* (22), 8683. <https://doi.org/10.1039/c3cs60173k>.
- (86) Maiman, T. H. Stimulated Optical Radiation in Ruby. *Nature* **1960**, *187* (4736), 493–494. <https://doi.org/10.1038/187493a0>.
- (87) Butler, J. F.; Calawa, A. R.; Phelan, R. J.; Harman, T. C.; Strauss, A. J.; Rediker, R. H. PbTe DIODE LASER. *Appl. Phys. Lett.* **1964**, *5* (4), 75–77. <https://doi.org/10.1063/1.1754062>.
- (88) Butler, J. F.; Calawa, A. R.; Phelan, R. J.; Strauss, A. J.; Rediker, R. H. PbSe Diode Laser. *Solid State Commun.* **1964**, *2* (10), 303–304. [https://doi.org/10.1016/0038-1098\(64\)90530-7](https://doi.org/10.1016/0038-1098(64)90530-7).
- (89) Vainio, M.; Halonen, L. Mid-Infrared Optical Parametric Oscillators and Frequency Combs for Molecular Spectroscopy. *Phys. Chem. Chem. Phys.* **2016**, *18* (6), 4266–4294. <https://doi.org/10.1039/C5CP07052J>.
- (90) Faist, J.; Capasso, F.; Sivco, D. L.; Sirtori, C.; Hutchinson, A. L.; Cho, A. Y. Quantum Cascade Laser. *Science* **1994**, *264* (5158), 553–556. <https://doi.org/10.1126/science.264.5158.553>.
- (91) Schwaighofer, A.; Brandstetter, M.; Lendl, B. Quantum Cascade Lasers (QCLs) in Biomedical Spectroscopy. *Chem. Soc. Rev.* **2017**, *46* (19), 5903–5924. <https://doi.org/10.1039/C7CS00403F>.
- (92) Vurgaftman, I.; Weih, R.; Kamp, M.; Meyer, J. R.; Canedy, C. L.; Kim, C. S.; Kim, M.; Bewley, W. W.; Merritt, C. D.; Abell, J.; Höfling, S. Interband Cascade Lasers. *J. Phys. Appl. Phys.* **2015**, *48* (12), 123001. <https://doi.org/10.1088/0022-3727/48/12/123001>.
- (93) Janassek, P.; Hartmann, S.; Molitor, A.; Michel, F.; Elsässer, W. Investigations of the Polarization Behavior of Quantum Cascade Lasers by Stokes Parameters. *Opt. Lett.* **2016**, *41* (2), 305. <https://doi.org/10.1364/OL.41.000305>.
- (94) Faist, J. Wallplug Efficiency of Quantum Cascade Lasers: Critical Parameters and Fundamental Limits. *Appl. Phys. Lett.* **2007**, *90* (25), 253512. <https://doi.org/10.1063/1.2747190>.

- (95) Bai, Y.; Bandyopadhyay, N.; Tsao, S.; Slivken, S.; Razeghi, M. Room Temperature Quantum Cascade Lasers with 27% Wall Plug Efficiency. *Appl. Phys. Lett.* **2011**, *98* (18), 181102. <https://doi.org/10.1063/1.3586773>.
- (96) Schwaighofer, A.; Alcaraz, M. R.; Lux, L.; Lendl, B. pH Titration of  $\beta$ -Lactoglobulin Monitored by Laser-Based Mid-IR Transmission Spectroscopy Coupled to Chemometric Analysis. *Spectrochim. Acta. A. Mol. Biomol. Spectrosc.* **2020**, *226*, 117636. <https://doi.org/10.1016/j.saa.2019.117636>.
- (97) Schwaighofer, A.; Montemurro, M.; Freitag, S.; Kristament, C.; Culzoni, M. J.; Lendl, B. Beyond Fourier Transform Infrared Spectroscopy: External Cavity Quantum Cascade Laser-Based Mid-Infrared Transmission Spectroscopy of Proteins in the Amide I and Amide II Region. *Anal. Chem.* **2018**, *90* (11), 7072–7079. <https://doi.org/10.1021/acs.analchem.8b01632>.
- (98) Alcaráz, M. R.; Schwaighofer, A.; Kristament, C.; Ramer, G.; Brandstetter, M.; Goicoechea, H.; Lendl, B. External-Cavity Quantum Cascade Laser Spectroscopy for Mid-IR Transmission Measurements of Proteins in Aqueous Solution. *Anal. Chem.* **2015**, *87* (13), 6980–6987. <https://doi.org/10.1021/acs.analchem.5b01738>.
- (99) Akhgar, C. K.; Ramer, G.; Žbik, M.; Trajnerowicz, A.; Pawluczyk, J.; Schwaighofer, A.; Lendl, B. The next Generation of IR Spectroscopy: EC-QCL Based Mid-IR Transmission Spectroscopy of Proteins with Balanced Detection. *Anal. Chem.* **2020**, *acs.analchem.0c01406*. <https://doi.org/10.1021/acs.analchem.0c01406>.
- (100) Akhgar, C. K.; Ebner, J.; Alcaraz, M. R.; Kopp, J.; Goicoechea, H.; Spadiut, O.; Schwaighofer, A.; Lendl, B. Application of Quantum Cascade Laser-Infrared Spectroscopy and Chemometrics for In-Line Discrimination of Coeluting Proteins from Preparative Size Exclusion Chromatography. *Anal. Chem.* **2022**, *94* (32), 11192–11200. <https://doi.org/10.1021/acs.analchem.2c01542>.
- (101) Akhgar, C. K.; Ebner, J.; Spadiut, O.; Schwaighofer, A.; Lendl, B. QCL–IR Spectroscopy for In-Line Monitoring of Proteins from Preparative Ion-Exchange Chromatography. *Anal. Chem.* **2022**, *94* (14), 5583–5590. <https://doi.org/10.1021/acs.analchem.1c05191>.
- (102) Waclawek, J. P.; Bauer, V. C.; Moser, H.; Lendl, B. 2f-Wavelength Modulation Fabry-Perot Photothermal Interferometry. *Opt. Express* **2016**, *24* (25), 28958–28967. <https://doi.org/10.1364/OE.24.028958>.
- (103) Lukasiewicz, G. V. B.; Astrath, N. G. C.; Malacarne, L. C.; Herculano, L. S.; Zanuto, V. S.; Baesso, M. L.; Bialkowski, S. E. Pulsed-Laser Time-Resolved Thermal Mirror Technique in Low-Absorbance Homogeneous Linear Elastic Materials. *Appl. Spectrosc.* **2013**, *67* (10), 1111–1116. <https://doi.org/10.1366/13-07068>.
- (104) Lukasiewicz, G. V. B.; Malacarne, L. C.; Astrath, N. G. C.; Zanuto, V. S.; Herculano, L. S.; Bialkowski, S. E. A Theoretical and Experimental Study of Time-Resolved Thermal Mirror with Non-Absorbing Heat-Coupling Fluids. *Appl. Spectrosc.* **2012**, *66* (12), 1461–1467. <https://doi.org/10.1366/12-06743>.
- (105) Ricchiuti, G.; Dabrowska, A.; Pinto, D.; Ramer, G.; Lendl, B. Dual-Beam Photothermal Spectroscopy Employing a Mach-Zehnder Interferometer and an External Cavity Quantum Cascade Laser for Detection of Water Traces in Organic Solvents. *Anal. Chem.* **2022**, *94* (47), 16353–16360. <https://doi.org/10.1021/acs.analchem.2c03303>.
- (106) Ricchiuti, G.; Dabrowska, A.; Pinto, D.; Ramer, G.; Lendl, B. Dual-Beam Photothermal Spectroscopy Employing a Mach-Zehnder Interferometer and an External Cavity Quantum Cascade Laser for Detection of Water Traces in Organic Solvents. *Anal. Chem.* **2022**, *94* (47), 16353–16360. <https://doi.org/10.1021/acs.analchem.2c03303>.
- (107) Pinto, D.; Waclawek, J. P.; Lindner, S.; Moser, H.; Ricchiuti, G.; Lendl, B. Wavelength Modulated Diode Probe Laser for an Interferometric Cavity-Assisted Photothermal Spectroscopy Gas Sensor. *Sens. Actuators B Chem.* **2023**, *377*. <https://doi.org/10.1016/j.snb.2022.133061>.
- (108) Pinto, D.; Moser, H.; Waclawek, J. P.; Dello Russo, S.; Patimisco, P.; Spagnolo, V.; Lendl, B. Parts-per-Billion Detection of Carbon Monoxide: A Comparison between Quartz-Enhanced Photoacoustic and Photothermal Spectroscopy. *Photoacoustics* **2021**, *22*.

- <https://doi.org/10.1016/j.pacs.2021.100244>.
- (109) Waclawek, J. P.; Lewicki, R.; Moser, H.; Brandstetter, M.; Tittel, F. K.; Lendl, B. Quartz-Enhanced Photoacoustic Spectroscopy-Based Sensor System for Sulfur Dioxide Detection Using a CW DFB-QCL. *Appl. Phys. B Lasers Opt.* **2014**, *117* (1), 113–120. <https://doi.org/10.1007/s00340-014-5809-y>.
  - (110) Waclawek, J. P.; Moser, H.; Lendl, B. Balanced-Detection Interferometric Cavity-Assisted Photothermal Spectroscopy Employing an All-Fiber-Coupled Probe Laser Configuration. *Opt. Express* **2021**, *29* (5), 7794–7808. <https://doi.org/10.1364/OE.416536>.
  - (111) Hayden, J.; Giglio, M.; Sampaolo, A.; Spagnolo, V.; Lendl, B. Mid-Infrared Intracavity Quartz-Enhanced Photoacoustic Spectroscopy with Pptv – Level Sensitivity Using a T-Shaped Custom Tuning Fork. *Photoacoustics* **2022**, *25*. <https://doi.org/10.1016/j.pacs.2022.100330>.
  - (112) V. D. dos Santos, A. C.; Hondl, N.; Ramos-Garcia, V.; Kuligowski, J.; Lendl, B.; Ramer, G. AFM-IR for Nanoscale Chemical Characterization in Life Sciences: Recent Developments and Future Directions. *ACS Meas. Sci. Au* **2023**. <https://doi.org/10.1021/acsmeasuresciau.3c00010>.
  - (113) V. D. dos Santos, A. C.; Lendl, B.; Ramer, G. Systematic Analysis and Nanoscale Chemical Imaging of Polymers Using Photothermal-Induced Resonance (AFM-IR) Infrared Spectroscopy. *Polym. Test.* **2022**, *106*, 107443. <https://doi.org/10.1016/j.polymertesting.2021.107443>.
  - (114) Yilmaz, U.; Sam, S.; Lendl, B.; Ramer, G. Bottom-Illuminated Photothermal Nanoscale Chemical Imaging with a Flat Silicon ATR in Air and Liquid. *Anal. Chem.* **2024**. <https://doi.org/10.1021/acs.analchem.3c04348>.
  - (115) Ramer, G.; Balbekova, A.; Schwaighofer, A.; Lendl, B. Method for Time-Resolved Monitoring of a Solid State Biological Film Using Photothermal Infrared Nanoscopy on the Example of Poly-L-Lysine. *Anal. Chem.* **2015**, *87* (8), 4415–4420. <https://doi.org/10.1021/acs.analchem.5b00241>.
  - (116) David, M.; Disnan, D.; Lardschneider, A.; Wacht, D.; Hoang, H. T.; Ramer, G.; Detz, H.; Lendl, B.; Schmid, U.; Strasser, G.; Hinkov, B. Structure and Mid-Infrared Optical Properties of Spin-Coated Polyethylene Films Developed for Integrated Photonics Applications. *Opt. Mater. Express* **2022**, *12* (6), 2168. <https://doi.org/10.1364/OME.458667>.
  - (117) Ramer, G.; Reisenbauer, F.; Steindl, B.; Tomischko, W.; Lendl, B. Implementation of Resonance Tracking for Assuring Reliability in Resonance Enhanced Photothermal Infrared Spectroscopy and Imaging. *Appl. Spectrosc.* **2017**, *71* (8), 2013–2020. <https://doi.org/10.1177/0003702817695290>.
  - (118) Dabrowska, A.; Lindner, S.; Schwaighofer, A.; Lendl, B. Mid-IR Dispersion Spectroscopy – A New Avenue for Liquid Phase Analysis. *Spectrochim. Acta. A. Mol. Biomol. Spectrosc.* **2023**, *286*, 122014. <https://doi.org/10.1016/j.saa.2022.122014>.
  - (119) Hayden, J.; Martín-Mateos, P.; Acedo, P.; Lendl, B. A Quantitative Comparison of Dispersion- and Absorption-Spectroscopic Gas Sensing. In *Proc SPIE Int Soc Opt Eng*; Soskind Y.G., Olson C., Eds.; SPIE, 2017; Vol. 10110. <https://doi.org/10.1117/12.2252624>.
  - (120) Hayden, J.; Hugger, S.; Fuchs, F.; Lendl, B. A Quantum Cascade Laser-Based Mach–Zehnder Interferometer for Chemical Sensing Employing Molecular Absorption and Dispersion. *Appl. Phys. B Lasers Opt.* **2018**, *124* (2). <https://doi.org/10.1007/s00340-018-6899-8>.
  - (121) Lindner, S.; Hayden, J.; Schwaighofer, A.; Wolflehner, T.; Kristament, C.; González-Cabrera, M.; Zlabinger, S.; Lendl, B. External Cavity Quantum Cascade Laser-Based Mid-Infrared Dispersion Spectroscopy for Qualitative and Quantitative Analysis of Liquid-Phase Samples. *Appl. Spectrosc.* **2020**, *74* (4), 452–459. <https://doi.org/10.1177/0003702819892646>.
  - (122) Martín-Mateos, P.; Hayden, J.; Lendl, B.; Acedo, P. High-Speed Line-Locked Heterodyne Phase Sensitive Dispersion Spectroscopy. In *Conf. Lasers Electro-Optics, CLEO - Proc.*; Institute of Electrical and Electronics Engineers Inc., 2018.
  - (123) Mayerhöfer, T. G.; Dabrowska, A.; Schwaighofer, A.; Lendl, B.; Popp, J. Beyond Beer's Law: Why the Index of Refraction Depends (Almost) Linearly on Concentration. *ChemPhysChem* **2020**, *21* (8), 707–711. <https://doi.org/10.1002/cphc.202000018>.
  - (124) Mayerhöfer, T. G.; Pahlow, S.; Ivanovski, V.; Popp, J. Dispersion Related Coupling Effects in IR Spectra on the Example of Water and Amide I Bands. *Spectrochim. Acta. A. Mol. Biomol.*

- Spectrosc.* **2023**, 288, 122115. <https://doi.org/10.1016/j.saa.2022.122115>.
- (125) Nafie, L. A. Vibrational Optical Activity: From Discovery and Development to Future Challenges. *Chirality* **2020**, 32 (5), 667–692. <https://doi.org/10.1002/chir.23191>.
- (126) Nafie, L. A. Dual Polarization Modulation: A Real-Time, Spectral-Multiplex Separation of Circular Dichroism from Linear Birefringence Spectral Intensities. *Appl. Spectrosc.* **2000**, 54 (11), 1634–1645. <https://doi.org/10.1366/0003702001948664>.
- (127) Hug, W.; Hangartner, G. A Novel High-Throughput Raman Spectrometer for Polarization Difference Measurements. *J. Raman Spectrosc.* **1999**, 30 (9), 841–852. [https://doi.org/10.1002/\(SICI\)1097-4555\(199909\)30:9<841::AID-JRS456>3.0.CO;2-1](https://doi.org/10.1002/(SICI)1097-4555(199909)30:9<841::AID-JRS456>3.0.CO;2-1).
- (128) Hug, W. Virtual Enantiomers as the Solution of Optical Activity's Deterministic Offset Problem. *Appl. Spectrosc.* **2003**, 57 (1), 1–13. <https://doi.org/10.1366/000370203321165142>.
- (129) Lipp, E. D.; Nafie, L. A. Fourier Transform Infrared Vibrational Circular Dichroism: Improvements in Methodology and Mid-Infrared Spectral Results. *Appl. Spectrosc.* **1984**, 38 (1), 20–26. <https://doi.org/10.1366/0003702844554459>.
- (130) Jordanov, B.; Schrader, B. An ATR Method for Measurement of IR Circular Dichroic Spectra. *J. Mol. Struct.* **1986**, 141, 297–300. [https://doi.org/10.1016/0022-2860\(86\)80338-6](https://doi.org/10.1016/0022-2860(86)80338-6).
- (131) Jordanov, B.; Korte, E. H.; Schrader, B. Differential FTIR Spectroscopy with Polarized Radiation. *J. Mol. Struct.* **1988**, 174, 147–152. [https://doi.org/10.1016/0022-2860\(88\)80149-2](https://doi.org/10.1016/0022-2860(88)80149-2).
- (132) Martin, D. H.; Puplett, E. Polarised Interferometric Spectrometry for the Millimetre and Submillimetre Spectrum. *Infrared Phys.* **1970**, 10 (2), 105–109. [https://doi.org/10.1016/0020-0891\(70\)90006-0](https://doi.org/10.1016/0020-0891(70)90006-0).
- (133) Nafie, L. A.; Buijs, H.; Rilling, A.; Cao, X.; Dukor, R. K. Dual Source Fourier Transform Polarization Modulation Spectroscopy: An Improved Method for the Measurement of Circular and Linear Dichroism. *Appl. Spectrosc.* **2004**, 58 (6), 647–654. <https://doi.org/10.1366/000370204872926>.
- (134) Sato, H.; Shimizu, M.; Watanabe, K.; Yoshida, J.; Kawamura, I.; Koshoubu, J. Multidimensional Vibrational Circular Dichroism Apparatus Equipped with Quantum Cascade Laser and Its Use for Investigating Some Peptide Systems Containing D -Amino Acids. *Anal. Chem.* **2021**, 93 (5), 2742–2748. <https://doi.org/10.1021/acs.analchem.0c02990>.
- (135) Phal, Y.; Yeh, K.; Bhargava, R. Concurrent Vibrational Circular Dichroism Measurements with Infrared Spectroscopic Imaging. *Anal. Chem.* **2021**, 93 (3), 1294–1303. <https://doi.org/10.1021/acs.analchem.0c00323>.
- (136) Oakberg, T. C. Modulated Interference Effects: Use of Photoelastic Modulators with Lasers. *Opt. Eng.* **1995**, 34 (6), 1545. <https://doi.org/10.1117/12.203086>.
- (137) Polnau, E. Origin of Modulated Interference Effects in Photoelastic Modulators. *Opt. Eng.* **1996**, 35 (11), 3331. <https://doi.org/10.1117/1.601073>.
- (138) Pfeifer, M.; Lüdeke, S.; Fischer, P. Mid-IR Laser-Based Vibrational Optical Activity; Mahadevan-Jansen, A., Petrich, W., Eds.; San Francisco, California, USA, 2012; p 821906. <https://doi.org/10.1117/12.906421>.
- (139) Sato, H.; Yamagishi, A.; Shimizu, M.; Watanabe, K.; Koshoubu, J.; Yoshida, J.; Kawamura, I. Mapping of Supramolecular Chirality in Insect Wings by Microscopic Vibrational Circular Dichroism Spectroscopy: Heterogeneity in Protein Distribution. *J. Phys. Chem. Lett.* **2021**, 12 (32), 7733–7737. <https://doi.org/10.1021/acs.jpclett.1c01949>.
- (140) Kemp, J. C. Symmetric Birefringence Modulator. US3867014A, February 18, 1975.
- (141) Hobbs, P. C. D. Shot Noise Limited Optical Measurements at Baseband with Noisy Lasers (Proceedings Only); Roy, R., Ed.; Boston, MA, 1991; pp 216–221. <https://doi.org/10.1117/12.25014>.
- (142) Waclawek, J. P.; Kristament, C.; Moser, H.; Lendl, B. Balanced-Detection Interferometric Cavity-Assisted Photothermal Spectroscopy. *Opt. Express* **2019**, 27 (9), 12183–12195. <https://doi.org/10.1364/OE.27.012183>.
- (143) Montemurro, M.; Schwaighofer, A.; Schmidt, A.; Culzoni, M. J.; Mayer, H. K.; Lendl, B. High-Throughput Quantitation of Bovine Milk Proteins and Discrimination of Commercial Milk Types by External Cavity-Quantum Cascade Laser Spectroscopy and Chemometrics. **2019**, 9.

- (144) Dabrowska, A.; David, M.; Freitag, S.; Andrews, A. M.; Strasser, G.; Hinkov, B.; Schwaighofer, A.; Lendl, B. Broadband Laser-Based Mid-Infrared Spectroscopy Employing a Quantum Cascade Detector for Milk Protein Analysis. *Sens. Actuators B Chem.* **2022**, *350*, 130873. <https://doi.org/10.1016/j.snb.2021.130873>.
- (145) Hermann, D. R.; Ramer, G.; Kitzler-Zeiler, M.; Lendl, B. Quantum Cascade Laser-Based Vibrational Circular Dichroism Augmented by a Balanced Detection Scheme. *Anal. Chem.* **2022**, *94* (29), 10384–10390. <https://doi.org/10.1021/acs.analchem.2c01269>.
- (146) Hermann, D.-R.; Ramer, G.; Riedlsperger, L.; Lendl, B. Chiral Monitoring Across Both Enantiomeric Excess and Concentration Space: Leveraging Quantum Cascade Lasers for Sensitive Vibrational Circular Dichroism Spectroscopy. *Appl. Spectrosc.* **2023**, *77* (12), 1362–1370. <https://doi.org/10.1177/00037028231206186>.
- (147) Michnowski, R.; Trajnerowicz, A. *BALANCED DETECTION MODULE WITH MANUAL GAIN REGULATION*.
- (148) Capasso, F.; Gmachl, C.; Paiella, R.; Tredicucci, A.; Hutchinson, A. L.; Sivco, D. L.; Baillargeon, J. N.; Cho, A. Y.; Liu, H. C. New Frontiers in Quantum Cascade Lasers and Applications. *IEEE J. Sel. Top. Quantum Electron.* **2000**, *6* (6), 931–947. <https://doi.org/10.1109/2944.902142>.
- (149) Urbanová, M.; Setnička, V.; Volka, K. Measurements of Concentration Dependence and Enantiomeric Purity of Terpene Solutions as a Test of a New Commercial VCD Spectrometer. *Chirality* **2000**, *12* (4), 199–203. [https://doi.org/10.1002/\(SICI\)1520-636X\(2000\)12:4<199::AID-CHIR6>3.0.CO;2-L](https://doi.org/10.1002/(SICI)1520-636X(2000)12:4<199::AID-CHIR6>3.0.CO;2-L).
- (150) < 1782 > Vibrational Circular Dichroism Spectroscopy—Theory and Practice. [https://doi.org/10.31003/USPNF\\_M9234\\_02\\_01](https://doi.org/10.31003/USPNF_M9234_02_01).
- (151) Guidance for Industry PAT - A Framework for Innovative Pharmaceutical Development, Manufacturing, and Quality Assurance.
- (152) Teng, Y.; Gu, C.; Chen, Z.; Jiang, H.; Xiong, Y.; Liu, D.; Xiao, D. Advances and Applications of Chiral Resolution in Pharmaceutical Field. *Chirality* **2022**, *34* (8), 1094–1119. <https://doi.org/10.1002/chir.23453>.
- (153) Rathore, A. S.; Bhambure, R.; Ghare, V. Process Analytical Technology (PAT) for Biopharmaceutical Products. *Anal. Bioanal. Chem.* **2010**, *398* (1), 137–154. <https://doi.org/10.1007/s00216-010-3781-x>.
- (154) Maruthamuthu, M. K.; Rudge, S. R.; Ardekani, A. M.; Ladisch, M. R.; Verma, M. S. Process Analytical Technologies and Data Analytics for the Manufacture of Monoclonal Antibodies. *Trends Biotechnol.* **2020**, *38* (10), 1169–1186. <https://doi.org/10.1016/j.tibtech.2020.07.004>.
- (155) Joshi, V.; Shivach, T.; Yadav, N.; Rathore, A. S. Circular Dichroism Spectroscopy as a Tool for Monitoring Aggregation in Monoclonal Antibody Therapeutics. *Anal. Chem.* **2014**, *86* (23), 11606–11613. <https://doi.org/10.1021/ac503140j>.
- (156) Beć, K. B.; Grabska, J.; Huck, C. W. Biomolecular and Bioanalytical Applications of Infrared Spectroscopy – A Review. *Anal. Chim. Acta* **2020**, *1133*, 150–177. <https://doi.org/10.1016/j.aca.2020.04.015>.
- (157) < 782 > Vibrational Circular Dichroism Spectroscopy. [https://doi.org/10.31003/USPNF\\_M9233\\_02\\_01](https://doi.org/10.31003/USPNF_M9233_02_01).
- (158) Bose, P. K.; Polavarapu, P. L. Acetate Groups as Probes of the Stereochemistry of Carbohydrates: A Vibrational Circular Dichroism Study. *Carbohydr. Res.* **1999**, *322* (1–2), 135–141. [https://doi.org/10.1016/S0008-6215\(99\)00211-6](https://doi.org/10.1016/S0008-6215(99)00211-6).
- (159) Socrates, G.; Socrates, G. *Infrared and Raman Characteristic Group Frequencies: Tables and Charts*, 3rd ed.; Wiley: Chichester ; New York, 2001.
- (160) Tsangaris, J. M.; Baxevanidis, G. Th. Complexes of Quinine with Cu(II), Ni(II), Co(II) and Cr(III) Chlorides. *Z. Für Naturforschung B* **1974**, *29* (7–8), 532–537. <https://doi.org/10.1515/znB-1974-7-815>.
- (161) Tam, C. N.; Bour, P.; Keiderling, T. A. An Experimental Comparison of Vibrational Circular Dichroism and Raman Optical Activity with 1-Amino-2-Propanol and 2-Amino-1-Propanol as Model Compounds. *J. Am. Chem. Soc.* **1997**, *119* (30), 7061–7064. <https://doi.org/10.1021/ja963239h>.

- (162) Nicu, V. P.; Debie, E.; Herrebout, W.; Van der Veken, B.; Bultinck, P.; Baerends, E. J. A VCD Robust Mode Analysis of Induced Chirality: The Case of Pulegone in Chloroform. *Chirality* **2009**, *21* (1E), E287–E297. <https://doi.org/10.1002/chir.20817>.
- (163) Joseph-Nathan, P.; Gordillo-Román, B. Vibrational Circular Dichroism Absolute Configuration Determination of Natural Products. In *Progress in the Chemistry of Organic Natural Products 100*; Kinghorn, A. D., Falk, H., Kobayashi, J., Eds.; Progress in the Chemistry of Organic Natural Products; Springer International Publishing: Cham, 2015; Vol. 100, pp 311–452. [https://doi.org/10.1007/978-3-319-05275-5\\_4](https://doi.org/10.1007/978-3-319-05275-5_4).
- (164) Setnička, V.; Urbanová, M.; Bouř, P.; Král, V.; Volka, K. Vibrational Circular Dichroism of 1,1'-Binaphthyl Derivatives: Experimental and Theoretical Study. *J. Phys. Chem. A* **2001**, *105* (39), 8931–8938. <https://doi.org/10.1021/jp011485w>.
- (165) Wang, Q.; Pietropaolo, A.; Fortino, M.; Song, Z.; Bando, M.; Naga, N.; Nakano, T. Photo Racemization of 2,2'-dihydroxy-1,1'-binaphthyl Derivatives. *Chirality* **2022**, *34* (2), 317–324. <https://doi.org/10.1002/chir.23400>.
- (166) Guo, C.; Shah, R. D.; Dukor, R. K.; Cao, X.; Freedman, T. B.; Nafie, L. A. Determination of Enantiomeric Excess in Samples of Chiral Molecules Using Fourier Transform Vibrational Circular Dichroism Spectroscopy: Simulation of Real-Time Reaction Monitoring. *Anal. Chem.* **2004**, *76* (23), 6956–6966. <https://doi.org/10.1021/ac049366a>.
- (167) Wold, S.; Sjöström, M.; Eriksson, L. PLS-Regression: A Basic Tool of Chemometrics. *Chemom. Intell. Lab. Syst.* **2001**, *58* (2), 109–130. [https://doi.org/10.1016/S0169-7439\(01\)00155-1](https://doi.org/10.1016/S0169-7439(01)00155-1).
- (168) Tibshirani, R. Regression Shrinkage and Selection Via the Lasso. *J. R. Stat. Soc. Ser. B Methodol.* **1996**, *58* (1), 267–288. <https://doi.org/10.1111/j.2517-6161.1996.tb02080.x>.
- (169) Keiderling, T. A.; Lakhani, A. Conformational Studies of Biopolymers, Peptides, Proteins, and Nucleic Acids. A Role for Vibrational Circular Dichroism. In *Comprehensive Chiroptical Spectroscopy*; Berova, N., Polavarapu, P. L., Nakanishi, K., Woody, R. W., Eds.; Wiley, 2012; pp 707–758. <https://doi.org/10.1002/9781118120392.ch22>.
- (170) Goncharova, I.; Novotná, J.; Urbanová, M. Stacked and Continuous Helical Self-Assemblies of Guanosine Monophosphates Detected by Vibrational Circular Dichroism. *Anal. Bioanal. Chem.* **2012**, *403* (9), 2635–2644. <https://doi.org/10.1007/s00216-012-6014-7>.
- (171) Mallamace, F.; Corsaro, C.; Mallamace, D.; Vasi, S.; Vasi, C.; Dugo, G. The Role of Water in Protein's Behavior: The Two Dynamical Crossovers Studied by NMR and FTIR Techniques. *Comput. Struct. Biotechnol. J.* **2015**, *13*, 33–37. <https://doi.org/10.1016/j.csbj.2014.11.007>.
- (172) Barth, A. Infrared Spectroscopy of Proteins. *Biochim. Biophys. Acta BBA - Bioenerg.* **2007**, *1767* (9), 1073–1101. <https://doi.org/10.1016/j.bbabbio.2007.06.004>.
- (173) Dabrowska, A.; Schwaighofer, A.; Lindner, S.; Lendl, B. Mid-IR Refractive Index Sensor for Detecting Proteins Employing an External Cavity Quantum Cascade Laser-Based Mach-Zehnder Interferometer. *Opt. Express* **2020**, *28* (24), 36632. <https://doi.org/10.1364/OE.403981>.
- (174) Asher, S. A.; Ianoul, A.; Mix, G.; Boyden, M. N.; Karnoup, A.; Diem, M.; Schweitzer-Stenner, R. Dihedral  $\psi$  Angle Dependence of the Amide III Vibration: A Uniquely Sensitive UV Resonance Raman Secondary Structural Probe. *J. Am. Chem. Soc.* **2001**, *123* (47), 11775–11781. <https://doi.org/10.1021/ja0039738>.
- (175) Ryu, S. R.; Czarnik-Matusiewicz, B.; Dukor, R. K.; Nafie, L. A.; Jung, Y. M. Analysis of the Molten Globule State of Bovine  $\alpha$ -Lactalbumin by Using Vibrational Circular Dichroism. *Vib. Spectrosc.* **2012**, *60*, 68–72. <https://doi.org/10.1016/j.vibspec.2012.02.006>.
- (176) Krupová, M.; Kessler, J.; Bouř, P. Recent Trends in Chiroptical Spectroscopy: Theory and Applications of Vibrational Circular Dichroism and Raman Optical Activity. *ChemPlusChem* **2020**, *85* (3), 561–575. <https://doi.org/10.1002/cplu.202000014>.
- (177) Litwińczuk, A.; Ryu, S. R.; Nafie, L. A.; Lee, J. W.; Kim, H. I.; Jung, Y. M.; Czarnik-Matusiewicz, B. The Transition from the Native to the Acid-State Characterized by Multi-Spectroscopy Approach: Study for the Holo-Form of Bovine  $\alpha$ -Lactalbumin. *Biochim. Biophys. Acta BBA - Proteins Proteomics* **2014**, *1844* (3), 593–606. <https://doi.org/10.1016/j.bbapap.2013.12.018>.
- (178) Berry, H. G.; Gabrielse, G.; Livingston, A. E. Measurement of the Stokes Parameters of Light. *Appl. Opt.* **1977**, *16* (12), 3200. <https://doi.org/10.1364/AO.16.003200>.

- (179) Yamada, I.; Nishii, J.; Saito, M. Incident Angle and Temperature Dependence of WSi Wire-Grid Polarizer. *Infrared Phys. Technol.* **2014**, *63*, 92–96. <https://doi.org/10.1016/j.infrared.2013.12.009>.
- (180) Stangner, T.; Zhang, H.; Dahlberg, T.; Wiklund, K.; Andersson, M. Step-by-Step Guide to Reduce Spatial Coherence of Laser Light Using a Rotating Ground Glass Diffuser. *Appl. Opt.* **2017**, *56* (19), 5427. <https://doi.org/10.1364/AO.56.005427>.
- (181) Liger, V. V. Optical Fringes Reduction in Ultrasensitive Diode Laser Absorption Spectroscopy. *Spectrochim. Acta. A. Mol. Biomol. Spectrosc.* **1999**, *55* (10), 2021–2026. [https://doi.org/10.1016/S1386-1425\(99\)00074-8](https://doi.org/10.1016/S1386-1425(99)00074-8).
- (182) Pancoska, P.; Wang, L.; Keiderling, T. A. Frequency Analysis of Infrared Absorption and Vibrational Circular Dichroism of Proteins in D<sub>2</sub>O Solution: Frequency Analysis of Protein VCD and IR Spectra. *Protein Sci.* **1993**, *2* (3), 411–419. <https://doi.org/10.1002/pro.5560020313>.
- (183) Giugliarelli, A.; Sassi, P.; Paolantoni, M.; Morresi, A.; Dukor, R.; Nafie, L. Vibrational Circular Dichroism Spectra of Lysozyme Solutions: Solvent Effects on Thermal Denaturation Processes. *J. Phys. Chem. B* **2013**, *117* (9), 2645–2652. <https://doi.org/10.1021/jp311268x>.
- (184) Schwaighofer, A.; Alcaráz, M. R.; Araman, C.; Goicoechea, H.; Lendl, B. External Cavity-Quantum Cascade Laser Infrared Spectroscopy for Secondary Structure Analysis of Proteins at Low Concentrations. *Sci. Rep.* **2016**, *6* (1), 33556. <https://doi.org/10.1038/srep33556>.
- (185) Paterlini, M. G.; Freedman, T. B.; Nafie, L. A. Vibrational Circular Dichroism Spectra of Three Conformationally Distinct States and an Unordered State of Poly(L-Lysine) in Deuterated Aqueous Solution. *Biopolymers* **1986**, *25* (9), 1751–1765. <https://doi.org/10.1002/bip.360250915>.
- (186) Cheng, J. C.; Nafie, L. A.; Allen, S. D.; Braunstein, A. I. Photoelastic Modulator for the 055–13-Mm Range. *Appl. Opt.* **1976**, *15* (8), 1960. <https://doi.org/10.1364/AO.15.001960>.
- (187) Dartigalongue, T.; Hache, F. Precise Alignment of a Longitudinal Pockels Cell for Time-Resolved Circular Dichroism Experiments. *J. Opt. Soc. Am. B* **2003**, *20* (8), 1780. <https://doi.org/10.1364/JOSAB.20.001780>.
- (188) Li, M.; Ling, J.; He, Y.; Javid, U. A.; Xue, S.; Lin, Q. Lithium Niobate Photonic-Crystal Electro-Optic Modulator. *Nat. Commun.* **2020**, *11* (1), 4123. <https://doi.org/10.1038/s41467-020-17950-7>.

## Appendix

### Appendix A: Published scientific papers

In this part, the scientific papers resulting from this cumulative thesis are presented. The contributions from the author are rated, 1-3 with a high number corresponding to a high contribution, for each publication in the corresponding category.

	Publication		
	I	II	III
<b>Data acquisition</b>	3	2	3
<b>Data analysis</b>	3	2	3
<b>Interpretation</b>	2	3	3
<b>Manuscript writing</b>	3	3	3

#### Publication I

##### **Quantum Cascade Laser-Based Vibrational Circular Dichroism Augmented by a Balanced Detection Scheme**

Hermann, D. R.; Ramer, G.; Kitzler-Zeiler, M.; Lendl, B.

*Analytical Chemistry* **2022**, 94 (29), 10384–10390.

# Quantum Cascade Laser-Based Vibrational Circular Dichroism Augmented by a Balanced Detection Scheme

Daniel R. Hermann, Georg Ramer, Markus Kitzler-Zeiler, and Bernhard Lendl\*



Cite This: *Anal. Chem.* 2022, 94, 10384–10390



Read Online

ACCESS |



Metrics & More

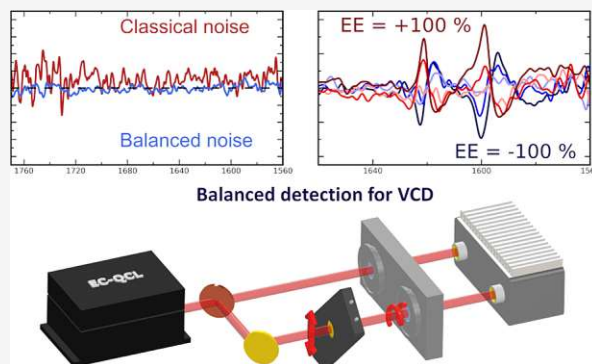


Article Recommendations



Supporting Information

**ABSTRACT:** Vibrational circular dichroism (VCD) constitutes a powerful technique, enabling the determination of the absolute configuration of molecules without the need for specialized reagents. While delivering critical information, VCD signals commonly are several orders of magnitude weaker than classical absorbance signals, which so far necessitated long measurement times to achieve acceptable signal-to-noise ratios (SNRs) in VCD experiments. We present here an improved setup for the measurement of VCD in the range between 5.6 and 6.5  $\mu\text{m}$ . Employing an external cavity quantum cascade laser (EC-QCL) as a high-power light source, we collected spectra with competitive noise levels in less than 5 min. The basis for this improvement was a balanced detection module combined with an optical path catered to VCD measurements. With the stabilization provided by the two-detector setup, noise originating from the laser source could be suppressed effectively. Noise level improvement up to a factor of 4 compared to the classical single detector EC-QCL-VCD could be reported. Compared to commercial Fourier transform infrared (FT-IR) instruments, the presented setup offers measurement time reductions of a factor of at least 6, with comparable noise levels. The applicability of the setup for qualitative and quantitative VCDs was proven. With the comparatively high temporal resolution provided, the monitoring of optically active processes will be possible in future applications.



Vibrational circular dichroism (VCD) is defined as the difference in absorbance for left and right circularly polarized lights in the infrared region (IR).<sup>1</sup> VCD is sensitive to the absolute configuration of chiral molecules, as well as to the structure of larger biomolecules like proteins and nucleic acids.<sup>1–3</sup> It is the logical extension of electronic circular dichroism (ECD or CD), which is the application of chiroptical spectroscopy in the ultraviolet and visible light ranges.<sup>4,5</sup> While ECD has been routinely used for structural studies of proteins, it is limited to samples containing suitable chromophores.<sup>1,5,6</sup> In contrast, IR, the spectral region in which VCD operates, is rich in band characteristics for different classes of organic molecules.<sup>7</sup> Due to the significant increase of accessible molecules, VCD presents a more attractive tool for the study of chiral samples than ECD.<sup>8,9</sup> Indeed, VCD has been used to straightforwardly determine the absolute configuration of small molecules and even monitor enantiomeric excess during reaction monitoring.<sup>3,9,10</sup>

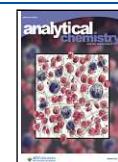
While VCD offers obvious advantages due to its unique sensitivity to structural differences and a broad range of accessible samples, the collection of VCD spectra comes with significant challenges.<sup>11–13</sup> VCD signals are 4–6 orders of magnitude weaker than classical absorbance, which necessitates low noise levels.<sup>11,14</sup> Additionally, artifacts originating from birefringence can distort or overlap the already weak signals.<sup>11,15</sup> The beginning of the VCD instrumentation lies

in dispersive spectrometers, which used longer integration times by decreasing the scanning rate to obtain satisfactory signal-to-noise ratios. As with classical IR spectroscopy, Fourier transform infrared (FT-IR) spectrometers have replaced dispersive instruments for the measurement of VCD spectra.<sup>11</sup> FT-IR instruments (and also dispersive instruments) can increase the signal-to-noise ratio by averaging increasing numbers of repeated spectral scans. This decreases the noise by  $\sqrt{n}$  ( $n$  is the number of averaged scans) and is well suited for modern FT-IR instruments capable of high scanning speeds.<sup>14</sup> Since the noise levels necessary for obtaining usable VCD spectra are significantly lower than for classical absorbance measurements, the number of averaged scans and with it the measurement time increases substantially.<sup>14</sup> Typical acquisition times for VCD range from  $\sim 30$  min to several hours, depending on the sample and solvent system.<sup>16</sup> Especially challenging are samples in aqueous solutions since

**Received:** March 22, 2022

**Accepted:** July 4, 2022

**Published:** July 14, 2022



the high absorbance of water in the IR region significantly reduces the spectral throughput.<sup>17,18</sup>

Nearly all modern VCD instruments are based on FT-IR technology and employ thermal light sources like globars that for a long time were among the only broadly available light sources in the mid-IR region. One alternative is tunable mid-IR lasers. Here, quantum cascade lasers (QCLs), first introduced in 1994, are especially attractive for their high brilliance and intrinsically linearly polarized emission.<sup>19</sup> Modern external cavity (EC)-QCLs offer tuning ranges of several hundreds of wavenumbers, large enough to observe multiple vibrational modes, and are available commercially for the whole mid-IR spectral range. Their high spectral output can be leveraged in highly absorbing samples, increasing the usable path length and the limit of detection.<sup>20–22</sup>

In 2008, Lüdeke et al. presented the first VCD spectra collected with an EC-QCL as a light source.<sup>23</sup> The acquired spectra corresponded well with the classical FT-IR VCD spectra and proved the suitability of EC-QCLs for VCD experiments.<sup>23</sup> However, despite the obvious useful properties of EC-QCLs, they also suffer from some disadvantages. Tunable QCLs feature a structured emission spectrum, with a maximum near the middle of the emitted spectral range and comparatively very weak spectral power at the spectral edges. Furthermore, intensity drifts, low-frequency noise, and, if the laser is operated in a pulsed mode, pulse-to-pulse fluctuations add additional noise to the system. Those noise sources are not present in classical thermal light sources.<sup>22,24</sup>

One approach for low noise laser spectroscopy is “balanced detection”: the laser beam is split into two beams of intensities as similar to each other as possible, which are directed onto two matched detectors. Only one light path contains the sample, while both channels carry the noise present in the laser. The signals collected from the detectors are then subtracted. This ensures that fluctuations present in the light source are canceled, as they are present in both channels. The signal of interest, on the other hand, is only present in one channel.<sup>22,24</sup> This method was already successfully applied in mid-infrared EC-QCL absorbance measurements of proteins in solution, where a noise reduction by a factor of 20 compared to single detection schemes was demonstrated.<sup>22</sup>

In the current study, we extended the benefits of EC-QCL mid-IR spectroscopy with balanced detection to VCD measurements. A dedicated balanced detection scheme was implemented using two closely matched HgCdTe (MCT) detectors and a two-path transmission cell. Employing a photoelastic modulator (PEM), we introduced rotational sensitivity in one path of the balanced detection system, enabling the acquisition of EC-QCL-VCD spectra. The noise reduction provided by the application of a balanced detection scheme was evaluated, both in comparison with single detector schemes and with classical FT-IR VCD noise levels. Furthermore, the practical application of the balanced detection EC-QCL-VCD was investigated for qualitative studies as well as for enantiomeric excess studies with the enantiomeric pair R- and S-1,1'-bi-2-naphthol (BINOL).

## EXPERIMENTAL SECTION

**Reagents.** CHCl<sub>3</sub> (99.2%, stabilized with 0.6% ethanol), (R)-(+)-1,1'-bi-2-naphthol (R-BINOL, 99%), and (S)-(–)-1,1'-bi-2-naphthol (S-BINOL, 99%) were purchased from Sigma-Aldrich (St. Louis) and used without further purification. For sample solutions, the appropriate amount of

pure sample was dissolved in CHCl<sub>3</sub>. Enantiomeric excess (EE) and samples with EE values of +100%, +60%, +20%, –20%, –60%, and –100% were prepared by mixing 100 mM R- and S-BINOL stock solutions. EE levels are calculated as

$$EE = \frac{n_A - n_B}{n_A + n_B} * 100\% \quad (1)$$

with  $n_A$  and  $n_B$  referring to the molar concentration of components A and B, respectively (here: R- and S-BINOL).<sup>9</sup>

**Optical Setup.** Briefly, the high-sensitivity VCD EC-QCL spectroscopy setup introduces a polarization modulator into one arm of a balanced detection scheme (see Figure 1). An

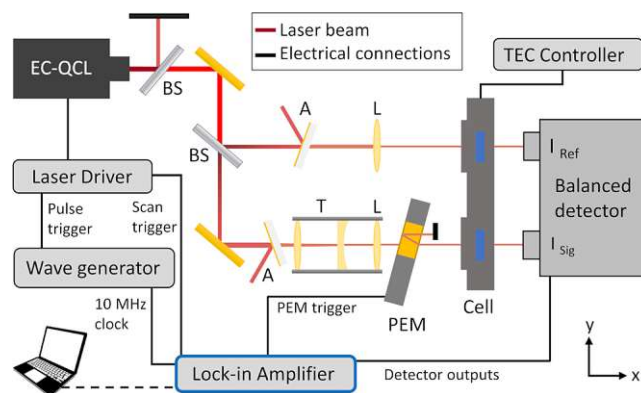


**Figure 1.** Optical setup used for the balanced VCD measurements. This setup encompasses an EC-QCL as a light source, beam splitters (BS), attenuators (A), a telescope system to reduce the beam diameter (T), focusing lenses (L), a photoelastic modulator (PEM), a double-path transmission cell (Cell), temperature stabilized by a thermoelectrical cooling (TEC) controller, and a balanced detector module.

external cavity QCL (EC-QCL, Hedgehog, Daylight Solutions Inc., San Diego), tunable from 1780 to 1550 cm<sup>–1</sup>, was used as a light source. The EC-QCL emits a beam in the TEM<sub>00</sub> spatial mode with linear polarization (vertical, nominally > 100:1) and a spot size of around 2.5 mm (1/e<sup>2</sup> width). Operating with a current of 540 mA, a repetition rate of 1 MHz, and a pulse length of 200 ns, the laser reached a duty cycle of 20%. The laser head temperature was stabilized at 19 °C. Water cooling was used to remove excess heat.

A waveform generator (DG4102, RIGOL, Beijing, China) was used to trigger the laser. The internal clock of the waveform generator was synchronized to the lock-in amplifier used for signal recovery (see the Data Acquisition section). Spectra were collected in the “sweep mode”, whereby the EC-QCL tunes across its spectral range at a constant tuning speed without stopping. The sweep speed was set to 640 cm<sup>–1</sup>/s. Several attenuators were placed in the beam path before the sample to keep the intensity reaching the detector within the detector’s dynamic range. Attenuation was necessary, as decreasing the laser current results in a reduced spectral range of the EC-QCL.

The laser beam first passed a beam splitter (nominal 50/50), attenuating the beam by diverting half of the intensity onto a beam stop, and then was redirected by a gold mirror to another beam splitter (nominal 50/50). Here, the laser beam was divided into a reference and a sample beam (the reflected and the transmitted beams, respectively). Both the sample and the reference beams were diverted onto gold-sputtered BaF<sub>2</sub>

windows, wedged by  $0.5^\circ$  to prevent interference from reflections. (Sputtered windows were used instead of the commonly used metallic meshes, as the latter were found to strongly affect the beam profile.) The attenuated reference beam was focused by a ZnSe lens ( $f = 200$  mm) through one cell of the double-path transmission cell onto the reference detector. All ZnSe lenses are sourced from Thorlabs (Newton, NJ) and AR-coated to a reflectivity below 1% between 4.5 and  $7.5\ \mu\text{m}$ . Reflective focusing was avoided, as reflections on metal surfaces show polarization-dependent bias and can introduce artifacts in the VCD spectra.<sup>15,25,26</sup>

The attenuated sample beam was directed into a cage system. First, the beam diameter was reduced by a Galilean telescope ( $f = 75$  and  $-25.4$  mm) to below 1 mm. Then, the beam was focused via a ZnSe lens ( $f = 200$  mm, identical to the reference beam) onto the sample detector. After the cage system, the beam passed a 42 kHz ZnSe photoelastic modulator (Hinds instrument, Hillsboro) with a broad-band antireflection coating. The modulator was set to a quarter-wave retardation at  $6\ \mu\text{m}$ . For QCLs, the output polarization is oriented orthogonal to the gain medium layers, resulting in a vertical linear polarized laser beam, without the need for additional components like polarizers.<sup>19</sup> The stress axis of the modulator was orientated at  $45^\circ$  relative to the laser polarization direction. To further reduce interference effects at the modulation frequency, the modulator was tilted by  $15^\circ$  around the vertical axis.<sup>27</sup> In combination with the beam diameter reduction by the telescope, this allowed the blockage of the reflected beam. The now circular polarized laser light passed through the other cell in the double-path transmission cell.

The detector used in this setup is a balanced detection module with a manual gain regulation (Vigo System S.A., Poland). It is composed of two thermoelectrically cooled MCT detectors with a detectivity of  $1.45 \times 10^{10}\ \text{cm Hz}^{1/2}/\text{W}$  (at  $10.6\ \mu\text{m}$ , 100 kHz). The detector elements and the corresponding electronics were chosen to ensure that both detectors have a similar response. This increases the efficiency of the common mode rejection in the balance detection scheme. Both detectors are equipped with a manual adjustable dark current compensation. The electrical gain of the reference channel can also be adjusted manually. Both sample and reference channel outputs are accessible via SMA connectors. Additionally, a third channel outputs the difference between the sample and reference voltage, determined via a differential amplifier in the detector. This additional channel is referred to as the balanced channel.

The custom-made double-path cell comprised two  $160\ \mu\text{m}$  long cells with  $\text{CaF}_2$  windows and was set to a temperature of  $20\ ^\circ\text{C}$  ( $\pm 0.001\ ^\circ\text{C}$ ). The temperature was controlled by a thermoelectrical cooling controller (Meerstetter Engineering GmbH, Rubigen, Switzerland). The setup was encompassed in an acrylic glass housing and constantly purged with dry air to prevent the interference from water vapor during the spectra acquisition. For the spectra depicted in this work, approximately  $400\ \mu\text{L}$  of sample solution was manually injected and 700 spectra were averaged. This resulted in a total measurement time of 290 s (4 min 50 s). The classical absorbance spectra as well as the VCD spectra were baseline-corrected with the pure solvent measured under the same conditions.

**Data Acquisition.** A lock-in amplifier (MFLI, Zurich Instruments, with F5M and MD extensions) was used to extract the phase-sensitive information from the detector

signals. As mentioned, the laser pulsing scheme was controlled by a waveform generator, which was kept at a constant phase to the MFLI via a 10 MHz sync connection. Using the lock-in, the intensity  $I$ , which corresponds to the intensity of the laser after the sample, is recovered from the 1 MHz component of the detector output. The  $\Delta I_{\text{L-R}}$  signal is the amplitude of the detector signal at the PEM modulation frequency  $f_{\text{PEM}}$ , which carries the chiroptical information. The PEM outputs a rectangular pulse at  $f_{\text{PEM}}$ . By feeding this signal to a phase-locked loop (PLL) of the lock-in amplifier, the phase and frequency of the PEM are determined and used to demodulate  $\Delta I_{\text{L-R}}$ .

It is important to keep in mind that in the balanced detection setup, not only  $\Delta I_{\text{L-R}}$  but also  $I$  can be positive and negative; thus, for all signals, phase-sensitive detection is required. The correct phases were set when starting the experiment and were found to not require adjustment later. During the measurements, the  $I$  and  $\Delta I_{\text{L-R}}$  components of the balanced output as well as the  $I$  of the reference detector output were collected. The general equation for calculating the VCD spectra is

$$\text{VCD} = \frac{1}{\ln 10 * J_1(\delta_{\text{PEM}})} * \frac{\Delta I_{\text{L-R}}}{I} \quad (2)$$

with  $J_1$  being the first-order Bessel function and  $\delta_{\text{PEM}}$  being the maximum retardation of the PEM.<sup>7</sup> For the single channel configuration, the  $\Delta I_{\text{L-R}}$  and  $I$  components are extracted from the sample channel detector signal and inserted into eq 2. For the balanced configuration,  $\Delta I_{\text{L-R}}$  and  $I$  are extracted from the balanced channel output. At the beginning of a measurement day, the  $I$  component of the reference output is recorded. For each spectrum, the stored  $I$  is then added to the  $I$  component of the balanced output. The sum of balanced  $I$  and reference  $I$  is then used in eq 2 to calculate the VCD spectrum. The  $\Delta I_{\text{L-R}}$  recorded from the balanced channel does not require a correction by a reference.

The sampling rate of the lock-in amplifier was set to 6696 Sa/s. For each wavenumber, 10 data points were collected, resulting in a total of 2300 data points per spectrum. All signals were demodulated using a fourth-order digital low pass filter (resulting in a filter roll-off of 24 dB/oct) and, in this case, a time constant of  $745.8\ \mu\text{s}$  (corresponding to 3 dB attenuation at 92.8 Hz). The time constant was chosen relative to the scanning frequency of the laser.

Before further evaluation, the spectra were low-pass-filtered using a finite impulse response (FIR) digital filter (Kaiser window, cutoff of 220 Hz). The wavenumber axis was calibrated using the positions of water vapor bands. By comparing the bandwidth of water vapor spectra collected with the setup to FT-IR spectra at different resolutions, a spectral resolution of  $1.6\ \text{cm}^{-1}$  was estimated.

**Partial Least-Squares Analysis.** Multivariate data analysis was performed in Python 3 using the scikit-learn package,<sup>28,29</sup> implemented based on in-house written scripts. No preprocessing was applied to the baseline-corrected enantiomeric excess VCD spectra, and a leave-one-out cross-validation method was applied. A partial least-squares (PLS) regression was constructed, with the enantiomeric excess levels and the baseline-corrected VCD spectra being used as response and independent variables, respectively. Since the data set was quite small ( $n = 18$ , 6 levels in 3 replicates), this method was appropriate. The chosen spectral range was optimized from

1653 to 1561  $\text{cm}^{-1}$  based on the root-mean-square error of the cross-validation (RMSECV). The model was built with two latent variables chosen based on the optimal RMSECV while avoiding overfitting. Besides cross-validation, external validation was performed with five samples (EE levels:  $-100\%$ ,  $-60\%$ ,  $-20\%$ ,  $0\%$ ,  $+20\%$ ) prepared with different stock solutions and measured on a different day.

## RESULTS AND DISCUSSION

**Applicability for VCD.** In Figure 2, the absorbance and VCD spectra of 100 mM R- and S-BINOL in  $\text{CHCl}_3$  are

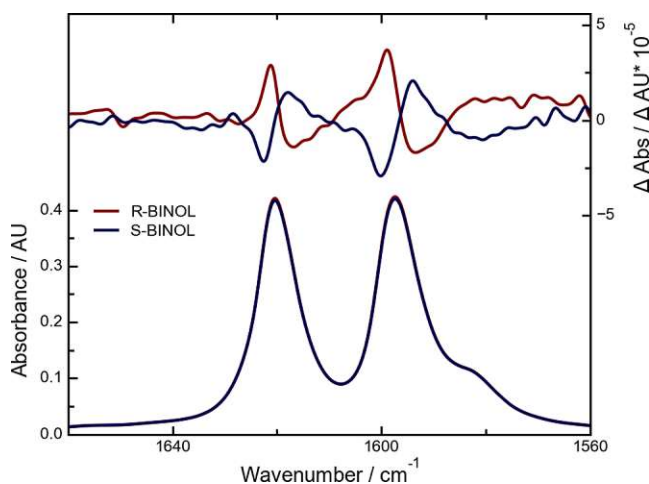


**Figure 2.** Absorbance (left axis) and VCD (right axis) of R-BINOL (blue) and S-BINOL (red) in  $\text{CHCl}_3$ . The samples were measured at a concentration of 0.1 M with a path length of 160  $\mu\text{m}$ . 700 scans were averaged, corresponding to a 290 s integration time.

shown. The absorbance and VCD spectra were baseline-corrected with the pure solvent. As expected, no difference between the absorbance spectra of the two enantiomers is observed, whereas their VCD spectra show a clear mirror image relation. The position and orientation of the bands in the VCD spectrum match those from the literature recorded using conventional FT-IR VCD instrumentation well.<sup>30,31</sup>

**Balanced Detection for VCD Noise Reduction.** The noise in single detector and balanced detection was evaluated as the difference between two subsequent VCD spectra of the solvent ( $\text{CHCl}_3$ ). Ideally, the result should be a zero line.<sup>17,21</sup> Examples of these noise spectra are shown in Figure 3B. The potential for improving noise levels through the averaging of scans was evaluated for both single detector and balanced detection. Up to 1500 scans were averaged before calculating the RMS noise levels between 1600 and 1730  $\text{cm}^{-1}$ . In Figure 3A, the average RMS value of five replicates is plotted against the number of averaged scans.

The performance of the balanced detection scheme is better than that of the standard single detector method, with a noise reduction by a factor of around 3.7. As this reduction shows promise, the improvement is not as large as we expected from comparable works with classical IR absorbance.<sup>22</sup> A probable explanation for smaller improvement is the normalization inherent to VCD spectra. To obtain raw VCD spectra, the signal collected at the PEM frequency is divided by the one collected at the laser frequency. Through this process, parts of the pulse-to-pulse fluctuations are compensated regardless of the detector configuration. Nevertheless, the data presented

still show improvement in the noise levels by the application of balanced detection as well as an increased repeatability of the spectra. This is shown by the reduced deviations (error bars) between the replicates for the balanced detection scheme when compared to those for the single detector scheme.

The superior performance of the balanced detection scheme also becomes apparent in the spectra shown in Figure 3B. Here, typical VCD noise spectra for the single and the balanced detection setup are overlaid. The baseline produced by the balanced detection stays around zero for the whole spectral range, with no clear peaks visible. In comparison, the baseline obtained from the single detector scheme deviates considerably from the zero line. When comparing the baselines to the peaks depicted in Figures 2 and 4A, this improvement can be contextualized. Especially for lower EE values, the peaks are in the range of the noise floor of the single detector baseline. This would hinder a correct interpretation of the spectra, necessitating longer measurement times to decrease the noise to sufficient levels.

Biological samples, due to their inherent chirality and structural orientation, present themselves as obvious analytes for VCD studies. However, proteins, for example, seldom exhibit VCD signals more intense than  $2 \times 10^{-5}$ .<sup>18,32</sup> For these samples, the reduced noise of the balanced detection setup is an obvious advantage. Protein spectra typically take several hours to collect with classical FT-IR spectrometers. A single detector scheme would need a significantly longer measurement time than the balanced detection setup and offer less improvement compared to FT-IR spectra.

In addition to the graphs in Figure 3, the overall noise performance is summarized in Table 1. All shown values are calculated between 1730 and 1600  $\text{cm}^{-1}$  for spectra collected by averaging 1500 scans (10 min measurements). The values for the FT-IR performance are taken from the literature. As already mentioned, the RMS noise values for the balanced detection are around 3.7 times lower than for single detector setup, being  $1.45 \times 10^{-6}$  compared to  $5.45 \times 10^{-6}$ . The available FT-IR data are collected with 3 times longer averaging times and reach RMS noise levels of  $2.8 \times 10^{-6}$ .<sup>33</sup> For balanced operation, the EC-QCL-based setup reached a noise level nearly 2 times better in a third of the measurement time. Besides the RMS noise, the noise height is also a relevant noise parameter for VCD spectra. The relevant chapter (1782) of the U.S. pharmacopeia defines it as the maximum deviation from the zero line over the spectral range of interest.<sup>34</sup> This value was also calculated and is shown in Table 1. The noise height for the balanced detection system is almost 4 times lower than for a single detector system, with  $3.83 \times 10^{-6}$  and  $15.2 \times 10^{-6}$ , respectively. The available FT-IR data were collected after 60 min of averaging and deviated from zero by  $5 \times 10^{-5}$ , 13 times higher than the deviation achieved for the balanced detection setup.

Besides lower noise levels and shorter measurement times, our EC-QCL-based setup also offers a higher spectral resolution. Typical FT-IR VCD spectra are collected at resolutions between 4 and 8  $\text{cm}^{-1}$ , while our data were presented at a resolution of 1.6  $\text{cm}^{-1}$ .

**Enantiomeric Excess Studies.** In addition to studying the spectrum of enantiomers, VCD also allows the quantification of enantiomeric excess. This application is more challenging as the bands in VCD spectra of mixed enantiomers are lower than in enantiopure samples. Solutions with different levels of enantiomeric excess were prepared and measured in triplicate.

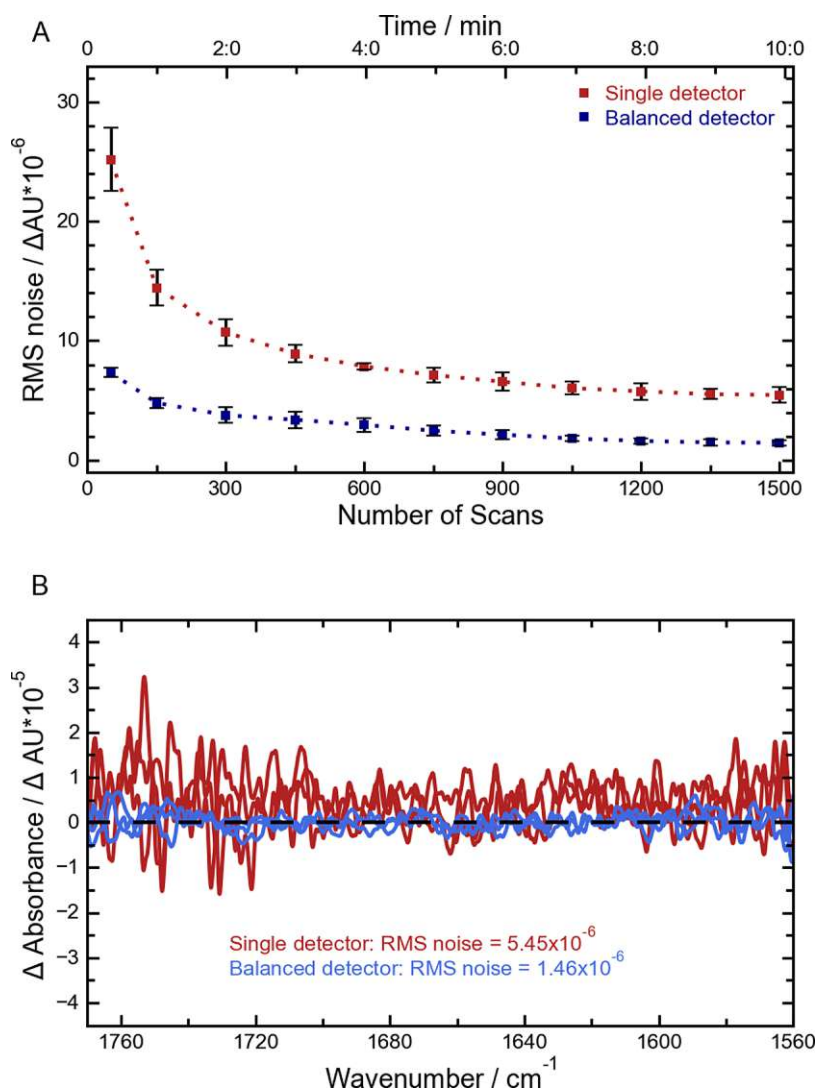


**Figure 3.** (A) RMS noise level in the single detector configuration and the balanced detector configuration. The RMS noise level (average of five measurements) of the VCD spectra for each configuration is plotted as a function of integration time and number of scans used for averaging. The error bars correspond to the standard deviation between the measurements. (B) Typical noise spectra for VCD spectra of  $CHCl_3$  obtained after averaging 1500 spectra for single or balanced detector configuration. The RMS noise value for each configuration is also shown.

The EE levels were varied from +100 to −100 in steps of 40 %. The resulting spectra are shown in Figure 4A. With decreasing enantiomeric excess levels, the VCD couplets centered at 1619 and 1596  $cm^{-1}$ , respectively, changed their orientation. The negative couplets (negative VCD intensity at the higher wavenumber, positive intensity at lower wavenumber) characteristic of R-BINOL decrease in intensity and evolve into the positive couplets expected from S-BINOL. The intensity and orientation of the couplet centered at 1596  $cm^{-1}$  were used to describe the enantiomeric excess in a univariate linear model. The resulting correlation line can be found in the Supporting Information (see Figure S4). The  $r^2$  of 0.997 indicates a high correlation, and the  $p$ -value of the slope ( $p = 3.3 \times 10^{-6}$ ) attests the significance of the correlation. The limit of detection (LOD) for the EE was calculated according to

$$LOD [\%EE] = \frac{3 \times RMS\ noise}{slope} \quad (3)$$

where RMS noise stands for the root-mean-square (RMS) noise, and slope stands for the slope of the calibration curve.<sup>22</sup>

The obtained value was 10.5 % EE. Taking the used total (R- + S-BINOL) concentration of 100 mM into account, this corresponds to a concentration difference of 5.25 mM between the enantiomers.

The use of a multivariate method such as partial least-squares regression (PLSR) could help to further improve this value, as these methods are less susceptible to noise over a few wavenumbers. To test this, a PLSR model was constructed based on the spectra shown in Figure 4A. The predictions obtained from this model can be seen in Figure 4B. The predicted (cross-validated) and actual volumetric enantiomeric excess levels show a high correlation with an  $R^2$  of 0.991. The  $R^2$  of the calibration model was 0.996, and the root-mean-square error (RMSE) was 4.31 % EE. Further statistical parameters can be seen in Table 2.

To validate the performance of the model, a leave-one-out cross-validation was performed. Due to the small sample size, this approach is appropriate. The cross-validation showed an  $R^2$  of 0.991 and a slightly higher RMSE of 6.64 % EE than for the calibration. Since the calculation of the LOD for the multivariate method is not as straightforward as for univariate

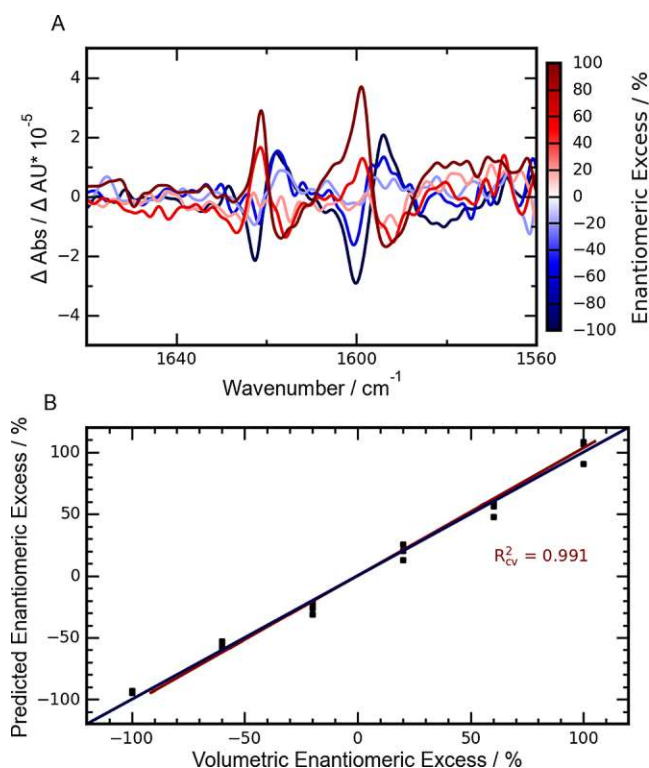


**Figure 4.** (A) VCD spectra obtained by measuring different levels of enantiomeric excess. For the corresponding enantiomeric excess level, the reader is referred to the depicted color bar. The concentration of BINOL was 100 mM in a cell with a path length of 160  $\mu\text{m}$ , and 700 spectra were averaged. (B) Linear correlation of the predicted enantiomeric excess values (cross-validated) and the volumetric enantiomeric excess of the prepared samples. The obtained fit is plotted in red, with the corresponding  $R^2$  being depicted beside the graph. The blue line indicates a perfect correlation.

**Table 1. Noise Characteristics for the Single Detector Scheme, the Balanced Detection Scheme, and Values for FT-IR Spectrometer from the Literature**

	RMS noise [10 <sup>-6</sup> $\Delta\text{AU}$ ]	time [min]	noise height [10 <sup>-6</sup> $\Delta\text{AU}$ ]	time [min]
single	5.45	10	15.2	10
balanced	1.46	10	3.83	10
FT-IR <sup>33,34</sup>	2.8	30	50	60

**Table 2. Statistical Parameters for the PLS Model Constructed Based on the Enantiomeric Excess Study**

	$R^2$	RMSE [%]
calibration <sup>a</sup>	0.996	4.31
cross-validation <sup>b</sup>	0.991	6.64
prediction <sup>c</sup>	0.964	8.16

<sup>a</sup>Full data set (6 levels, 3 replicates = 18 data points). <sup>b</sup>Leave-one-out cross-validation. <sup>c</sup>Five unrelated samples (EE: -100 to +20). RMSE: root-mean-square error.

models, the RMSE of the cross-validation was taken as a measure of accuracy.<sup>35</sup> This value corresponds to a concentration difference of 3.32 mM in our case. To further evaluate the applicability of the model, external validation was performed with five samples prepared and measured on a different day. The obtained  $R^2$  of 0.964 indicates a still high correlation, and an RMSE of 8.16 % is comparable to the

RMSE of the cross-validation. This indicates a robust model, without the presence of overfitting.

Enantiomeric excess prediction by VCD was already studied, with great success on FT-IR instruments. While these studies achieved better RMSECV than the one we performed in these experiments, this comparison needs to be contextualized.<sup>3,9,36</sup> Since the studies were performed with substantially different concentration ranges, the RMSECVs were normalized to the molar concentration. The resulting detectable molar differences attested to our setup a performance comparable to or better than most published results, with measurement times reduced by a factor of 4.<sup>3,9</sup> Only one study achieved a better sensitivity, which was enabled by a measurement time longer by a factor of 120.<sup>36</sup> Based on these data, the advantages provided by balanced detection EC-QCL-VCD enabled enantiomeric excess studies with comparatively low concentrations (100 mM) and low VCD signals while still providing a high temporal resolution. This can extend the applicability of VCD to samples where only low concentrations are accessible and which are characterized by low VCD signals without losing temporal resolution. The accuracy and robustness of the model could be improved by measuring additional sample points, applying longer measurement times, and evaluating different concentration ranges. However, this is beyond the scope of this study.

## CONCLUSIONS

We presented an improved method to measure EC-QCL-based VCD spectra. The combination of an EC-QCL and a balanced detection module used in the study enables the leveraging of the high brilliance of EC-QCLs without introducing additional noise into the spectra. Relevant noise parameters were improved by up to a factor of 4 compared to single detector measurements. The applicability for VCD measurements was examined with qualitative and quantitative experiments using R- and S-BINOL as model substances. Enantiomeric excess studies were possible with measurement times below 5 min for samples with low molar concentrations. The noise levels are significantly lower than for commercial FT-IR instruments even at acquisition times shorter by a factor of up to 6.

Of course, this comparison needs to be contextualized by the strengths and weaknesses of FT-IR and EC-QCLs, respectively. FT-IR instruments offer a broad coverage (up to several thousand wavenumbers) with a constant noise floor over this range while being restricted in terms of sensitivity by the relatively weak light source. EC-QCLs, on the other hand, provide a comparatively limited spectral coverage (several hundred wavenumbers) and are characterized by a higher noise level at the edges of their spectral emission but can leverage their high intensity to minimize limits of detections even with strongly absorbing solvents. Due to these differences, the perfect technique depends mostly on the envisioned application. FT-VCD has an edge when dealing with the absolute configuration determination or complex sample mixtures with multiple bands over a broad spectral area. EC-QCL-VCD, on the other hand, can excel in applications like EE determination or also with biomolecules like proteins in an aqueous solution. For these applications, a smaller spectral area is perfectly sufficient, and the higher sensitivity provided by the EC-QCL can prove to be advantageous here.

Employing a dedicated balanced detection scheme for VCD measurements enables the collection of low noise spectra with

a high temporal and spectral resolution when compared to state-of-the-art FT-IR VCD instruments. This allows a comprehensive monitoring of processes where the chirality of the sample changes over time, like folding mechanisms of biological molecules. Indeed, our previous work on EC-QCL suggests that the high spectral power density of the laser will provide further gains in sensitivity over FT-IR when analyzing samples in aqueous solutions.<sup>22</sup>

## ■ ASSOCIATED CONTENT

### SI Supporting Information

The Supporting Information is available free of charge at <https://pubs.acs.org/doi/10.1021/acs.analchem.2c01269>.

Noise height against measurement times, detector signals at the laser frequency for the reference, the sample and the balanced channel, detector signals at the PEM frequency for the sample and the balanced channel, and univariate calibration line for the enantiomeric excess study (PDF)

## ■ AUTHOR INFORMATION

### Corresponding Author

**Bernhard Lendl** – Institute of Chemical Technologies and Analytics, TU Wien, 1060 Vienna, Austria; [orcid.org/0000-0003-3838-5842](https://orcid.org/0000-0003-3838-5842); Email: [bernhard.lendl@tuwien.ac.at](mailto:bernhard.lendl@tuwien.ac.at)

### Authors

**Daniel R. Hermann** – Institute of Chemical Technologies and Analytics, TU Wien, 1060 Vienna, Austria; [orcid.org/0000-0003-2605-8203](https://orcid.org/0000-0003-2605-8203)

**Georg Ramer** – Institute of Chemical Technologies and Analytics, TU Wien, 1060 Vienna, Austria; [orcid.org/0000-0001-8307-5435](https://orcid.org/0000-0001-8307-5435)

**Markus Kitzler-Zeiler** – Photonics Institute, TU Wien, 1040 Vienna, Austria

Complete contact information is available at:

<https://pubs.acs.org/10.1021/acs.analchem.2c01269>

### Author Contributions

The manuscript was written through contributions of all authors. All authors have given approval to the final version of the manuscript.

### Notes

The authors declare no competing financial interest.

## ■ ACKNOWLEDGMENTS

The authors acknowledge financial support through the COMET Centre CHASE, funded within the COMET—Competence Centers for Excellent Technologies programme by the BMK, the BMDW, and the Federal Provinces of Upper Austria and Vienna. The COMET programme is managed by the Austrian Research Promotion Agency (FFG). The authors acknowledge TU Wien Bibliothek for financial support through its Open Access Funding Programme. M. K.-Z. acknowledges financial support by the Austrian Science fund FWF (Grant. No. 15590).

## ■ REFERENCES

- (1) Ranjbar, B.; Gill, P. *Chem. Biol. Drug Des.* **2009**, *74*, 101–120.
- (2) Slade, D.; Ferreira, D.; Marais, J. P. J. *Phytochemistry* **2005**, *66*, 2177–2215.
- (3) Nafie, L. A.; McConnell, O.; Minick, D.; Kellenbach, E.; He, Y.; Wang, B.; Dukor, R. K.; Bartberger, M. D.; Pappa, H. N. *Pharmacoepial Forum* **2013**, *39*, 311–452.
- (4) Burgueño-Tapia, E.; Joseph-Nathan, P. *Nat. Prod. Commun.* **2015**, *10*, 1785–1795.
- (5) Rogers, D. M.; Jasim, S. B.; Dyer, N. T.; Auvray, F.; Réfrégiers, M.; Hirst, J. D. *Chem* **2019**, *5*, 2751–2774.
- (6) Joseph-Nathan, P.; Gordillo-Román, B. *Prog. Chem. Org. Nat. Prod.* **2015**, *100*, 311–452.
- (7) Nafie, L. A. *Vibrational Optical Activity*; John Wiley & Sons, Ltd.: Chichester, UK, 2011; Vol. 492.
- (8) Polyanchko, A. M.; Andrushchenko, V. V.; Bouř, P.; Wieser, H. *Circ. Dichroism: Theory Spectrosc.* **2011**, 67–126.
- (9) Guo, C.; Shah, R. D.; Dukor, R. K.; Cao, X.; Freedman, T. B.; Nafie, L. A. *Anal. Chem.* **2004**, *76*, 6956–6966.
- (10) Freedman, T. B.; Cao, X.; Dukor, R.; Nafie, L. A. *Chirality* **2003**, *15*, 743–758.
- (11) Keiderling, T. *Molecules* **2018**, *23*, 2404.
- (12) Whitmore, L.; Wallace, B. A. *Biopolymers* **2008**, *89*, 392–400.
- (13) Nafie, L. A.; Keiderling, T. A.; Stephens, P. J. *J. Am. Chem. Soc.* **1976**, *98*, 2715–2723.
- (14) Lakhani, A.; Malon, P.; Keiderling, T. A. *Appl. Spectrosc.* **2009**, *63*, 775–785.
- (15) Malon, P.; Keiderling, T. A. *Appl. Spectrosc.* **1988**, *42*, 32–38.
- (16) Kurouski, D. *Anal. Chim. Acta* **2017**, *990*, 54–66.
- (17) Baumruk, V.; Keiderling, T. A. *J. Am. Chem. Soc.* **1993**, *115*, 6939–6942.
- (18) Ma, S.; Freedman, T. B.; Dukor, R. K.; Nafie, L. A. *Appl. Spectrosc.* **2010**, *64*, 615–626.
- (19) Faist, J.; Capasso, F.; Sivco, D. L.; Sirtori, C.; Hutchinson, A. L.; Cho, A. Y. *Science* **1994**, *264*, 553–556.
- (20) Schwaighofer, A.; Montemurro, M.; Freitag, S.; Kristament, C.; Culzoni, M. J.; Lendl, B. *Anal. Chem.* **2018**, *90*, 7072–7079.
- (21) Brandstetter, M.; Lendl, B. *Sens. Actuators, B* **2012**, *170*, 189–195.
- (22) Akhgar, C. K.; Ramer, G.; Žbik, M.; Trajnerowicz, A.; Pawluczyk, J.; Schwaighofer, A.; Lendl, B. *Anal. Chem.* **2020**, *92*, 9901–9907.
- (23) Lüdeke, S.; Pfeifer, M.; Fischer, P. *J. Am. Chem. Soc.* **2011**, *133*, 5704–5707.
- (24) Hobbs, P. C. D. Shot Noise Limited Optical Measurements at Baseband with Noisy Lasers (Proceedings Only). In *Laser Noise*, Roy, R., Ed.; 1991; Vol. 1376, pp 216–221.
- (25) Xie, P.; Diem, M. *Appl. Spectrosc.* **1996**, *50*, 675–680.
- (26) Tsankov, D.; Eggimann, T.; Wieser, H. *Appl. Spectrosc.* **1995**, *49*, 132–138.
- (27) Oakberg, T. C. *Opt. Eng.* **1995**, *34*, 1545.
- (28) Van Rossum, G.; Drake, F. L. *Python 3 Reference Manual*; CreateSpace: Scotts Valley, CA, 2009.
- (29) Pedregosa, F.; Varoquaux, G.; Gramfort, A.; Michel, V.; Thirion, B.; Grisel, O.; Blondel, M.; Prettenhofer, P.; Weiss, R.; Dubourg, V.; Vanderplas, J.; Passos, A.; Cournapeau, D.; Brucher, M.; Perrot, M.; Duchesnay, E. *J. Mach. Learn. Res.* **2011**, *12*, 2825–2830.
- (30) Nicu, V. P.; Baerends, E. J.; Polavarapu, P. L. *J. Phys. Chem. A* **2012**, *116*, 8366–8373.
- (31) Setnicka, V.; Urbanová, M.; Bouř, P.; Král, V.; Volka, K. *J. Phys. Chem. A* **2001**, *105*, 8931–8938.
- (32) Shanmugam, G.; Polavarapu, P. L. *J. Am. Chem. Soc.* **2004**, *126*, 10292–10295.
- (33) Urbanová, M.; Setnicka, V.; Volka, K.; Jun, B.; Weaver, D. L.; Schultz, C. P.; Boese, M. T. D.; Drews, H. H. Application Note AN \# 52 Fourier Transform Vibrational Circular Dichroism.
- (34) *The United States Pharmacopoeia: the National Formulary (USP42/NF37)*; United States Pharmacopoeial Convention, Inc.: Rockville, Md., 2018.
- (35) Allegrini, F.; Olivieri, A. C. *Anal. Chem.* **2014**, *86*, 7858–7866.
- (36) Kott, L.; Petrovic, J.; Phelps, D.; Roginski, R.; Schubert, J. *Appl. Spectrosc.* **2014**, *68*, 1108–1115.

## Publication II

### **Chiral Monitoring Across Both Enantiomeric Excess and Concentration Space: Leveraging Quantum Cascade Lasers for Sensitive Vibrational Circular Dichroism Spectroscopy**

Hermann, D.-R.; Ramer, G.; Riedlsperger, L.; Lendl, B.

*Applied Spectroscopy* **2023**, 77 (12), 1362–1370.

# Chiral Monitoring Across Both Enantiomeric Excess and Concentration Space: Leveraging Quantum Cascade Lasers for Sensitive Vibrational Circular Dichroism Spectroscopy

Daniel-Ralph Hermann , Georg Ramer, Lisa Riedlsperger, and Bernhard Lendl 

## Abstract

Recently, high-throughput quantum cascade laser-based vibrational circular dichroism (QCL-VCD) technology has reduced the measurement time for high-quality vibrational circular dichroism spectra from hours to a few minutes. This study evaluates QCL-VCD for chiral monitoring using flow-through measurement of a changing sample in a circulating loop. A balanced detection QCL-VCD system was applied to the enantiomeric pair R/S-1,1'-bi-2-naphthol in solution. Different mixtures of the two components were used to simulate a racemization process, collecting spectral data at a time resolution of 6 min, and over three concentration levels. The goal of this experimental setup was to evaluate QCL-VCD in terms of both molar and enantiomeric excess (EE) sensitivity at a time resolution relevant to chiral monitoring in chemical processes. Subsequent chemometric evaluation by partial least squares regression revealed a cross-validated prediction accuracy of 2.8% EE with a robust prediction also for the test data set (error = 3.5% EE). In addition, the data set was also treated with the least absolute shrinkage and selection operator (LASSO), which also achieved a robust prediction. Due to the operating principle of LASSO, the obtained coefficients constituted a few discrete spectral frequencies, which represent the most variance. This information can be used in the future for dedicated QCL-based instrument design, gaining a higher time resolution without sacrificing predictive capabilities.

## Keywords

Vibrational circular dichroism, quantum cascade laser absorption spectroscopy, QCL-VCD, chemometrics, chiral sensing, mid-infrared

Date received: 7 March 2023; accepted: 1 September 2023

## Introduction

Chirality is a prominent characteristic in the chemical and biological world, present in both single molecules and large biopolymers. In biopolymers such as proteins and DNA, it manifests in the form of helices or the complex tertiary structures of proteins.<sup>1</sup> Single molecule chirality on the other hand is defined as their mirror image being not superposable on the molecule, thereby forming enantiomeric pairs.<sup>2</sup> Enantiomers exhibit the same physical (boiling point, etc.) and chemical (pH, stability, etc.) properties and are therefore nearly indistinguishable. However, enantiomers react substantially differently when being deposited in a chiral environment or encountering a chiral reaction partner.<sup>3</sup> This issue becomes significant since the overwhelming majority of biological systems are comprised of chiral building blocks (L-amino acids and D-carbohydrates) and/or exhibit macromolecular chirality.<sup>1,3</sup> As a consequence, the enantiomeric identity, also called absolute configuration (AC), of a pharmaceutical agent drastically influences the effects or side effects

it has in a pharmaceutical concept.<sup>3,4</sup> This is also true for racemic drugs, which are 50:50 mixtures of the enantiomeric pair. These effects can result in the enantiomers exhibiting different pharmacokinetics or therapeutical indices, limiting the effectiveness of racemic mixtures.<sup>3</sup> Also, chiral drug design can, if not properly understood, result in one enantiomer being a pharmaceutical agent and the other one constituting a toxin or harmful substance, as exemplified by the thalidomide scandal in the 1950s.<sup>2,4,5</sup> Consequently, the assignment of AC was added to the review process for new pharmaceuticals by the European Medicines Agency.<sup>2</sup>

Research Division of Environmental Analytics, Process Analytics and Sensors, Institute of Chemical Technologies and Analytics, TU Wien, Vienna, Austria

### Corresponding Author:

Bernhard Lendl, Research Division of Environmental Analytics, Process Analytics and Sensors, Institute of Chemical Technologies and Analytics, TU Wien, Vienna 1060, Austria.  
Email: [bernhard.lendl@tuwien.ac.at](mailto:bernhard.lendl@tuwien.ac.at)

Owing to their similarity, the differentiation of enantiomers constitutes a nontrivial analytical problem. A number of solutions have emerged, differing in terms of applicability, time resolution, and ease of use. X-ray crystallography, the analysis of the dispersion on crystalized pure components is able to easily resolve ACs but is limited both in terms of applicability and ease of use.<sup>2,6</sup> Achieving a useable crystal requires extensive experience, is time-consuming, and is not always possible, making it not suitable for routine analytics. If an analyte features a suitable functional group, derivatization with a compound of known AC can enable nuclear magnetic resonance (NMR) spectroscopy to identify differences between the enantiomers of the analyte.<sup>2,7</sup> Again, this method is not broadly applicable and requires derivatization as a pretreatment step. Due to the different interactions of enantiomers with circularly polarized light, they are also accessible by optical methods.<sup>8,9</sup> If the interaction is measured by recording the differential absorption for left- and right-handed circular polarized light, the process is called circular dichroism (CD). This method can be further divided according to the wavelength region used, differentiating between electronic CD (ECD), operating in the ultraviolet visible (UV–Vis) region, and vibrational CD (VCD), analyzing infrared (IR) light, predominantly in the mid-IR (MIR) region.<sup>1,10</sup> ECD is characterized by a relatively high signal intensity, making it easy to use. It can also be combined with high-pressure liquid chromatography instruments outfitted with chiral columns (e.g., cyclodextrin-based) to improve its resolving power.<sup>11</sup> However, it relies on the availability of suitable chromophores in the UV–Vis range (e.g., aromatics), limiting the applicability to specific molecule groups.<sup>6,12</sup> In contrast, the MIR region contains bands specific to vibrations in chemical bonds, making it broadly applicable to organic molecules.<sup>13,14</sup> In contrast to ECD, VCD is plagued by low intensities,  $10^{-4}$ – $10^{-5}$  relative to the classical absorbance, making the measurement time-consuming, ranging from 1 h to up to 12 h depending on the sample–solvent system (but still quicker than X-ray crystallography and NMR) and restricted to highly concentrated solutions.<sup>10,14,15</sup> As a consequence, Fourier transform IR spectroscopy (FT-IR) VCD has mostly been routinely applied for AC determination of finished products, where concentration and time resolution restrictions are not a problem.<sup>4,16</sup> However, further applications, e.g., chiral monitoring of chemical reactions are not feasible with those restrictions in place.

The commercialization of high-power MIR semiconductor lasers, quantum cascade lasers (QCLs), provides an opportunity to remedy this problem, as they provide inherently linearly polarized light of high brilliance.<sup>17</sup> QCLs have enabled the extension of MIR spectroscopy beyond the limits of classical FT-IR instruments, with new sensing schemes and higher sensitivity.<sup>18,19</sup> Nevertheless, while QCL-VCD instruments constitute a valid alternative to conventional FT-IR instruments, they have yet to outperform them in the past.<sup>20–22</sup> By employing a balanced detection scheme, we recently

demonstrated performance for VCD sensing in a solution that outperformed FT-IR-based VCD instruments, both in terms of noise floor and measurement time.<sup>23</sup> An important advantage of the balanced detector approach is the efficient elimination of pulse-to-pulse intensity fluctuation of external cavity-QCLs (EC-QCLs) leading to low noise levels. This is however only possible when highly matched mercury–cadmium–telluride (MCT) detector elements are used as in this case of a dedicated balanced MCT detector.<sup>19</sup> In our previous work, spectra were recorded in the stopped-flow mode only.

This advancement opens up opportunities for chiral monitoring, as in accordance with the principle of quality by design chiral pharmaceutical manufacturing often focuses on ensuring an enantiomeric pure final product by reaction control.<sup>2,3</sup> One important parameter during these processes is enantiomeric excess (EE), the ratio between the two enantiomers, which approaches  $\pm 100\%$  during chiral catalysis.<sup>1</sup> In the interest of an efficient process design, this critical value should be controlled over the whole course of the reaction. Improved QCL-VCD spectroscopy now offers the possibility of fast VCD spectral acquisition, providing chiral information on a time base of a few minutes. This information can be used to assess the progress of a reaction, take corrective action when needed, or determine the end point of it. In this study, we applied a modification of our already published balanced detection EC-QCL VCD instrument to follow the changes in the EE of mixtures of R/S-1,1'-bi-2-naphthol, a commonly used motif for chiral catalysis.<sup>24</sup> We demonstrate the ability of QCL-VCD for monitoring a chiral reaction: in a continuous flow cell experiment starting at an enantiopure solution of S-(–)-1,1'-bi-2-naphthol (S-BINOL), aliquots of a solution containing the second enantiomer in the same concentration were added to simulate racemization. The sample solution was continuously circulated between the measurement cell and the mixing vessel, to simulate the environment most probably present in an on-line monitoring scheme. The changes in EE were introduced at intervals of a few minutes, significantly higher than the sampling rate offered by conventional FT-IR VCD instruments. Concurrently, QCL-VCD spectra were collected with an acquisition time of below 3 min, providing a competitive sampling rate for monitoring applications. To generate EE information as needed for process monitoring or control, the collected spectral data set was then evaluated with different multivariate techniques, to generate models for the prediction of EE from the spectral data.

## Experimental

### Material and Methods

**Chemicals.** The studied enantiomeric pair, R-(+)-1,1'-bi-2-naphthol (R-BINOL, 99%) and S-BINOL (99%) and the used solvent  $\text{CHCl}_3$  ( $\geq 99.5\%$ , stabilized with 0.006% amylene) were

purchased from Sigma Aldrich and used without further purification. Stock solutions of R-BINOL and S-BINOL, respectively ( $c = 100$  mM), were prepared by dissolving the appropriate amount of sample in  $\text{CHCl}_3$  and diluting it as needed. The chosen concentrations (100 mM, 80 mM, and 40 mM) constituted the starting points for the closed-flow cell experiments.

**Optical Setup.** The EC-QCL-based VCD setup used for these measurements is a slight modification of our previously published balanced detection VCD instrument.<sup>23</sup> In brief, the instrument (Figure I) utilizes the inherently linearly polarized (nominally 100:1, vertical) emission of a tunable EC-QCL (Daylight Solutions Inc.) directly for polarization modulation. This laser was operated in pulsed mode, with a current of 550 mA and a pulsing scheme of 1  $\mu\text{s}$  pulses at a repetition rate of 200 kHz. This driving scheme was chosen by evaluating the performance in terms of noise levels in the VCD spectra (Figure S3, Supplemental Material). At this duty cycle of 20%, a water-cooled heat sink was necessary to keep the laser head at the optimum operating temperature of 19 °C. The intensity of the laser beam intensity was reduced by half by a beamsplitter and further on directed on a second beamsplitter (both 50:50 nominally) by a gold mirror. The second beamsplitter introduces the double beam geometry characteristic for our balanced detection system. Both the transmitted (hereafter called sample) and reflected (hereafter called reference) laser beam subsequently passed wedged ( $0.5^\circ$  angle)  $\text{BaF}_2$  windows, sputtered with gold to act as reflective attenuators, keeping the intensity reaching the detectors in their dynamic range. In the sample beam path, the initial laser beam diameter of 2.5 mm ( $1/e^2$  width) was reduced by a factor of 3 by the implementation of a Galilean telescope ( $f = 75$  mm and  $f = -25.4$  mm, ZnSe lenses) to below 1 mm. Both beam paths were

focused by ZnSe lenses ( $f = 200$  mm) through the two cells of a custom-made, double-path transmission cell (160  $\mu\text{m}$  path length), kept at  $20^\circ\text{C} \pm 1$  mK, onto two closely matched MCT detector elements. These detector elements were integrated into a balanced detection module with manual gain regulation (Vigo System S.A.) and thermoelectrically cooled to 201 K. A photoelastic modulator (PEM) (Hinds Instruments) was placed in the sample beam path, between the 200 mm focal length ZnSe lens and the transmission cell. The stress axis of this modulator was oriented at  $45^\circ$  to the polarization axis of the EC-QCL's emission and additionally tilted around its vertical axis, to separate the reflected from the transmitted beam to reduce interference effects. This was facilitated by the reduced beam diameter in the sample path. In contrast to our already published work, the reflected beam in this iteration is blocked by a 1 mm aperture, which allowed us to decrease the tilting angle of the PEM to  $10^\circ$  while still being able to separate the reflected and transmitted beam. This helped to further reduce artifacts in the VCD measurements and increased the stability of the setup. The optical setup was placed in an acrylic glass housing and constantly purged with dry air to counter the interference of water vapor in the accessible spectral range.

**Data Acquisition.** The EC-QCL was operated in sweeping mode, continuously scanning between 1670 and 1550  $\text{cm}^{-1}$  at a speed of 640  $\text{cm}^{-1}/\text{s}$ . To ensure a phase-sensitive data acquisition, the pulse trigger, a transistor–transistor logic (TTL) signal denoting the frequency of the laser pulses, was fed to a phase-locked loop (PLL) of the used lock-in amplifier (MFLI, Zurich Instruments, with F5M and MD extensions; Switzerland). Additionally, the scan trigger, a TTL signal signaling the start of the spectral scan, was also fed to a PLL

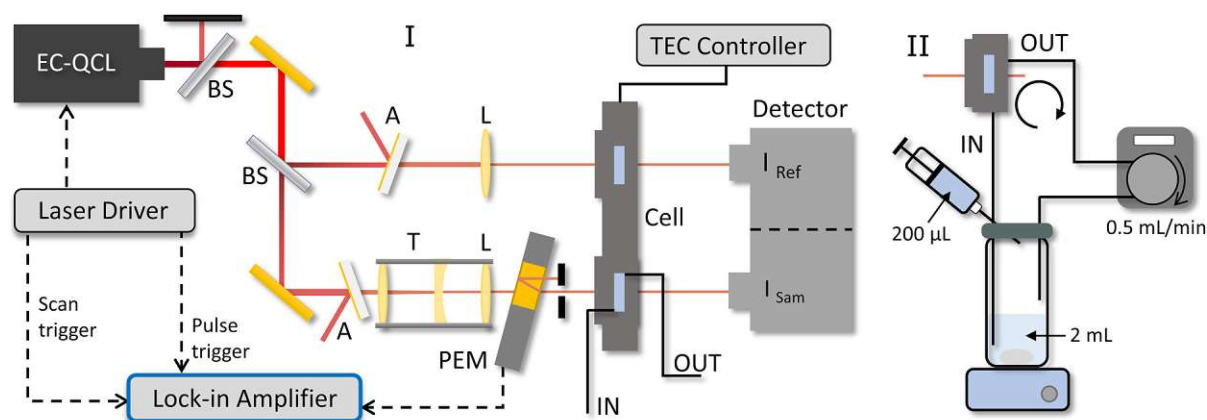


**Figure I.** (I) Optical setup used for this study. An EC-QCL is used as a light source, with beamsplitters (BS) and attenuators (A), as well as a telescope (T) and focusing lenses (L) encompassing the optical components. The analyte in solution is kept in a double-path transmission cell (Cell), a PEM and a detector are also incorporated. The dashed lines indicate coaxial cable connections, with the arrows indicating the direction. (II) Reservoir for the flow-through system, composed of a magnetic stirrer, a sealed glass vessel, a peristaltic pump, and a syringe for the addition of the opposite enantiomer.

of the MFLI, enabling reproducible spectral acquisition. The PEM driving amplitude was adjusted to lead to quarter wave retardation in the middle of the spectral range probed by the EC-QCL. Its trigger was also fed to another PLL routine of the MFLI, to ensure the phase-sensitive acquisition of its 42 kHz modulation cycle. The voltage outputs from the reference detector and the balanced output, generated by analog subtraction of the reference and signal detector output, were demodulated at 200 and 42 kHz. The data extracted at those frequencies correspond to the intensity of the laser after the sample,  $I$ , and the chirality-sensitive information introduced by the PEM's modulation  $\Delta I_{L-R}$ , respectively. The sampling rate of the lock-in amplifier was set relative to the scan speed of the laser to 6696 Sa/s. This resulted in a ratio of 10 data points per wavenumber, and with the chosen spectral range 1200 data points were collected per spectrum. The time constant of the lock-in amplifier was set relative to the sampling rate and was fixed to 745.8  $\mu$ s in this case, leading to a 3 dB attenuation at 92.8 Hz. While the  $\Delta I_{L-R}$  component, extracted from the balanced output, could be used as collected, the  $I$  component extracted from the same output needed correction. Since the balanced output corresponds to the difference between the two detectors, it must be offset to obtain a correct single-channel IR intensity spectrum. This was done by recording and storing the  $I$  signal from the reference output once each measurement day and adding this stored signal to each  $I$  spectrum collected from the balanced output. With this corrected  $I$  data and the simultaneously extracted  $\Delta I_{L-R}$  the VCD spectrum could be calculated according to

$$\text{VCD} = \frac{I}{\ln 10 \times J_1(\delta_{\text{PEM}})} \times \frac{\Delta I_{L-R}}{I} \quad (1)$$

with  $J_1$  being the first-order Bessel function and  $\delta_{\text{PEM}}$  being the retardation of the PEM relative to the transmitted wavenumber.

**Continuous Flow VCD Measurements.** For the closed flow cell experiments, 2 mL of S-BINOL at the chosen concentration (40 mM, 80 mM, or 100 mM) were aliquoted in a flask, which was clamped close to prevent evaporation of the solvent. Two Teflon tubes (0.5 mm inner diameter) were inserted through the clamp allowing for automated sampling from the flask and the return of the sample after having passed the flow cell. The solution was continuously mixed by a magnetic stirrer and pumped through the sample cell of the double path length transmission cell at a speed of 0.5 mL/min by means of a peristaltic pump. Following the measurement of this first spectrum, 200  $\mu$ L of R-BINOL, with the same concentration, was added to the flask via a syringe and circulated for 3 min to ensure a complete mixing. Then IR and VCD spectra were collected by averaging 700 scans between 1670 and 1550  $\text{cm}^{-1}$ , resulting in a measurement time of 2:44 min. This process of adding 200  $\mu$ L of R-BINOL,

3 min mixing, and spectra acquisition was repeated until the racemic mixture was reached in the flask, resulting in 11 data points for each experiment carried out for the respective starting concentration, with a spacing of around 6 min (3 min mixing + 2:44 min acquisition). The corresponding EE levels could be calculated according to

$$\text{EE}_i [\%] = \frac{c_S \times V_S - \sum_i c_R \times V_{\text{step}}}{c_S \times V_S + \sum_i c_R \times V_{\text{step}}} \times 100 \quad (2)$$

with  $c_S/c_R$  being the concentration of the S- or R-enantiomer, respectively,  $V_S$  being the volume of S-BINOL (2 mL throughout the monitoring),  $V_{\text{step}}$  being the volume of each step (200  $\mu$ L) and  $\sum_i c_R \times V_{\text{step}}$  therefore being the molar quantity of R-BINOL present in the mixture present after each injection step (the molar amount of S-BINOL does not change during the monitoring), resulting in the corresponding EE levels  $\text{EE}_i$ . Artifacts originating from birefringence in the optical train were reproducible enough to allow the baseline correction of both IR and VCD spectra by the pure solvent spectrum.

**Data Processing.** All data processing, including multivariate analysis, was performed in Python 3, utilizing the Scikit-Learn and SciPy modules, on the basis of in-house written routines.<sup>25,26</sup> While the data processing in the current case was done after the experiments to construct the calibration model, it can also be performed in parallel to the spectral acquisition. Loading the spectral data, performing the processing outlined in the following paragraphs, and applying the developed models take up around 21 ms, which is negligible in comparison to the time for acquiring a spectrum. The raw single channel spectra were low-pass filtered with a Whittaker–Eilers smoother (fourth-order, 3 dB attenuation at 3  $\text{cm}^{-1}$  resolution) resulting in a final resolution of 1.8  $\text{cm}^{-1}$ .<sup>27,28</sup> Due to baseline shifts over the course of the flow through experiments, the VCD spectra were corrected with asymmetrically reweighted penalized least squares smoothing.<sup>29</sup> Additionally, these spectra are convoluted with a fringe pattern in a similar intensity range to the spectral features. Due to this interference, we also applied a fast Fourier transform low-pass filter (cut off at 90 Hz) to preserve the original waveform while discarding interference fringes.

**Multivariate Analysis.** The data set generated by the monitoring experiments comprised three levels of concentrations, with 11 steps of EE changes each. To compare the different data sets, we transferred the EE levels of our observations to a different quantity, the difference in molar concentrations (difM), corresponding to the differences in concentration between the two enantiomers. This parameter considers the molar concentrations, is similar to the limit of detection used in classical absorption spectroscopy, and enables us to

combine the three monitoring runs to generate a data set spanning both different EE levels as well as different concentration levels. The conversion was done according to:

$$\text{difM [mM]} = \frac{\text{EE [\%]}}{100} \times c_{\text{BINOL}} [\text{mM}] \quad (3)$$

with  $c_{\text{BINOL}}$  being the concentration of BINOL (both enantiomers) present in the sample, which was taken from the absorbance spectrum of each observation. As a result, the data set for the multivariate analysis constituted a matrix of VCD spectra ( $33 \times 1200$ ) as an independent variable and a response vector of difM values ( $1 \times 33$ ). This data set was randomly split into a training and test set with a ratio of 26:7 (80:20 ratio) to assess the predictive capabilities of the generated models. Different chemometric models were evaluated and each model was optimized based on the root mean squared error of cross-validation (RMSECV), with a leave-one-out cross-validation (LOOCV) applied. First, a conventional partial least squares regression (PLSR) was constructed, with the spectral coverage limited to 1635 to 1560  $\text{cm}^{-1}$ , to increase the robustness of the model. The number of components was chosen to be 2, based on the minimal RMSECV. Another applied method was the least absolute shrinkage and selection operator (LASSO), which is a  $\ell_1$  regularization technique that implicitly performs feature selection when generating a regression curve. During the selection process, the coefficients of less important features are reduced to zero, resulting in few nonzero spectral features.<sup>30</sup> This method was also applied to a reduced spectral data set, restricted to the region between 1635 and 1560  $\text{cm}^{-1}$ . The relevant parameter in this is the penalty term  $\lambda$ , which was set based on the minimal RMSECV to  $1.42 \times 10^{-6}$ .

## Results and Discussion

**VCD Spectra of BINOL Mixtures.** The intensity of VCD signals depends on the concentration of the analyte as well as the EE of the mixture. As a consequence, it is to be expected that

the magnitude of the bands in VCD spectra collected during our simulated racemization decreases over time. This can be seen in Figure 2, which depicts the EE levels and concentrations. Both the EE levels and the concentration steps behave as expected, with a concentration and EE-dependent decrease in intensity for the BINOL signals. The quite significant signals around 1560  $\text{cm}^{-1}$  and below can be attributed to noise as a consequence of the low intensity and stability of the laser at the edge of its emission spectrum. The actual VCD signals are relatively weak compared to those normally presented for EE studies.<sup>31–33</sup> This is especially true for the 40 mM samples, and those spectra are therefore susceptible to interferences from spectral noise or artifacts. As can be seen in Figure S1 (Supplemental Material), the mentioned fringe pattern, while not high in amplitude in general, is still able to significantly interfere with the analyte spectra. We propose that these interference effects occur due to slight changes in path length during the pumping process, which does not occur for the reference cell. This difference is picked up by the balanced detection and transferred to the measurement. Since the reflectivity for  $\text{CaF}_2$  is comparatively weak ( $\sim 2.6\%$  at 6  $\mu\text{m}$  and normal incidence) the interference is also weak and not visible in the classical IR spectra. For the VCD spectra, however, which are also comparatively weak, this small interference becomes significant and necessitates removal during the preprocessing step. As can be seen in Fig. 2, this removal worked with varying success. However, while the intensity differences between the 40 mM spectra and the interference fringes are too small to enable complete removal, the spectra could still be used as the basis for a robust chemometric evaluation.

**Chemometric Evaluation.** While EE is an important quality parameter and is the quantification goal in this study as well, it was not chosen as the response variable for the chemometric evaluation. The presented spectra cover both different EE levels as well as different concentration ranges, making the combination of data sets not feasible without modification. One option would be the conversion of VCD

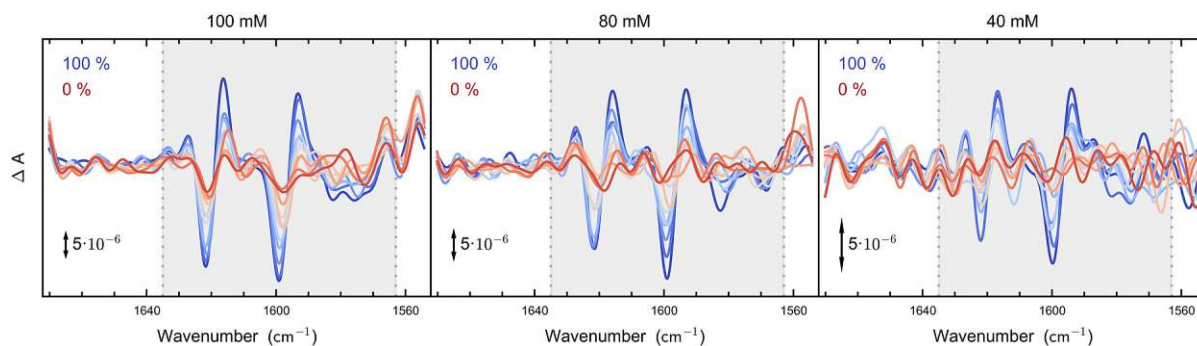


**Figure 2.** Baseline corrected and filtered VCD spectra for the chosen concentrations 100, 80, and 40 mM (left to right). The EE levels follow a trend from +100% (dark blue) to 0% (dark red). Black arrows indicate a  $\Delta\text{AU}$  value of  $5 \times 10^{-6}$ . The shaded area between the dotted lines indicates the spectral data used for the multivariate statistical evaluation (1635–1560  $\text{cm}^{-1}$ ).

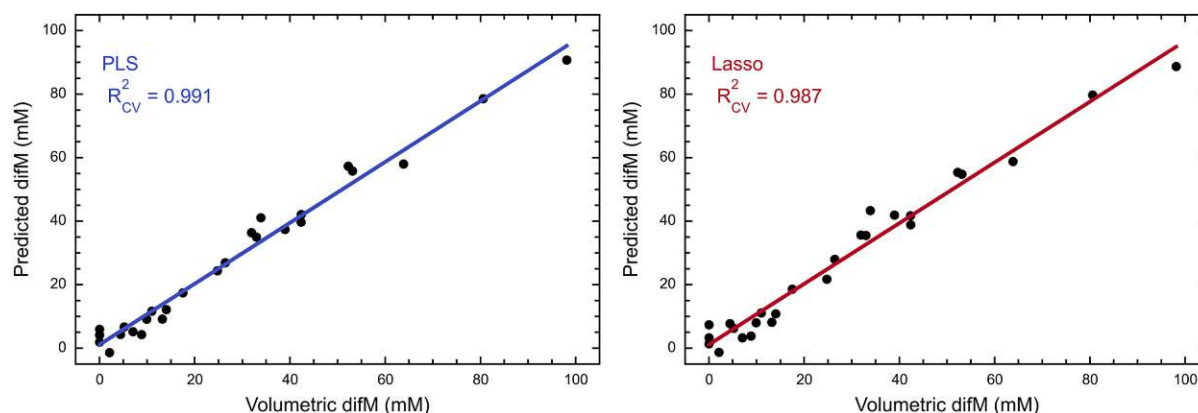


**Figure 3.** Cross-validated predicted enantiomeric differences versus volumetric (“real”) differences for PLS (left) and LASSO (right). The corresponding  $R^2$  are indicated in the figure.

spectra to dissymmetry factors, which normalizes the VCD intensities by the IR absorption.<sup>34</sup> A problem with this method is that the noise, which is not insignificant at these intensity levels, gets also amplified significantly. While there exist workflows to deal with this issue, those rely on a human-set threshold, introducing a bias into the model. Also, for the application of QCL-VCD toward monitoring, we aim to relate the prediction accuracy directly to the concentration of the analyte. This information is accessible via the IR absorbance on the same timescale as the VCD information, enabling the generation of a more flexible model. We therefore converted the EE levels to difM, molar differences between the different enantiomers, by the concentration taken from the IR absorbance spectra. Then the data sets were combined, resulting in a data set of 33 samples spanning different EE and concentration levels.

Both PLSR and LASSO rely on one customizable parameter during model building, called latent variables (LVs) and alpha, respectively. Both models were optimized by varying the respective parameters and assessing the model performance by the RMSECV, obtained by LOOCV. For both methods, an optimum model was selected (cf. Figure S2, Supplemental Material) and subsequently applied to the test set. The cross-validated prediction was assessed for conclusiveness by plotting the predicted and actual difM against each other, as can be seen in Figure 3, taking  $R^2$  as a figure of merit. While  $R^2$  for the partial least squares (PLS) model was marginally higher than the one for the LASSO model, the values indicate a high correlation and a significant predictive capability for both models.

Following this, the performance was further evaluated, with the results being compared in Table I. Both the difM and the % EE values were listed. The % EE was recovered from the difM values according to Eq. 3 for each used concentration.

When assessing a model for performance, one of the most important quality parameters is the presence of overfitting. Overfitting occurs, when the model relies significantly

**Table I.** Figures of merit for the PLS and LASSO models. The RMSECV and RMSEP are listed in both in mM and in % EE for better comparison to previous studies.

		PLS	LASSO
RMSECV	mM	2.8	3.4
	% EE	(2.8–7.0)	(3.4–8.4)
RMSEP	mM	3.5	3.6
	% EE	(3.5–8.8)	(3.6–9.0)

on small changes in the data, noise, or instrument-specific artifacts, for example, and is therefore not based on chemical reality, but on unspecific randomness in the data. In terms of figures of merit, overfitting manifests itself in a significant difference between the RMSECV and root mean squared error of prediction (RMSEP), since the model is too closely fitted to the training set. For both models built in this study, the RMSECV and RMSEP are closely matched, highlighting the high predictive accuracy and robustness of the models.

In general, the accuracy of the PLSR is higher than the LASSO model, providing excellent values for both RMSEP and RMSECV. Besides comparing the figures of merit, the loadings underlying the PLSR are of interest to ensure the chemical relevance of the chemometric evaluation. The corresponding loadings for LV 1 and LV 2 are plotted in Figure 4 against the spectral frequencies. When comparing the loadings, especially of LV 1, to the spectral bands the model relies on, also plotted in Figure 4, a close resemblance is apparent. For LV 2, this relationship is partially lost, but still, the correspondence of the loadings to the spectral data is clear. Overall, the model provides a robust and fast quantification of EE (or difM) in solution.

As for the LASSO model, its figures of merit, while not as excellent as the ones achieved for PLSR, still are satisfactory and indicate a good performance of the model. The difference between RMSECV and RMSEP is negligible, proving the robustness of the model for predictive purposes.

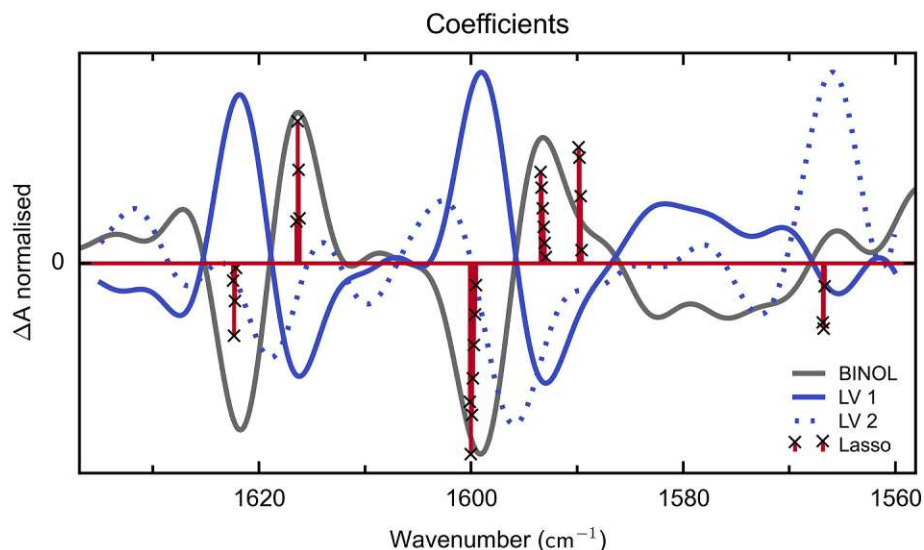


**Figure 4.** Normalized coefficients of the used model versus the spectral frequency (in wavenumbers). Both the loadings of the two LVs used for the PLS model and the coefficients of the LASSO model are plotted for comparison purposes. A normalized example spectra of BINOL (100 mM, 100% EE) was added to compare the generated coefficients to the spectral data.

Additionally, the penalizing scheme which is the basis for the LASSO model provides intriguing possibilities for QCL-VCD monitoring. As a consequence, the model relies only on a few discrete wavenumber positions, as can be seen in Figure 4. Both conventional FT-IR VCD instruments, which have simultaneous access to the whole MIR spectral range due to the Fellgett advantage, and tunable EC-QCL instruments can leverage PLSR to gain high sensitivity by relying on changes over multiple wavenumbers.<sup>35</sup> Additionally, instead of recording a continuous spectrum, the QCL can also be set to only measure at discrete wavelengths, further increasing the possible time resolution. By selecting these wavelengths based on a LASSO model, improved time resolution can be coupled with comparable predictive accuracy. Going further than that, by building on the information provided by LASSO new QCL-based chiral monitoring can be designed in a comprehensive way. Already commercially available systems such as QCL arrays or Vernier like QCL-Xt, can provide discrete wavelength emission spread over a larger wavelength area.<sup>36</sup> By careful wavelength selection those devices can be constructed with both high time resolution and high monitoring capabilities accessible.

## Conclusion

In this work, a comprehensive study on the application of EC-QCL-VCD for chiral monitoring was presented. The enantiomeric pair R/S-1,1'-bi-2-naphthol, a commonly used chiral scaffold, served as a model system. All spectra were recorded in a 160  $\mu\text{m}$   $\text{CaF}_2$  flow cell while pumping the sample at a flow rate of 0.5 mL/min. In the wavelength range accessible by the employed EC-QCL, the resulting VCD signals are in the order of  $1 \times 10^{-5}$ – $3 \times 10^{-5}$   $\Delta\text{AU}$ , which is on the lower

end of the typically studied signal heights. A flow-through system was set up and a series of EE levels were studied in a simulated racemization. In addition to the changes in chiral properties, the experiment also included different concentration levels, to observe the predictive capabilities of QCL-VCD with low-concentration samples. The molar difference in enantiomer concentrations was introduced as a way to generalize EE ratios for different overall concentrations of both enantiomers, providing a more flexible variable and the opportunity to combine the different data sets. Chemometric evaluation yielded RMSECV and RMSEP as low as 2.8% and 3.5% EE, respectively, highlighting the robust and accurate monitoring capability offered by QCL-VCD. In addition, evaluation by LASSO regression yielded a way to design optimized monitoring devices with selected wavelength coverage, offering even higher time resolution than the one already presented in this work.

At this point, it should be noted that this ability to sample a few, select wavelengths, is part of the advantage allowing EC-QCL-VCD to measure significantly faster than conventional FT-IR-VCD. While short measurement times are crucial in some applications, such as process analytical technologies (PAT) or reaction monitoring, in other applications (e.g., structural analytics of unknown compounds) broad spectral is more important. In these applications, FT-IR-VCD has a clear advantage over EC-QCL-VCD. Dispersive VCD, which uses a thermal source but no FT-IR, lies somewhat in between both techniques. Like EC-QCL-VCD, these instruments can restrict their spectral coverage to achieve higher throughput and/or higher sensitivity. Even though they are not in widespread use dispersive VCD instruments are still present in the VCD publication landscape.<sup>37,38</sup> Dedicated dispersive VCD instruments have proven their validity most prominently for the measurements

of biopolymers, as similarly to QCLs they can focus on a small spectral range, which is often enough for, i.e., protein analytics.<sup>39</sup> Additionally, it has to be said that for the available molecule, ECD could also be used as an analytical tool, as BINOL contains chromophores in the UV-Vis range. Due to its inherent differences in wavelength and energy of employed light, ECD can offer high signal-to-noise ratio data even at below-second resolution.<sup>40</sup> However, those high-speed monitoring schemes are restricted to single wavelength operations, consequently, the broader wavelength range available for EC-QCLs or even QCL arrays can offset this difference by relying on statistical evaluation. Also, ECD is only a direct competition with QCL-VCD if the analyte contains suitable chromophores, which is not a given for most molecules. Thus, even taking the above-mentioned limitations into account, we believe that just like QCLs have opened up new avenues of detection schemes, sensor design, and real-life applications for classical absorption spectroscopy, similar developments can be expected to follow for chiral analytics, especially considering the prevalent drive to miniaturize sensor equipment.<sup>22,41–44</sup> We anticipate that QCL-VCD can contribute favorably to chiral reaction monitoring and eventually control in the lab and PAT settings.

### Declaration of Conflicting Interests

The authors declared no potential conflicts of interest with respect to the research, authorship, and/or publication of this article.

### Funding

The authors disclosed receipt of the following financial support for the research, authorship, and/or publication of this article: This work was supported by the COMET Centre CHASE, funded within the COMET-Competence Centers for Excellent Technologies Programme by the BMK, the BMDW, and the Federal Provinces of Upper Austria and Vienna. The COMET Programme is managed by the Austrian Research Promotion Agency (FFG).

### ORCID iDs

Daniel-Ralph Hermann  <https://orcid.org/0000-0003-2605-8203>  
Bernhard Lendl  <https://orcid.org/0000-0003-3838-5842>

### Supplemental Material

All supplemental material mentioned in the text is available in the online version of the journal.

### References

1. B. Ranjbar, P. Gill. "Circular Dichroism Techniques: Biomolecular and Nanostructural Analyses: A Review". *Chem. Biol. Drug Des.* 2009. 74(2): 101–120.
2. F. Saito, P.R. Schreiner. "Determination of the Absolute Configurations of Chiral Alkanes: An Analysis of the Available Tools". *Eur. J. Org. Chem.* 2020. 2020(40): 6328–6339.
3. G. Hancu, A. Modroiu. "Chiral Switch: Between Therapeutical Benefit and Marketing Strategy". *Pharmaceuticals*. 2022. 15(2): 240.
4. J. Bogaerts, R. Aerts, T. Vermeyen, C. Johannessen, W. Herrebout, et al. "Tackling Stereochemistry in Drug Molecules with Vibrational Optical Activity". *Pharmaceuticals*. 2021. 14(9): 877.
5. E. Tokunaga, T. Yamamoto, E. Ito, N. Shibata. "Understanding the Thalidomide Chirality in Biological Processes by the Self-Disproportionation of Enantiomers". *Sci. Rep.* 2018. 8(1): 17131.
6. S.S. Wesolowski, D.E. Pivonka. "A Rapid Alternative to X-ray Crystallography for Chiral Determination: Case Studies of Vibrational Circular Dichroism (VCD) to Advance Drug Discovery Projects". *Bioorg. Med. Chem. Lett.* 2013. 23(14): 4019–4025.
7. P. Joseph-Nathan, B. Gordillo-Román. "Vibrational Circular Dichroism Absolute Configuration Determination of Natural Products". In: A.D. Kinghorn, H. Falk, J. Kobayashi, editors. *Progress in the Chemistry of Organic Natural Products* 100. Cham: Springer International Publishing, 2015. Pp. 311–452.
8. G.H. Wagnière. "On the Interaction of Light with Molecules: Pathways to the Theoretical Interpretation of Chiroptical Phenomena". In: N. Berova, P.L. Polavarapu, K. Nakanishi, R. W. Woody, editors. *Comprehensive Chiroptical Spectroscopy: Instrumentation, Methodologies, and Theoretical Simulations*. Chichester, UK: Wiley, 2011. Chap. 1, Pp. 1–34.
9. M. Krupová, J. Kessler, P. Bouř. "Recent Trends in Chiroptical Spectroscopy: Theory and Applications of Vibrational Circular Dichroism and Raman Optical Activity". *ChemPlusChem*. 2020. 85(3): 561–575.
10. M. Górecki, G. Groszek, J. Frelek. "Chirality Sensing of Bioactive Compounds with Amino Alcohol Unit via Circular Dichroism". *Chirality*. 2017. 29(10): 589–598.
11. T.J. Ward, K.D. Ward. "Chiral Separations: A Review of Current Topics and Trends". *Anal. Chem.* 2012. 84(2): 626–635.
12. D. Kourouski. "Advances of Vibrational Circular Dichroism (VCD) in Bioanalytical Chemistry: A Review". *Anal. Chim. Acta*. 2017. 990: 54–66.
13. J. Coates. "Interpretation of Infrared Spectra, a Practical Approach". In: R.A. Meyers, editor. *Encyclopedia of Analytical Chemistry: Applications, Theory, and Instrumentation*. Chichester, UK: John Wiley and Sons, 2006. P. A5606.
14. P.G. Rodríguez-Ortega, M. Sánchez-Valera, J.J. López-González, M. Montejo. "Fourier Transform Infrared Spectroscopy and Vibrational Circular Dichroism Assisted Elucidation of the Solution-State Supramolecular Speciation in Racemic and Enantiopure Ketoprofen". *Appl. Spectrosc.* 2022. 76(2): 216–227.
15. M. Pazderková, T. Pazderka, M. Shanmugasundaram, R.K. Dukor, et al. "Origin of Enhanced VCD in Amyloid Fibril Spectra: Effect of Deuteriation and pH". *Chirality*. 2017. 29(9): 469–475.
16. L.A. Nafie. "Vibrational Circular Dichroism: A New Tool for the Solution-State Determination of the Structure and Absolute Configuration of Chiral Natural Product Molecules". *Nat. Prod. Commun.* 2009. 3(3): 415–466.
17. J. Faist, F. Capasso, D.L. Sivco, C. Sirtori, et al. "Quantum Cascade Laser". *Science*. 1994. 264(5158): 553–556.
18. S. Freitag, M. Baer, L. Buntzoll, G. Ramer, A. Schwaighofer, et al. "Polarimetric Balanced Detection: Background-Free Mid-IR Evanescent Field Laser Spectroscopy for Low-Noise, Long-Term Stable Chemical Sensing". *ACS Sens.* 2021. 6(1): 35–42.
19. C.K. Akhgar, G. Ramer, M. Žbik, A. Trajnerowicz, et al. "The Next Generation of IR Spectroscopy: EC-QCL-Based Mid-IR

- Transmission Spectroscopy of Proteins with Balanced Detection". *Anal. Chem.* 2020. 92(14): 9901–9907.
20. A. Lambrecht, M. Pfeifer, W. Konz, J. Herbst, F. Axtmann. "Broadband Spectroscopy with External Cavity Quantum Cascade Lasers Beyond Conventional Absorption Measurements". *Analyst.* 2014. 139(9): 2070–2078.
  21. A. Rüther, M. Pfeifer, V.A. Lórenz-Fonfría, S. Lüdeke. "pH Titration Monitored by Quantum Cascade Laser-Based Vibrational Circular Dichroism". *J. Phys. Chem. B.* 2014. 118(14): 3941–3949.
  22. Y. Phal, K. Yeh, R. Bhargava. "Concurrent Vibrational Circular Dichroism Measurements with Infrared Spectroscopic Imaging". *Anal. Chem.* 2021. 93(3): 1294–1303.
  23. D.R. Hermann, G. Ramer, M. Kitzler-Zeiler, B. Lendl. "Quantum Cascade Laser-Based Vibrational Circular Dichroism Augmented by a Balanced Detection Scheme". *Anal. Chem.* 2022. 94(29): 10384–10390.
  24. Q. Wang, A. Pietropaolo, M. Fortino, Z. Song, et al. "Photo Racemization of 2,2'-Dihydroxy-1,1'-Binaphthyl Derivatives". *Chirality.* 2022. 34(2): 317–324.
  25. F. Pedregosa, G. Varoquaux, A. Gramfort, V. Michel, et al. "Scikit-Learn: Machine Learning in Python". *J. Mach. Learn. Res.* 2011. 12: 2825–2830.
  26. P. Virtanen, R. Gommers, T.E. Oliphant, M. Haberland, et al. "Scipy 1.0: Fundamental Algorithms for Scientific Computing in Python". *Nat. Methods.* 2020. 17(3): 261–272.
  27. P.H.C. Eilers. "A Perfect Smoother". *Anal. Chem.* 2003. 75(14): 3631–3636.
  28. M. Werts. "Whittaker-Eilers Smoother in Python". 2022. <https://github.com/mhvwerts/whittaker-eilers-smoother> [accessed Jan 17 2023].
  29. S.-J. Baek, A. Park, Y.-J. Ahn, J. Choo. "Baseline Correction Using Asymmetrically Reweighted Penalized Least Squares Smoothing". *Analyst.* 2015. 140(1): 250–257.
  30. R. Tibshirani. "Regression Shrinkage and Selection via the LASSO". *J. R. Stat. Soc. Ser. B Methodol.* 1996. 58(1): 267–288.
  31. C. Guo, R.D. Shah, R.K. Dukor, X. Cao, et al. "Determination of Enantiomeric Excess in Samples of Chiral Molecules Using Fourier Transform Vibrational Circular Dichroism Spectroscopy: Simulation of Real-Time Reaction Monitoring". *Anal. Chem.* 2004. 76(23): 6956–6966.
  32. M.P. Mower, D.G. Blackmond. "In-Situ Monitoring of Enantiomeric Excess During a Catalytic Kinetic Resolution". *ACS Catal.* 2018. 8(7): 5977–5982.
  33. M. Urbanová, V. Setnička, K. Volka. "Measurements of Concentration Dependence and Enantiomeric Purity of Terpene Solutions as a Test of a New Commercial VCD Spectrometer". *Chirality.* 2000. 12(4): 199–203.
  34. C.L. Covington, P.L. Polavarapu. "Similarity in Dissymmetry Factor Spectra: A Quantitative Measure of Comparison Between Experimental and Predicted Vibrational Circular Dichroism". *J. Phys. Chem. A.* 2013. 117(16): 3377–3386.
  35. T. Keiderling. "Instrumentation for Vibrational Circular Dichroism Spectroscopy: Method Comparison and Newer Developments". *Molecules.* 2018. 23(9): 2404.
  36. N. Villa, G. Strübi, T. Gresch, J. Butet, et al. "Quantum Cascade Lasers with Discrete and Non-Equidistant Extended Tuning Tailored by Simulated Annealing". *Opt. Express.* 2019. 27(19): 26701.
  37. P. Niederhafner, M. Šafařík, J. Neburková, T.A. Keiderling, et al. "Monitoring Peptide Tyrosine Nitration by Spectroscopic Methods". *Amino Acids.* 2021. 53(4): 517–532.
  38. A. Lakhani, P. Malon, T.A. Keiderling. "Comparison of Vibrational Circular Dichroism Instruments: Development of a New Dispersive VCD". *Appl. Spectrosc.* 2009. 63(7): 775–785.
  39. T.A. Keiderling, A. Lakhani. "Mini Review: Instrumentation for Vibrational Circular Dichroism Spectroscopy, Still a Role for Dispersive Instruments". *Chirality.* 2018. 30(3): 238–253.
  40. D. Leung, E.V. Anslyn. "Rapid Determination of Enantiomeric Excess of A-Chiral Cyclohexanones Using Circular Dichroism Spectroscopy". *Org. Lett.* 2011. 13(9): 2298–2301.
  41. A. Schwaighofer, M. Brandstetter, B. Lendl. "Quantum Cascade Lasers (QCLs) in Biomedical Spectroscopy". *Chem. Soc. Rev.* 2017. 46(19): 5903–5924.
  42. T. Lubinski, B. Plotka, S. Janik, L. Canini, W. Mantele. "Evaluation of a Novel Noninvasive Blood Glucose Monitor Based on Mid-Infrared Quantum Cascade Laser Technology and Photothermal Detection". *J. Diabetes Sci. Technol.* 2021. 15(1): 6–10.
  43. B. Hinkov, F. Pilat, L. Lux, P.L. Souza, et al. "A Mid-Infrared Lab-on-a-Chip for Dynamic Reaction Monitoring". *Nat. Commun.* 2022. 13(1): 4753.
  44. A. Ebner, R. Zimmerleiter, C. Cobet, K. Hingerl, et al. "Sub-Second Quantum Cascade Laser Based Infrared Spectroscopic Ellipsometry". *Opt. Lett.* 2019. 44(14): 3426.

### Publication III

#### **External cavity quantum cascade laser vibrational circular dichro-ism spectroscopy for fast and sensitive analysis of proteins at low concentrations**

Hermann, D.-R.; Ramer, G.; Lendl, B.

*Submitted to Analytical Chemistry* **2024**

# External cavity quantum cascade laser vibrational circular dichroism spectroscopy for fast and sensitive analysis of proteins at low concentrations

Daniel-Ralph Hermann, Georg Ramer and Bernhard Lendl\*

Research Division of Environmental Analytics, Process Analytics and Sensors, Institute of Chemical Technologies and Analytics, TU Wien, Getreidemarkt 9, 1060 Vienna, Austria

\*Email: bernhard.lendl@tuwien.ac.at

**ABSTRACT:** Proteins are characterized by their complex levels of structures, which in turn define their function. Understanding and evaluating these structures is therefore crucial to illuminating biological processes. One of the possible analytical methods is vibrational circular dichroism (VCD), which expands the structural sensitivity of classical IR absorbance spectroscopy by the chiral sensitivity of circular dichroism. While this technique is powerful, it is plagued by low signal intensities and long measurement times. Here we present an optical setup leveraging the high brilliance of a quantum cascade laser to measure proteins in D<sub>2</sub>O at a path length of 204  $\mu\text{m}$ . It was compared to classical Fourier-transform infrared spectroscopy (FT-IR) in terms of noise levels and in its applicability to secondary structure elucidation of proteins. Protein concentrations as low as 2 mg/mL were accessible by the laser-based system at a measurement time of 1 h. Further increase of the time resolution was possible by adapting the emission to cover only the amide I' band. This allowed for the collection of spectral data at a measurement time of 5 min without a loss of performance. With this high time resolution, we are confident that dynamic processes of protein can now be monitored by VCD, increasing our understanding of these reactions.

Asymmetric structures are a common occurrence across the chemical world, being present in small molecules up to large biological systems.<sup>1,2</sup> In the context of chemistry, asymmetry is part of the broader context of chirality, defined as the inability of a structure to be superimposed on its mirror image.<sup>3</sup> For small molecules, this quality results in the presence of enantiomers or diastereomers, depending on a change in rotation in one or more chiral centers respectively.<sup>4</sup> This quality also translates to biological systems, as e.g. proteinogenic amino acids in most organisms are made up exclusively of L-amino acids.<sup>5</sup> In addition to this fundamental level, the macromolecules formed by bio-polymers, e.g. proteins or nucleic acids, also present a form of chirality.<sup>6,7</sup> Based on the different side chains, the amino acids backbone arranges itself into either  $\alpha$ -helices,  $\beta$ -sheets, random coils and turn structures.<sup>8</sup> These secondary structures constitute the basis for the subsequent orientation into tertiary or even quaternary structures, which again define the function of the protein. Proteins operate for the most part either as biocatalysts, e.g. enzymes, or as receptors. Both types of reactions rely heavily on geometric recognition of the target molecule by the biopolymer, warranting a closer look on both structures.<sup>7</sup>

Consequently, both the analytics of chirality and specifically of protein structure are the target of intensive research.<sup>9,10</sup> Since proteins are mostly involved in chemical reactions, there is a need for analytics able to operate at high time resolution and with proteins in their natural environment, i.e. aqueous solutions.<sup>11,12</sup> Vibrational spectroscopy, specifically infrared

(IR) absorption spectroscopy satisfies this criteria and has been used to study proteins for decades now.<sup>13,14</sup>

IR spectroscopy relies on vibrational and rotational movements of molecules under excitation with light between 2.5 - 25  $\mu\text{m}$ , commonly collected by a Fourier transform infrared spectrometer (FT-IR).<sup>15</sup> Protein studies are based on vibrations occurring in their peptide backbone, with the most intense bands being the amide I and amide II bands.<sup>16</sup> The amide I band (1700-1600  $\text{cm}^{-1}$ ) mostly originates from the C=O stretching vibration and is predominantly used for structure assignment. In contrast, the amide II band (1600-1500  $\text{cm}^{-1}$ ) is a combination band of the N-H in plane bending and the C-N stretching vibrational modes.<sup>16</sup> The intensities, band shapes and peak maxima of these peaks change drastically as a consequence of the dipole-dipole interactions, hydrogen bonding arising from different secondary structure orientations. Therefore, the structure of the proteins can be assessed based on these characteristics, with increasing predication accuracy achieved by chemometric evaluation (Partial-least squares, multivariate curve resolutions-alternating least-squares or band fitting).<sup>8,17-19</sup>

If more in depth information is necessary, the method of classical IR absorption spectroscopy can be augmented by including a polarization modulation scheme.<sup>20,21</sup> By generating alternately left and right handed circularly polarized light and calculating the difference in absorbance between them vibrational circular dichroism (VCD) can be measured. Chiral structures exhibit substantially different VCD signals, e.g.

enantiomers lead to bands with opposite signs. VCD is therefore capable of determining the absolute configuration of small molecules in solution, leading to its broad usage in the pharmaceutical industry.<sup>22,23</sup> While such a clear assignment is of course impossible for proteins, the added chiral dimension can improve the prediction accuracy for secondary structure determination.<sup>6,12</sup>

Protein VCD signals are located in the same region as their IR absorbance counterparts, but are characterized by sharper bands, and the occurrence of both positive and negative peaks. Unfortunately, VCD signals also differ from their parent absorbance band by a decrease in intensity of  $\sim 10^{-4}$ , necessitating low noise and therefore time-consuming spectral acquisitions up to 12 h. In an effort to keep the routine measurement time down to a few hours, VCD spectra of biomolecules are generally collected at a spectral resolution of  $8\text{ cm}^{-1}$ , allowing for faster scan acquisition times in an FT-IR instrument.<sup>24–26</sup>

For protein structure analytics the low signal intensities of VCD are exacerbated by the interfering absorption of the HOH-bending vibration of water at  $\sim 1643\text{ cm}^{-1}$ .<sup>16,17</sup> The resulting decrease in spectral throughput limits the useable optical pathlength for classical FT-IR spectroscopy to  $<10\text{ }\mu\text{m}$  and for FT-IR VCD studies to  $\sim 6\text{ }\mu\text{m}$ , with correspondingly high concentrations  $> 100\text{ mg/mL}$  for VCD measurements.<sup>17,25,26</sup> This can lead to problems with solubility and crowding effects, making VCD protein studies challenging. One way around this problem is to replace  $\text{H}_2\text{O}$  by  $\text{D}_2\text{O}$ , since the higher mass of deuterium shifts the bending vibration to  $1200\text{ cm}^{-1}$ , leaving the amide bands unobstructed.<sup>10</sup> Consequently pathlengths between  $25$  and  $50\text{ }\mu\text{m}$  can be routinely used for protein VCD studies in  $\text{D}_2\text{O}$ .<sup>26–29</sup>

Besides changing the experimental conditions, the use of a more intense light source can offset the high absorbance of  $\text{H}_2\text{O}$ . In the mid-IR range, this became possible with the development of quantum cascade lasers (QCL). By relying on inter sub band transitions as opposed to the interband transitions underlying classical laser designs, QCLs emit high power, highly polarized light tunable over the infrared spectral region.<sup>30,31</sup> Modern external cavity QCLs (EC-QCL) incorporate a grating, allowing for a coverage of up to  $500\text{ cm}^{-1}$  by a single chip laser. This broad coverage also makes protein IR studies possible, with the high power of the laser facilitating the use of higher pathlengths. Indeed, laser-based IR spectrometers were employed for protein structure analytics in  $\text{H}_2\text{O}$  ( $\sim 25\text{ }\mu\text{m}$  pathlength) and  $\text{D}_2\text{O}$  ( $\sim 478\text{ }\mu\text{m}$ ) at comparatively low concentrations.<sup>10,11,17</sup>

The use of QCLs for VCD spectral acquisition was first reported in 2011 for small molecules in  $\text{CDCl}_3$  and  $\text{H}_2\text{O}$  between  $1320$  and  $1220\text{ cm}^{-1}$ .<sup>32</sup> However, QCL-VCD remained a niche application and failed to outperform FT-IR VCD spectrometer in terms of signal to noise levels. Beginning with 2020, renewed interest led to a number of publications on the subject from multiple groups.<sup>33–36</sup> These outlined more evolved optical design, e.g. QCL-VCD microscopy, and also contained some studies on peptides in  $\text{H}_2\text{O}$  and  $\text{D}_2\text{O}$  at  $25\text{ }\mu\text{m}$ , although with no accessible amide I VCD vibration. Furthermore, it was finally possible to outperform FT-IR VCD in terms of signal to noise ratio, by means of balanced detection. This scheme is used to compensate for the pulse-to-pulse fluctuations and  $1/f$  noise originating in the laser.<sup>35,37</sup>

Building upon the recent advancements, we present a balanced detection QCL based instrument for VCD measurements of low concentrated proteins in  $\text{D}_2\text{O}$ . The acquired spectra are compared in terms of noise and band position with reference FT-IR VCD spectra. The accessible concentration range for the  $204\text{ }\mu\text{m}$  pathlength cell is evaluated and proteins comprised of different secondary structures are compared. Additionally, further possible improvements of time resolution and sensitivity are discussed.

## Experimental

**Instrumental Setup** The reference FT-IR VCD and absorbance spectra were collected with a Vertex 70v spectrometer equipped with a PMA50 accessory (both Bruker, Germany), containing a  $42\text{ kHz}$  photoelastic modulator (PEM, Hinds Instruments, USA), set to a phase shift of  $0.5\pi$  at  $1555\text{ cm}^{-1}$ . A low-pass filter (cut-off:  $1828\text{ cm}^{-1}$ ) was placed before the linear polarizer and a resolution of  $8\text{ cm}^{-1}$  was used for both absorbance and VCD spectra. The samples were placed in a  $23\text{ }\mu\text{m}$  pathlength cell with  $\text{CaF}_2$  windows and spectra were collected for  $1\text{ h}$ .

The laser-based instrument used for this study is an optical setup developed specifically for low noise QCL-VCD measurements. It is based on an iteration of our previously published balanced detection system and can be seen in Figure 1.<sup>35</sup>

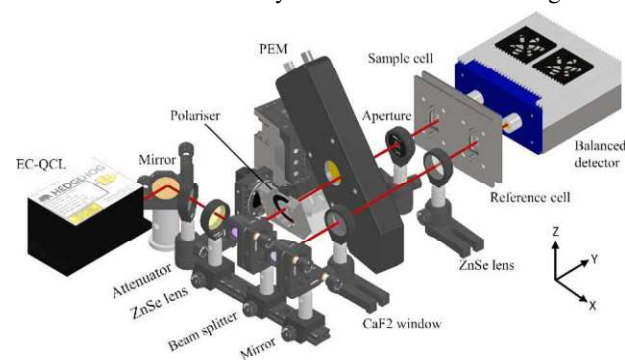


Figure 1. Optical setup used for the QCL-VCD measurements of proteins in  $\text{D}_2\text{O}$ .

An EC-QCL (Daylight Solutions Inc. USA) tunable between  $1360$  and  $1760\text{ cm}^{-1}$  and operated at  $860\text{ mA}$  provided the high-power IR light used for the measurements. It was operated at  $400\text{ kHz}$  pulse repetition rate with a pulse duration of  $700\text{ ns}$  and set to a temperature of  $19\text{ }^\circ\text{C}$ . Excess heat was removed by a liquid cooling system. Following redirection by a gold mirror, the laser light was attenuated by a reflective attenuator (gold sputtered  $\text{CaF}_2$  window). This attenuation was necessary in order to keep the laser intensity in the linear range of the detector. An attenuation of the laser intensity by reducing the laser current was not a valid alternative, as this would have resulted in a limited spectral range.

Subsequently, the laser beam was focused on the sample cell by means of a  $200\text{ mm}$  ZnSe lens (AR coated, Thorlabs Inc., USA). After the lens, the beam was directed onto a  $\text{CaF}_2$  beam splitter (Thorlabs Inc., USA), with the reflected and transmitted beam designated the sample and reference beam respectively. The transmitted beam was directed through an angled  $\text{CaF}_2$  window, acting as an attenuator, and

refocused by a 50 mm ZnSe lens. This was done to keep the intensity reaching the reference detector as equal as possible to the one for the sample detector over the whole tuning range.

The sample beam on the other hand first passed a KRS-5 wire grid polariser (1:300 extinction, Optometrics, USA), used to improve the polarization purity of the laser emission. This was necessary since closer inspection of the laser's polarization, see Figure S1, revealed an elliptic polarization with vertical orientation. The polarizer was tilted around the X-axis by 35°, reducing the reflection for the vertically oriented laser emission according to the Fresnel equations. This was done to reduce interference effects arising from the coherent laser beam. Subsequently a PEM was placed in the sample beam. This optical element modulated the polarization at a frequency of 50 kHz and was set to  $0.5\pi$  at 1555 cm<sup>-1</sup>. The PEM was tilted by 10° around the Z-axis, to shift the reflected beam from the transmitted one. The beam diameter reduction by the ZnSe lens enabled the complete separation of the beams, with the reflected beam being blocked by a 1 mm aperture (Thorlabs Inc., USA).

After passing the sample and reference cell, both at 204 μm, the respective beams were collected by the balanced detection module (VIGO Photonics S.A., Poland). The detector elements were thermoelectrically cooled to 201 K and closely matched in their detectivity. The optical setup was built on a temperature stabilized breadboard (300x450 mm, Thorlabs Inc, USA) set to 22 °C, which approximately corresponded to room temperature. Furthermore, it was enclosed in an acrylic glass housing and flushed with dry air to prevent water vapor interference.

**Data acquisition** To extract the correct intensities corresponding to the laser and VCD channel respectively phase sensitive detection was implemented by a MFLI lock-in amplifier (with the F5M and MD extensions, Zurich instruments, Switzerland). The reference signal from the PEM controller was fed to the trigger input of the MFLI and one oscillator was set to the 8<sup>th</sup> harmonic (400 kHz) of this signal, with the corresponding demodulator outputting a reference signal at this frequency. This signal was used to time the laser pulsing scheme in reference to the PEM modulation cycle, enabling the utilization of 25 % of the laser intensity at the maximum of the PEM cycle, see Figure S2. The high duty cycle of 28 % ensured efficient detection by the lock-in amplifier. A scan trigger connected the laser controller to the MFLI, enabling the referencing of the data acquisition to the spectral sweep.

During the spectral acquisition, the balanced detector signal was collected. This signal is the result of the subtraction between the sample and reference detector, providing the noise reduction characteristic for balanced detection. The collected signal was demodulated at the PEM's fundamental frequency ( $I_{PEM}^B(\bar{\nu})$ ) and its 8<sup>th</sup> harmonic ( $I_{Laser}^B(\bar{\nu})$ ). Once before the measurement, the reference detector signal ( $I_{Laser}^R(\bar{\nu})$ ) is collected to provide an offset for the balanced detector signal. The VCD signal as a function of the wavenumber ( $\bar{\nu}$ ) can then be calculated according to:

$$\Delta A(\bar{\nu}) = \frac{1}{J_1[\alpha_M^0(\bar{\nu})] \log 10} \left[ \frac{I_{PEM}^B(\bar{\nu})}{I_{Laser}^B(\bar{\nu}) + I_{Laser}^R(\bar{\nu})} \right] \quad (1)$$

with  $J_1[\alpha_M^0(\bar{\nu})]$  being the first order Bessel function, its argument is the amplitude of the phase shift applied by the PEM [ $\alpha_M^0(\bar{\nu})$ ].

For this study, the laser was continuously sweeping between 1400-1710 cm<sup>-1</sup> or 1580-1710 cm<sup>-1</sup> at a speed of 40 cm<sup>-1</sup>/s, and the signal was collected at 838 Sa/s (~20 samples/cm<sup>-1</sup>). For each covered area, the number of sweeps per scan were set to result in 5 minutes of acquisition time

**Data acquisition** Both the FT-IR and QCL-VCD scans were baseline corrected to compensate for drifts before averaging.<sup>38</sup> The QCL-VCD spectra were collected at an unfiltered resolution of 0.5 cm<sup>-1</sup> and were smoothed by fitting a 3<sup>rd</sup> order spline to match the 8 cm<sup>-1</sup> resolution of the FT-IR spectra.<sup>39</sup> Both the absorbance and VCD spectra were corrected by the D<sub>2</sub>O background.

**Chemicals and sample preparation** Bovine serum albumin (BSA, purity ≥ 98 %), lysozyme from hen egg white, β-lactoglobulin from bovine milk (purity ≥ 90 %) and D<sub>2</sub>O (99.9 % D) were purchased from Sigma Aldrich and used as received. The analytes were dissolved in the appropriate volume of D<sub>2</sub>O and used in a timely manner. For the comparison spectra, the concentration for FT-IR VCD was prepared and an aliquot was diluted for the QCL-VCD measurements. For the BSA calibration curve, a stock solution of 48 mg/mL was diluted according to the desired concentration. Around 100 and 300 μL of the prepared solutions were used to fill the FT-IR and QCL cells respectively.

## Results and discussion

**Noise comparison** Before actual protein VCD measurements the noise floor for the QCL setup had to be evaluated. For this purpose, 24 D<sub>2</sub>O scans at 5 min each were collected for each system and the dataset was split in half to generate a background and a sample block. The difference between the background and sample spectra was calculated for an increasing number of averages. The resulting root mean square error (RMS) against the measurement time can be seen in Figure 2, plotted at the native QCL resolution and at different smoothing settings. At the native QCL resolution of 0.5 cm<sup>-1</sup>, the spectra are quite noisy due to an overlaying interference pattern originating in the wire grid polarizer, see also Figure S3.

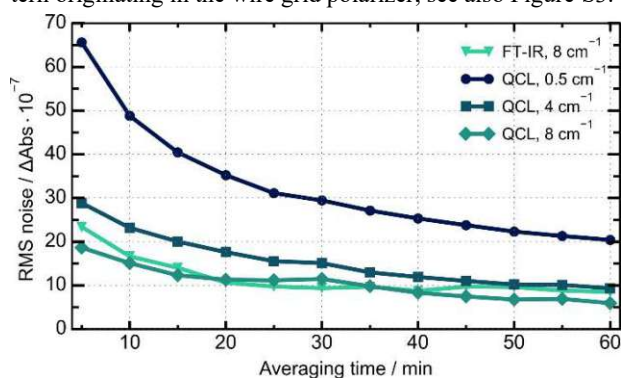


Figure 2. Root mean square (RMS) noise as a function of measurement time for the FT-IR VCD spectra and the QCL-VCD spectra at different smoothing settings. The data was calculated for the area between 1405 and 1705 cm<sup>-1</sup>.

Subsequent smoothing to a resolution of  $4\text{ cm}^{-1}$  and  $8\text{ cm}^{-1}$  respectively removed the distortions and the noise floor approached the FT-IR level. Indeed, at the maximum averaging time of 60 minutes the noise levels are at the same level, with a slight advantage for the QCL when compared to the FT-IR at the same resolution. Therefore, we could assume that the spectra collected on both instruments are of comparable quality. Additionally, the higher pathlength used during the EC-QCL VCD measurements ( $204\text{ }\mu\text{m}$  vs  $23\text{ }\mu\text{m}$ ) should translate to a higher signal to noise (SNR) by a factor of approx. 9. Consequently, a more encompassing comparison between FT-IR VCD and QCL-VCD for protein studies could be performed.

To evaluate the resolving power of the system in terms of secondary structure determination, three proteins were selected for measurement. Bovine serum albumin is composed mainly of  $\alpha$ -helices, with no  $\beta$ -sheet contributions. Lysozyme in contrast is a combination of  $\alpha$ -helices and turn structures, with a small fraction of  $\beta$ -sheet. The last protein studied is  $\beta$ -lactoglobulin, a milk protein composed of a mixture of  $\alpha$ -helices and  $\beta$ -sheets<sup>9,20</sup>

For the FT-IR samples, a concentration of  $60\text{ mg/mL}$  was chosen, to ensure an adequate solubility for all protein samples. The QCL samples were diluted to  $8\text{ mg/mL}$  to ensure a better comparison, since with the higher pathlength of this system a concentration of  $60\text{ mg/mL}$  would lead to total absorption. The spectra for both systems were collected for 1 h and are depicted in Figure 3 A and B for the QCL and FT-IR system respectively.

When comparing the classical absorbance spectra between the proteins, there are some differences for the amide bands. Due to the vibrations, it is based on, the amide II band also shifts alongside the  $\text{H}_2\text{O}$ - $\text{D}_2\text{O}$  shift. Consequently, the amide II area is less useful for evaluation, since it is influenced by the degree of deuteration achieved for the proteins. In addition,

due to the hygroscopic nature of  $\text{D}_2\text{O}$  a DOH-bending vibration can occur at  $\sim 1455\text{ cm}^{-1}$ , which distorts this spectral region.<sup>40</sup> This is most probable the origin of the shift in intensity at the amide II' region which translates also to the VCD spectra. We will therefore focus on the amide I' band for the purpose of this study.

For the amide I' band of both BSA and lysozyme the band maximum lies at  $\sim 1649\text{ cm}^{-1}$ , with the only difference being a difference in intensity. These characteristics are present in both systems used and also agree well with literature values.<sup>9,26</sup> In contrast, the  $\beta$ -lactoglobulin band maxima is shifted to  $\sim 1636\text{ cm}^{-1}$ , with a slight shoulder at  $\sim 1652\text{ cm}^{-1}$ , which again agrees well with literature.<sup>11,41</sup> So, while the spectra agree well with expectations, a difference according to secondary structure components cannot be easily assigned, at least between lysozyme and BSA.

This is different when the focus is switched to the corresponding amide I' VCD bands. For BSA, a strong couplet between  $1662$  and  $1648\text{ cm}^{-1}$  can be found in both systems. In addition, the deuteration of the protein leads to a sideband at  $1628\text{ cm}^{-1}$ .<sup>20</sup> A difference between the systems can be observed for the relative height of the positive band, which we attribute to shifts arising from the baseline correction and calibration.

As for the lysozyme band shape, it exhibits two negative peaks at  $1660$  and  $1635\text{ cm}^{-1}$ . Again, the difference in intensity varies between the systems, which can be attributed to the sensitivity of lysozyme to incomplete deuteration.<sup>26</sup>

The amide I' band of  $\beta$ -lactoglobulin contains a characteristic set of peaks, with one small negative band at  $1660\text{ cm}^{-1}$ , a positive band at  $1638\text{ cm}^{-1}$  and one strong negative band at  $1621\text{ cm}^{-1}$ . These bands agree well between the systems as well as with literature values.<sup>42</sup>

For the sample set of proteins, the different combinations of

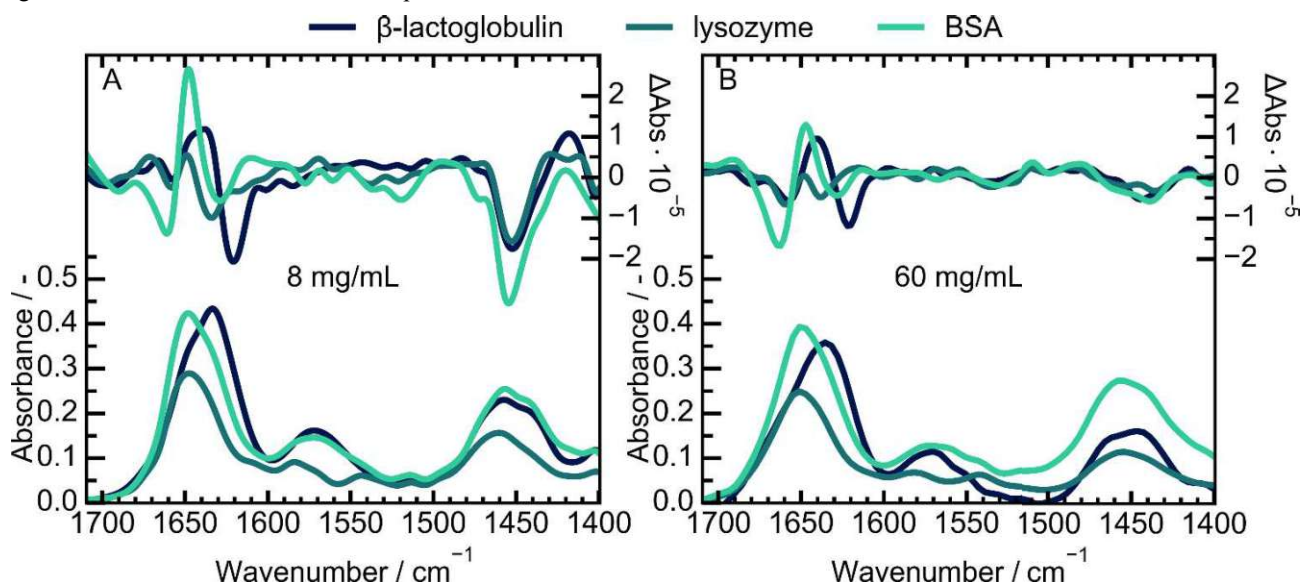


Figure 1. Absorbance and VCD spectra of  $\beta$ -lactoglobulin, lysozyme and bovine serum albumin (BSA) in  $\text{D}_2\text{O}$ . The spectra were collected with the QCL-VCD setup (A) at a concentration of  $8\text{ mg/mL}$  and a commercial FT-IR VCD spectrometer at a concentration of  $60\text{ mg/mL}$  (B).

secondary structures led to characteristic peaks in the VCD amide I' bands. In contrast, the assignment based on amide I' absorbance data was less conclusive. This is also true for the QCL-VCD spectra, which matches the FT-IR reference spectra well and allows for the evaluation of protein VCD bands at a concentration of 8 mg/mL within 1 h of measurement time.

**Accessible concentration range** With the validity of QCL-VCD protein spectra confirmed against FT-IR reference measurements, the sensitivity of the system needs to be evaluated. For this purpose, a dilution series of BSA in D<sub>2</sub>O was prepared and the measurement time was again 1 h. The concentrations ranged from 2-14 mg/mL, corresponding to maximum absorbance values between 0.08 and 0.78. Figure 4 depicts the resulting VCD spectra and their corresponding absorbance spectra. The intensity of the amide I' absorbance and VCD band follows a linear relationship against the concentration even down to 2 mg/mL. With the resulting linear fit, see Figure S4, the limit of detection (LOD), corresponding to a SNR of 3, could be estimated. For the noise ( $5.93 \cdot 10^{-7} \Delta\text{AU}$ ) at the used 1 h acquisition time, this results in a LOD of 0.32 mg/mL. An improvement of this value is possible by increasing the number of averaged spectra, reducing the noise in the process. Alternatively, the signal could be increased by increasing the pathlength of the transmission cell. This constitutes a promising approach, as for classical IR absorbance studies pathlengths of up to 478  $\mu\text{m}$  have been reported.<sup>10</sup> However, this was not feasible for this study, as D<sub>2</sub>O shows a small absorption feature  $\sim 1550 \text{ cm}^{-1}$ , which is compounded to a significant decrease of the laser intensity over a broad area, see Figure S5. Since the maxima of the laser spectral emission profile lie outside of this area, this high absorbance could not be adequately compensated.

Even so, the shown performance benefits quite substantially from the longer path length available for QCL-VCD studies. Comparatively low concentrated samples could be measured and their VCD bands were well resolved.

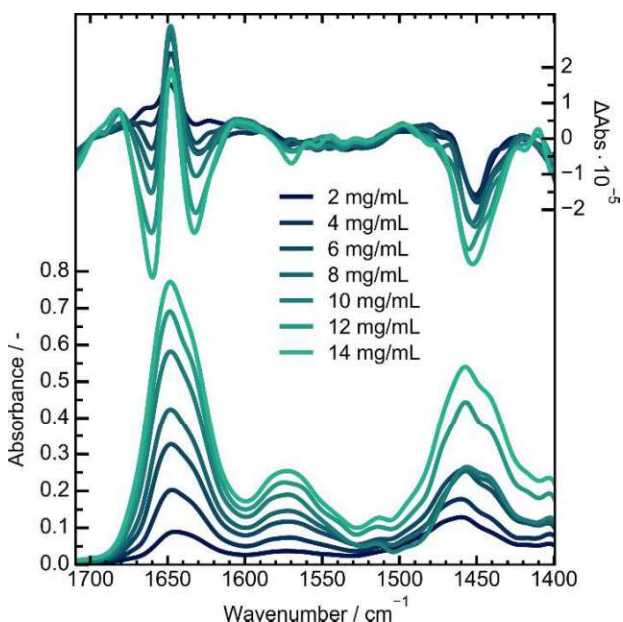


Figure 4. VCD and IR absorbance spectra collected for BSA in D<sub>2</sub>O in varying concentrations.

**Further improvements of acquisition speeds** With the performance of the system for broadband spectral acquisition of proteins in D<sub>2</sub>O established, the possibility of even faster acquisition speeds was explored. EC-QCL instruments scan over their accessible wavelength range by changing the angle of an internal grating. Therefore, the spectral information is gathered as a function of time and the measurement time is directly proportional to the spectral coverage. One can make use of this characteristic if only a few spectral features contain the necessary information, e.g. protein studies. Since most studies of secondary structure evaluation base their analysis on the amide I' absorbance and VCD bands, data containing only these bands should be sufficient.<sup>10,18,20,26</sup>

Following this logic, we let the laser sweep between 1710-1580  $\text{cm}^{-1}$ , covering the amide I' band and some additional baseline on both sides. This enabled the collection of more spectra per unit of time, reducing the noise as consequence of the increased number of averaged scans. A comparison of the noise levels for D<sub>2</sub>O spectra, see Figure S 6, confirmed this expectation. Noise level improvements were observed down to  $2.73 \cdot 10^{-7} \Delta\text{AU}$  for the tested maximum acquisition time of 30 minutes. However, even for 5 minutes of spectral averaging the noise level was deemed sufficient for protein measurements. deemed sufficient

For these measurements, 10 mg/mL solutions each of the studied proteins were prepared. This concentration was chosen to better represent a typical VCD experiment, where the desired absorbance lies between 0.4 and 0.8 AU. Figure 5 depicts the collected IR and VCD measurements for 5 minutes of averaging. The spectral features are well resolved, even for the low intensity signals of lysozyme. The influence of the secondary structure on the corresponding VCD bands is again visible and corresponds well to the broadband data. Accord-

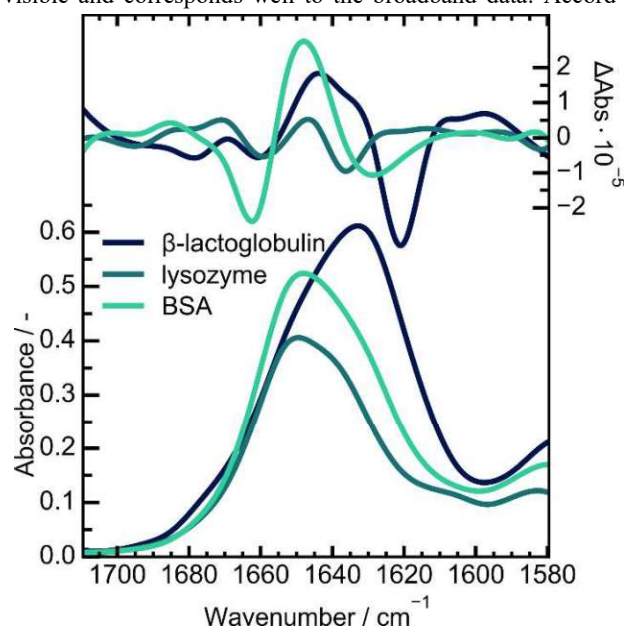


Figure 2. IR absorbance and VCD spectra of 10 mg/mL of  $\beta$ -lactoglobulin, lysozyme and BSA in D<sub>2</sub>O. The spectra were acquired between 1710 and 1580  $\text{cm}^{-1}$  after a measurement time of 5 min.

ingly, it can be said that protein studies in D<sub>2</sub>O can be performed at 5 minutes of measurement time at adequate noise levels, if the information contained in the amide I' band is

## Conclusion

In conclusion, EC-QCL based analysis of proteins in D<sub>2</sub>O enabled the use of a comparatively long pathlength, making lower concentrations of proteins accessible to evaluation by VCD. The achieved noise for the spectral range between 1400–1710 cm<sup>-1</sup> was comparable to the noise floor of FT-IR for the same measurement time. The increased analyte signal due to the longer pathlength allowed for LOD values of 0.32 mg/mL at measurement times of 1 h. At this measurement time, it was also possible to discriminate the influence of different secondary structure composition on the VCD bands.

Further reduction of the measurement time was made possible by adjusting the laser to only cover the spectral range between 1580–1710 cm<sup>-1</sup>. With this mode of operation, the amide I' VCD band of different proteins could be resolved even at 5 min of acquisition time. This opens up applications of VCD to support classical absorbance studies like thermal stability investigations by providing additional chiral information at similar time scales.<sup>10,42</sup>

For the sake of completeness, it has to be said that the advantages of QCLs demonstrated here can be most efficiently leveraged when a small and well-defined spectral area is of interest, e.g. amide bands of proteins. For more complicated sample-matrix systems or more in-depth studies the broad coverage offered by FT-IR VCD instruments still has the upper hand in the foreseeable future. Furthermore, a chip with a maximum emission near 1555 cm<sup>-1</sup> would increase the spectral throughput, allowing for an even longer pathlength and increased sensitivity.

Nevertheless, we believe that the system shown here, and the data generated is proof of the utility of EC-QCL VCD for biomolecules. Especially for protein studies, often times only a small spectral area carries sufficient information, and high sensitivity and high time resolution are more important than broad applicability. This is specifically the advantage our EC-QCL VCD system enjoys over commercial instruments. We believe this can be leveraged to provide additional information compared to classical IR absorbance evaluation of proteins.

## ASSOCIATED CONTENT

### Supporting Information

The Supporting Information is available free of charge on the ACS Publications website.

Stokes parameters of the laser source (Figure S 1), digitized detector signal (Figure S 2), Unfiltered baseline (Figure S 3), Calibration lines for BSA in D<sub>2</sub>O (Figure S 4), D<sub>2</sub>O absorbance and laser emission spectrum (Figure S 5), RMS noise against measurement time (Figure S 6) (PDF)

### Data availability

The experimental data and corresponding data evaluation is available on Zenodo in the form of a Docker container.

## AUTHOR INFORMATION

### Corresponding Author

**Bernhard Lendl** – *Institute of Chemical Technologies and Analytics, TU Wien, 1060 Vienna, Austria; orcid.org/0000-0003-3838-5842; Email: bernhard.lendl@tuwien.ac.at*

### Authors

**Daniel-Ralph Hermann** – *Institute of Chemical Technologies and Analytics, TU Wien, 1060 Vienna, Austria; orcid.org/0000-0003-2605-8203*

**Georg Ramer** – *Institute of Chemical Technologies and Analytics, TU Wien, 1060 Vienna, Austria; orcid.org/0000-0001-8307-5435*

### Author Contributions

**Daniel-Ralph Hermann:** investigation, formal analysis, visualization, writing – original draft. **Georg Ramer:** writing – reviewing and editing, Supervision, conceptualization. **Bernhard Lendl:** Supervision, writing – reviewing and editing, project administration, funding acquisition, conceptualization. All authors have given approval to the final version of the manuscript.

### Notes

The authors declare no competing financial interest.

## ACKNOWLEDGMENT

This work has received funding by the Austrian Wirtschaftsservice (AWS, project no. P2389335). The authors acknowledge TU Wien Bibliothek for financial support through its Open Access Funding Programme.

## REFERENCES

- (1) Kurouski, D. Advances of Vibrational Circular Dichroism (VCD) in Bioanalytical Chemistry. A Review. *Analytica Chimica Acta* **2017**, *990*, 54–66. <https://doi.org/10.1016/j.aca.2017.08.014>.
- (2) Knoppe, S.; Bürgi, T. Chirality in Thiolate-Protected Gold Clusters. *Acc. Chem. Res.* **2014**, *47* (4), 1318–1326. <https://doi.org/10.1021/ar400295d>.
- (3) *The IUPAC Compendium of Chemical Terminology: The Gold Book*, 4th ed.; Gold, V., Ed.; International Union of Pure and Applied Chemistry (IUPAC): Research Triangle Park, NC, 2019. <https://doi.org/10.1351/goldbook>.
- (4) Sen, A.; Bouchet, A.; Lepère, V.; Le Barbu-Debus, K.; Scuderi, D.; Piuze, F.; Zehnacker-Rentien, A. Conformational Analysis of Quinine and Its Pseudo Enantiomer Quinidine: A Combined Jet-Cooled Spectroscopy and Vibrational Circular Dichroism Study. *J. Phys. Chem. A* **2012**, *116* (32), 8334–8344. <https://doi.org/10.1021/jp3047888>.
- (5) Hancu, G.; Modroiu, A. Chiral Switch: Between Therapeutic Benefit and Marketing Strategy. *Pharmaceuticals* **2022**, *15* (2), 240. <https://doi.org/10.3390/ph15020240>.
- (6) Hilario, J.; Kubelka, J.; Keiderling, T. Vibrational Circular Dichroism of Biopolymers: Summary of Methods and Applications. In *Vibrational Spectroscopy of Biological and Polymeric Materials*; Braiman, M., Gregoriou, V., Eds.; CRC Press, 2005; pp 253–324. <https://doi.org/10.1201/9781420027549.ch6>.
- (7) Barron, L. D. “A Careful Disorderliness” in Biomolecular Structure Revealed by Raman Optical Activity. *Spectrochimica Acta Part A: Molecular and Biomolecular Spectroscopy* **2023**, *300*, 122959. <https://doi.org/10.1016/j.saa.2023.122959>.

- (8) Cai, S.; Singh, B. R. A Distinct Utility of the Amide III Infrared Band for Secondary Structure Estimation of Aqueous Protein Solutions Using Partial Least Squares Methods. *Biochemistry* **2004**, *43* (9), 2541–2549. <https://doi.org/10.1021/bi030149y>.
- (9) Ma, S.; Freedman, T. B.; Dukor, R. K.; Nafie, L. A. Near-Infrared and Mid-Infrared Fourier Transform Vibrational Circular Dichroism of Proteins in Aqueous Solution. *Appl Spectrosc* **2010**, *64* (6), 615–626. <https://doi.org/10.1366/000370210791414434>.
- (10) Schwaighofer, A.; Alcaráz, M. R.; Araman, C.; Goicoechea, H.; Lendl, B. External Cavity-Quantum Cascade Laser Infrared Spectroscopy for Secondary Structure Analysis of Proteins at Low Concentrations. *Sci Rep* **2016**, *6* (1), 33556. <https://doi.org/10.1038/srep33556>.
- (11) Schwaighofer, A.; Alcaraz, M. R.; Lux, L.; Lendl, B. pH Titration of  $\beta$ -Lactoglobulin Monitored by Laser-Based Mid-IR Transmission Spectroscopy Coupled to Chemometric Analysis. *Spectrochimica Acta Part A: Molecular and Biomolecular Spectroscopy* **2020**, *226*, 117636. <https://doi.org/10.1016/j.saa.2019.117636>.
- (12) Keiderling, T. A.; Lakhani, A. Conformational Studies of Biopolymers, Peptides, Proteins, and Nucleic Acids. A Role for Vibrational Circular Dichroism. In *Comprehensive Chiroptical Spectroscopy*; Berova, N., Polavarapu, P. L., Nakanishi, K., Woody, R. W., Eds.; Wiley, 2012; pp 707–758. <https://doi.org/10.1002/9781118120392.ch22>.
- (13) Murphy, B. M.; Zhang, N.; Payne, R. W.; Davis, J. M.; Abdulfattah, A. M.; Matsuura, J. E.; Herman, A. C.; Manning, M. C. Structure, Stability, and Mobility of a Lyophilized IgG1 Monoclonal Antibody as Determined Using Second-Derivative Infrared Spectroscopy. *Journal of Pharmaceutical Sciences* **2012**, *101* (1), 81–91. <https://doi.org/10.1002/jps.22753>.
- (14) Butreddy, A.; Janga, K. Y.; Ajjarapu, S.; Sarabu, S.; Dudhipala, N. Instability of Therapeutic Proteins — An Overview of Stresses, Stabilization Mechanisms and Analytical Techniques Involved in Lyophilized Proteins. *International Journal of Biological Macromolecules* **2021**, *167*, 309–325. <https://doi.org/10.1016/j.ijbiomac.2020.11.188>.
- (15) Griffiths, P. R.; De Haseth, J. A. *Fourier Transform Infrared Spectrometry*, 1st ed.; Wiley, 2007. <https://doi.org/10.1002/047010631X>.
- (16) Mallamace, F.; Corsaro, C.; Mallamace, D.; Vasi, S.; Vasi, C.; Dugo, G. The Role of Water in Protein's Behavior: The Two Dynamical Crossovers Studied by NMR and FTIR Techniques. *Computational and Structural Biotechnology Journal* **2015**, *13*, 33–37. <https://doi.org/10.1016/j.csbj.2014.11.007>.
- (17) Akhgar, C. K.; Ramer, G.; Žbik, M.; Trajnerowicz, A.; Pawluczyk, J.; Schwaighofer, A.; Lendl, B. The Next Generation of IR Spectroscopy: EC-QCL-Based Mid-IR Transmission Spectroscopy of Proteins with Balanced Detection. *Anal. Chem.* **2020**, *92* (14), 9901–9907. <https://doi.org/10.1021/acs.analchem.0c01406>.
- (18) Vijayakumar, S.; Schwaighofer, A.; Ramer, G.; Lendl, B. Multivariate Curve Resolution -Alternating Least Squares Augmented with Partial Least Squares Baseline Correction Applied to Mid-IR Laser Spectra Resolves Protein Denaturation by Reducing Rotational Ambiguity. *Spectrochimica Acta Part A: Molecular and Biomolecular Spectroscopy* **2024**, *315*, 124228. <https://doi.org/10.1016/j.saa.2024.124228>.
- (19) Stani, C.; Vaccari, L.; Mitri, E.; Birarda, G. FTIR Investigation of the Secondary Structure of Type I Collagen: New Insight into the Amide III Band. *Spectrochimica Acta Part A: Molecular and Biomolecular Spectroscopy* **2020**, *229*, 118006. <https://doi.org/10.1016/j.saa.2019.118006>.
- (20) Pancoska, P.; Wang, L.; Keiderling, T. A. Frequency Analysis of Infrared Absorption and Vibrational Circular Dichroism of Proteins in D<sub>2</sub>O Solution: Frequency Analysis of Protein VCD and IR Spectra. *Protein Science* **1993**, *2* (3), 411–419. <https://doi.org/10.1002/pro.5560020313>.
- (21) Baumruk, V.; Keiderling, T. A. Vibrational Circular Dichroism of Proteins in H<sub>2</sub>O Solution. In *Fifth International Conference on the Spectroscopy of Biological Molecules*; Theophanides, T., Anastassopoulou, J., Fotopoulos, N., Eds.; Springer Netherlands: Dordrecht, 1993; pp 117–118. [https://doi.org/10.1007/978-94-011-1934-4\\_41](https://doi.org/10.1007/978-94-011-1934-4_41).
- (22) Saito, F.; Schreiner, P. R. Determination of the Absolute Configurations of Chiral Alkanes — An Analysis of the Available Tools. *Eur. J. Org. Chem.* **2020**, *2020* (40), 6328–6339. <https://doi.org/10.1002/ejoc.202000711>.
- (23) Ribeiro, A. R. L.; Maia, A. S.; Ribeiro, C.; Tiritan, M. E. Analysis of Chiral Drugs in Environmental Matrices: Current Knowledge and Trends in Environmental, Biodegradation and Forensic Fields. *TrAC Trends in Analytical Chemistry* **2020**, *124*, 115783. <https://doi.org/10.1016/j.trac.2019.115783>.
- (24) Nafie, L. A. *Vibrational Optical Activity: Principles and Applications*, 1st ed.; Wiley, 2011. <https://doi.org/10.1002/9781119976516>.
- (25) Ryu, S. R.; Czarnik-Matusewicz, B.; Dukor, R. K.; Nafie, L. A.; Jung, Y. M. Analysis of the Molten Globule State of Bovine  $\alpha$ -Lactalbumin by Using Vibrational Circular Dichroism. *Vibrational Spectroscopy* **2012**, *60*, 68–72. <https://doi.org/10.1016/j.vibspec.2012.02.006>.
- (26) Giugliarelli, A.; Sassi, P.; Paolantoni, M.; Morresi, A.; Dukor, R.; Nafie, L. Vibrational Circular Dichroism Spectra of Lysozyme Solutions: Solvent Effects on Thermal Denaturation Processes. *J. Phys. Chem. B* **2013**, *117* (9), 2645–2652. <https://doi.org/10.1021/jp311268x>.
- (27) Synytsya, A.; Judexová, M.; Hrubý, T.; Tatarkovič, M.; Miškovíčová, M.; Petruželka, L.; Setnička, V. Analysis of Human Blood Plasma and Hen Egg White by Chiroptical Spectroscopic Methods (ECD, VCD, ROA). *Anal Bioanal Chem* **2013**, *405* (16), 5441–5453. <https://doi.org/10.1007/s00216-013-6946-6>.
- (28) Tobias, F.; Keiderling, T. A. Role of Side Chains in  $\beta$ -Sheet Self-Assembly into Peptide Fibrils. IR and VCD Spectroscopic Studies of Glutamic Acid-Containing Peptides. *Langmuir* **2016**, *32* (18), 4653–4661. <https://doi.org/10.1021/acs.langmuir.6b00077>.
- (29) Mukherjee, S.; Gopinath, A.; Madhan, B.; Shanmugam, G. Vibrational Circular Dichroism Spectroscopy as a Probe for the Detection of Collagen Fibril and Fibrillation in Solution. *Biosensors and Bioelectronics: X* **2022**, *10*, 100108. <https://doi.org/10.1016/j.biosx.2022.100108>.
- (30) Faist, J.; Capasso, F.; Sivco, D. L.; Sirtori, C.; Hutchinson, A. L.; Cho, A. Y. Quantum Cascade Laser. *Science* **1994**, *264* (5158), 553–556. <https://doi.org/10.1126/science.264.5158.553>.
- (31) Isensee, K.; Kröger-Lui, N.; Petrich, W. Biomedical Applications of Mid-Infrared Quantum Cascade Lasers — a Review. *Analyst* **2018**, *143* (24), 5888–5911. <https://doi.org/10.1039/C8AN01306C>.
- (32) Lüdeke, S.; Pfeifer, M.; Fischer, P. Quantum-Cascade Laser-Based Vibrational Circular Dichroism. *J. Am. Chem. Soc.* **2011**, *133* (15), 5704–5707. <https://doi.org/10.1021/ja200539d>.
- (33) Phal, Y.; Yeh, K.; Bhargava, R. Concurrent Vibrational Circular Dichroism Measurements with Infrared Spectroscopic Imaging. *Anal. Chem.* **2021**, *93* (3), 1294–1303. <https://doi.org/10.1021/acs.analchem.0c00323>.
- (34) Sato, H.; Shimizu, M.; Watanabe, K.; Yoshida, J.; Kawamura, I.; Koshoubu, J. Multidimensional Vibrational Circular Dichroism Apparatus Equipped with Quantum Cascade Laser and Its Use for Investigating Some Peptide Systems Contain-

- ing D -Amino Acids. *Anal. Chem.* **2021**, 93 (5), 2742–2748. <https://doi.org/10.1021/acs.analchem.0c02990>.
- (35) Hermann, D. R.; Ramer, G.; Kitzler-Zeiler, M.; Lendl, B. Quantum Cascade Laser-Based Vibrational Circular Dichroism Augmented by a Balanced Detection Scheme. *Anal. Chem.* **2022**, 94 (29), 10384–10390. <https://doi.org/10.1021/acs.analchem.2c01269>.
- (36) Hermann, D.-R.; Ramer, G.; Riedlsperger, L.; Lendl, B. Chiral Monitoring Across Both Enantiomeric Excess and Concentration Space: Leveraging Quantum Cascade Lasers for Sensitive Vibrational Circular Dichroism Spectroscopy. *Appl Spectrosc* **2023**, 77 (12), 1362–1370. <https://doi.org/10.1177/00037028231206186>.
- (37) Hobbs, P. C. D. Shot Noise Limited Optical Measurements at Baseband with Noisy Lasers (Proceedings Only); Roy, R., Ed.; Boston, MA, 1991; pp 216–221. <https://doi.org/10.1117/12.25014>.
- (38) Erb, D. Pybaselines: A Python Library of Algorithms for the Baseline Correction of Experimental Data, 2024. <https://doi.org/10.5281/ZENODO.5608581>.
- (39) Virtanen, P.; Gommers, R.; Oliphant, T. E.; Haberland, M.; Reddy, T.; Cournapeau, D.; Burovski, E.; Peterson, P.; Weckesser, W.; Bright, J.; van der Walt, S. J.; Brett, M.; Wilson, J.; Millman, K. J.; Mayorov, N.; Nelson, A. R. J.; Jones, E.; Kern, R.; Larson, E.; Carey, C. J.; Polat, İ.; Feng, Y.; Moore, E. W.; VanderPlas, J.; Laxalde, D.; Perktold, J.; Cimrman, R.; Henriksen, I.; Quintero, E. A.; Harris, C. R.; Archibald, A. M.; Ribeiro, A. H.; Pedregosa, F.; van Mulbregt, P.; SciPy 1.0 Contributors; Vijaykumar, A.; Bardelli, A. P.; Rothberg, A.; Hilboll, A.; Kloeckner, A.; Scopatz, A.; Lee, A.; Rokem, A.; Woods, C. N.; Fulton, C.; Masson, C.; Häggström, C.; Fitzgerald, C.; Nicholson, D. A.; Hagen, D. R.; Pasechnik, D. V.; Olivetti, E.; Martin, E.; Wieser, E.; Silva, F.; Lenders, F.; Wilhelm, F.; Young, G.; Price, G. A.; Ingold, G.-L.; Allen, G. E.; Lee, G. R.; Audren, H.; Probst, I.; Dietrich, J. P.; Silterra, J.; Webber, J. T.; Slavič, J.; Nothman, J.; Buchner, J.; Kulick, J.; Schönberger, J. L.; de Miranda Cardoso, J. V.; Reimer, J.; Harrington, J.; Rodríguez, J. L. C.; Nunez-Iglesias, J.; Kuczynski, J.; Tritz, K.; Thoma, M.; Newville, M.; Kümmerer, M.; Bolingbroke, M.; Tartre, M.; Pak, M.; Smith, N. J.; Nowaczyk, N.; Shebanov, N.; Pavlyk, O.; Brodtkorb, P. A.; Lee, P.; McGibbon, R. T.; Feldbauer, R.; Lewis, S.; Tygier, S.; Sievert, S.; Vigna, S.; Peterson, S.; More, S.; Pudlik, T.; Oshima, T.; Pingel, T. J.; Robitaille, T. P.; Spura, T.; Jones, T. R.; Cera, T.; Leslie, T.; Zito, T.; Krauss, T.; Upadhyay, U.; Halchenko, Y. O.; Vázquez-Baeza, Y. SciPy 1.0: Fundamental Algorithms for Scientific Computing in Python. *Nat Methods* **2020**, 17 (3), 261–272. <https://doi.org/10.1038/s41592-019-0686-2>.
- (40) Provis-Evans, C. B.; Farrar, E. H. E.; Grayson, M. N.; Webster, R. L.; Hill, A. K. Highly Sensitive Real-Time Isotopic Quantification of Water by ATR-FTIR. *Anal. Chem.* **2020**, 92 (11), 7500–7507. <https://doi.org/10.1021/acs.analchem.9b05635>.
- (41) Dabrowska, A.; David, M.; Freitag, S.; Andrews, A. M.; Strasser, G.; Hinkov, B.; Schwaighofer, A.; Lendl, B. Broadband Laser-Based Mid-Infrared Spectroscopy Employing a Quantum Cascade Detector for Milk Protein Analysis. *Sensors and Actuators B: Chemical* **2022**, 350, 130873. <https://doi.org/10.1016/j.snb.2021.130873>.
- (42) Vijayakumar, S.; Rowlette, J.; Schwaighofer, A.; Lendl, B. Laser-Based Mid-Infrared Spectroscopy for Monitoring Temperature-Induced Denaturation of Bovine Serum Albumin and De-/Stabilization Effects of Sugars. *Anal. Chem.* **2023**, 95 (15), 6441–6447. <https://doi.org/10.1021/acs.analchem.3c00489>.

## Appendix B: Curriculum Vitae

### Daniel-Ralph Hermann

Email	hermann_daniel@gmx.at
ORCID ID	<a href="https://orcid.org/0000-0003-2605-8203">https://orcid.org/0000-0003-2605-8203</a>

### Education

<i>PhD candidate</i>	06/2020 – 07/2024
Technische Universität Wien, Institute of Chemical Technologies and Analytics, Wien (Austria)	
Topic: <i>“Vibrational Circular Dichroism in the liquid phase – Opportunities through mid-IR lasers”</i>	
Supervisor: Univ. Prof. Dipl.-Ing. Dr.techn. Bernhard Lendl	
<i>Master thesis</i>	02/2019 – 07/2019
Austrian Biotech University of Applied Sciences, Tulln (Austria)	
Topic: <i>“Application of SERS substrates in the characterization of prokaryotic and human cell systems”</i>	
Supervisor: Mag. Dr. Katerina Prohaska	
<i>Master of Sciences in Natural Sciences</i>	09/2017 – 09/2019
Austrian Biotech University of Applied Sciences, Tulln (Austria)	
Completed with distinction	
<i>Bachelor thesis</i>	02/2017 – 05/2017
University of Natural Resources and Life Sciences - Department of Biotechnology, Vienna (Austria)	
Topic: <i>“Investigation of cell culture media stability for growth and recombinant antibody production”</i>	
Supervisor: Univ.Prof. Dipl.-Ing. Dr.nat.techn. Renate Kunert	
<i>Bachelor of Sciences in Natural Sciences</i>	09/2014 – 09/2017
Austrian Biotech University of Applied Sciences, Tulln (Austria)	
Completed with merit	

### Positions

<i>Project assistant</i>	06/2020 – 07/2024
TU Wien, Institute of Chemical Technologies and Analytics, Vienna (Austria)	
<i>Research intern</i>	01/2020 – 06/2020
National University Galway, Department of Physical Chemistry, Galway (Ireland)	
<i>Research assistant</i>	09/2019 - 12/2019
Austrian Biotech University of Applied Sciences, Tulln (Austria)	

### Academic publications

- 1 Hermann, D.-R.; Ramer, G.; Riedlsperger, L.; Lendl, B. *Chiral Monitoring Across Both Enantiomeric Excess and Concentration Space: Leveraging Quantum Cascade Lasers for Sensitive Vibrational Circular Dichroism Spectroscopy*. *Appl Spectrosc* 2023, 77 (12), 1362–1370. <https://doi.org/10.1177/00037028231206186>.
- 2 Zimmermann, D.; Lilek, D.; Posch, N.; Hermann, D. R.; Pytel, N.; Herbinger, B.; Prohaska, K. *Classification of Single Cells by Raman Spectroscopy and Machine Learning: Comparison of Common Algorithms*. In *Scientific Computing 2023 Conference Proceedings*; Verlag der FH JOANNEUM Gesellschaft mbH: Graz, 2023; Vol. 1, pp 12–19.
- 3 Lendl, B.; Hermann, D.-R.; Ramer, G.; Zeiler, M. *Enantiomeric Excess Determination by Quantum Cascade Laser Vibrational Circular Dichroism: A Chemometric Approach*. In *Photonic Instrumentation Engineering X*; Soskind, Y., Busse, L. E., Eds.; SPIE: San Francisco, United States, 2023; p 52. <https://doi.org/10.1117/12.2650526>.
- 4 Hermann, D. R.; Ramer, G.; Kitzler-Zeiler, M.; Lendl, B. *Quantum Cascade Laser-Based Vibrational Circular Dichroism Augmented by a Balanced Detection Scheme*. *Anal. Chem.* 2022, 94 (29), 10384–10390. <https://doi.org/10.1021/acs.analchem.2c01269>.
- 5 Hermann, D.-R.; Lilek, D.; Daffert, C.; Fritz, I.; Weinberger, S.; Rumpler, V.; Herbinger, B.; Prohaska, K. *In Situ Based Surface-Enhanced Raman Spectroscopy (SERS) for the Fast and Reproducible Identification of PHB Producers in Cyanobacterial Cultures*. *Analyst* 2020, 145 (15), 5242–5251. <https://doi.org/10.1039/D0AN00969E>.

## Conference contributions

- 1 Hermann, D.-R., Ramer, G., & Lendl, B. (2023). Towards chiral monitoring - Quantum cascade lasers for rapid vibrational circular dichroism. In *Anakon 2023 Book of Abstracts* (pp. 428–428). TU Wien.
- 2 Hermann, D.-R., Ramer, G., Riedlsperger, L., & Lendl, B. (2023). Chiral sensing for liquid analysis – Synergies between Quantum Cascade Lasers and Vibrational Circular Dichroism. In *ICAVS12: 12th International Conference on Advanced Vibrational Spectroscopy: Abstract Book* (pp. 344–344). Faculty of Chemistry Jagiellonian University in Krakow.
- 3 Hermann, D.-R., Ramer, G., & Lendl, B. (2022, October 6). *Rapid Vibrational Circular Dichroism – Opportunities through the combination of External Cavity Quantum Cascade lasers and balanced detection* [Conference Presentation]. SciX 2022 (Covington, KY), Covington, United States of America (the).
- 4 Hermann, D.-R., Ramer, G., & Lendl, B. (2022, July 19). *Balanced detection combined with a Quantum Cascade laser for rapid Vibrational Circular Dichroism* [Poster Presentation]. The 32nd International Symposium on Chirality, Chicago, United States of America (the).
- 5 Hermann, D.-R., Ramer, G., & Lendl, B. (2022, May 14). *Fast investigation of chirality: Balanced detection and Quantum Cascade Lasers for improved Vibrational Circular Dichroism* [Conference Presentation]. 10. ASAC Junganalytikerinnenforum, Tulln, Austria.
- 6 Hermann, D.-R., Ramer, G., KITZLER-ZEILER, M., & Lendl, B. (2022, April 12). *Quantum Cascade laser based VCD characterised by a high temporal resolution* [Conference Presentation]. SpringSciX 2022 (University of Liverpool, UK), Liverpool, United Kingdom of Great Britain and Northern Ireland (the).